Investigation and development of power-generating building material systems based on air-cathode microbial fuel cell using *Geobacter sulfurreducens*

Vom Fachbereich
Bau- und Umweltingenieurwissenschaften
der Technischen Universität Darmstadt
zur Erlangung des akademischen Grades eines
Doktor-Ingenieur (Dr.-Ing.)
Genehmigte

Dissertation

eingereicht von

M. Sc. Shifan Zhang

Darmstadt 2023

Referent: Prof. Dr.ir. E.A.B. Koenders
Korreferent: Prof. Dr. Susanne Lackner

Acknowledgements

Abstract

The increasing environmental pollution, carbon emissions, and limited fossil fuel reserves necessitate the gradual replacement of fossil fuels with sustainable and renewable green energy sources. However, current green energy sources have specific requirements for their application, such as solar energy requiring sufficient sunlight and wind energy requiring sufficient wind without negative impacts on the environment. Hydrogen fuel cells are also gradually being utilized as a clean energy source. As a means of power generation, the key factor in fuel cells is the catalytic effect on the reaction. In nature, there exists a group of electrochemically active microorganisms that are widely distributed in soil and wastewater. They act as natural catalysts in fuel cells. Although these microbial fuel cells have seen significant improvements in power generation in recent years, their application has not been widely promoted due to cost.

Concrete is the most widely used building material in the world. Its low raw material cost, high compressive strength, and simple production process make it an attractive and easily applicable material in the field of construction and building. If mineral materials can be used to make fuel cells, the manufacturing cost would be greatly reduced, which would greatly benefit the development of fuel cells.

In order to use mineral materials as electrodes for fuel cells, they must have a low enough electrical resistance. This PhD research is based on the theory of percolation and studies two types of building materials, Portland cement and geopolymer, from a microstructural perspective. By comparing their differences in microstructure and the changes in electrical conductivity of their mixes in dry and wet conditions, it is found that when the volume fraction of conductive fillers exceeds its percolation threshold, the overall electrical conductivity of the composite is no longer related to its water content. In other words, the conductive mechanism in the mix is mainly in the form of electronic conduction, and the ionic conduction in the solution has little impact on the electrical conductivity of the mix. The geopolymer, due to their excellent microstructure, make it possible for direct electronic transitions of conductive fillers. Therefore, graphite-geopolymer composite have better electronic conductivity than graphite-portland cement composite at the same graphite content.

To study the conductive mechanism of geopolymer and graphite mixture more in-depth, a Monte Carlo method was employed to simulate the percolation threshold of the mixture. The model, based on the HYMOSTRUC3D framework, is a three-dimensional model that considers the particle size distribution, and it can accurately describe the spatial distribution and interactions of different particles. By introducing the concept of effective volume fraction, the influence of pores on the mixture was eliminated. The effective medium model simulated the relationship between the overall electrical conductivity and graphite effective volume fraction, which was consistent with experimental data.

The microstructural properties of geopolymers make it possible to create high-performance electrical conductive materials using low-cost graphite particles. The porous structure of this mixture also

provides necessary growth space for microorganisms, leading to the formation of more biofilm. In order to verify the feasibility of this mineral-based electrode as a microbial fuel cell, a single-strain *Geobacter sulfurreducens* culture was used to cultivate a dual-chamber microbial fuel cell. During the one-week testing period, the microbial fuel cell with the graphite geopolymer anode had a peak operating current density of 155.9 A·s/cm² even higher than the operating current density of 144.5 A·s/cm² with graphite as the electrode.

This research also explored the feasibility of large-scale application of microbial fuel cells using the mineral-based electrode. The study found that the mineral-based electrode can be used to power a green LED light, and by connecting 224 soil-based microbial fuel cells in series and parallel, and creating a control board for energy collection, it was possible to power a lighting system in a bike shed. The Ph.D. thesis demonstrates the feasibility of using mineral-based materials as electrodes in microbial fuel cells and explains the conductive mechanism in the composite. Due to its superior electrical conductivity, the mineral-based material can also be used in other types of fuel cells and even rechargeable batteries.

Table of contents

x

List of Symbols

k_{IET}^0	heterogeneous electron transfer rate	-
W_{elec}	electrical work	J
ΔG_r	Gibbs free energy for the specific conditions	J
ΔG_r^0	Gibbs free energy under standard conditions	J
R	universal gas constant, 8.31447	J mol^{-1} K^{-1}
T	absolute temperature	K
E	the electric field strength gradient	V/m
ΔE	uncertainty of energy	J
Δt	uncertainty of time	s
Δx	distance between the two graphite particles	m
$\hbar$	reduced Planck constant, 1.054571800 x 10^{-34}	-
E_{emf}	potential difference between the cathode and anode	V
E_{emf}^0	standard cell electromotive force	J
E_{cell}	electric potential	V
Q	the Charge transferred in the reaction	C
n	number of electrons per reaction mol	-
F	Faraday's constant, 96485	C/mol
E_{emf}	potential difference between the cathode and anode	J
p	stoichiometric coefficients for product	-
r	stoichiometric coefficients for reactants	-
η_{act}	activation loss	J
η_{ohmic}	ohmic loss	J
η_{conc}	concentration loss	J
σ_p	conductivity of the solution	S/m
e	electron charge	C
Z_i	chemical valence of the i-th free ion	-
γ_i	ion electromobility	m^2/(s·V)
C_i	the concentration of the ions in solution	mol/m^3
v_i	the rate of migration of free electrons	m/s
ρ	the resistivity	Ω·m
R	the resistance	Ω
A	the cross-section area	m^2
L	the length	m
ΔE_{MN}	voltage difference between points M and N	V
R_{MN}	the resistance between points M and N	Ω
I	current flow	A

A	the cross-section area	m^2
σ	Electrical conductivity	S/m
a	a constant	-
k	Boltzmann constant	-
ΔE_p	local polarization energy across the barrier	J
τ	tunneling factor	-
σ_{eff}	effective conductivity of the composite	S/m
σ_0	conductivity of the conductive phase	S/m
σ_1	conductivity of the low-conductivity phase	S/m
φ_2	volume fraction of the conductive phase	-
φ_c	percolation threshold	-
k_E	the Einstein coefficient	-
Φ_{max}	maximum packing fraction of the dispersed particles	-
V_{eff}	effective volume fraction	-
$V_{graphite}$	volume of graphite particle	-
V_{solid}	volumes of graphite and other solid phases	-
Y	fraction of particles smaller than size x	-
D_n	particle size for which Y = 1/e (about 0.37)	-
n	shape parameter that characterizes the slope of the distribution function	-
$G(x)$	cumulative distribution function	-
x	particle size	-
b	fitting parameter	-
n	distribution parameter	-
φ_i	current conductive percolation threshold	-
φ_a	the average value of all φ_i	-
R_{int}	internal resistance	Ω
R_{ext}	external resistance	Ω

List of abbreviations

ACS	American Chemical Society
AFM	Atomic force microscopy
FM	Atomic force microscopy
BES	Bioelectrochemical system
BET	Brunauer, Emmett and Teller
BSE	Back scattered electron
CB	Carbon black
CE	Counter electrode
CEM	Cement
CLSM	Confocal laser scanning microscope
CM	Composite material
CNT	Carbon nanotubes
DC	Direct current
DECHEMA	Deutsche Gesellschaft für chemisches Apparatewesen
DET	Direct electron transfer
DFI	DECHEMA Research Institute
DIN	Deutsche Industrie-Norm
DNA	Deoxyribonucleic acid
DSMZ	Deutsche Sammlung von Mikroorganismen und Zellkulturen
EAM	Electrochemically active microorganisms
EDS	Energy Dispersive Spectroscopy
EET	Extracellular electron transfer
EFM	Electrostatic force microscopy
EG	Expanded graphite
EIS	Electrochemical impedance measurements
EMT	Effective Medium Theory
EN	European Norm
EPS	Extracellular polymeric substance
ESA	Electroactive surface area
GIC	Graphite intercalation compound
GNP	Graphite nanoplatelets
GP	Geopolymer
GPG	Geopolymer graphite Composite
Gtoe	Gigatonne of Oil Equivalent
HDPE	High density polyethylene
IET	Indirect electron transfer

ISO	International Organization for Standardization
IUPAC	International Union of Pure and Applied Chemistry
LDPE	Low density polyethylene
LED	Light-emitting diode
LOI	Loss on ignition
MEC	Microbial electrosynthesis
MET	Mediated electron transfer
MFC	Microbial fuel cell
MG	Maxwell-Garnett
MIP	Mercury intrusion porosimetry
MK	Metakaolin
MPPT	Maxim power point tracking
NFG	Natural flake graphite
NHE	Normal hydrogen electrode
OCV	Open circuit voltage
OD_{600}	Optical density at λ = 600 nm
OD_{MW}	Average value of OD_{600}
OD_{Target}	Target value of the optical density
PC	Portland Cement
PCE	Polycarboxylate ether
PCG	Portland cement graphite composite
PE	Polyethylene
PEM	Proton exchange membrane
PSA	Projected surface area
PSD	Particle size distribution
PT	Percolation threshold
REV	Representative elementary volume
RT	Room temperature
RVC	Reticulated vitreous carbon
SEM	Scanning electron microscope
SSA	Specific surface area
SD	Standard deviation
TEM	Transmission electron microscopy
TT	40 degrees 7 days constant temperature
WE	Working electrode

1 General introduction

1.1 Research background

The global economy's energy consumption, which drives human society, is mainly dependent on fossil fuels. As the world economy becomes more globalized and commercial expansion accelerates, human progress brings increasing complications, including water pollution, environmental degradation, energy scarcity, uneven energy distribution, and ecological damage. In the coming years, energy costs will likely play a major role in shaping human economic development and lifestyle, and could ultimately impact the progress of human civilization as energy is fundamental for human survival. The continued reliance on fossil fuels leads to the emission of large amounts of harmful gases, such as CO_2, NO_x, and hydrofluorocarbons. To address energy scarcity and environmental pollution, researchers are constantly searching for new alternative energy sources. The European Commission's Joint Research Centre's 2020 energy report found that primary energy demand has grown from around 9.6 Gtoe (Gigatonne of Oil Equivalent) in 2000 to around 14.8 Gtoe in 2020, where it reached its peak) [1]. Over the next 30 years, primary energy demand will need to decrease to around 13.1 Gtoe. Alongside this decline in overall demand, the energy mix will also gradually be transformed starting in 2020 and will be completed over the next 30 years. The implementation of climate policies by countries and the increasing role of new technologies will shape the future evolution of the energy structure. Among these, renewable energy sources such as hydropower, bioenergy, solar energy, wind power, and geothermal energy will be the fastest-growing energy sources, increasing their share of primary energy demand to 59 % by 2050 (see Figure 1).
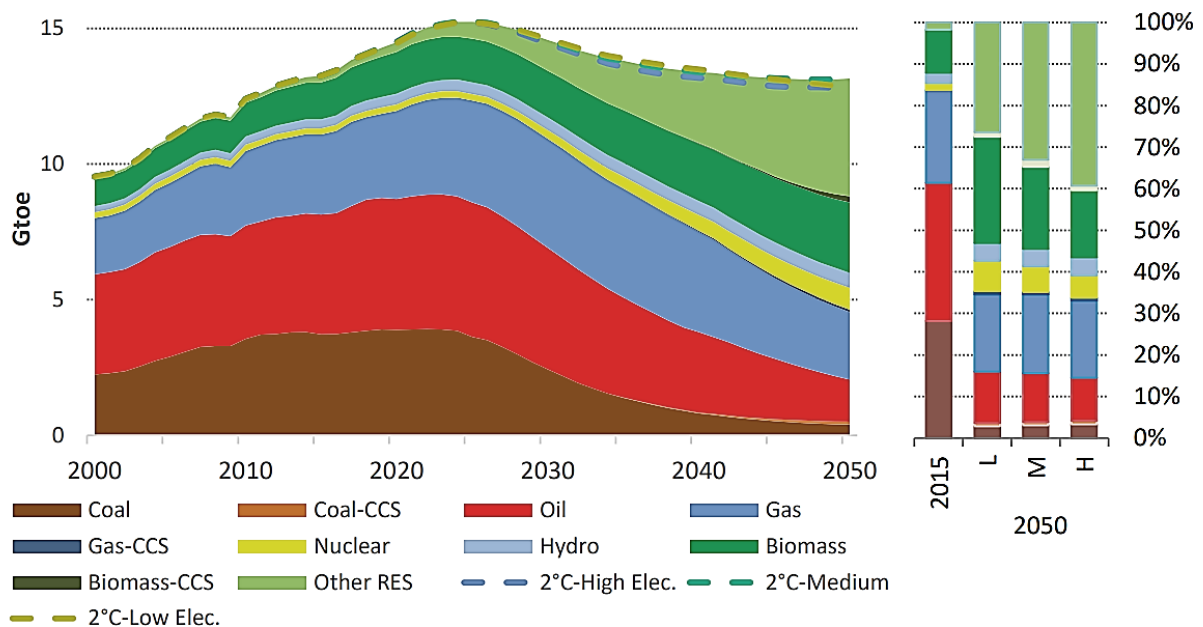
Figure 1: World primary energy demand by fuel 2000–2050, 2°C-Medium scenario [1].

Many renewable energy sources are highly dependent on environmental factors such as geographic location, solar radiation, and weather conditions. As demand for these technologies continues to grow, they are becoming increasingly integral to the modern energy system. Alongside improving existing renewable energy technologies, the development of novel green energy sources is also crucial.

Bioelectrochemical systems (BESs) have recently gained attention as an emerging technology for effectively recovering energy (electricity, methane, hydrogen, etc.) from waste [2]. BESs have shown significant potential for development and have emerged as a new area of research in environmental science, microbiology, and electrochemistry. Microbial fuel cells (MFCs), one of the earliest and most well-established aspects of BESs, utilize microbial catalysis to convert chemical energy directly into electrical energy [3].

1.2   Research objectives

In comparison to other energy sources, the power density of MFCs is significantly lower [4], which presents a significant limitation in their development. One potential solution to this issue is the large-scale stacking of MFCs [5], however, this approach increases cost and may not be feasible for widespread implementation. Cost is a major obstacle for the widespread application of MFCs. Even with the emergence of membraneless MFCs [6], the electrode remains a significant portion of total cost. The development of cost-effective electrodes with comparable power production efficiency could open up new opportunities for the advancement of MFCs. The study of MFCs encompasses multiple disciplines, including electrochemistry, microbiology, materials science and engineering, molecular biology, and environmental engineering [3]. Research in the field of MFCs typically focuses on a single aspect, such as the mechanisms behind extracellular electron transfer (EET), identification of electroactive bacteria, expanding the product spectrum, or optimization of reactor designs [7]. This thesis examines the potential for engineering applications of MFCs through the development of high-quality and cost-effective mineral electrode materials. The main objectives of the research include:

- Development and analysis of direct current (DC) electrical conductive multiphase porous electrodes using mineral materials.
- Use of computer-aided tools and Monte Carlo methods to simulate percolation thresholds and an effective medium theory to simulate the DC electrical conductivity of multiphase porous building materials.
- Testing and verification of the feasibility and influencing factors of the mineral anode using MFCs with *Geobacter sulfurreducens*.
- Exploration of the possibility of using mineral materials to make MFC cell stacks using soil-based MFCs.

Achieving these objectives will significantly advance the development of BESs and open new possibilities for the engineering application of MFCs.

1.3 Outline

The present thesis investigates the feasibility of using mineral materials as electrodes for MFCs. Its outline is shown in Figure 2. Firstly, the basic theory of BESs and the principles and models related to the DC conductivity of multiphase materials are introduced. Then, the design and development of mineral anodes are performed, followed by DC electrical conductivity simulations based on the Monte Carlo methods and effective medium theory. The electrochemical performance of MFCs using these mineral anodes was confirmed by analyzing the electrical conductivity and electrochemical experiments using *Geobacter sulfurreducens* as a single microbial strain. Finally, a prototype design is proposed and evaluated, and potential applications for large-scale implementation are outlined based on the performance of the outcomes.
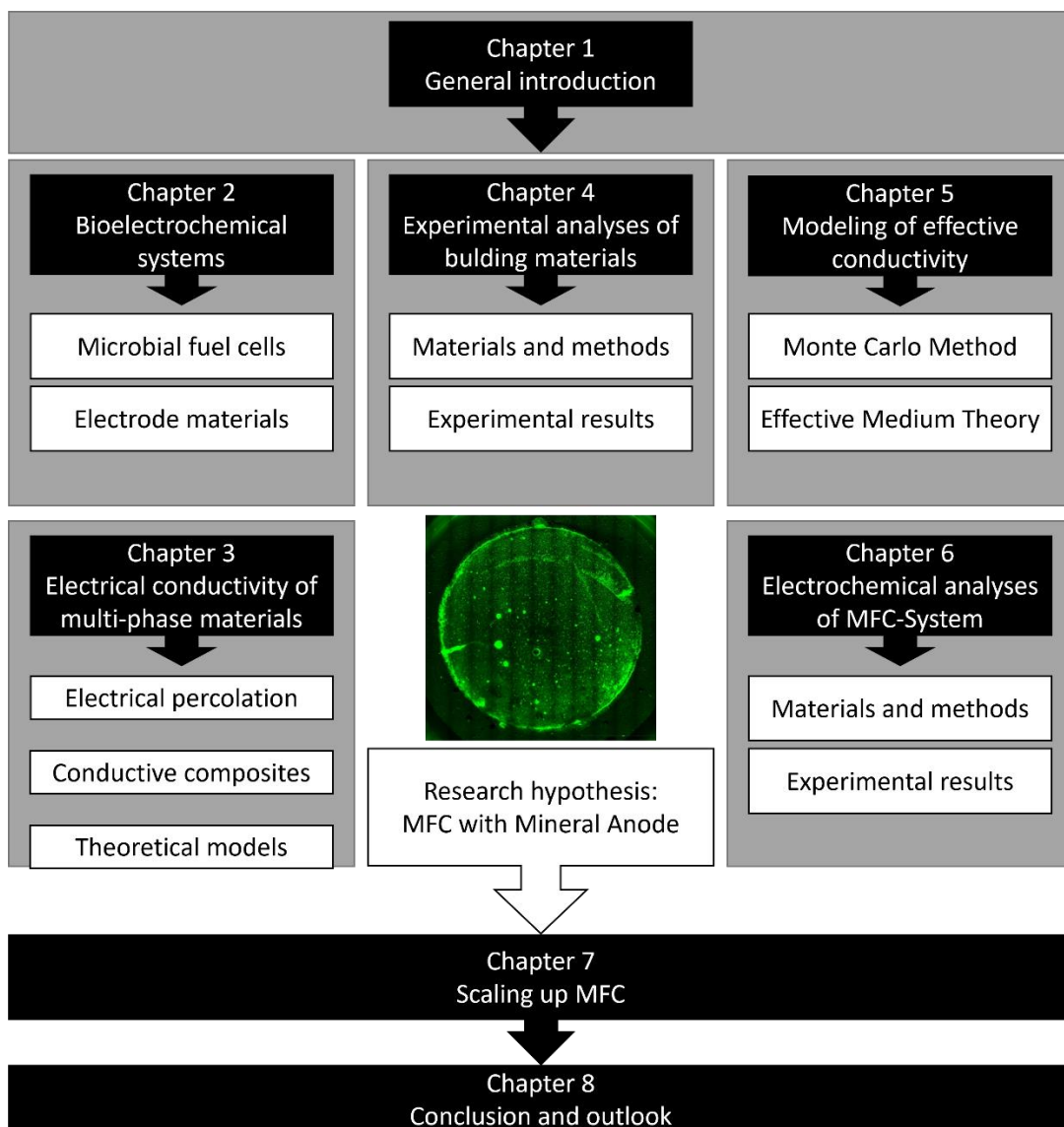
Figure 2: Outline of this thesis.

2 Bioelectrochemical systems

2.1 Introduction

The bioelectrochemical system is an emerging technology for the recovery of energy from biomass. This technology has two main applications: electricity production, such as in microbial fuel cells, and resource recovery, such as in microbial electrosynthesis (MEC). Logan & Rabaey [8] have provided an overview of anodic and cathodic reactions in bioelectrochemical systems (see Figure 3). This describes an overview of the anodic and cathodic reactions that occur in BESs. These reactions can be initiated by planktonic or biofilm cells, or through direct electrochemical catalysis. The anodic reactions involve the degradation of polymeric materials into simpler compounds, such as fatty acids and hydrogen, which can be used to generate electrical current. Other bioconversion reactions, such as the conversion of glycerol to ethanol, can also produce compounds that can be used for current generation. At the cathode, reactions can result in the generation of electrical power or the formation of additional products. The purple indicating reactions that do not directly generate current, green indicating reactions that can produce current, yellow indicating reactions that can occur spontaneously or can be accelerated with additional power, and orange indicating reactions that require additional power [8].
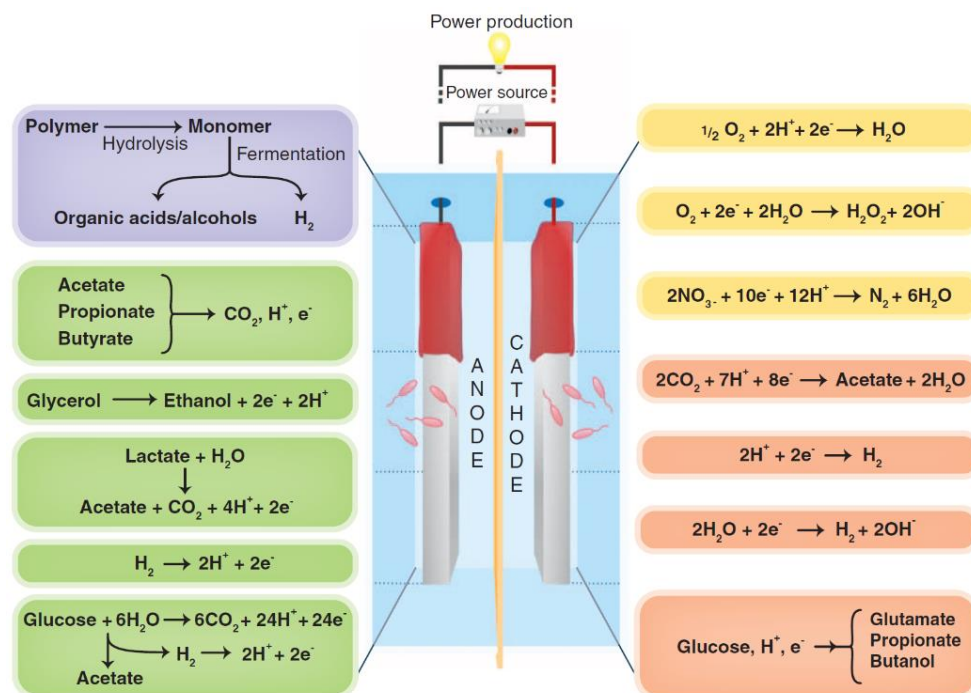
Figure 3: Schematic Representation of Anodic and Cathodic Reactions in Bioelectrochemical Systems. Purple indicates reactions that do not directly result in current generation; green, reactions that can produce current; yellow, reactions that can occur spontaneously or can be accelerated by adding additional power; orange, power addition is required [8].

This study focuses on air-cathode microbial fuel cells. The half-cell reaction at the anode primarily involves the generation of electrons and protons (H^+) by electricity-producing microorganisms through the oxidation of organic compounds. These generated electrons are then conducted to the cathode surface through the anode and external circuit. On the cathode side, the electron acceptor (oxygen) undergoes a reduction reaction through the synergistic action of electrons and protons conducted from the anode [9].

2.1.1 Electrochemically active microorganisms

Microorganisms are an essential component of bioelectrochemical systems, playing a critical role in the conversion of organic matter into electrical energy. The microorganisms that can be utilized in BESs are electrochemically active microorganisms (EAMs) [10]. EAMs are microorganisms that are capable of transferring electrons to or from an electrode surface. These microorganisms can be found in various environments, including freshwater and marine systems, soils, and industrial wastewaters [2], [8], [10]. The most well-studied EAMs are bacteria, with the majority being anaerobic [11], [12]. Anaerobic bacteria do not require oxygen to survive and grow. They can be further divided into two categories: facultative anaerobic bacteria and obligate anaerobic bacteria. Facultative anaerobic bacteria can survive in the presence or absence of oxygen, while obligate anaerobic bacteria require an oxygen-free environment to survive.

EAMs are commonly found in microbial fuel cells, where they act as catalysts to oxidize organic compounds and generate electrical current. Research on EAMs has mainly focused on understanding the mechanisms behind extracellular electron transfer (EET) and identifying potential EAMs for use in MFCs. Additionally, EAMs have been explored for their potential in other bioelectrochemical systems such as microbial electrosynthesis, bioremediation, and bioenergy production. Two commonly studied genera are *Shewanella* and *Geobacter* [13]. *Shewanella putrefaciens* [14] and *Shewanella oneidensis* [12] are both facultative anaerobic microbes capable of reducing iron oxides and transferring electrons directly to the anode of MFCs through the use of bacterial nanowires (see Figure 4-A). The Transmission electron microscopy image of biofilm of strain KN400 of *Geobacter sulfurreducens* grown on split anode [15] and SEM image of *Shewanella oneidensis* MR-1 [16] are shown in Figure 4. *Geobacter metallireducens* and *Geobacter sulfurrenducens* [17] also possess the ability to reduce iron and generate nanowires [18] (see Figure 4-B). In MFCs utilizing acetic acid as a substrate, the community structure shifts towards a dominance of *Geobacter,* resulting in a higher output current density [19] [20].

The utilization of pure microbial cultures in bioelectrochemical systems allows for a greater understanding of the mechanisms of electron transfer at the microbial level and a reduction in complexity compared to mixed cultures. However, many microorganisms found in nature exist in mixed communities, which can have a symbiotic relationship. Cao et al. [21] have shown that pure microbial cultures in MFC systems have a lower electricity generation capacity and are less adaptable to complex environments compared to mixed consortia. Future research should focus on optimizing the culture

control of multiple strains in MFCs, following a thorough understanding of the mechanisms of electricity production in pure cultures.
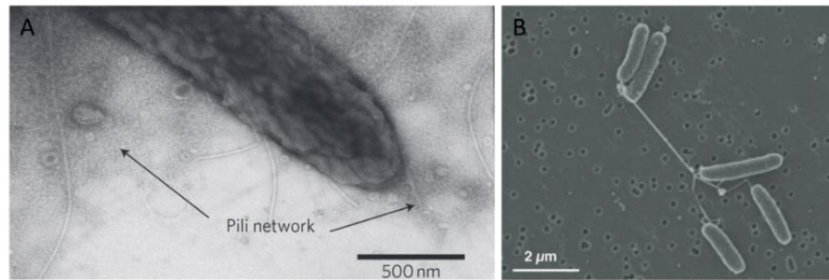
Figure 4: A: Transmission electron microscopy (TEM) image of biofilm of strain KN400 of *Geobacter sulfurreducens* grown on split anode [15]. Scale bar, 500 nm. B: SEM image of *Shewanella oneidensis* MR-1 [16].

2.1.2   Extracellular electron transfer mechanisms

The mechanism of microbial extracellular electron transfer in bioelectrochemical systems is not yet fully understood, but two main mechanisms have been proposed: direct electron transfer (DET) and mediated electron transfer (MET) [22]. As shown in Figure 5, DET occurs through conductive biofilms formed by microorganisms, where the microorganisms transfer electrons directly through conductive "nanowires" (indicated by red lines). MET, on the other hand, requires an intermediate medium for electron transfer. Both mechanisms may be present in a single microorganism, and the specific mechanism used by a microorganism may depend on the environment and conditions within the BES [23].
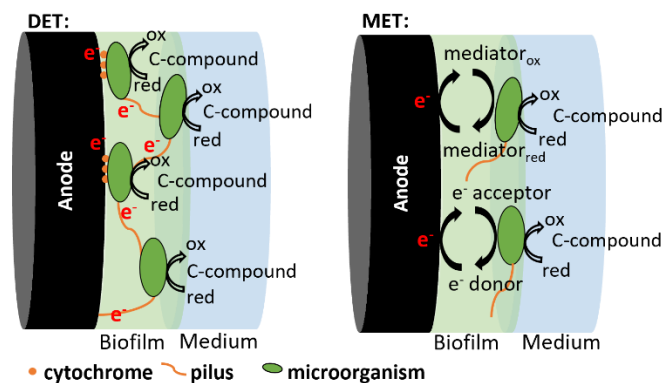
Figure 5: Different mechanisms of extracellular electron transfer: direct electron transfer (DET) and mediated electron transfer (MET), modified from Sydow [24].

Direct electron transfer

In MFCs, certain electrochemically active microorganisms have the ability to transfer electrons directly to the anode, which is known as direct electron transfer [18]. This mechanism requires the EAMs to be in close proximity to the electrode surface, and the efficiency of electron transfer can be hindered by the formation of biofilms that separate the microorganisms from the electrode surface.

Kim et al. [25] have shown that the amount of electron transfer is positively correlated with the biomass on the electrode surface and the electrode area. In 2003, Bond & Lovley [26] discovered that *Geobacter sulfurreducens* biofilms can transfer electrons to electrodes without the need for any intermediate electron carriers, which opened up new areas of research and led to the development of more efficient microbial electrochemical systems. The mechanism by which this occurs is thought to involve the transfer of electrons through "nanowires" within the biofilm, as observed through scanning channel microscopy [12], [18]. The existence of these nanowires has been further supported by experiments using atomic force microscopy to visualize electron flow through the nanowires generated by *Geobacter sulfurreducens* [27]. The electron transfer mechanism has been directly demonstrated by introducing an electric current into the nanowires and observing the electron flow using atomic force microscopy, as shown in Figure 6 [27]. Figure 6a presents images captured using Transmission electron microscopy (TEM) of cells expressing pili and flagellar filaments. Figure 6b illustrates a schematic representation of Atomic force microscopy (AFM) used to image intact pili and flagella. Figure 6c shows AFM images of cells with pili and flagellar filaments. Figure 6d displays the height profile of the pili (red) and flagellar filaments (black) at the positions shown in Figure 6c. Figure 6e through Figure 6g, respectively, depict the initial charge distribution on the filament (black) mapped in the first Electrostatic force microscopy (EFM) scan, the charge injected into the filament by gently touching the conducting AFM tip with a single point on the filament (the injected charge is shown as a white dot), and the propagation of the injected charge (in white) visualized in the second EFM scan.
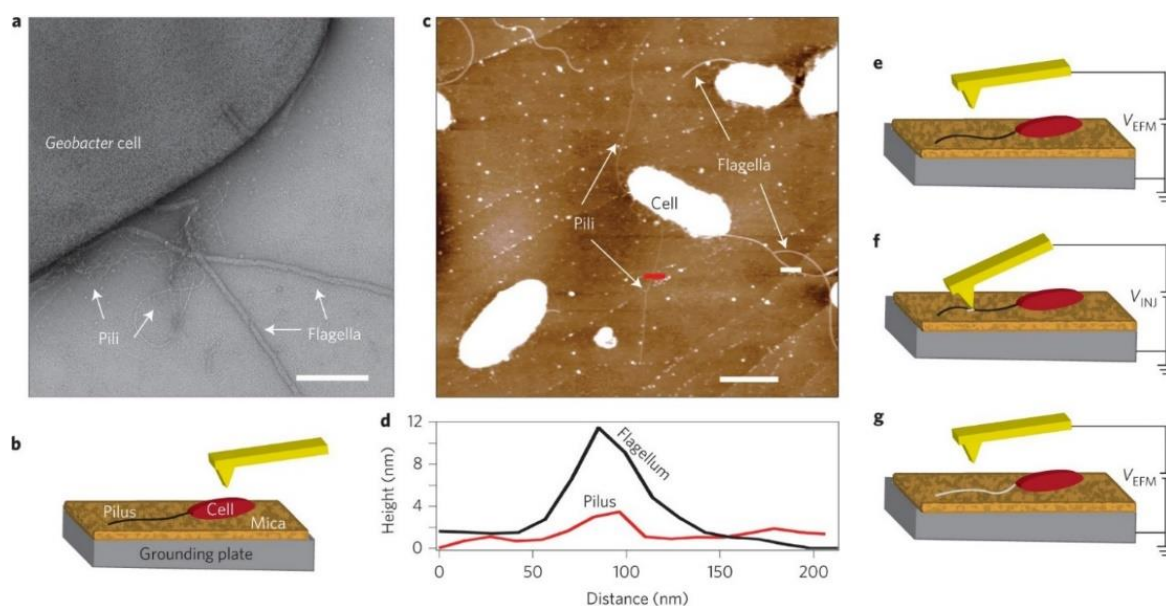
Figure 6: Strategy for direct visualization of charge propagation along native bacterial proteins with ambient EFM. a) presents images captured using Transmission electron microscopy (TEM) of cells expressing pili and flagellar filaments. b) illustrates a schematic representation of Atomic force microscopy (AFM) used to image intact pili and flagella. c) shows AFM images of cells with pili and flagellar filaments. d) displays the height profile of the pili (in red) and flagellar filaments (in black) at the positions shown in c). e) through g), respectively, depict the initial charge distribution on the filament (in black) mapped in the first Electrostatic force microscopy (EFM) scan, the charge injected into the filament by gently touching the conducting AFM tip with a single point on the filament (the

injected charge is shown as a white dot), and the propagation of the injected charge (in white) visualized in the second EFM scan [27].

Mediated electron transfer

In Microbial Fuel Cells, mediated electron transfer is a mechanism for the transfer of electrons from the microorganisms at the anode to the electrode. MET requires the presence of an electron mediator, which is a substance that facilitates the transfer of electrons between the microorganisms and the electrode. The electron mediator can be a chemical compound that is synthesized and added to the MFC system [28] or it can be a substance that is naturally excreted by the microorganisms themselves [29].

Indirect electron transfer by microorganisms has the advantage of high spatial and temporal yield. However, studies have shown that while many microbial communities are capable of spontaneously secreting electron transfer intermediates [30], kinetic analyses have shown that this mechanism still limits the rate of electron transfer, making direct electron transfer a preferred method in research and applications [31].

2.1.3   Biofilm formation

In microbial fuel cell systems, electrochemically active microorganisms often form biofilms in order to survive and reproduce in complex and dynamic environments [32]. Biofilm formation, the most common growth mode of microorganisms, is a dynamic process influenced by various factors and can be divided into five stages (Figure 7): Initial adhesion of cells, secretion of extracellular polymeric substance (EPS) to enhance adhesion, formation of micro-communities, maturation and differentiation of biofilm structure, and dissipation of cells [33], [34].
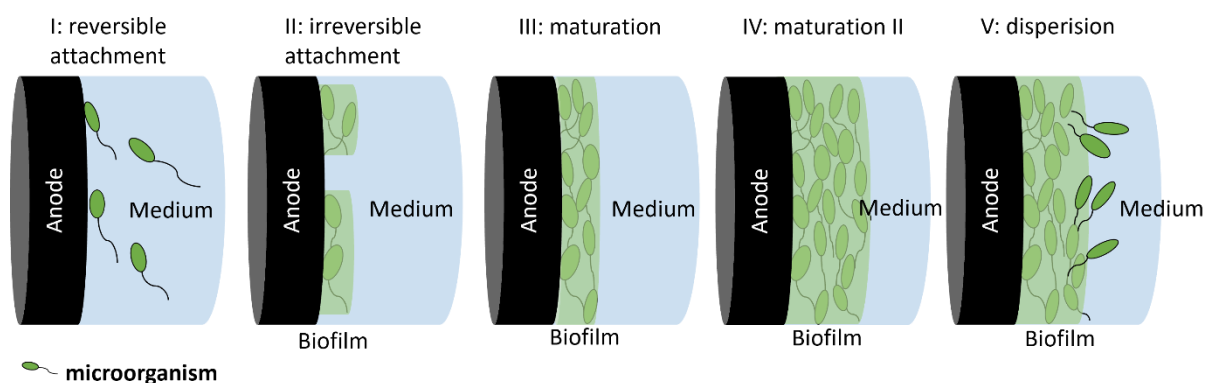
Figure 7: Schematic of the five stages of biofilm development modified from Monroe [35]. I: initial adhesion of cells, II: secretion of extracellular polymeric substance (EPS) to enhance adhesion, III: formation of micro-communities, IV: maturation and differentiation of biofilm structure, V: dissipation of cells.

The formation of biofilms in microbial fuel cells is a result of interactions between microorganisms and material surfaces. The properties of the material surface, such as electrostatic interactions, van der

Waals forces, surface energy, hydrophilicity, roughness, and functional chemical groups, can affect the attachment and membrane formation of microorganisms on the surface. These characteristics play a role in the adhesion behavior of cells to the material surface and the subsequent formation of the biofilm [36].

The interactions that occur when a microorganism approaches a material surface and develops adhesion are primarily electrostatic and van der Waals forces. The majority of bacterial cell surfaces carry a negative charge [37], allowing for the rapid and tight adhesion of bacteria to positively charged materials through electrostatic attraction. In a study by Terada et al. [38], the surface of polyethylene was modified to be both positively and negatively charged and it was found that the cell adhesion density of Escherichia coli was 23 times higher on the positively charged surface compared to the negatively charged surface. Furthermore, surface roughness and morphological patterns of materials have been shown to have significant effects on bacterial adhesion and biofilm formation [37], [38]. The roughness of a material can alter its surface energy and hydrophilicity, thus impacting cell adhesion [41]. Additionally, the initial adhesion of microorganisms and the formation of biofilms can be controlled by modifying the chemical properties of the material surface. Common methods of surface chemical modification include covalent modification, non-covalent modification, controlled release of small molecules, and degradation of polymeric surfaces [42].

The physical and chemical properties of the anode surface are intimately linked to the state of microbial membrane formation. Guo et al. [36] summarized impact of material surfaces on the electrode characteristics and microbial electrocatalysis in BES (Figure 8). Specific Surface Area (SSA) is a measure of the total surface area of an electrode per unit of projected surface area or electrode volume. It is used to estimate the total surface area available for electrochemical reactions. Projected Surface Area (PSA) is the largest two-dimensional area obtained from the projection of a planar surface or a 3-D material. It is used to estimate the total surface area available for microbial attachment. Electroactive Surface Area (ESA) is the actual surface area that is available for electrochemical reactions (i.e. solvated, electrically connected area). It can be used to estimate the total surface area available for microbial attachment and electron transfer. These properties are important for electrode characteristics and microbial electrocatalysis in bioelectrochemical systems because they affect the rate and efficiency of the electrochemical reactions taking place. A higher SSA, PSA, and ESA can lead to a higher rate of electron transfer and a greater efficiency of the bioelectrochemical system. Additionally, the ESA can be used to estimate the maximum current density that the electrode can sustain.

The influence of the properties of electrode materials from the nano- and micron-scale to the macro-scale on the electrocatalytic performance of microorganisms was analyzed. The properties of electrodes play a significant role in microbial electrocatalysis. The surface topography and chemistry of the electrodes influence the bioelectrocatalytic process at multiple levels, including adherence of cells, formation and structure of biofilms, and electrical connectivity between cells and electrodes through direct or indirect mechanisms. At the nanometer scale, the interactions at the single cell level are

influenced by the surface chemistry of the electrode, which is crucial for both direct and mediated electron transfer mechanisms. The effectiveness and stability of the initial attachment of microorganisms to the electrode surface is a crucial factor. Factors that influence this attachment include the specific surface area of the electrode, the hydrophilicity of the surface, the double layer formed at the electrode-electrolyte interface, the molecular mechanisms of electron transfer, the presence of anchoring points for the microorganisms, the toxicity of the surface, and the stability of the surface. At the micrometer scale, modifying the surface of electrodes at the microscale level increases the surface area for biofilm development and abiotic reactions. It is important to consider strategies for promoting the clustering of microorganisms and minimizing resistance to electron and ion transfer, such as optimizing the aspect ratio, specific surface area, and balancing the electrical conductivity and permeability of the material. Electrode types and configurations also have an impact on the process or operational level, influencing factors such as convection and flow path, system resistance, and overall performance parameters. It is important to consider these factors in order to optimize the efficiency and long-term operation of microbial fuel cells.
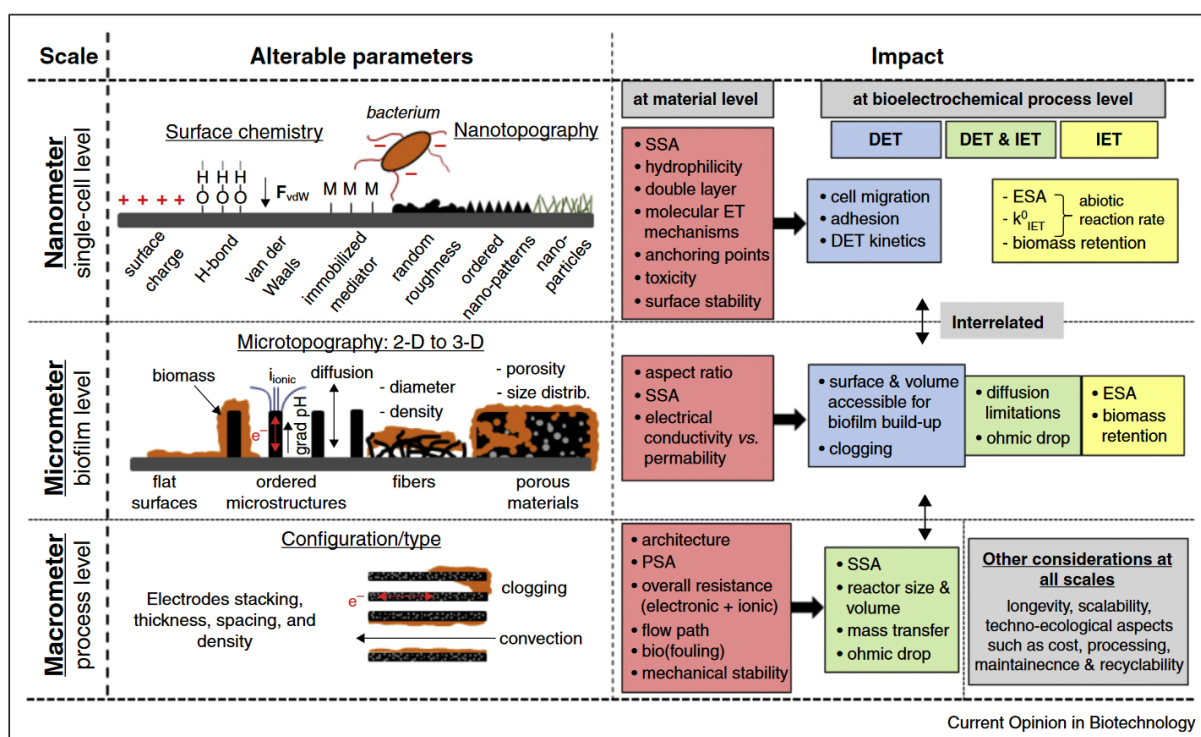
Figure 8: An overview of the impact of material surfaces on the characteristics of electrodes and microbial electrocatalysis in bioelectrochemical systems. 2-D/3-D: two/three-dimensional; DET: direct electron transfer; IET: indirect electron transfer; k_{IET}^0: heterogeneous electron transfer rate, constant for abiotic reaction; PSA: projected surface area; SSA: specific surface area [it is the total surface area of the electrode per unit of projected surface area or electrode volume; ESA: electroactive surface area [36].

The study of biofilms in microbial fuel cells typically involves analyzing them in two-dimensional environments. However, when the electrode used in the MFC is a porous material, the size of the pores in the three-dimensional electrode can greatly impact the formation and electrical production

performance of the biofilm. Bian et al. [43] have investigated the effect of pore size on MFC power production performance using 3D printing methods. They found that a pore size of 300 micrometers produced the highest maximum voltage and power density (see Figure 9: left). Additionally, the use of 3D porous carbon anodes was found to be more efficient for interfacial charge transfer and more biocompatible, leading to higher maximum voltages compared to carbon cloth anodes. The maximum power density generated by the MFC with carbon cloth anode reached 69.0 ± 4.7 mWm^{-2}, compared to 233.5 ± 11.6 mWm^{-2} attained by the 300 µm 3D printed carbonaceous porous anode (Figure 9: right). It was clearly shown in Figure 9 that the 3D printed carbonaceous porous anodes greatly enhanced the capability of power generation in MFCs and increased the power density by $22 - 238.4$ %, indicating the excellent electrochemical properties of 3D printed carbonaceous porous anodes. Maximum power densities from the *Shewanella* MR-1 culture decreased in the order: 300 µm > 200 µm > 400 µm > 100 µm > 500 µm > carbon cloth. Additionally, research has also been done on the thickness of biofilms on different types of electrodes [4], such as graphene, and the results showed that biofilms on 3D graphene anodes with 100 micrometer spacing can reach thicknesses of $150 - 200$ µm, while 2D graphene electrodes had biofilm thicknesses of only $20 - 40$ µm.
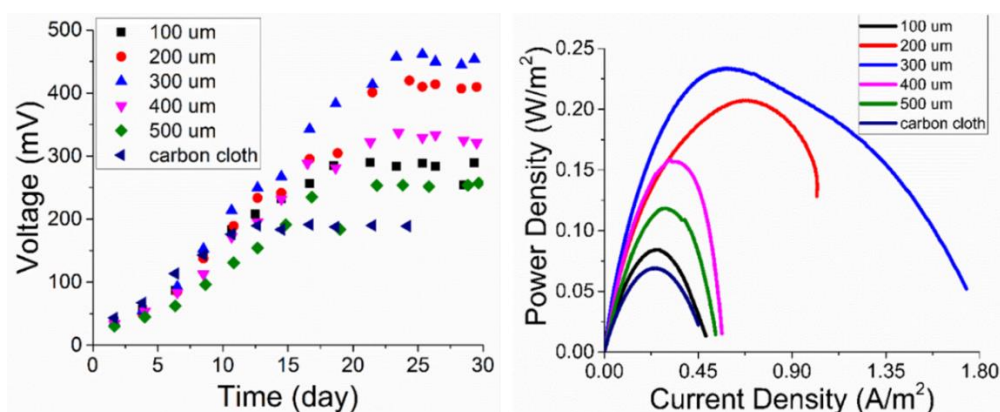
Figure 9: Left: Voltage generation of MFCs with 3D printed carbonaceous porous anodes with pore sizes of 100 – 500 µm and with a carbon cloth anode. Right: The power density curves of MFCs with with 3D printed carbonaceous porous anodes with pore sizes of 100 – 500 µm, based on the same projected surface area of the air-cathode (6 cm^2) [43].

2.2   Microbial fuel cells

The history of microbial fuel cell research can be traced back to 1911, when British botanist Potter [44] used platinum as an electrode and placed it in a culture medium containing *Escherichia coli* or common *yeast*, resulting in an open-circuit voltage of $0.33 - 0.5$ V and a current of 0.2 mA, thus initiating MFC research. In 1931, Cohen et al. [45] expanded on these observations by demonstrating that the potential of a vigorously growing bacterial culture reached 0.5-1 V compared to the control medium. In 1962, Rohrback et al. [46] designed the first MFC to generate electricity through glucose fermentation using *Clostridium butyricum* as an inoculum. In the 1980s, the widespread use of electronic transfer intermediates significantly improved the power output of MFCs, making them more practical for use as low-power power supplies. In 1984, Delaney et al. [47] improved MFCs and

validated MFC systems using a variety of microorganisms and intermediates, which were experimentally shown to increase both the rate of electron transfer and the rate of reaction. In the 21st century, researchers such as Bond et al. [48] used marine sediments to construct MFCs, and in 2004, Liu & Logan [49] successfully constructed an intermediate-free proton exchange membrane MFC with a maximum output power of 494 mW/m^2, drawing increased attention to MFCs. In 2005, Reguera et al. [18] discovered that the microorganism *Geobacter sulfurreducens* produces "nanowires" that facilitate electron transfer. This discovery led to the development of more specialized types of fuel cells. Two years later, Logan et al. [50] achieved an MFC with a maximum output of 2400 mW/m^2 using graphite fiber brushes as anodes. Tender et al. [51] reported on the utilization of MFCs to power weather buoys in 2008, marking the first recorded application of MFCs in literature. In 2018, Liao et al. [52] designed a soil-based microbial fuel cell, taking advantage of the naturally occurring diverse microorganisms in soil, including electrogenic bacteria and microorganisms rich in complex sugars and other nutrients. A schematic representation of the a forementioned historical milestones is depicted in Figure 10.
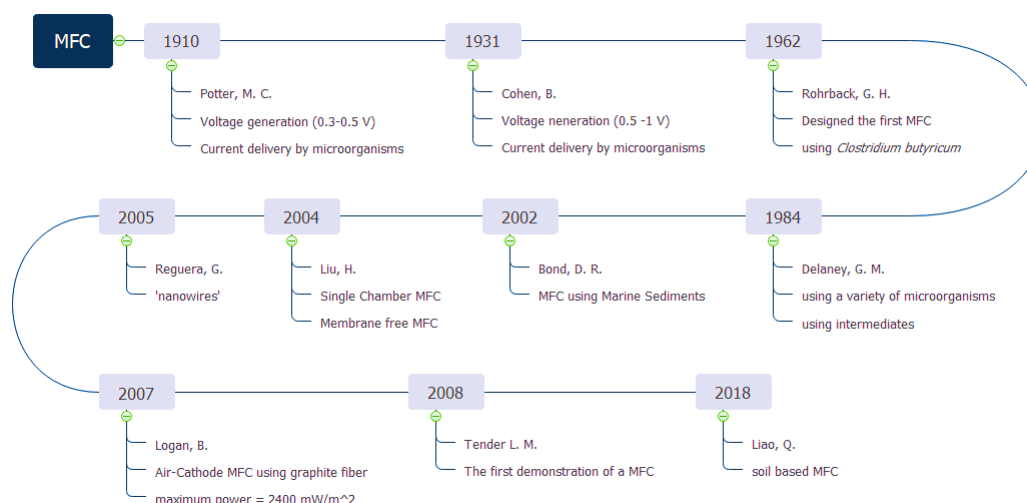
Figure 10: A schematic representation of the historical milestones of MFC.

In recent years, researchers have developed specific types of MFCs. As a type of bioelectrochemical system that uses microorganisms to convert organic matter into electrical energy, the potential applications of MFCs include:

- Wastewater treatment: MFCs can be used to treat and degrade organic pollutants in wastewater, while simultaneously generating electricity [53].
- Renewable energy generation: MFCs can be used to generate electricity from organic waste materials such as agricultural waste, food waste, or sewage [54].
- Remote power generation: MFCs can be used as a power source in remote or off-grid locations, such as in developing countries or in disaster-stricken areas [55].
- Sensors and monitoring: MFCs can be used to power sensors [56] and monitoring devices [57], such as in water quality monitoring systems.

- Industrial processes: MFCs can be integrated into industrial processes such as fermentation [58] and biorefining [59], to generate electricity and improve process efficiency.
- Autonomous power source: MFCs can be used as a sustainable power source for autonomous systems such as drones and underwater vehicles [60].

2.2.1 MFC set-up and configuration

The setup of an MFC typically consists of two main components: the anode and the cathode. The anode chamber is where the microorganisms reside and convert organic matter into electrons and protons through metabolic processes. The cathode chamber is where the electrons and protons are recombined to generate electrical energy [61].

MFCs can be designed in different configurations, such as double chamber, single chamber, and stacked, each with their own advantages and limitations (Figure 11). Double chamber MFCs consist of an anodic and a cathodic chamber that are connected externally through a wire and internally through a proton exchange membrane. The anodic chamber is anaerobic and the cathodic chamber is aerobic. This configuration allows for large-scale wastewater treatment to produce electricity. However, the cathodic chamber needs consistent solution replacement with aeration to provide oxygen. Single chamber MFCs have only one defined anodic chamber [49]. This design allows for power production at a small scale with less internal resistance, promoting low cost and high efficiency. However, it has limitations such as evaporation, high-rate oxygen diffusion, and liquid outflow. Stacked MFCs can be stacked in parallel or series to enhance power production. A parallel connection yields higher current output, while a series connection yields higher voltage output. Stacked MFCs can be further subdivided into horizontal and vertical stacks. High current density is achieved in parallel connections, and it is important to consider factors such as substrate flow rate, height, organic concentrations, and reactor volume when using stacked MFCs [53].
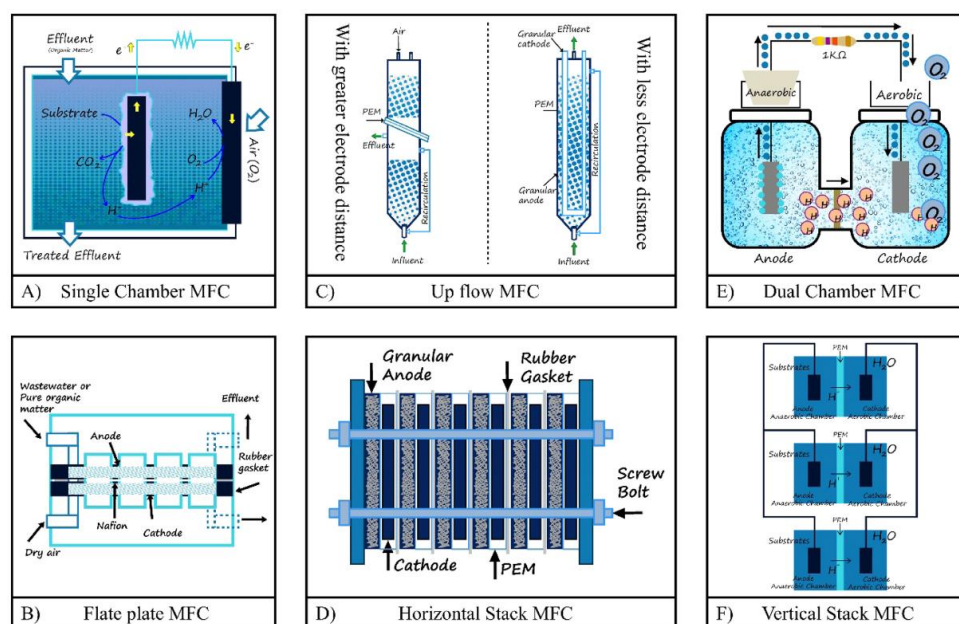
Figure 11: Schematic representation of different types of MFCs [53].

The most common type of MFC configuration is the dual-chamber MFC, also referred to as an H-cell [48], is depicted in Figure 12. In the anode chamber, microorganisms utilize nutrients in the anode fluid to produce electrons, protons, and metabolites, which are transferred to the anode surface through nanowires or carriers. These electrons are then transported to the cathode via an external circuit, while protons migrate to the cathode through a proton exchange membrane (PEM) in the solution [62]. At the cathode surface, oxidizing agents such as oxygen, combine with the protons and electrons transferred from the anode to form water [63]. The anode and cathode reactions are represented by equations (2-1) and (2-2) respectively.
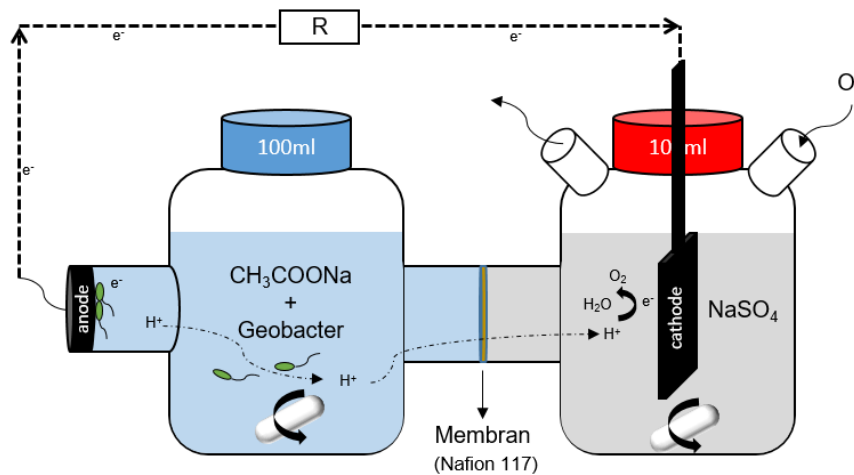
Figure 12: Schematic diagram of a microbial fuel cell (H-Cell).

Anodic half-reaction：

$$(CH_2O)_n + nH_2O \rightarrow nCO_2 + 4nH^+ + 4ne^- \qquad (2\text{-}1)$$
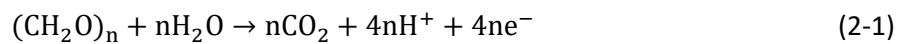
Cathodic half-reaction：

$$O_2 + 4H^+ + 4e^- \rightarrow 2H_2O \qquad (2\text{-}2)$$

2.2.2   Thermodynamics in MFC

The voltage generated by an MFC is a complex phenomenon that is influenced by multiple factors, including the time required for the microorganisms to establish themselves on the electrode, the presence of enzymes or structures necessary for electron transfer, and the potentials of different bacteria in mixed cultures. The thermodynamic relationships [64] between the electron donors and acceptors in the MFC also play a role in determining the maximum voltage that can be generated. By understanding these relationships, it is possible to gain a better understanding of the limitations of MFC operation.

Thermodynamics is the study [64]–[66] of energy conversions, and in microbial fuel cells, the energy stored in biomass is converted into electrical energy. According to the Gibbs free energy principle, the maximum electrical work that a system can do (W_{elec}) is equal to the negative change in Gibbs free energy of the system (ΔG_r) under isothermal and pressure conditions, as described in equation (2-3) [65]. This relationship provides insight into the maximum voltage that can be generated by the MFC based on the thermodynamic properties of the electron donors and acceptors involved in the process.

$$W_{elec} = -\Delta G_r = -(\Delta G_r^0 + RT\ln(\Pi)) \tag{2-3}$$

where W_{elec} [J] is the electrical work, ΔG_r [J] is the Gibbs free energy for the specific conditions, ΔG_r^0 [J] is the Gibbs free energy under standard conditions usually defined as 298.15 K, 1 bar pressure, and 1 M concentration for all species, R (8.31447 J mol^{-1} K^{-1}) is the universal gas constant, T [K] is the absolute temperature, and Π [unitless] is the reaction quotient calculated as the activities of the products divided by those of the reactants.

The electrical work W_{elec} achieved by moving the charge Q at a potential difference E_{emf} is shown in equation (2-4):

$$W_{elec} = E_{emf}Q \tag{2-4}$$

where E_{emf} [V] is the potential difference between the cathode and anode, and Q [C] is the charge transferred in the reaction. The transfer of charge in an MFC can be represented by the movement of electrons. This can be mathematically represented using equation (2-5):

$$Q = nF \tag{2-5}$$

where n is the number of electrons per reaction mol and F [C/mol] is the Faraday's constant equals 96485 C/mol.

From Equations (2-3), (2-4), and (2-5), the relationship between the overall cell electromotive force E_{emf} and the Gibbs free energy for the specific conditions ΔG_r is shown in equation (2-6) as follows.

$$E_{emf} = -\frac{\Delta G_r}{nF} = -\frac{\Delta G_r^0}{nF} - \frac{RT}{nF}ln(\Pi) \tag{2-6}$$

where E_{emf} [J] is the potential difference between the cathode and anode, ΔG_r [J] is the Gibbs free energy for the specific conditions, ΔG_r^0 [J] is the Gibbs free energy under standard conditions usually defined as 298.15 K, 1 bar pressure, and 1 M concentration for all species, R (8.31447 J mol^{-1} K^{-1}) is the universal gas constant, T [K] is the absolute temperature, n is the number of electrons per reaction mol and F [C/mol] is the Faraday's constant equals 96485. Π is the reaction quotient, which means the ratio of the activities of the products divided by the reactants raised to their respective stoichiometric coefficients. By the International Union of Pure and Applied Chemistry (IUPAC) convention, all reactions are written in the direction of chemical reduction, so that the products are always the reduced species, and the reactants are the oxidized species (oxidized species + e- ->reduced species). Also by IUPAC convention, the standard conditions means a temperature of 298 K, and chemical concentrations of 1 M for liquids and 1 bar for gases (1 bar = 0.9869 atm=100 kPa). All values of E_{emf}^0 are calculated with respect to that of hydrogen under standard conditions, which is defined to be $E_{emf}^0(H_2) = 0$, referred to as the "normal hydrogen electrode" (NHE). Thus, the standard potentials for all chemicals is obtained with $\Pi = 1$, relative to a hydrogen electrode [66]. If all reactions are evaluated at standard conditions, $\Pi = 1$, then:

$$E_{emf}^0 = -\frac{\Delta G_r^0}{nF} \qquad (2\text{-}7)$$

where E_{emf}^0 [J] is the standard cell electromotive force, ΔG_r^0 [J] is the Gibbs free energy under standard conditions usually defined as 298.15 K, 1 bar pressure, and 1 M concentration for all species, n is the number of electrons per reaction mol and F [C/mol] is the Faraday's constant equals 96485.

The standard free energy change of the overall reaction, ΔG_r^0, can be derived from the tabulated standard free energy change of the standard state, ΔG_f^0, using the following relationship:

$$\Delta G_r^0 = \Sigma\, \Delta G_f^0 \text{ (Products) - } \Sigma\, \Delta G_f^0 \text{ (Educts)} \qquad (2\text{-}8)$$

The potential generated by a fuel cell can be determined through the energy balance between the reactants and products. The theoretical cell potential, also known as the maximum electromotive force (E_{emf}), can be calculated using Nernst equation and is represented by equation [65], [66]

$$E_{emf} = E_{emf}^0 - \frac{RT}{nF}\ln(\Pi) = E_{emf}^0 - \frac{RT}{nF}\ln\left(\frac{[products]^p}{[reactants]^r}\right) \qquad (2\text{-}9)$$

where E_{emf} is the maximum electromotive force, E^0_{emf} is the standard cell electromotive force, R is constant which equals 8.3144 [J/(mol·K)], T is the solution temperature [K], n is the Number of electron transfers, F is the Faraday constant which equals 96485 [C/mol], Π = [product] ^{p}/[reactants] ^{r}, p and r are the stoichiometric coefficients.

Acetate is commonly used as an exemplary fuel for microbial fuel cells (MFCs) because it is readily biodegradable and can be easily used by a wide range of microorganisms. Additionally, acetate is a common intermediate in many microbial metabolism pathways and is often present in wastewaters, making it an easily accessible fuel source. The use of acetate as a fuel in MFCs allows for the study and optimization of the microbial metabolism and electrochemical processes involved in the MFC system.

Electrode reactions of microbial fuel cells using acetate as an exemplary fuel are described below:

Anodic reaction [55] [56]: $CH_3COO^- + 4H_2O \rightarrow 2HCO_3^- + 9H^+ + 8e^-$

Cathodic reaction [56] [67]: $2O_2 + 8H^+ + 8e^- \rightarrow 4H_2O$

Overall reaction: $CH_3COO^- + 2O_2 \rightarrow 2HCO_3^- + H^+$
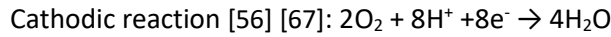
Table 1 shows the standard free energy of the reactants and products of each phase [68]. For the overall reaction, their ΔG^0_r and ΔE^0_{emf} values are calculated as follows:

(Overall reaction: $CH_3COO^- + 2O_2 \rightarrow 2HCO_3^- + H^+$)

ΔG^0_r = (2*(- 586.85) + 0) kJ mol^{-1} − (- 369.41 + 2*0) kJ mol^{-1}

= -804.29 kJ mol^{-1}

$$E^0_{emf} = -\frac{\Delta G^0_r}{nF} = \frac{-804.29 \text{ kJ mol}^{-1}}{8 \cdot 96500 \text{ C mol}^{-1}} = 1.042 \text{ V}$$

Table 1: Gibbs free energy under standard conditions [68].

Substance	O_2	H_2O	H^+	HCO^{3-}	CO_2	Acetate$^-$
ΔG^0_f at 25°C kJ mol^{-1}	0	-237.178	0	-586.85	-	-369,41

Similarly, the potential of the half-cell reaction can be calculated (based on the standard hydrogen electrode SHE) and therefore the individual electrodes. It must be taken into account that, according to IUPAC convention, the anode reaction must be reversed in order to make the product a reducing variety. This leads to:

(Anodic reaction [55] [56]: $2HCO_3^- + 9H^+ + 8e^- \rightarrow CH_3COO^- + 4H_2O$)
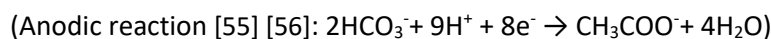
ΔG^0_{Anode} = (-369.41 + 4*(-237.178)) − (2*(-586.85) + 9*0) kJ mol^{-1}

= -144.422 kJ mol^{-1}

$$E^0_{Anode} = -\frac{\Delta G^0_{Anode}}{nF} = \frac{144.422 \text{ kJ mol}^{-1}}{8 \cdot 96500 \text{ C mol}^{-1}} = 0.187 \text{ } V \text{ vs. SHE}$$

(Cathodic reaction [56]: $2O_2 + 8H^+ + 8e^- \rightarrow 4H_2O$)

$\Delta G^0_{Cathode}$ = (4*(-237.178 kJ mol^{-1})) − (2*0 + 8*0)

= -948.712 kJ mol^{-1}

$E^0_{Cathode} = -\dfrac{\Delta G^0_{Cathode}}{nF} = \dfrac{948.712 \text{ kJ mol}^{-1}}{8 \cdot 96500 \text{ C mol}^{-1}} = 1.229 \; V$ vs. SHE

For acetate, the E^0_{Anode}=0.187 V, with a concentration of 1 g/L (16.9 mM) and under conditions of neutral pH = 7 and an alkalinity set by the bicarbonate concentration of HCO_3^- = 5 mM, The anodic potential is:

$2HCO_3^- + 9H^+ + 8e^- \rightarrow C_2H_3O_2^- + 4H_2O$
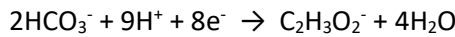
$$
\begin{aligned}
E_{Anode,emf} \quad &= E^0_{Anode} - \frac{RT}{8F} \ln\left(\frac{[CH_3COO^-]}{[HCO_3^-]^2[H^+]^9}\right) \\[2mm]
&= 0{,}187 - \frac{8{,}31 \dfrac{J}{mol \cdot K} \times 298.15K}{8 \times 9{,}65 \times \dfrac{10^4 C}{mol}} \ln \frac{0.0169}{(0.005)^2 \times (10^{-7}M)^9} \\[2mm]
&= -0.3 \; V
\end{aligned}
$$

When H^+ is oxidized by oxygen according to the Nernst equation. At an air concentration of 20 %, pH = 7, and $E^0_{Cathode}$ = 1.229 V, the cathodic potential is:

$0.5O_2 + 2H^+ + 2e^- \rightarrow H_2O$
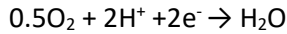
$$
\begin{aligned}
E_{Cathode,emf} \quad &= E^0_{Cathode} - \frac{RT}{2F} \ln\left(\frac{[H_2O]}{[O_2]^{0.5}[H^+]^2}\right) \\[2mm]
&= 0{,}187 - \frac{8{,}31 \dfrac{J}{mol \cdot K} \times 298{,}15K}{2 \times 9{,}65 \times \dfrac{10^4 C}{mol}} \ln \frac{1}{(0.2)^{0.5} \times (10^{-7}M)^2} \\[2mm]
&= 0.805 \; V
\end{aligned}
$$

For the air cathode MFC with 1g/L acetate as substrate (HCO_3^-= 5mM, pH = 7), the maximum cell potential:

$$E_{emf} = E_{Cathode,emf} - E_{Anode,emf} = 0.805 - (-0.3) = 1.105 \; V$$

2.2.3 Electrochemical losses encountered in the MFC

In an ideal fuel cell, the electrode is assumed to be in optimal condition and the chemical reaction proceeds at an infinite rate with negligible internal resistance. Under such conditions, the fuel cell can convert the free energy of fuel oxidation into electrical energy, resulting in potentially high energy conversion efficiency. However, in reality, microbial fuel cells deviate from this ideal scenario. They possess significant internal resistance and their electrochemical reactions occur at a limited rate,

resulting in a substantial gap between the observed open-circuit potential and the theoretical value, even under open-circuit conditions. To optimize the performance of microbial fuel cells, researchers have focused on minimizing electrochemical losses in various parts of the cell. These losses can be broadly classified as activation losses, ohmic losses, and bacterial metabolic losses, as summarized by Logan [56]. The actual voltage output of a fuel cell can be calculated by starting with the thermodynamically predicted voltage and subtracting the various overvoltage losses.

Microbial Fuel Cells use a polarization curve to evaluate their performance. This curve is plotted as a function of cell voltage to current density [69]. As depicted in Figure 13, different regions in the curve represent the voltage loss due to various electrochemical property limits. Region A (activation overpotential) represents the potential loss caused by cathode and anode activity (electrode kinetics), corresponding to the internal resistance to charge transfer. Region B (ohmic resistances) represents the potential loss caused by ohmic polarization control and corresponds to the ohmic resistance. Region C (concentration losses/mass transport limitations) represents the potential loss caused by mass transfer limitations and corresponds to the diffusion internal resistance. Region D (sum of all internal losses) represents the losses caused by the internal current and corresponds to the open circuit voltage drop [70].
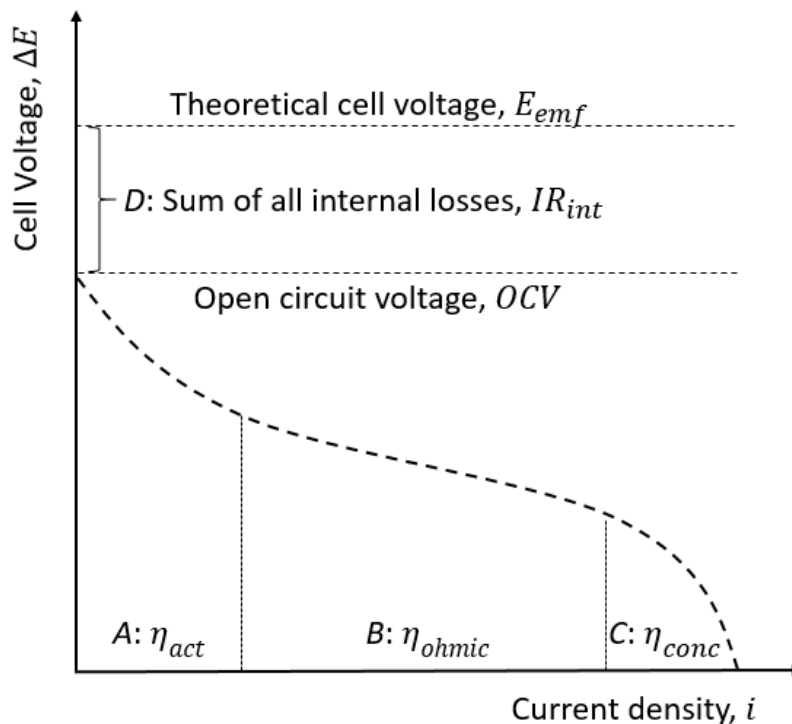
Figure 13: Schematic representation of the polarization behavior of a microbial fuel cell, modified from Noori [70].

The practical electric potential of an MFC can be determined by subtracting the activation loss, ohmic loss, and concentration loss from the theoretical electric potential. This is represented mathematically

as:

$$E_{cell} = E_{emf} - \eta_{act} - \eta_{ohmic} - \eta_{conc} \qquad \text{(2-10)}$$

where E_{emf} is the maximum cell potential, η_{act} is the activation loss, η_{ohmic} is the ohmic loss and η_{conc} is the concentration loss.

2.2.4   Summary and Discussion

The commercial feasibility of microbial fuel cells determines the development potential of this technology. MFCs are still in the developmental stage and current research is focused on breaking through the technical limitations of individual MFCs and issues related to the implementation of large-scale MFC systems.

Simple and efficient MFC design is essential to achieve effective action of large-scale applications. The use of high surface area electrodes can increase the contact area between the MFC and the microorganisms, thus increasing its power output. The cost of an individual MFC is also an important consideration. Sievers et al. [71] showed that for an MFC to be economically viable, its total cost must be less than 4,000 € per kW. This corresponds to a maximum cost of about 8 € per square meter, including the cost of electrodes, membranes and other necessary equipment. Electrodes made from common building materials, which have cost advantages over conventional metal and carbon electrodes, can help reduce costs and increase the feasibility of large-scale MFC systems. The use of membrane-free MFCs is another cost reduction strategy, but this approach requires careful design to overcome limitations such as energy losses.

Connecting multiple MFCs is necessary for practical use due to the low power output of a single MFC. However, this resulted in the question of how to connect the MFCs and how to minimize energy losses throughout the system. In addition, the power output of the entire system may fluctuate due to the instability of the microorganisms used, making it necessary to use intelligent coordination methods to overcome the various challenges of implementing an MFC system.

2.3   Electrode materials used in MFCs

Electrode materials are critical components in microbial fuel cells as they play a significant role in the overall performance of the device. The anode serves as the site for microbial attachment, biofilm formation, proton and electron production and transfer, which directly affects the power output of the MFC. Anode material should have properties such as high electrical conductivity, biocompatibility, chemical stability, high surface area, high porosity and appropriate mechanical strength. The cathode serves as the site for oxygen reduction, which is essential for the overall electrochemical reaction to

take place. Cathode material should have properties such as high electrical conductivity, high oxygen reduction activity and chemical stability.

The selection of appropriate anode and cathode materials is crucial for the development of high-performance MFCs. The use of materials that possess the forementioned properties can lead to an increase in power output, energy conversion efficiency and overall device performance.

2.3.1 Anode Materials

The current research on microbial fuel cells primarily focuses on carbon-based materials as anodes, such as carbon brushes [50], carbon mesh [72], carbon paper [66], carbon felts, and reticulated vitreous carbon (RVC) [66]. Logan [50] conducted a study in which he constructed MFCs using carbon brush and carbon paper as anodes under the same conditions, and found that the power yield of the former was four times higher than the latter at 2400 mW/m^2 and 600 mW/m^2 respectively, thus making carbon brush a more suitable anode material. This significant difference in power yield is attributed to the shift from 2D to 3D electrodes. Carbon materials, such as graphite, have excellent electrical conductivity and chemical stability, but their low porosity and surface area limit their ability to support microorganism adsorption. Increasing the surface area of the anode, for example by using graphite felt instead of graphite rod, can improve MFC performance. Graphite fiber brush is another commonly used anode material, due to its high surface area and low electrode resistance. Other carbon-like materials, such as carbon mesh, carbon felt, and carbon paper, have also been developed and used in MFCs studies. Carbon felt and carbon paper can be used as filler-type anodes, which enhance the connection between fillers and the carbon paper, reducing the anode resistance.

Metal materials, although having better electrical conductivity compared to carbon-based materials, are less frequently used in MFC systems due to their lack of corrosion resistance, which is a requirement for anode materials. Most metallic anodes are made of stainless steel and titanium, but these materials also have a smooth surface which is not conducive to the attachment of electricity-producing microorganisms and the formation of biofilms, resulting in lower power production compared to MFCs with carbon anodes [11].

In addition to carbon- and metal-based materials, researchers are also investigating new anode materials such as carbon nanomaterials, ceramics, conductive polymers, and composites. Massazza [73] utilized rurabuyn suboxides and an ice-templating technique to produce ceramic electrodes with 88 % porosity, which were inoculated with Geobacter sulfurreducens as the electricity-producing microorganism. The resulting MFC achieved a current density of 128.7 A/m^2, which is among the highest reported in the literature. However, due to the diversity of testing methods, microorganisms used, and other factors, comparisons of the performance of different anode materials can be difficult. Nevertheless, by reviewing the literature, it is possible to gain insight into which types of anode materials have better power production and application potential. As shown in Figure 14, regardless of whether carbon-based or metal-based materials are used, the current density increases with the enhancement of the effective specific surface area of the electrode. Three-dimensional porous

electrodes are the optimal structural morphology. Based on this, future optimization of the pore structure and improvement of the material's conductivity can further enhance the performance of MFC anodes.
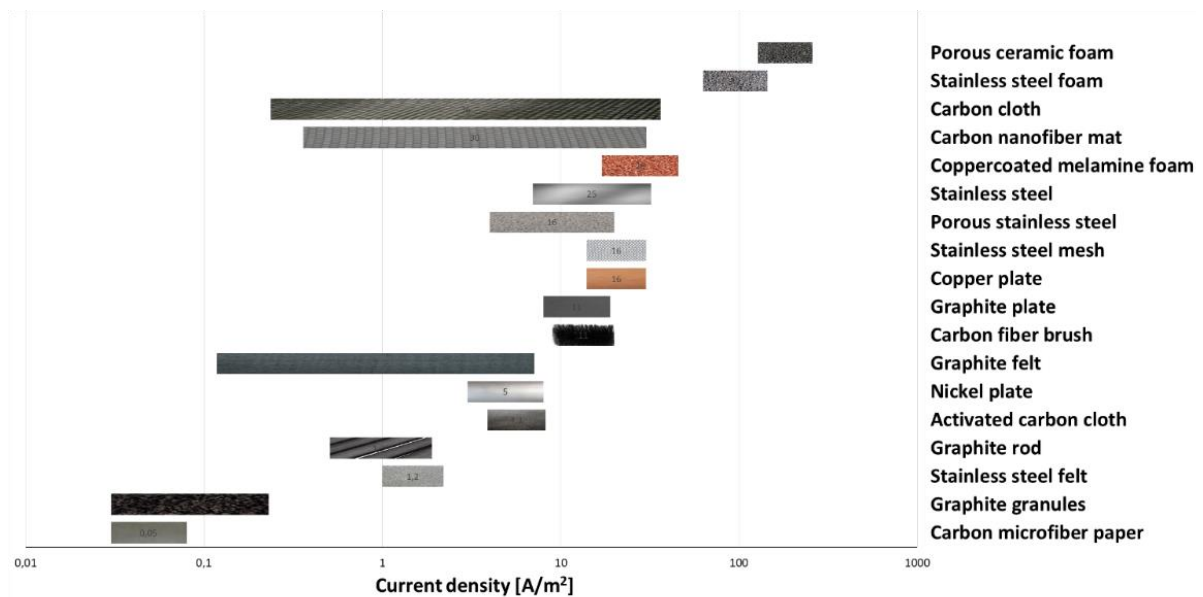
Figure 14: Comparison of the current state-of-the-art- electrodes [4], [31], [50], [50], [73]–[82], [82]–[94].

2.3.2 Cathode Materials

The cathode of an MFC is responsible for reducing oxygen or other oxidants to produce electricity. Cathode materials used for MFC can be broadly classified into three categories: conventional cathode materials, non-precious metal catalysts, and carbon-based materials. Conventional cathode materials include platinum, gold, and silver, which are known for their high electrical conductivity and good catalytic activity [95]. However, their high cost is a major drawback in practical applications. Non-precious metal catalysts, such as cobalt, nickel, and copper, have been tested as cathode materials for MFCs due to their low cost and good catalytic activity. These materials have been found to be effective in catalyzing oxygen reduction reactions, but their stability and durability in MFCs need to be improved. Carbon-based materials, such as carbon cloth, carbon paper and carbon felt, have been widely used as cathode materials for MFCs. They are low cost, have high surface area, good electrical conductivity and good chemical stability. However, their catalytic activity is relatively low.

2.3.3 Modification of electrode materials

Modification of electrode materials in MFCs is an effective way to improve performance, as it alters the physical and chemical properties to enhance microbial attachment and electron transfer. This section will focus on conventional modification techniques for anode materials, as the modification of cathode materials mainly involves changes in catalysts. The modification methods often require

complex equipment, multiple steps, high temperature conditions, and/or long treatment times. Therefore, more simple or effective modification techniques are still in high demand and a research hotspot for MFCs.

After gaining a thorough understanding of the factors that affect anode performance, researchers have sought to improve the electrical performance of microbial fuel cells by artificially modifying and optimizing the anode material. The main goal of these methods is to enhance biofilm formation and/or improve electron transport dynamics [96]. There are two main methods of improving the properties of anode materials: chemical modification and modification with other methods.

Table 2 lists some of the methods of anode modification and their effects. These methods are primarily aimed at increasing the effective surface area of the anode, and promoting the attachment of microorganisms, which is essential to the performance of the fuel cell. Chemical modification is suitable for many carbon electrode materials and is considered one of the most effective ways to improve electrode performance. The process involves heating the carbon material to a high temperature under a nitrogen environment, then exposing it to an ammonia atmosphere for a certain period of time before cooling it down to room temperature. Chemical modification mainly increases the attachment of microorganisms by using negatively charged microorganisms, and also indirectly increases the surface area of the anode material. In comparison, the overall improvement in power production performance of the MFC is greater when using other nano-conducting materials for modification. This is due to the increased attachment of nanomaterials, which significantly increases the effective surface area of the anode. These nano-carbon-based materials have good biocompatibility, making the modification effect on the MFC anode more pronounced.

Table 2: Modifications of the anode performance for MFC.

Anode	Treatment	Enhancement	Effect	Ref.
Chemically treated				
Graphite	H_2SO_4 + HNO_3	2.4	Increased bacteria adhesion Increased surface area	[97]
Carbon cloth	NH_4HCO_3	1.42		[98]
Carbon cloth	NH_3	1.2		[99]
Other modification methods				
Stainless steel	Graphene	18	Increased surface area Increased bacterial adhesion Increased biocompatibility	[100]
Carbon cloth	Graphene	3		[101]
Carbon cloth	Graphene-Ni foam	12.86		[102]
Carbon cloth	Carbonized Kapok	18.92		[103]
Carbon mesh	Heated	1.03		[95]
Graphite particles	Nitric acid	1.59		[95]

Other electrode modification methods include heat treatment, acid treatment, etc. These methods aim to remove impurities from the electrode surface and increase the active area, conductivity and/or quinone/quinone functional groups on the surface.

3 Electrical conductivity of multi-phase materials

3.1 Introduction

Multi-phase composites are used in many applications in life. They are often made from a mixture of two or more materials, thus taking full advantages of each material and achieving adequate performance requirements at a relatively low cost. Some materials, such as polymers and cements, are not inherently conductive, but are often required to have electrical properties in certain scenarios. Therefore, people often improve the electrical properties of the substrate by adding materials with conductive properties. This has led to the birth of composite conductive materials such as conductive polymers, conductive concrete, conductive geopolymers, and conductive asphalt. They all belong to the multi-phase conductive composites and have similar conductive mechanism.

3.1.1 Ionic conductivity

Ionic conductivity is the ability of a material to conduct electricity as a result of the movement of ions within the material. This is typically observed in electrolytes, which are materials that contain ions that can move freely under the influence of an applied electric field. Ionic conductivity is often observed in liquids, such as acids and bases, as well as in solid electrolytes like ceramics, glasses, and polymers. The ionic conductivity of a material is influenced by the concentration of ions and the mobility of the ions in the material. It is typically measured in units of siemens per meter [S/m].

The electrical conductivity of building materials with a porous structure increases when they are wet due to the migration of free ions in the pore solution (e.g., Na^+, K^+, Ca^{2+}, SO_4^{2-} and OH^-) under the influence of an electric field. The conductivity of the solution can be described by the following equation, assuming that interactions between ions are neglected [104]:

$$\sigma_p = \sum_i e Z_i \gamma_i C_i \tag{3-1}$$

where σ_p[S/m] is the conductivity of the solution, e[C] is the electron charge, Z_i[-] is the chemical valence of the i-th free ion, γ_i [m²/(s·V)] is the ion electromobility and C_i[mol/m³] is the concentration of the ions in solution.

The electromobility of an ion reflects the rate at which the ion migrates in solution under the action of a unit:

$$\gamma_i = \frac{v_i}{E} \tag{3-2}$$

where v_i[m/s] is the rate of migration of free electrons and E [V/m] is the electric field strength gradient.

The calculation of ionic conductivity is based on the concentration of individual ions present in the material. In the case of cementitious material, the ion concentrations of Na^+ and K^+ can be determined using the pore water volume and Taylor's method [105]. The concentrations of Ca^{2+}, SO_4^{2-} and OH^- can then be calculated using the solubility equilibrium of calcium hydroxide and gypsum in the pore solution, as well as the anion and cation charge balance equation [106]. However, the movement of free ions in an electric field is a complex process. The migration of dissolved ions is not only influenced by the properties of the solution in which they are present, but also by the properties of the ions themselves. In the process of electrical conductivity in a solution, free ions are subject to forces such as the electric field force, the friction force with the contact medium, the ion atmosphere relaxation force, and ion interactions. The electrical conductivity of a multi-phase material can depend on both ionic conductivity and electronic conductivity. The relative contribution of each type of conductivity will depend on the specific material and its microstructure as well as the operating conditions. In general, electronic conductivity is usually higher than ionic conductivity in most materials. This work focuses on the conductive mechanism dominated by electrons in the dry state, and thus, the ionic conductivity is not taken into account.

3.1.2 Electronic conductivity

Electronic conductivity refers to the ability of a material to conduct electrical current due to the movement of free electrons. It is a measure of the ability of a material to conduct electricity and is typically measured in units of siemens per meter (S/m) or ohm-meters ($\Omega \cdot m$). Electronic conductivity can be affected by various factors such as temperature, pressure, and the presence of impurities or defects in the material. Some materials, such as metals, are considered to have high electronic conductivity, while others, such as insulators, have low electronic conductivity.

The electrical conductivity of a material is typically quantified in terms of resistivity or conductivity. Resistivity is a fundamental property that characterizes the electrical resistance of a material, and is typically measured in units of ohm-meters [$\Omega \cdot m$]. It can be calculated using the formula:

$$\rho = \frac{RA}{L} \tag{3-3}$$

where ρ [$\Omega \cdot m$] is the resistivity, R [Ω] is the resistance, A [m^2] is the cross-section area and L [m] is the length.

This relationship is important in understanding the electrical properties of materials, including multi-phase materials. The electrical conductivity of a material is defined as the reciprocal of its resistivity, i.e.

$$\sigma = \frac{1}{\rho} = \frac{L}{RA} \tag{3-4}$$

where σ [S/m] is the resistivity, R [Ω] is the resistance, A [m²] is the cross-section area and L [m] is the length.

3.1.3   Measurements of the electrical conductivity of a multi-phase material

The electrical conductivity of a multi-phase material can be determined through various methods, such as the four-probe method [107], the van der Pauw method [108], and the Kelvin probe method [109]. The four-probe method involves measuring the electrical resistance of a material by passing a current through it and measuring the voltage drop across it using four electrodes. The van der Pauw method uses a circular sample and four electrodes to measure the resistance of the material. The Kelvin probe method measures the work function of a material, which can be used to infer its electrical conductivity. It is important to note that the electrical conductivity of a multi-phase material can be affected by the properties of each phase and the interactions between them. Therefore, it is crucial to consider the microstructure, composition and morphology of the multi-phase material when measuring its electrical conductivity.

The four-probe method is considered to be more accurate than the two-probe method for measuring the electrical conductivity of a material because it eliminates the effects of contact resistance at the electrodes [110]. In the four-probe method, two current-carrying probes are used to pass a current through the material, while two voltage-measuring probes are used to measure the voltage drop across the material. This configuration ensures that the current flows through the material and not through the electrodes, thus eliminating the effects of contact resistance. Additionally, the four-probe method allows for accurate measurements of materials that have a high resistivity and/or are not uniform in composition. This method is widely used in electronic, material science and other fields.

The four-probe method utilizes four identical electrodes that are embedded within the multi-phase material. The circuit diagram in Figure 15 is connected using a DC power supply. An ammeter is used to measure the current flow (I) through the material, and a voltmeter is used to measure the voltage difference between points M and N (ΔE_{MN}). The resistance between points M and N (R_{MN}) can be calculated by knowing the cross-sectional area of the material (A) and the distance between points M and N (L):

$$R_{MN} = \frac{\Delta E_{MN}}{I} = \frac{\rho L}{A} \tag{3-5}$$

where R_{MN} [Ω] is the resistance between points M and N, ΔE_{MN} [V] is the voltage difference between points M and N, I [A] is the current flow through the material , A [m²] is the cross-section area and L [m] is the length and ρ [Ω·m] is the resistivity y of the mixture.
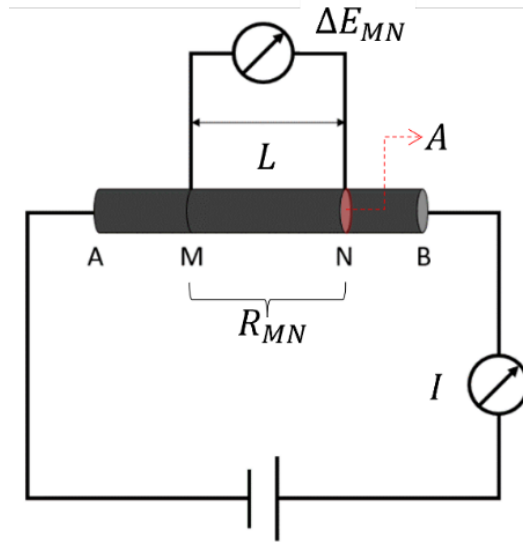
Figure 15: The circuit diagram used for the four-probe method.

The electrical conductivity σ of the mixture can be obtained:

$$\rho = \frac{A\Delta E_{MN}}{IL} = \frac{1}{\sigma} \tag{3-6}$$

3.2 Electrical percolation in multi-phase materials

The theory of percolation, first introduced in 1957 by Broadbent and Hammersley [111], examines the stochastic properties of a multi-phase material and its impact on the permeation of a fluid through it . Percolation is a phenomenon that occurs in systems made up of multiple phases, such as a mixture of particles in a fluid or a network of interconnected materials. It refers to the process by which a fluid or electrical current permeates through a porous medium, such as a mixture of particles or a network of interconnected materials. The percolation threshold is the point at which a system changes from being an insulator to a conductor, as the volume fraction of conductive particles reaches a critical value and forms a conductive network.

As can be seen in Figure 16, a two-dimensional dot matrix represents the conductive filler material as black squares, when the volume fraction of conductive filler material reaches the percolation threshold of 59 % [112], the conductive material in the mixture forms a conductive network, represented by red squares. This type of percolation is known as site percolation.
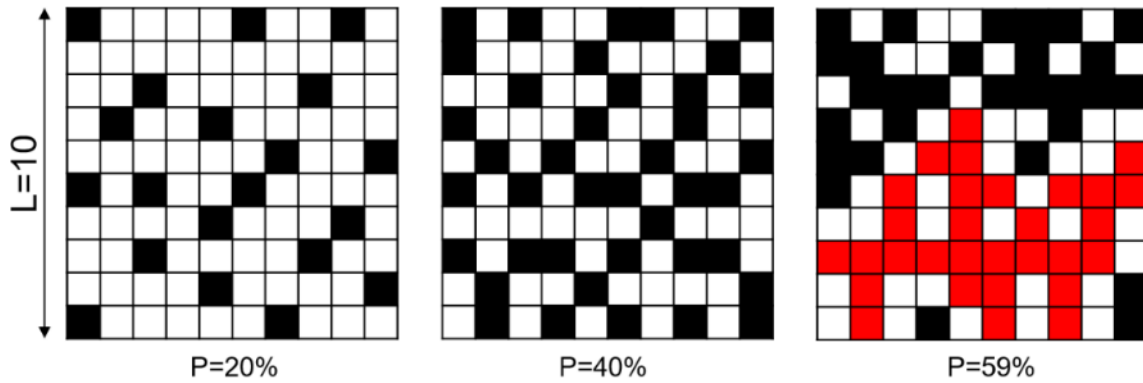
Figure 16: Site percolation on the square lattice: The black/red squares represent the occupied sites for three different concentrations: p = 0.2, 0.4, and 0.59. Size L=10. The critical probability Pc on the square lattice is 0.59 for site percolation in two dimensions.

The counterpart to site percolation is "bond percolation." In this model, connections are established between neighboring fields on a square grid, rather than between the fields themselves. This percolation type is useful in simulating the connectivity of porous materials when they are filled with ionic solutions, and can accurately reflect changes in ionic conductivity, as illustrated in Figure 17.
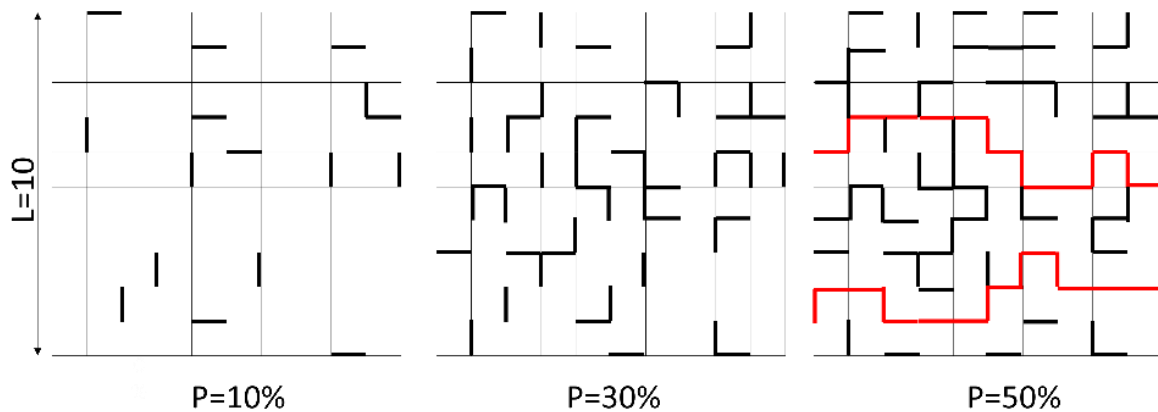
Figure 17: Bond percolation on a square lattice with occupation probability p = 0.1, 0.3 and 0.5. The black/red squares represent the 'bonds' between particles for three different concentrations. Size L = 10. The critical probability Pc on the square lattice is 0.5 for bond percolation in two dimensions.

The electrical conductivity of multi-phase materials depends on various factors, including the content, conductivity, shape, and distribution of each phase. The effective conductivity of a two-phase complex medium can be represented by a graph of conductivity versus the volume fraction of the conductive phase [113], as shown in Figure 18. The graph typically shows three main regions: the insulation zone, the percolation zone, and the conductive zone. In the insulation zone, the clusters of conductive fillers are small and not interconnected. In the percolation zone, the clusters formed by the conductive filler gradually form a large unit, and the overall conductivity changes significantly. In the

conductive zone, the conductivity of the compound tend to be equivalent to the conductivity of the conductive filler.
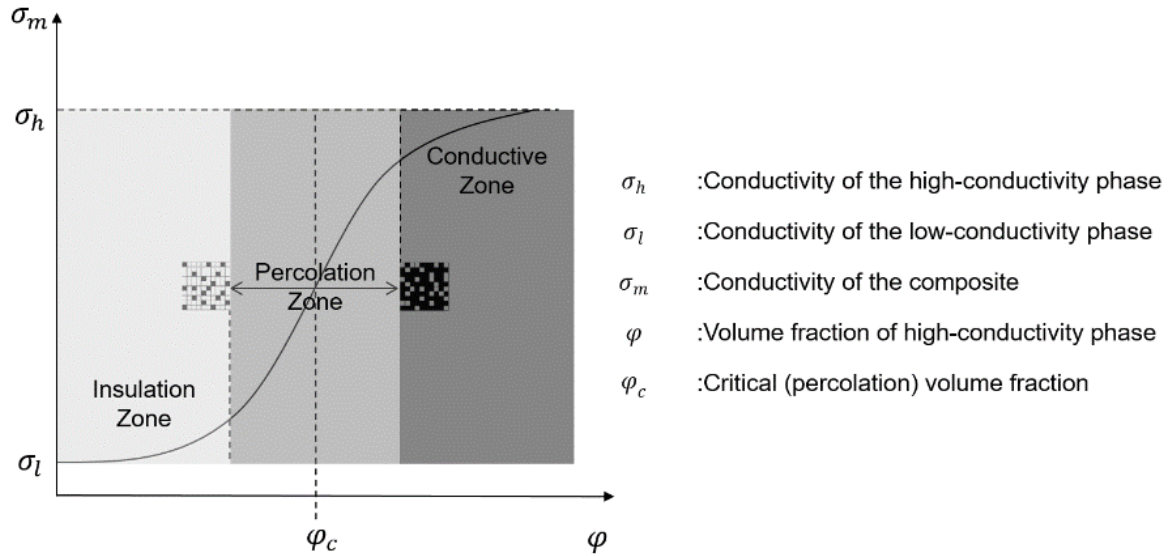
Figure 18: Schematic of Log conductivity versus electrical conductive filler concentration illustrating an S-shaped percolation curve, modified from Brigandi et al. [114]. Depending on the conductive filler content, there are three zones: insulation zone, percolation zone and conductive zone. In the insulation zone, the clusters of conductive fillers are small and not interconnected. In the percolation zone, the clusters formed by the conductive filler gradually form a large unit, and the overall conductivity changes significantly. In the conductive zone, the conductivity of the compound tend to be equivalent to the conductivity of the conductive filler.

3.2.1   Influence of the dimensionality on the percolation threshold

The percolation threshold is affected by the dimensionality of the system. In general, the percolation threshold decreases as the dimensionality increases. In other words, it is easier to form a percolating network in higher dimensional systems than in lower dimensional systems (see Table 3). This can be observed in both site percolation and bond percolation models. For example, in a two-dimensional site percolation system, the percolation threshold is typically around 0.59 [115], while in a three-dimensional system, it is around 0.31 [116]. Additionally, the percolation threshold also depends on the underlying lattice structure, such as square, triangular, or honeycomb lattice, which can also affect the threshold value.

Table 3: Percolation thresholds for d-dimensional simple cubic models.

Number of	Coordination number	Bond percolation	Site percolation
2	4	0.59 [115]	0.50[117]
3	6	0.31 [116]	0.25[118]
4	8	0.20 [119]	0.16[119]

3.2.2   Influence of the filler morphology on the percolation threshold

The morphology of the filler, including its shape and aspect ratio, can influence the percolation threshold because it affects the way the filler particles are packed and arranged within the matrix. A higher aspect ratio, for example, can lead to more effective packing of the filler particles and a lower percolation threshold. Additionally, the morphology of the filler can affect the connectivity between the filler particles and the matrix, which also plays a role in determining the percolation threshold. In general, the morphology of the filler can affect the percolation threshold by influencing the overall packing and connectivity of the particles within the matrix.

Sun et al. [120] investigated the impact of the morphology of conductive fillers on the percolation threshold. They observed that as the aspect ratio of the fillers increases, the mixture system requires fewer fillers to achieve higher electrical conductivity. Similarly, Xu & Jiao [121] also demonstrated the influence of filler aspect ratio on the percolation threshold by simulating percolation thresholds for different pore structures, as shown in Figure 19. The percolation volume fraction decreases from 0.3 to 0.03 as the aspect ratio increases from 1 to 10. As the aspect ratio of the filler increases, the mixture system requires fewer fillers to achieve higher electrical properties.
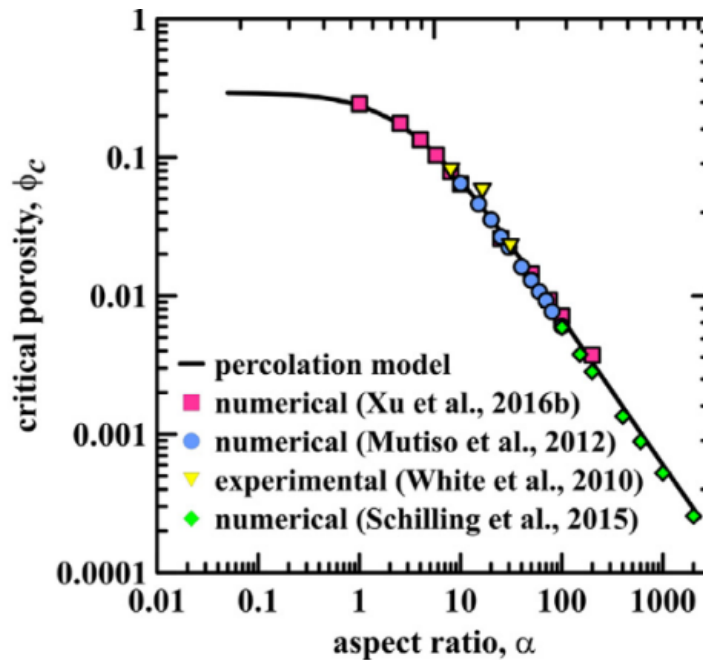
Figure 19: The excluded volume percolation model for φc versus the numerical and experimental data of the percolation threshold of over lapping spherocylindrical objects [121].

Additionally, the particle size of the material also plays a significant role in determining the percolation threshold. Smaller particle size allows for a lower volume fraction of fillers to achieve the same level of electrical conductivity (as shown in Figure 20) [122]. This is why carbon nanomaterials, such as graphene, are often used as conductive fillers due to their superior electrical conductivity compared to graphite and black carbon. The monolayer structure of graphene also allows for its

addition without compromising the mechanical strength of the mixture. However, the high cost of the material limits its wide-scale use.
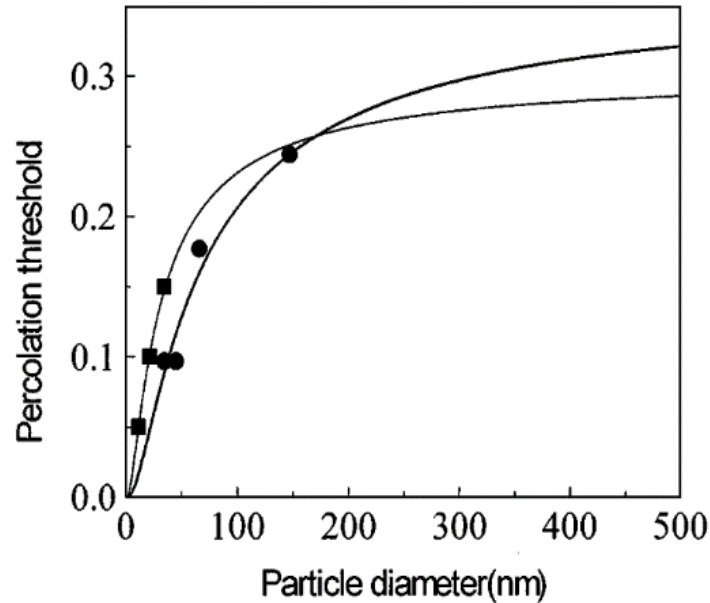
Figure 20: Plots of percolation threshold against particle diameter [122].

3.2.3   Influence of the gap between fillers on the percolation threshold

Hopping and tunneling effects can also influence the percolation threshold of a material. The hopping effect refers to the movement of charge carriers between localized states, and is more likely to occur in materials with lower conductivity. The tunneling effect refers to the quantum mechanical phenomenon where a charge carrier is able to pass through a potential barrier, and is more likely to occur in materials with high dielectric constants. These effects can affect the electrical conductivity of a material and thus may also affect the percolation threshold.

Cement and concrete are not typically considered high dielectric constant materials. Dielectric constant is a measure of a material's ability to store electrical energy in an electric field, and it is usually defined as the ratio of the capacitance of a material to the capacitance of a vacuum. Cement and concrete are typically insulators, meaning they have very low conductivity and therefore low dielectric constants. However, if a high content of graphite is added to the cement or concrete, it may become electrical conductive, and therefore its dielectric constant will increase. It is possible that a building material with high content of electrical conductive fillers may exhibit hopping and tunneling effects, which can influence the percolation threshold. Hopping and tunneling refer to mechanisms by which charge carriers can move through a material. In materials with high content of conductive fillers, these mechanisms may become more important and can affect the electrical conductivity of the material.

The authors Boonstra and Polley [123] observed through electron microscopy that electrical conductivity can occur even when conductive filler particles have not yet formed a chain-like structure. The principle of electron (hole) tunneling is a quantum mechanical phenomenon that describes the transfer of electrons through a potential barrier without the need for physical contact between the

particles. The theory was first proposed by Heisenberg's uncertainty principle [124], which states that the momentum and position of an object cannot be determined simultaneously and precisely. This principle was later formulated by Mandelshtam and Tamm [125] as the energy-time indeterminacy principle, see equation (2-17), which states that when two conductive filler particles are close enough, there will be enough energy to complete the tunneling effect and achieve the electron conduction process without physical contact.

$$\Delta E \Delta t \geq \frac{\hbar}{2} \tag{3-7}$$

where ΔE [J] is the uncertainty of energy, Δt [s] is the uncertainty of time and $\hbar$ [J·s] is the reduced Planck constant, Dirac constant, 1.054571800 x 10^{-34}.

A number of theoretical studies [126]–[128] have investigated the possibility of quantum-mechanical electron (hole) tunneling between closely spaced conducting grains within an insulating matrix. Sherman et al. [129] and Balberg [130] have also proposed conductivity models that involve a combination of percolation and tunneling [131]. The electron transfer between graphite layers is facilitated by this electron hopping mechanism. Graphite has a layered planar structure, as illustrated in Figure 21. The carbon atoms in each layer are arranged in a hexagonal crystal structure with an interatomic spacing of 0.142 nm and a layer spacing of 0.335 nm. Each carbon atom in a layer is covalently bonded to three neighboring carbon atoms in a hexagonal pattern, with weak Van der Waals, predominantly London-dispersionforces between the layers. As each carbon atom contributes one electron, which are free to move, graphite is an electrical conductor.
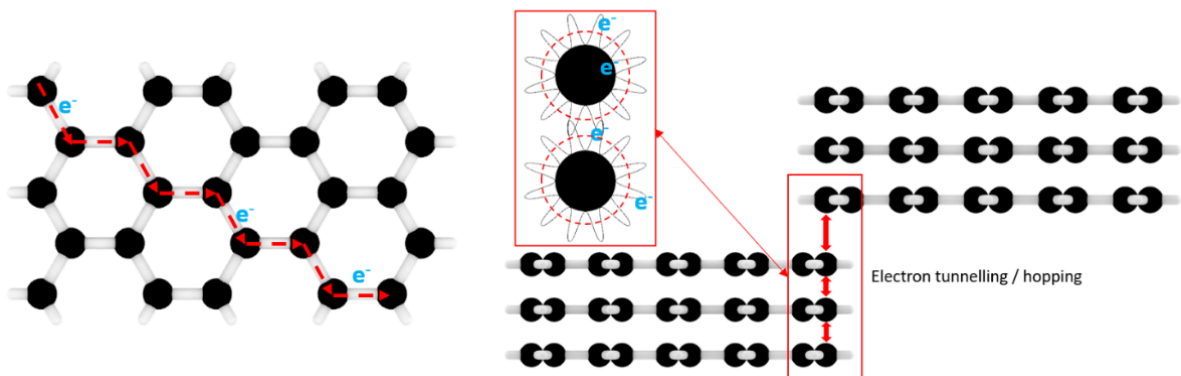
Figure 21: Electron transfer in graphite and between graphite. The carbon atoms in each layer are arranged in a hexagonal crystal structure. Each carbon atom in a layer is covalently bonded to three neighboring carbon atoms in a hexagonal pattern, with weak Van der Waals forces between the layers.

In situations where two conductive filler particles are close enough, the required time for electron crossing (Δt) is small enough that the energy-time uncertainty principle allows for infinite energy (ΔE) to facilitate electron conduction without physical contact, known as electron (hole) tunneling (Figure

22). When there is a solid/pore between two graphite particles, it creates a barrier E_0 for electron conduction between the two particles. As the distance between the two graphite particles (Δx) decreases, the time (Δt) required for an electron to travel from one particle to the other also decreases. According to the energy-time uncertainty principle, at a small enough distance, the electron may have a polarization energy (ΔE) to across the barrier E_0 through a quantum tunneling process, allowing for conduction without physical contact.
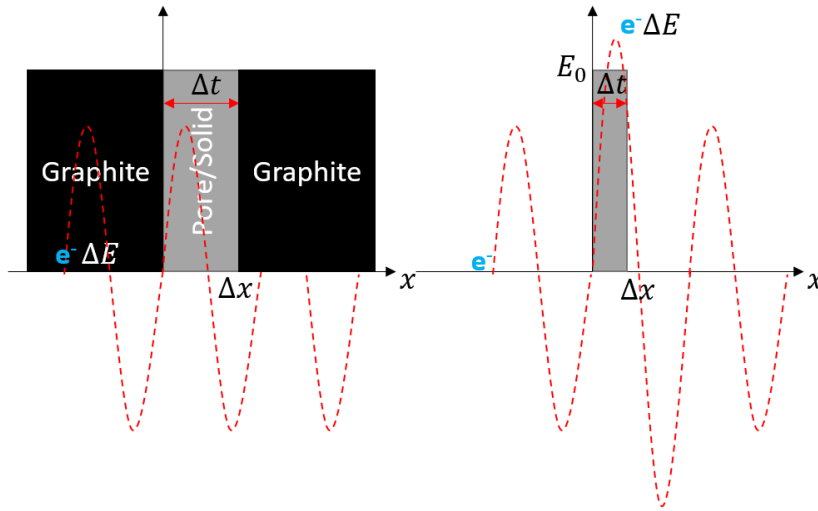
Figure 22: Principle of electron (hole) tunneling. Where Δt is the time required for an electron to travel from one particle to the other, E_0 is the barrier for electron conduction between the two particles, Δx is the distance between the two graphite particles, ΔE is local polarization energy across the barrier.

Hopping is a special case of tunneling in which the electrons can jump from the valence band of ions or molecules on one side of the gap to the conduction band on the other side without an energy exchange. However, in hopping, the electron must have its energy level increased to that of an appropriate band from which it can jump across the gap, thus involving an activation energy. The theoretical development of the hopping model was proposed by Mott [132], who derived an Mott's variable range hopping equation for the probability P of an electron hopping from one energy state to another through an insulator:

$$P = a\tau e^{-\Delta E/kT} + e^{\Delta E_p/kT} \tag{3-8}$$

where a is a constant, k is the Boltzmann constant, ΔE is the energy barrier, E is the cativation energy needed to hop the energy gap, T is the sample temperature in Kelvin, ΔE_p is the local polarization energy across the barrier, τ is the tunneling factor or characteristic hopping time and can be calculated as follows:

$$\tau = e^{-\alpha r} \tag{3-9}$$

where α is a constant and r is the spatial distance through which the electron must tunnel.

The Mott's variable range hopping equation can be used to understand the electron transfer between graphite particles in a multi-phase material [132]. As the distance between the graphite particles decreases, the probability of electron transfer increases. This can be modelled by the equation by adjusting the variables such as the distance between the energy states and the density of states. Additionally, the equation can be used to understand the influence of temperature on electron transfer. As the temperature increases, the probability of electron transfer also increases.

Regarding percolation thresholds, Mott's variable range hopping equation can be used to understand the relationship between the distance between conductive particles and the probability of electron transfer. As the distance between the particles decreases and the probability of electron transfer increases, the percolation threshold decreases. Therefore, the equation can be used to predict the threshold concentration of conductive particles needed to form a conductive network in the material.

3.2.4   Influence of the segregation volume on the percolation threshold

The segregation volume refers to the spatial distribution and size of the non-conductive particles, such as mineral materials, in a composite material. The percolation threshold and overall conductivity of the composite material can be influenced by the segregation volume and the way it is distributed, whether it is ordered or disordered. An ordered distribution of the non-conductive particles can lead to a lower percolation threshold compared to a random distribution, as it can prevent the formation of non-conductive "puddles" that are excluded from the overall conductive network. Additionally, it is more favorable to regulate the transport properties of the composite material through the morphology of the non-conductive network, rather than the conductive filler.

This Figure 23 presents visualizations and results of a study from Sahalianovand Lazarenko [133] on the conductivity and percolation threshold of segregated composite materials (CMs) filled with carbon black (CB) or carbon nanotubes (CNT) for different spatial configurations of non-conductive particles network and sizes of mineral particles. Subfigure (a) and (b) show the visualization of ordered and disordered segregated CMs filled with CB or CNT respectively. Subfigure (c) shows the dependence of conductivity on the ratio of the diameter of effective dielectric particles to the biggest size of filler particle for ordered and disordered segregated CMs with graphite nanoplatelets. Subfigure (d) shows the enhancement or decrease of the percolation threshold in segregated CMs compared to non-segregated CMs for different models and subfigure (e) shows a direct comparison of percolation thresholds obtained within the ordered and disordered models for different volume of excluded polymer fraction. Subfigure (f) shows the dependence of enhancement of percolation threshold in ordered segregated CMs compared to non-segregated CMs for different aspect ratios of CNT or graphite nanoplatelets.
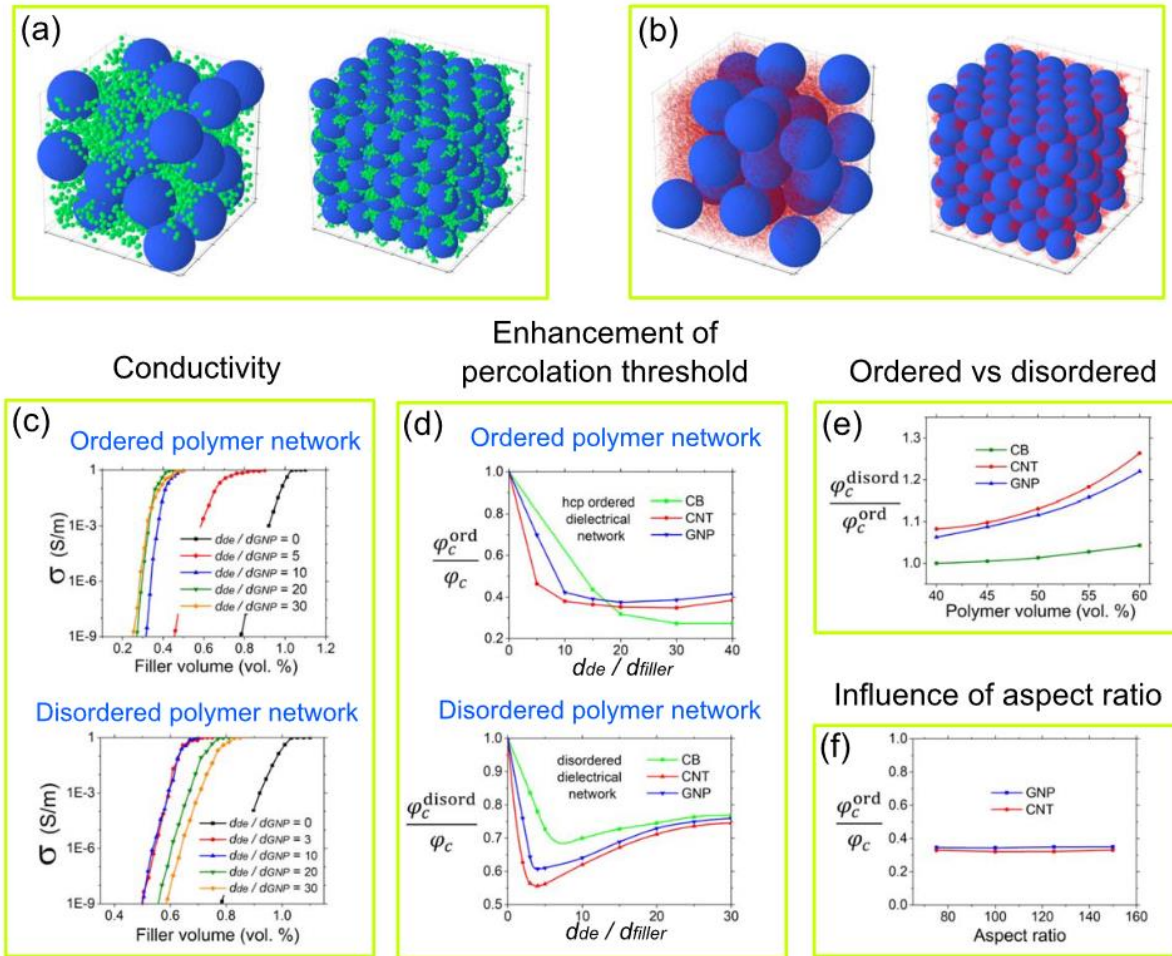
Figure 23: (a) Visualization of disordered and ordered segregated composites filled with carbon black (CB). (b) Visualization of disordered and ordered segregated composites filled with carbon nanotubes (CNT). (c) The conductivity of ordered or disordered segregated composite material (CM) with graphite nanoplatelets for different diameter of effective dielectric particles (d_{de})/ the biggest size of a filler particle (d_{filler}) ratios. (d) Enhancement (decrease) of the percolation threshold in segregated CM compared to non-segregated CM for ordered and disordered. (e) models for different d_{de}/d_{filler} ratios. (e) Direct compare of percolation thresholds obtained within the ordered and disordered models for different volume of excluded polymer fraction (d_{de}/d_{filler} =10). (f) Dependence of enhancement of percolation threshold in ordered segregated CM compared to non-segregated CM for different aspect ratios of CNT or graphite nanoplatelets (GNP) ($l_{CNT}=d_{GNP}$ =1 μm, d_{de}/d_{filler} =10) [133].

The spatial configuration of the segregation network has a greater impact on the transport properties of the composites than the morphology of the fillers. Specifically, ordered spatial distribution of segregated particles grains resulted in lower percolation thresholds compared to random distribution, due to the prevention of the formation of random filler clusters that are not part of the conductive network. Additionally, the size of segregated particles and the ratio between segregated particles and filler particle sizes also play a role in determining the conductivity of the composites.

3.3   Overview and Stadt-of-the-Art of Electrically conductive composites

Conductive mixtures are typically divided into two components: conductive filler and matrix. Wang and Aslani [134] listed and classified all conductive fillers into two main categories based on morphology: fibrous and particulate, with particle sizes ranging from nano to micro to macro. The primary objective of this research is to fabricate inexpensive anodes for microbial fuel cells. Therefore, price is the primary consideration, followed by durability and corrosion resistance, and finally, the aspect ratio and particle size to achieve the minimum percolation threshold.

From a percolation threshold perspective, the use of fibrous materials undoubtedly achieves the desired electrical conductivity with a small volume fraction. However, this only optimizes the overall conductive properties of the mixture. Since microorganisms adhere to the surface of the concrete electrode, a sufficient amount of conductive filler is required on that surface to satisfy the need for each biofilm to be in direct contact with the conductive network. Therefore, this thesis uses a single granular conductive material as a conductive filler to investigate the working performance of microbial fuel cells when using concrete electrodes. Both carbon black and graphite are highly conductive, but their shapes differ significantly. Carbon black is typically spherical with sizes ranging from a few to tens of nanometers, while graphite is typically flaky. Regular graphite sizes are usually in the micron range, with nano-graphite being smaller. The choice of conductive agent depends on the contact between them and the electrode material, which is a factor to consider when choosing one. Carbon black, with its smaller particle size, is theoretically easier to form conductive networks. However, it is much more expensive than natural graphite. Considering price, microscopic morphology, and other factors, graphite is chosen as the conductive filler for the experimental part of this thesis. Carbon nanomaterials may have more advantages for the formation of conductive networks, but due to their high cost, they are not considered here.

3.3.1   Graphite-Polymer Composites

Graphite-polymer composites are a class of materials that are composed of a conductive filler, such as graphite, and a polymer matrix. These composites have been extensively studied due to their potential technological applications, such as in electrical conductivity, thermal manaent, and electromagnetic interference shielding. The main objective of these studies is to fabricate materials that are inexpensive, durable, and have a low percolation threshold, which is the minimum concentration of filler needed for the host polymer to become sufficiently conductive.

The preparation of graphite-polymer composites typically involves intercalation of the graphite with a polymer, followed by in-situ polymerization. As shown in Figure 24-B, expanded graphite (EG) is often used as the conductive filler, which is prepared by rapidly heating a graphite intercalation compound (GIC) that is prepared from natural flake graphite (NFG) using a mixture of sulfuric and nitric acids. The expansion ratio of EG is generally 200-300 and this leads to a larger interplanar spacing that allows for easy intercalation by suitable monomer molecules and catalysts [135].

Pan et al.[135] prepared polystyrene/expanded graphite conductive composites by using two different methods. Method A is a process where a mixture of expanded graphite, e-caprolactam, and n-aminocaproic acid is first stirred at room temperature for 6 minutes in a blender. The mixture is then charged to a tubular reactor for polymerization under nitrogen protection at various temperatures for different periods of time. Method B, on the other hand, is a process where a high shear colloidal mill is used to mix the mixture of expanded graphite, e-caprolactam monomer, and n-aminocaproic acid catalyst for 6 hours. As shown in Figure 24-A, the percolation threshold for Method A is 0.75 vol. %, while it is 2.5 vol. % for Method B. The percolation threshold is lower for Method A because the intercalation of the monomer in the graphite, followed by in situ polymerization, results in a more homogenous distribution of the graphite within the polymer matrix. This leads to a higher degree of connectivity between the graphite particles and thus a lower percolation threshold. Method B likely results in a less homogenous distribution of the graphite within the polymer matrix, leading to a higher percolation threshold.
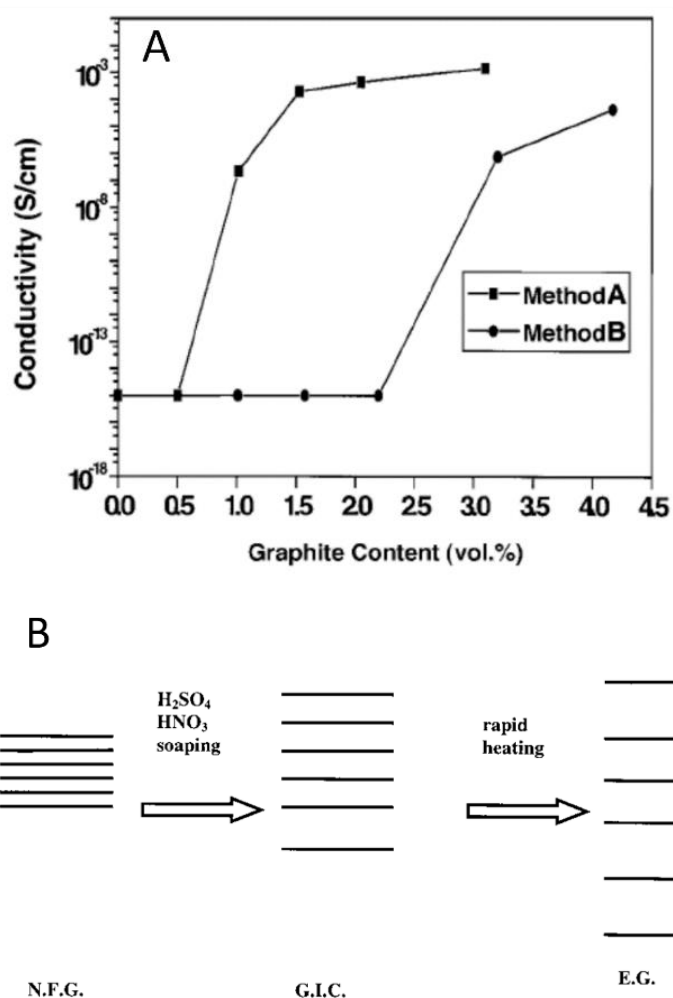
Figure 24: A) Electrical conductivity of nylon 6/graphite; Methods A and B have similar Thickness of about 10nm, Length of the graphite Methods A:3 μm, Method B: 1.5 μm. B) Schematic illustration of making expanded graphite. Expanded graphite (EG) can be easily obtained by rapid heating of a graphite intercalation compound (GIC), which can be prepared from a natural flake graphite (NFG), the black lines represent graphite sheets viewed from a direction parallel to the sheets [135].

Krupa et al. [136] blended graphite with a particle size of 31.6 µm into high density polyethylene (HDPE) and low density polyethylene (LDPE) to prepare conductive polymers. The study found that the percolation threshold for the blends was 11 vol-%. The authors attributed the high percolation threshold to the use of a larger particle size graphite filler compared to the 10nm used by other studies (e.g., Pan et al. [135]).
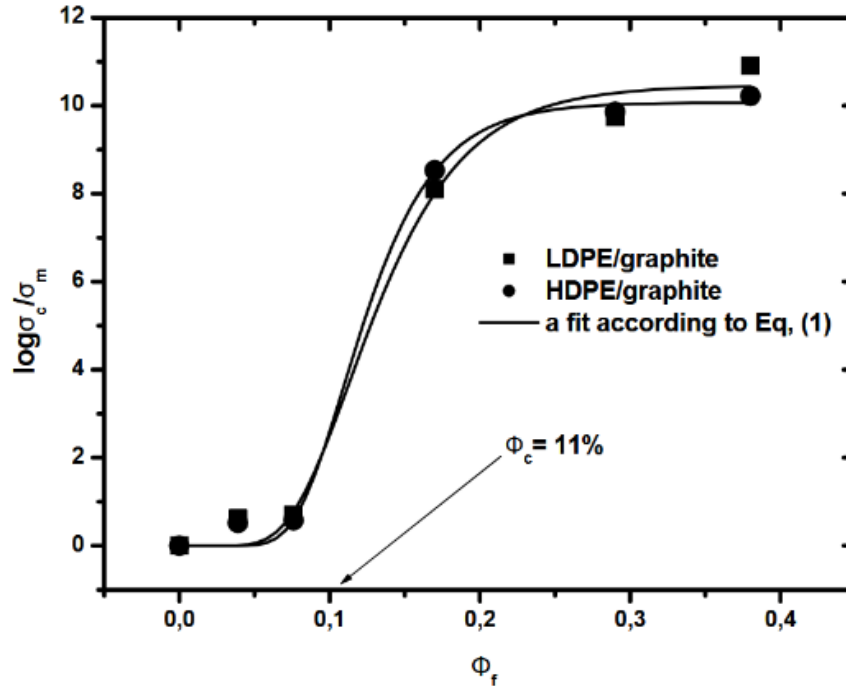
Figure 25: : Electrical conductivity (σ_c/σ_m) of the graphite filled LDPE (squares) and HDPE (circles) as a function of the volume filler content (Φ_f). Where σ_c is electrical conductivity of composites, σ_m is electrical conductivity of polymeric matrix and Φ_f is volume portion of filler. The percolation thresholds Φ_c is 11 vol.% [136].

3.3.2   Graphite-Cement Composites

The incorporation of electrical conductive fillers into cement or concrete has become an active area of research in recent years due to its potential applications in various fields such as electrochemical sensing, self-sensing concrete, and electromagnetic interference shielding. The addition of conductive fillers in cement or concrete can enhance their electrical conductivity, which is otherwise an insulator. The most common conductive fillers used in cement or concrete are carbon-based materials such as carbon black, graphite, and carbon nanotubes. These materials have high electrical conductivity and can be easily incorporated into cement or concrete matrix. In addition to enhancing the electrical conductivity, the incorporation of conductive fillers into cement or concrete can also improve other properties such as mechanical strength and durability.

Sun et al. [137] investigated the electrical conductivity of concrete and determined that there are three main mechanisms for electrical conductivity in concrete: ionic conductivity, which occurs through the movement of ions such as Ca^{2+}, OH^-, SO_4^{2-}, Na^+, and K^+ in the pore solution of the concrete under the influence of an applied electric field; electronic conductivity, which is achieved through the

movement of free electrons in internal metal or semiconductor materials; and hole conductivity, which arises from the movement of holes within the material. The subsequent discussion in the study focuses on electronic conductivity.

Frattini et al. [138] prepared conductive cements using graphite with a median particle size of 4.5 μm and CEM II/A-LL 42,5R. They achieved a conductivity of 2 S/m by varying the mass fractions of graphite. The variation of electrical conductivity with graphite content is shown in Figure 26. The samples were tested under two conservation conditions, room temperature (RT) and 40 degrees 7 days constant temperature (TT). As the graphite content was increased from 30 wt.% to 60 wt.%, the conductivity of the mixture increased from 105 to 1 S/m, which is typical of graphite. The percolation threshold was found to be 13.4 vol.-% for TT and 16.9 vol.-% for RT.
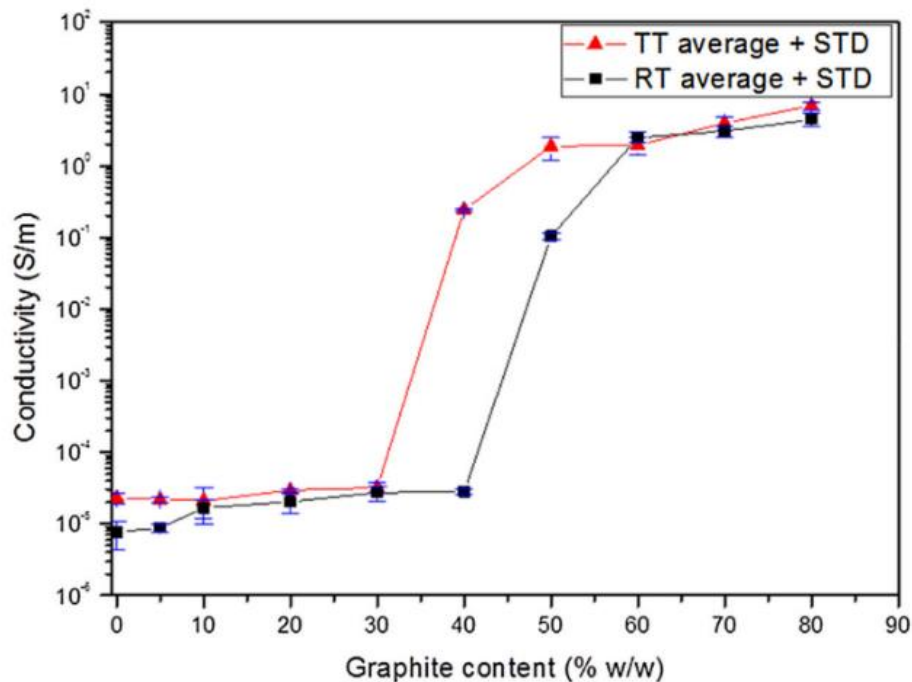
Figure 26: The variation of electrical conductivity with graphite content by room temperature (RT) and and 40 degrees 7 days constant temperature (TT), Standard deviation (STD) [138].

Frąc and Pichór [139] prepared conductive graphite-cement mixtures by incorporating expanded graphite as a conductive filler. They found that the mixture exhibited conductive percolation when the equivalent volume fraction of graphite was between 11 vol.-% and 17 vol.-%. The Figure 27 illustrates the relationship between graphite mass fraction and resistivity. As the graphite content increases, the resistivity changes significantly when the graphite content is greater than 3 wt.%. The conductive percolation region of the compound is between 4 wt.% and 6 wt.%. The resistivity of the compound stabilizes when the graphite content is greater than 8 wt.%. The expanded graphite used in the study had a particle size of 2-4 mm, which increases the aspect ratio of the conductive material and thus decreases the threshold for conductive percolation of the mixture, when compared to the graphite with a median particle size of 4.5 μm used by Frattini et al. [138]. They achieved a conductivity of 1.25 S/m by varying the mass fractions of graphite.
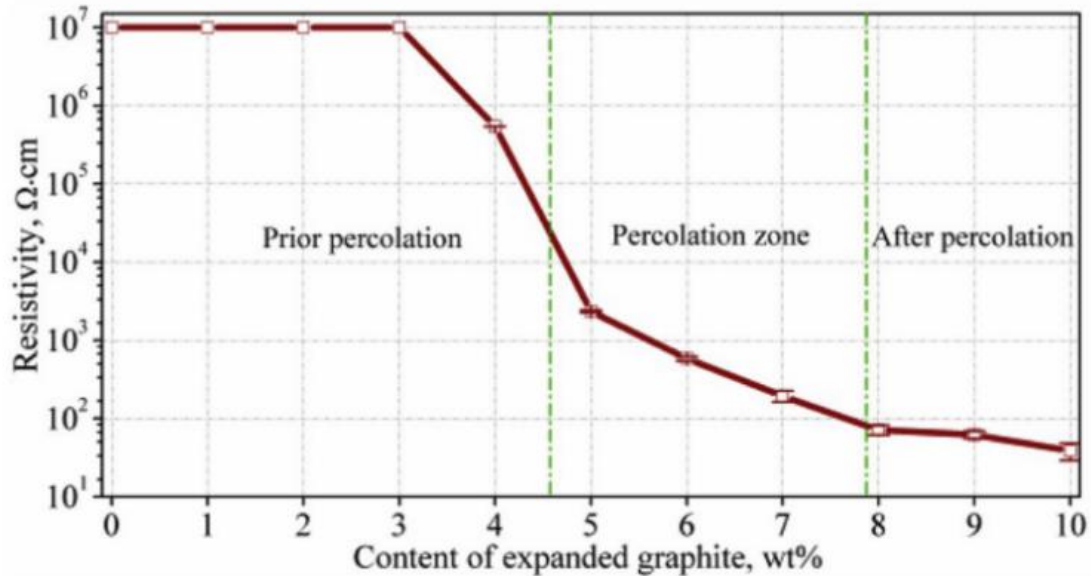
Figure 27: Variation of the resistivity of composites with expanded graphite content [139].

3.3.3 Graphite-Geopolymer Composites

Geopolymers are a type of alkali-activated materials that are formed by the reaction of a high content of amorphous aluminosilicate phase material with an alkali line activator solution [140]. They have been found to have some electrical conductivity when they are in a moist state, similar to Portland cement.

Hanjitsuvan et al. [141], [142] have shown that the electrical conductivity of fly ash geopolymer matrix can be influenced by factors such as the concentration of NaOH in the activator solution, the frequency spectrum and the liquid activator/ash ratio. The addition of conductive fillers such as graphite to geopolymers can also improve their electrical conductivity, as described by the percolation theory. Mizerová et al. [143] made conductive geopolymers by mixing fly ash geopolymer with PMM11 (graphite powder with a grain sizes from 1 to 9 mm) with mass fractions ranging from 2% to 10% of the fly ash (G2 to G10). As shown in Figure 28, the conductivity of the mixture did not change significantly until the mass fraction of graphite was greater than 8%, at which point a large increase in conductive properties, or percolation threshold, occurred at 8.7 to 12.7 vol.% (when the density of graphite equals 2.26 g/cm^3, and the density of fly ash range from 1.01 g/cm^3 to 1.78 g/cm^3). The maximum conductivity here reached only 6-7 mS/m, or 0.006-0.007 S/m. Fly ash consists of silt-sized particles which are generally spherical, typically ranging in size between 10 and 100 μm.

Rovnaník et al. [144] utilized graphite powder with an average grain size of 6.4 μm as a conductive filler in alkali-activated slag mortar. The average grain size of the slag particles obtained by laser granulometry was 15.5 μm. As the mass fraction of graphite increases from 0% to 30% of the slag mass, the resistance of the mixture decreases from 22x10^6 Ω·cm to 6x10^6 Ω·cm. The percolation threshold was observed to be between 10 wt.% and 15 wt.% of graphite. The addition of graphite at a mass fraction of 10 wt.% (equivalent to a volume fraction of 14 vol.-%, if the density of graphite equals 2.26

g/cm³, and the density of slag is 2.26 g/cm³) significantly improved the electrical properties of the alkali-activated slag. The maximum conductivity reached 0.033 mS/m.
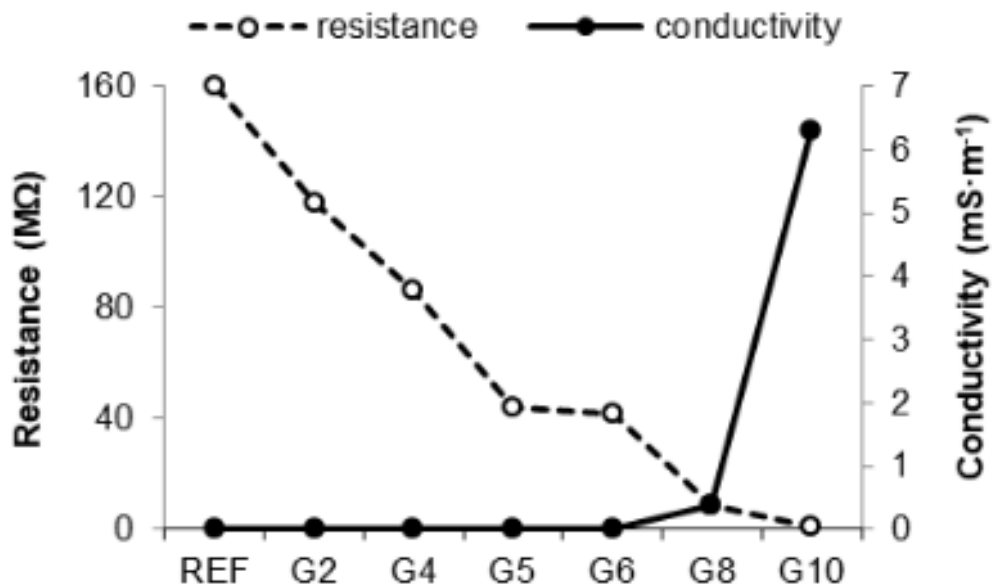
Figure 28: Resistance (at 100 Hz) and conductivity (at 100 MHz) of Fly ash geopolymers with different graphite content, graphite with mass fractions ranging from 2% to 10% of the fly ash (G2 to G10) [143].
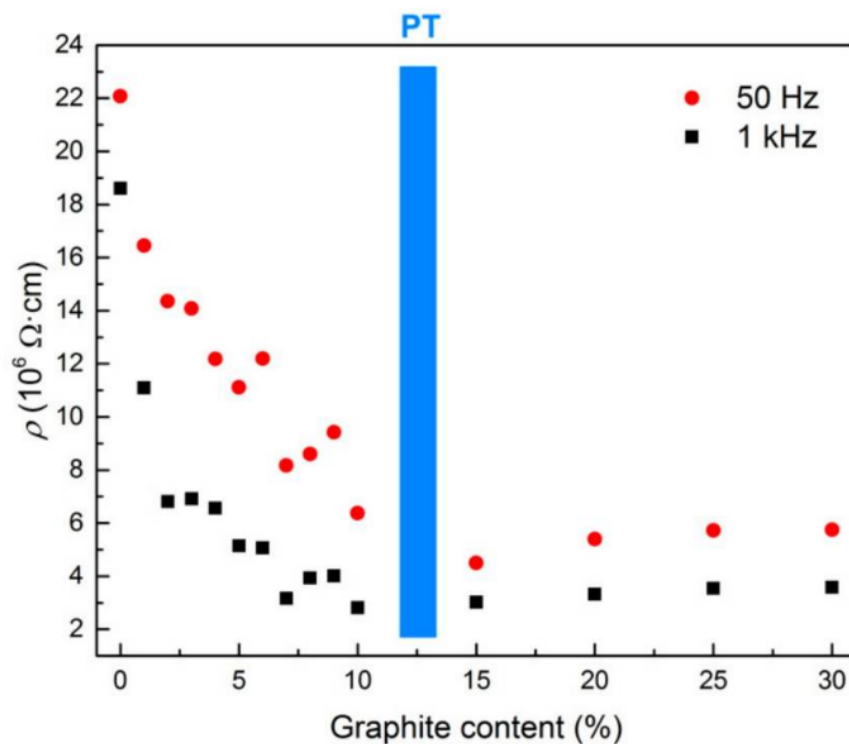
Figure 29: : Change in the electrical resistivity of AAS composites with respect to graphite content at 50 Hz and 1 kHz (PT = percolation threshold)The amount of graphite ranged from 1% to 30% of the slag mass [144].

Studies have shown that adding graphite powder with a grain size ranging from 6.4 to 15.5 μm as a conductive filler in alkali-activated slag mortar and fly ash geopolymer can improve the electrical conductivity of the composite. However, the conductivity is generally lower compared to graphite-cement and graphite-polymer composites, with maximum conductivity reaching 0.033 mS/m and 6-7 mS/m respectively. This could be due to the properties of the geopolymer matrix itself and the way it interacts with the conductive filler.

The segregation of the conductive filler particles within the geopolymer matrix could also potentially be a contributing factor to the lower conductivity observed in graphite-geopolymer composites compared to graphite-cement and graphite-polymer composites. This could result in a lack of connectivity between the conductive filler particles and reduced overall conductivity of the composite.

3.4 Theoretical models for electrical conductivity of multi-phase material
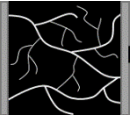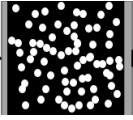
The effective conductivity of multi-phase medium research has more than a century of history, the famous scientists Maxwell [145], Rayleigh [146] and Einstein[147] and other related work is still often cited today, because this problem has always been very important issues, there are a wide range of applications. These functional composites have great prospects in aerospace, energy, electronics, biomedical and other high-tech fields [148], [149], in electromagnetic shielding [150], road deicing [151] and other special use scenarios, and even in everyday life. Therefore, the effective conductivity of multiphase dielectrics is very important for the research and preparation of new composite materials.

Non-dry concrete consists of a solid phase, a vapour phase and a liquid phase. Without the addition of conductive fillers, the electrical conductivity of concrete is related to the electrical conductivity of its pore solution and the way the pore solution exists in the concrete. This in turn depends on the porosity of the concrete, pore size distribution, connectivity, tortuosity and other internal factors as well as relative humidity, temperature and other external factors.

When the addition of conductive filler to form a conductive network, as the electronic conductivity of electrical conductivity is much greater than the ionic conductivity, according to the principle of minimum amount of action, the electron will preferentially choose to form a conductive pathway to the conductive filler for electronic conductivity. Therefore, the focus of this section is described for the effective conductivity of the multi-phase medium electron-conducting model. The ionic conductivity part is not considered.

Table 4 lists the main models of composite electrical conductivity.

Table 4: Theoretical models for electrical conductivity of multi-phase materials.

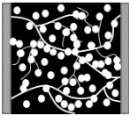|			
DC conductivity			
Examples	Pore solution	Matrix + Filler	Matrix + Filler + Pore
Conducting phases	Pore solution	Filler	Filler + Pore solution
Theoretical models			
Empirical based models	Archie's law [152]	Archie's law [152]	Modified Archie's law [153]
Percolation based models	Statistical percolation: Kirkpatrick percolation model [154] Thermodynamic percolation [155] Geometrical percolation [156]–[160] Structure Oriented Percolation: Nielsen percolation model [161], [162]		
Effective medium theory	Hashin-Shtrikman upper- and lowerbound [163] Waff model [164] Modified brick-layer model [165] Maxwell Garnett equation [166] Effective Media Equation nach Bruggeman [167]–[169] General Effective Media Equation [170]		

3.4.1 Percolation based models

One widely used model is the percolation theory, which predicts the conductivity of a composite material based on the volume fraction of the conductive filler, the aspect ratio and shape of the filler particles, and the electrical conductivity of the filler and matrix phases.

The Kirkpatrick percolation model [154], also known as the Kirkpatrick-Doll model, is a percolation-based model that can be used to predict the electrical conductivity of a multi-phase material. It was first proposed by Kirkpatrick in 1973. This model is based on the idea that the electrical conductivity of a composite material is dominated by the presence of a percolating cluster of conductive particles.

The Kirkpatrick model predicts that the electrical conductivity of a composite material is given by:

$$\sigma_{eff} = \sigma_0(\varphi_2 - \varphi_c)^t \tag{3-10}$$

where σ_{eff} [S/m] is the effective conductivity of the composite, σ_0 is the conductivity of the conductive phase, φ_2 is the volume fraction of the conductive phase, φ_c is the percolation threshold, which is the volume fraction of the conductive phase at which the electrical conductivity of the composite becomes non-zero, t is the conductivity exponent, which characterizes the rate of increase of the conductivity

as the volume fraction of the conductive phase increases, for the bond percolation = 1.6 ± 0.1; for the site percolation=1.9±0.1 [171].

This form of the model emphasizes that the electrical conductivity of the composite is controlled by the presence of a percolating cluster of conductive particles, and that the conductivity increases as the volume fraction of the conductive phase increases. The Kirkpatrick model is based on certain assumptions and simplifications, and its accuracy may be limited for certain types of systems.

The Nielsen model [160] is also a percolation-based model for predicting the electrical conductivity of multi-phase materials. It was first proposed by Nielsen in 1981 as an alternative to the Kirkpatrick-Doll model. Of the predictive models for all percolation thresholds, the Nielsen[162] model is the most prominent model for a description and interpretation the electrical conductivity of composites [172].

The Nielsen model predicts that the electrical conductivity of a composite material is given by:

$$\sigma_{eff} = \sigma_1 \left(\frac{1 + AB\varphi_2}{1 - B\psi\varphi_2} \right) \tag{3-11}$$

with:

$$B = \frac{\frac{\sigma_2}{\sigma_1} - 1}{\frac{\sigma_2}{\sigma_1} + A}$$

$$\psi = 1 + \left(\frac{1 - \Phi_{max}}{\Phi_{max}^2} \right) \varphi_2$$

$$A = k_E + 1$$

where: σ_{eff} is the effective conductivity of the composite, σ_1 is the conductivity of the host matrix, φ_2 is the volume fraction of the conductive phase, A is constant, depends upon the shape and orientation of the dispersed particles, B, and ψ are constants that depend on the microstructure of the composite, k_E is the Einstein coefficient [173], Φ_{max} is the maximum packing fraction of the dispersed particles. The value of A and the maximum packing fraction (Φ_{max}) for various two-phase systems can be found in Table 5.

The Nielsen model includes the effect of the ratio of the characteristic length to the characteristic width (L/D ratio) on the packing of particles, and provides maximum packing fractions for different packing shapes. However, it should be noted that this model takes into account a simplified set of factors compared to more comprehensive statistical percolation models. Specifically, the packing geometry is simplified and characterized by a single length scale, the particle size is treated as a single value without considering any size distribution, and the model does not account for factors such as the surface chemistry, intermolecular forces, or interactions between the filler particles and the substrate. Furthermore, it's worth noting that in building materials, seepage phenomenon often involves multiple influencing factors. Thus, simplified percolation models may not have a universal applicability and can only be used to describe trends in relation to specific physical quantities and percolation thresholds.

Table 5: Valuea of A and Maximum packing fraction for various two-phase systems [162].

Type of Dispersed Phase	Direction of heat Flow	A	Shape of Particle	Type of Packing	Maximum Packing Fraction Φ_{max}
Spheres	Any	1.5	Spheres	Hexagonal close	0.7405
Aggregates of spheres	Any	$2.5/\Phi_a - 1$	Spheres	Face centered cubic	0.7405
Randomly oriented rods: L/D = 2	Any	1.58	Spheres	Body centered cubic	0.601
Randomly oriented rods: L/D = 4	Any	2.08	Spheres	Simple cuibc	0.524
Randomly oriented rods: L/D = 6	Any	2.88	Spheres	Random close	0.637
Randomly oriented rods: L/D = 10	Any	4.93	Spheres	Random losse	0.601
Randomly oriented rods: L/D = 15	Any	8.38	Rods or fibers	Uniaxial hexagonal close	0.907
Uniaxially oriented fibers	Parallel to fibers	2L/D	Rods or fibers	Uniaxial simple cubic	0.785
Uniaxially oriented fibers	Perpendicular to fibers	0.5	Rods or fibers	Uniaxial random	0.82
			Rods or fibers	Three dimensional random	0.52

3.4.2 Effective medium theory based models

Effective Medium Theory is a theoretical model used to predict the macroscopic properties of composite materials. Developed by Maxwell [166], Landauer [174], Hashin and Shtrikman [163], Waff [164], and others, EMT provides a means to calculate the electrical conductivity of a variety of two-phase composite systems. The theory achieves this by averaging the properties of the individual components of a composite material. Due to the complex and often inhomogeneous nature of composite materials, it can be difficult to calculate the properties of these materials with complete accuracy. EMT provides an estimate of these properties by approximating the properties of the composite material as a whole [175], [176].

To understand Maxwell Garnett's theory, it is important to be familiar with the Lorentz model [177]. The Figure 30 gives the model of the Lorentz effective electric field. A sphere of appropriate radius is

centered at the point in the mixture where the particle under investigation is located. Lorentz uses a macroscopic form to deal with the dielectric at the far side of the particle under investigation, i.e., the dielectric outside the sphere is considered as a uniform and continuous medium. The effective field strength $\overrightarrow{E_e}$ acting on the Lorentz ball is the sum of the electric field strength $\overrightarrow{E_0}$ produced by the free charge on the pole plate, the electric field strength $\overrightarrow{E_1}$ produced by the polarized dielectric outside the ball and the electric field strength $\overrightarrow{E_2}$ produced by the polarized particle inside the ball.
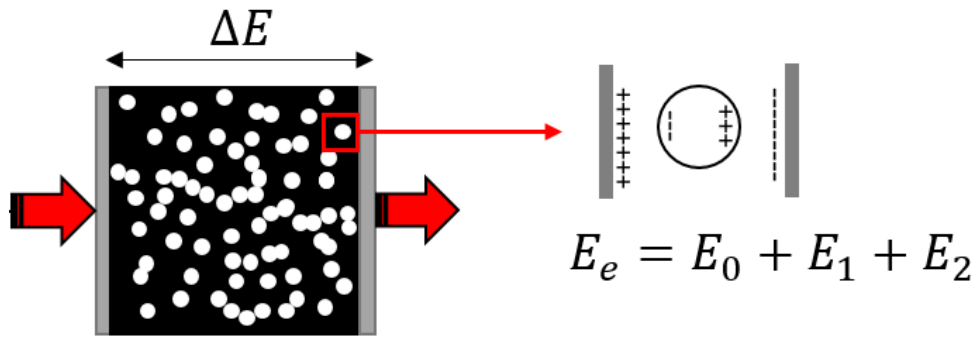
Figure 30: Lorentz Model.

$$\overrightarrow{E_e} = \overrightarrow{E_0} + \overrightarrow{E_1} + \overrightarrow{E_2} \tag{3-12}$$

where $\overrightarrow{E_0}$ is the strength of the electric field generated by the free charge on the pole plate. $\overrightarrow{E_0} = \rho/\varepsilon_0$. ρ is the free charge surface density. $\overrightarrow{E_1}$ is the strength of the electric field generated by the outer spherical polarized dielectric. $\overrightarrow{E_2}$ is the electric field strength generated by polarized particles in the sphere.

The electric field strength $\overrightarrow{E_1}$, generated by the dielectric polarized outside the sphere at the center of the sphere, consists of two components: one is the electric field strength $\overrightarrow{E_p}$ generated by the interaction of the polarized charge at the pole plate interface and the dielectric in vacuum; the other is the electric field strength $\overrightarrow{E_p'}$ established by the polarized charge on the surface of the Lorentz sphere in vacuum. Due to the symmetry of the Lorentz sphere, the electric field strength component formed by the interaction of the polarized charge on the sphere perpendicular to the $\vec{E}$ direction is zero.

$$\overrightarrow{E_1} = \overrightarrow{E_p} + \overrightarrow{E_p'} \tag{3-13}$$

where $\overrightarrow{E_p}$ is the strength of the electric field generated by the interaction of polarized charges at the pole plate interface with the dielectric in a vacuum. $\overrightarrow{E_p} = -\vec{P}/\varepsilon_0$. $\overrightarrow{E_p'}$ is the strength of the electric field established in vacuum by polarized charges on the surface of a Lorentz sphere. $\overrightarrow{E_p'} = \vec{P}/3\varepsilon_0$. $\vec{P}$ is the uniform dipole moment per unit volume.

In the case of a simple cubic crystal, the atoms induce equal moments under an external field, due to the symmetry of the cubic crystal:

$$\overrightarrow{E_2} = 0$$

Therefore, it follows that for a symmetric cubic crystal:

$$\textbf{SI}: \overrightarrow{E_e} = \vec{E} + \frac{\vec{P}}{3\varepsilon_0} \tag{3-14}$$

$$* \, \textbf{CGS}: \overrightarrow{E_e} = \vec{E} + \frac{4\pi}{3}\vec{P} \tag{3-15}$$

where $\vec{E}$ is the uniform applied field. $\vec{E} = \overrightarrow{E_0} + \overrightarrow{E_p}$, $\overrightarrow{E_0}$ is the strength of the electric field generated by the free charge on the pole plate. $\overrightarrow{E_0} = \rho/\varepsilon_0$. $\overrightarrow{E_p}$ is the strength of the electric field generated by the interaction of polarized charges at the pole plate interface with the dielectric in a vacuum. $\overrightarrow{E_p} = -\vec{P}/\varepsilon_0$. $\vec{P}$ is the uniform dipole moment per unit volume.

If the polarizability of each point is α, the dipole moment of the central point, and by symmetry that of all points, is therefore [177]:

$$p = \alpha\overrightarrow{E_e} \tag{3-16}$$

Then the dipole moment per unit volume within the cavity can be calculated from the definitions:

$$* \, \vec{P} = \frac{1}{V}\sum_i p_i = n\alpha\overrightarrow{E_e} \tag{3-17}$$

where n is number of points per unit volume.

According to classical electrodynamics, for an isotropic medium, the relationship between the applied electric field $\vec{E}$ and the potential shift $\vec{D}$ in the medium under the weak field approximation is:

$$\textbf{SI}: \vec{D} = \varepsilon\vec{E} = \varepsilon_0\vec{E} + \vec{P} = \varepsilon_0(1 + \alpha)\vec{E} = \varepsilon_r\varepsilon_0\vec{E} \tag{3-18}$$

$$* \mathbf{CGS}: \vec{D} = \varepsilon \vec{E} = \vec{E} + 4\pi \vec{P} \tag{3-19}$$

where ε_r is the relative dielectric constant, $\varepsilon_r = \dfrac{\varepsilon}{\varepsilon_0} = 1 + \chi_c$. ε_0 is the dielectric constant in vacuum. α is polarization ratio and ε is the dielectric constant.

By linking the above three * equations:

$$\frac{\varepsilon - 1}{\varepsilon + 2} = \frac{4\pi}{3} n\alpha \tag{3-20}$$

This shows the Clausius-Mossotting equation, which describes the relationship between the microscopic and macroscopic states of dielectric polarization, when all molecules are considered macroscopically [178].

$$\frac{\varepsilon - 1}{\varepsilon + 2} = \frac{4\pi}{3} \sum_i n_i \alpha_i \tag{3-21}$$

Thereafter, Maxwell and Garnett used a simple spherical model to assess the polarization rate. Assuming that the spherical molecule has a dielectric constant of ε_1 and a radius of a, the molecular polarization rate α is:

$$\alpha = \frac{\varepsilon_1 - 1}{\varepsilon_1 + 2} a^3 \tag{3-22}$$

Bringing in the Clausius-Mossotting equation yields the Maxwell-Garnett equation [179]:

$$\frac{\varepsilon - 1}{\varepsilon + 2} = \varphi_1 \frac{\varepsilon_1 - 1}{\varepsilon_1 + 2} \tag{3-23}$$

where φ_1 is the volume proportion of the molecule. The above equation is seen as a molecule with a dielectric constant of ε_1 and a volume proportion of φ_1 scattered in air with a dielectric constant of 1. The value of this theory is not only reflected in the molecular structure, it also can be extended and developed to the particle or composite structure. It can be viewed as a dielectric with dielectric

constant ε_1 and concentration φ_1 nested in a host with dielectric constant ε_0, and the formula can be further expressed as:

$$\frac{\varepsilon - \varepsilon_0}{\varepsilon + 2\varepsilon_0} = \varphi_1 \frac{\varepsilon_1 - \varepsilon_0}{\varepsilon_1 + 2\varepsilon_0} \tag{3-24}$$

The Maxwell-Garnett equation does not produce critical thresholds and is only applicable in the case of smaller filler volume fractions. The main drawback of the theory is that it requires that each conductive particle is replaced by an insulator particle, which is not the case for most composite dielectric structures. Another shortcoming is that it is not suitable for application to composite dielectric structures composed of multiple substances.

Bruggeman's theory [167]–[169] made a significant improvement on the Maxwell-Garnett theory. Consider a binary system with a dielectric volume fraction of φ_1 for a dielectric constant of ε_1 and φ_2 for a dielectric volume fraction of ε_2. First replace this complex system by a simple model which (as shown in Figure 31) is considered to be a uniform phase system with an effective dielectric constant of ε, with nested spheres of radius a and dielectric constant of ε_1. He assumes that the average flux bias due to dielectric polarization is zero, i.e.
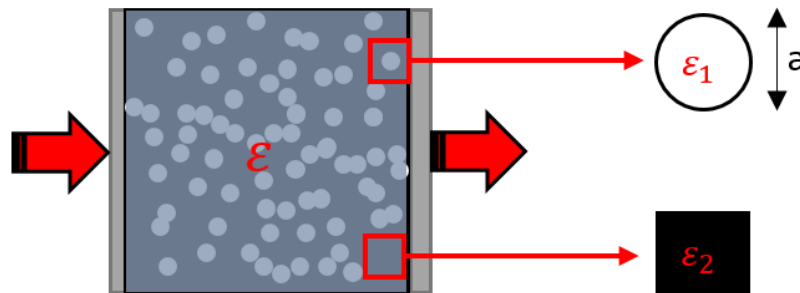
Figure 31: Bruggeman's theory.

$$\varphi_1 \Delta\phi_1 + \varphi_2 \Delta\phi_2 = 0 \tag{3-25}$$

$$\varphi_1 \frac{\varepsilon_1 - \varepsilon}{\varepsilon_1 + 2\varepsilon} + \varphi_2 \frac{\varepsilon_2 - \varepsilon}{\varepsilon_2 + 2\varepsilon} = 0 \tag{3-26}$$

The polarization of the dielectric occurs under the action of an external electric field, polarized charges appear during the polarization process, additional electric field E' is generated by these polarized charges inside and outside the dielectric. The sum of the additional electric field E' generated by the polarized charges and the applied electric field E_0 constitutes the field strength E at any point in space.

$$E = E_0 + E' \tag{3-27}$$

Generally, the change of spatial position affects the magnitude of the additional electric field E', which is uniform in the medium and can make the value of the total electric field E smaller because its direction is opposite to E_0. However, if the shape of the medium is not symmetrical, the above state may not be achieved. The electric field strength E affects the polarization strength P of the medium, so the total electric field E and the polarization strength P inside the medium decrease with the increase of the absolute value of the additional electric field E'. The additional field E' generated by the polarized charge in the medium always plays the role of decreasing the polarization intensity P, i.e., plays the role of weakening the polarization, and is therefore called the depolarization field.

$$E' = LP/\varepsilon \tag{3-28}$$

where ε is the dielectric constant of the medium. L is the demagnetization or depolarization coefficient.

The size of L is not related to the volume of the medium, but only to the shape of the medium. Take the ellipsoid as an example. The depolarization factor of the ellipsoid along the three orthogonal axes satisfies the following conditions:

$$L_x + L_y + L_z = 1 \tag{3-29}$$

The sphere is a symmetrical structure, so the depolarization factor is equal in all three directions:

$$L_x = L_y = L_z = 1/3 \tag{3-30}$$

The equation for the conductivity of a symmetric media, written in the more general form for oriented ellipsoids is [180], [181]

$$\varphi_1 \frac{\sigma_1 - \sigma}{\sigma_1 + \dfrac{1-L}{L}\sigma} + \varphi_2 \frac{\sigma_2 - \sigma}{\sigma_2 + \dfrac{1-L}{L}\sigma} = 0 \tag{3-31}$$

where L is the demagnetization or depolarization coefficient.

$$\varphi_1 \frac{\sigma_1 - \sigma}{\sigma_1 + \dfrac{1-\varphi_c}{\varphi_c}\sigma} + \varphi_2 \frac{\sigma_2 - \sigma}{\sigma_2 + \dfrac{1-\varphi_c}{\varphi_c}\sigma} = 0 \tag{3-32}$$

Rewritten in the following form is the well-known Bruggeman effective medium theory [167]–[169].

$$\frac{\varphi_2(\sigma_2 - \sigma_{eff})}{\sigma_2 + A\sigma_{eff}} + \frac{(1 - \varphi_2)(\sigma_1 - \sigma_{eff})}{\sigma_1 + A\sigma_{eff}} = 0 \tag{3-33}$$

with: $$A = \frac{1 - \varphi_c}{\varphi_c}$$

where σ_{eff} is the effective conductivity of the composite, σ_1 is the conductivity of the low-conductivity phase, σ_2 is the conductivity of the high-conductivity phase, φ_c is the percolation threshold and φ_2 is the volume fraction of the high-conductivity phase.

The Bruggeman effective medium theory is an extension of the Maxwell-Garnett theory, which uses a homogenization approach to predict the effective properties of multi-phase materials. This approach models the composite material as a homogeneous mixture of the various phases and uses volume fractions of the phases to calculate the effective properties of the composite.

3.4.3 Summary and Discussion

In summary, there are several different models and theories that can be used to model the electrical conductivity of multi-phase materials, each with their own strengths and weaknesses. Percolation-based models take into account the connectivity of the conductive particles within the material, while effective medium theories assume that the composite material can be represented by an equivalent homogeneous medium with an effective electrical conductivity. The choice of model will depend on the specific characteristics of the composite system being studied, such as the size, shape, and distribution of the particles, and the complexity of the microstructure. Some models are simple and efficient, but not accurate for complex systems, other models like thermodynamic or geometrical percolation models are more accurate but computationally intensive. Bruggeman effective medium theory is considered to be the most accurate and general of the effective medium theories, as it can be applied to a wide range of composite systems and takes into account the size, shape, and orientation of the particles. In this study, the computational method will be employed to simulate the percolation threshold of the mixture. It is particularly useful for simulating percolation in disordered systems and systems with complex microstructures, where analytical solutions may not be possible.

4 Experimental analysis of building materials

4.1 Introduction

The objective of this chapter is to investigate the effect of graphite as a conductive filler material on the electrical conductivity and mechanical properties of two types of mortar mixtures: Ordinary Portland Cement (PC) and Geopolymer (GP). Two composite mixtures were prepared and evaluated, PC-graphite (PCG) and GP-graphite (GPG) mixture. The experiments were carried out under controlled conditions at the Department of Materials in Civil Engineering at Technical University of Darmstadt.

4.2 Materials and Methods

4.2.1 Characterization methods

The particle size distribution (PSD) of metakaolin was measured using a Partica LA-950V2 laser granulometer from Horiba (Retsch). Compressive strength tests were conducted on samples measuring 80 mm x 40 mm x 40 mm, at a loading rate of 2.4 kN/s, in accordance with DIN EN 196-1. The DC resistance of all samples was measured using the four-probe method. The DC conductivity of PCG and GPG composites were tested in both 100 % saturated water (samples were submerged in deionized water for one day until the mass was constant) and dry conditions (samples were placed in a 105 °C oven for 7 days until the mass was constant). Laboratory power supplies (Voltcraft HPS-13015, Voltcraft, Germany) were utilized to provide a 12 V potential difference between the two ends of the samples. Current and voltage measurements were taken using a Desktop multimeter (Voltcraft VC650bt, Voltcraft, Germany) and Multimeter (Voltcraft vc830, Voltcraft, Germany), respectively. Mercury intrusion pore measurements were performed on 28-day cured specimens using a Pascal 140 and 440 Mercury Intrusion Porosimeter (ThermoFisher Scientific, Waltham, MA, USA) as previously described. For MIP measurements, samples were dried in an oven at 105 °C until the mass was constant. The distribution of graphite particles within the geopolymers was analyzed using scanning electron microscopy (SEM) (Philips XL-30 FEG, Netherlands) with an electron beam accelerating voltage of 20 kV. In the case of Energy Dispersive Spectroscopy (EDS) and back scattered electron (BSE) detection, SEM-BSE-EDS (Zeiss EVO LS25, Jena, Germany) was used with a LaB6 electron source. A polished portion of the graphite geopolymer compound was prepared for collecting EDS images using a Silicon Drift Detector (SDD 25 mm^2, 129 eV, silicon nitride window, 1.0 Mcps) (EDAX, AMETEK, Berwyn, USA). Samples were impregnated with low-viscosity liquid epoxy resin (EPOFIX, Struvers, Denmark) using a 20 kPa vacuum impregnation machine (CitoVac from Struvers, Ballerup, Denmark). The samples were then polished using a semi-automatic polishing machine (LaboSystem, Struers, Denmark). The polishing process began with diamond-based discs, with a hardness range of HV 150 to 2000, and a rotational speed of 300 rpm. This was followed by the use of a lubricated cloth and a

polycrystalline diamond spray, with particle sizes of 9, 3, and 1 micrometers, at a rotational speed of 150 rpm.

4.2.2 Portland cement raw material

In the experimental test series, fly ash (class F) and a commercially available Portland cement CEM I 42.5 N (HeildelbergCement AG, Germany) was utilized, in accordance with DIN EN 197-1 standards, to prepare PC mortar This pure Portland cement CEM I has a strength class of 42.5, which corresponds to a standard strength of at least 42.5 N/mm² after 28 days, as determined according to DIN EN 196-1:2016-11. The composition of the Portland cement is shown in Table 6.

Table 6: Chemical composition of Portland cement CEM I 42.5N from HeildelbergCement AG, Germany [182]. LOI: Loss on ignition.

Material	SiO_2	Al_2O_3	Fe_2O_3	CaO	MgO	K_2O	Na_2O	SO_3	Other	LOI
CEM I 42.5N	46.0	39.6	10.0	0.2	2.0	1.0	1.2	2.44	0.48	1.39

4.2.3 Metakaolin and waterglass raw material

The metakaolin (Metaver® R, a brand of metakaolin distributed by NEWCHEM GMBH) used in the study was a commercial product that was obtained through industrial-scale calcination of a quartz-rich clay from a primary geological deposit. The clay was heated in a rotary kiln for about four hours at a temperature of 700-750 degrees Celsius, with a production capacity of about 11 tons per hour. The metakaolin was analyzed using quantitative powder X-ray diffraction and Rietveld refinement, which revealed that it was composed of 46 % amorphous material, 40 % quartz and 10 % Muscovite (full mineralogical composition and chemical composition are given in Figure 32 and Table 7).
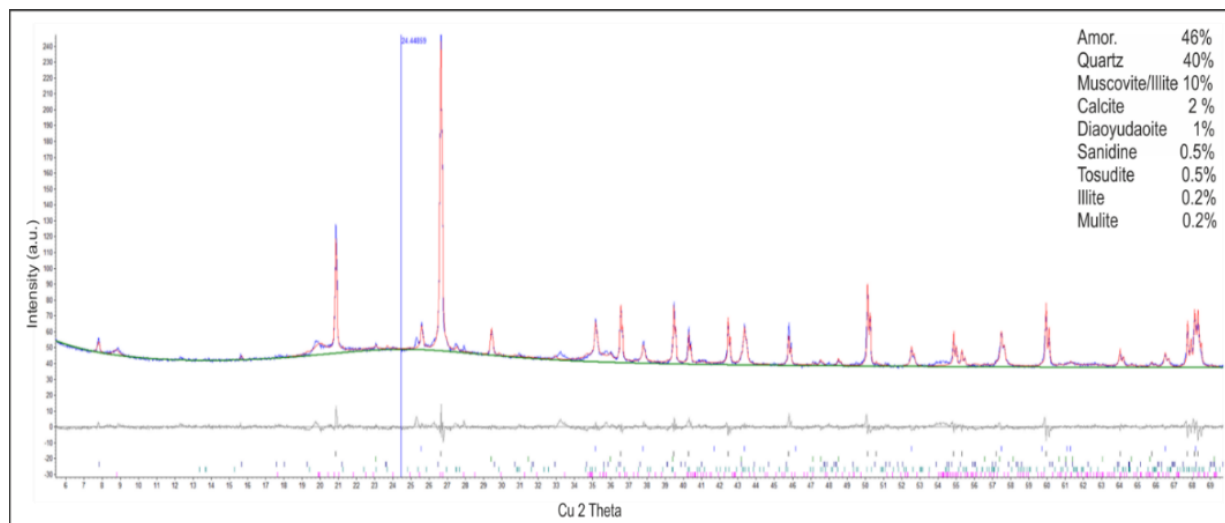
Figure 32: Powder X-ray diffraction quantitative analysis of the raw metakaolin based on Rietveld refinement (using DIFFRAC.TOPAS Version 5, Bruker)[182].

Additional characteristics provided by the manufacturer include the bulk density (2.6 g/cm^3), Blaine value (approximately 10,000 cm^2/g), Brunauer, Emmett and Teller (BET) surface area (approximately 17 m^2/g), and loose bulk density (0.5-0.7 g/cm^3).

Potassium silicate solution (waterglass) was used as alkaline activator, with a molar SiO_2/K_2O ratio of 1.5, 45 % total SiO_2 and K_2O "solid" content, 20 mPas viscosity and 1.51 g/cm³ density.

Table 7: Chemical composition of metakaolin (MK) and K-based silicate solution (waterglass) [182].

Material	SiO$_2$	Al$_2$O$_3$	CaO	TiO$_2$	Fe$_2$O$_3$	MgO	Na$_2$O	K$_2$O	H$_2$O
Metakaolin MK1	67.0	27.0	1.0	1	4	0.1	0.1	0.2	–
K-waterglass	22	–	–	–	–	–	–	23	55

The particle size distribution of metakaolin are shown in the following Figure 33.
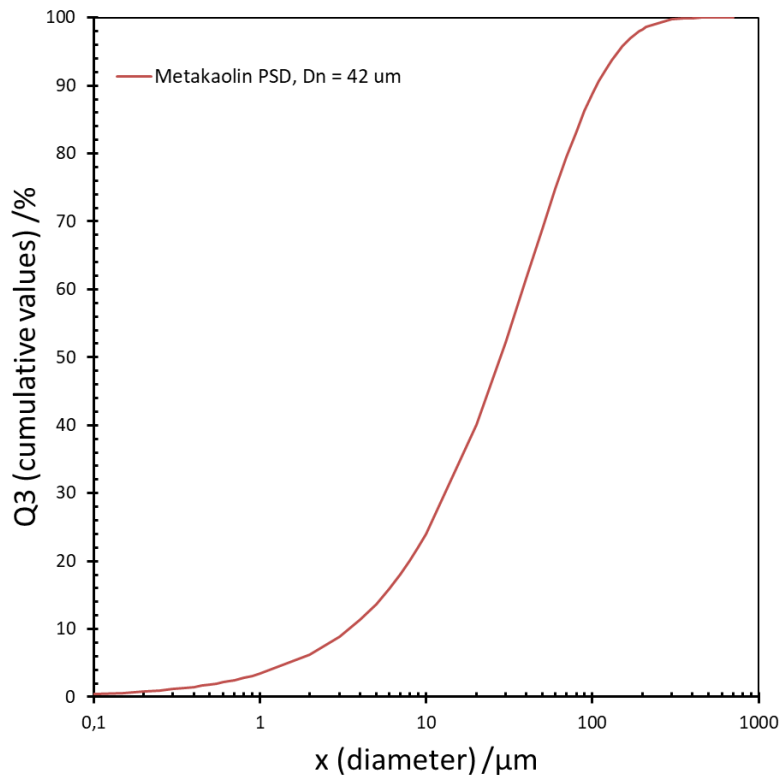
Figure 33: Particle size distribution of Metakaolin powder measured using a Partica LA-950V2 laser granulometer from Horiba.

4.2.4 Graphite raw material

Graphite is an ideal conductive filler material due to its high electrical conductivity and relatively low cost. The graphite used in this study is MECHANO-LUBE® 1 (H.C. Carbon GmbH, Germany), which is a high-purity, specifically ground natural graphite. The graphite was pressed into raw sheets of 3.5 cm diameter and the resistivity of the graphite was measured using a Keithley 2700 data acquisition

instrument. The technical data of graphite is given in and the particle size distribution of graphite powder is shown in Table 8.

Table 8: The technical data of natural graphite.

Material	Carbon	D_{10}	D_{50}	D_{90}	Spec. surface	Bulk density	Electrical conductivity
	wt. %	µm	µm	µm	m^2/g	g/l	S/m
Graphite	>99	1-3	4-6	8-11	10	250	183

Graphite powder was analyzed by scanning electron microscopy (Philips XL-30 FEG , Netherlands) using an electron beam at 30 kV as the accelerating voltage. The particle size distribution of graphite powder was measured using a Partica LA-950V2 laser granulometer from Horiba (Retsch). The results are shown in the following Figure 34.
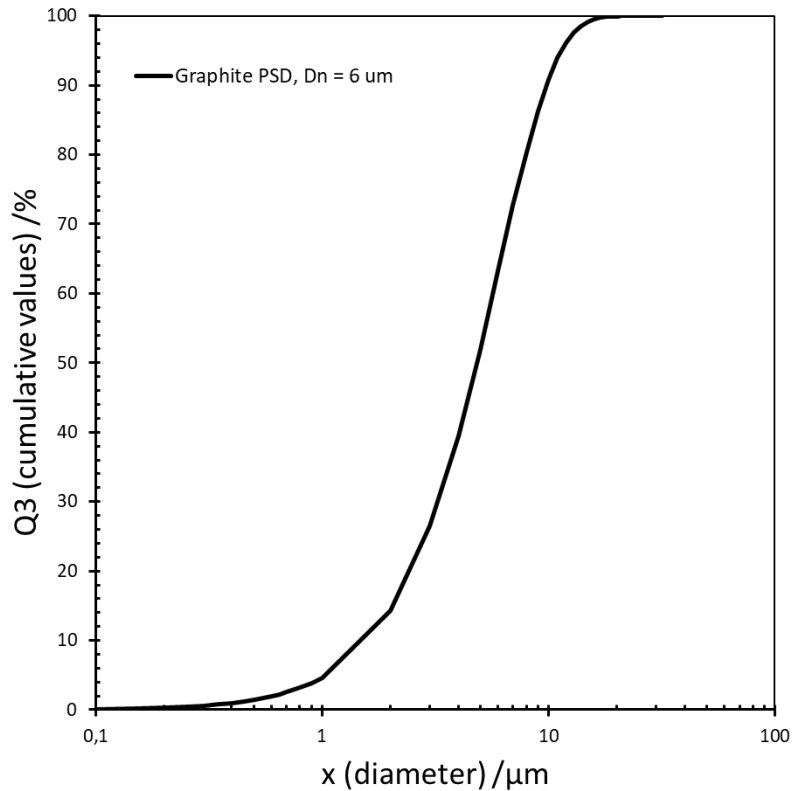
Figure 34: Particle size distribution of graphite powder measured using a Partica LA-950V2 laser granulometry from Horiba.

Figure 35 shows SEM images of the natural graphite. The flake graphite particles have thin plate shapes. The natural graphite is primarily composed of fine flake particles. While this may negatively impact the mechanical properties of the overall composite material, the use of graphite as a filler is cost-effective and the smaller particle size facilitates the formation of a high-quality conductive

network. As such, it is considered to be a superior conductive filler material compared to other options, such as graphene, for the preparation of conductive composite materials.
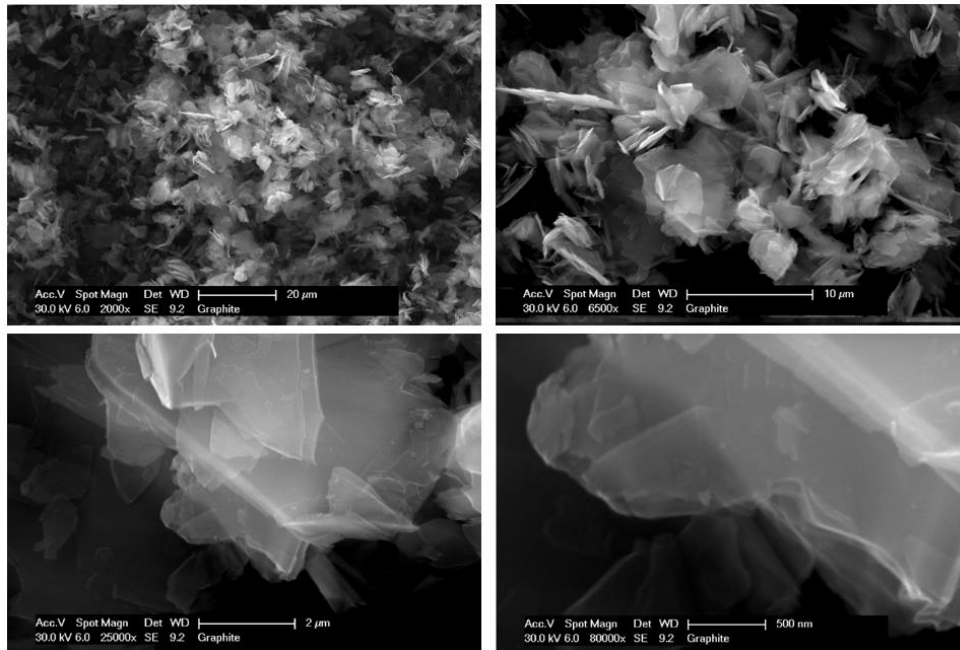
Figure 35: Scanning electron microscope images of the graphite powders.

4.2.5 Dispersing agent

Graphite is a non-polar solid that is challenging to disperse evenly in polar liquids due to its tendency to aggregate or float on the surface. In order to effectively distribute graphite in a conductive cement system, a dispersant is often used. A suitable dispersing agent, such as polycarboxylate ether (PCE) (Sika®ViscoCrete®-20 Gold), can be adsorbed onto the surface of the graphite particles through ionic charges and other surface interactions, allowing for improved wetting and uniform dispersion in the system.

4.2.6 Manufacture of PCG and GPG

All test specimens were prepared using a standard programmable mortar mixer (E092-01N, Mixmatic, Matest, Italy). The preparation of samples was conducted in a fully climate-controlled laboratory, where the ambient temperature was maintained at 20 °C and relative humidity at 60 %. The samples were cured and stored in sealed formwork under the same climatic conditions.

In this study, the effects of different graphite contents on the electrical conductivity and porosity of two composite materials, PCG and GPG, were investigated. 11 different types of PCG and 12 different types of GPG pastes were prepared using a standard programmable mortar mixer in a fully climate-controlled laboratory. The water-cement ratio for PCG was set at 0.6 and the graphite volume fractions were varied from 0 to 10 %. For GPG, the waterglass-metakaolin ratio was set at 0.8 and the graphite

volume fractions were varied from 0 to 10 %. In order to improve the porosity of GPG for use as an MFC anode, additional water was added to GPG with a volume fraction of 10% at various ratios. The mixture design is presented in Table 9 and Table 10.

Table 9: Name and Composition of the Electrode Materials Based on PC.

PCG	Graphite [g]	Cement [g]	Water [g]	PCE [g]	Fly ash [g]
PC Ref.	0	948	570	0	0
PC06 1C	28	948	570	0	0
PC06 3C	57	948	570	0	0
PC06 4C	85	948	570	0	0
PC06 9C	199	948	570	19.9	0
PC06 3F 8C	176	733	572	17.6	220
PC06 3F 9C	198	723	564	19.8	217
PC06 3F 10C	220	714	557	22	214
PC075 8C	176	843	632	17.6	0
PC075 9C	198	832	624	19.8	0
PC075 10C	220	820	615	22	0

Table 10: Name and Composition of the Electrode Materials Based on GP.

GPG	Graphite [g]	Metakaolin[g]	Waterglass [g]	PCE [g]	Water [g]
GP Ref.	0	1173.2	938.5	0	0
GP08 1W 1C	22	1133.3	906.6	2.2	22
GP08 1W 2C	44	1093.4	874.7	4.4	44
GP08 1W 3C	66	1053.5	842.8	6.6	66
GP08 1W 5C	110	973.7	779	11	110
GP08 1W 7C	154	894	715.2	15.4	154
GP08 1W 8C	176	854.1	683.3	17.6	176
GP08 1W 9C	198	814.2	651.3	19.8	198
GP08 1W 10C	220	774.	619.4	22	220
GP08 1.2W 10C	220	722	578	22	264
GP08 1.7W 10C	220	594	475	22	374
GP08 2W 10C	220	516.2	413	22	440

Prior to mixing, the interior of the mixing bowl of the mortar mixer was wiped with a damp cloth. The required amounts of raw materials were weighed and the PCE superplasticizer and water were combined and mixed thoroughly. Then, the mixture of PCE, water (in the case of GPG, a mixture of

water, water glass, and PCE), and graphite was added to the mixing bowl. Stirring was initiated at a speed of 80 rpm for 90 seconds. The speed was then increased to 285 rpm for 30 seconds, followed by a 30-second pause. During this time, the cement powder (metakaolin for GPG) was added. Mixing resumed at a speed of 80 rpm for 180 seconds and was paused again for 30 seconds. The interior walls and bottom of the mixer bowl were scraped manually to ensure thorough mixing. Mixing continued at the same speed for an additional 180 seconds, followed by an increase in mixing speed to 285 rpm for 60 seconds, marking the end of the mixing process. The fresh mortar was filled into the mold, placed on a vibrating table, and vibrated at a frequency of 40 rpm for 40 seconds to remove any entrapped air bubbles. The mold was then sealed.

To facilitate the measurement of the hardened DC resistivity, four stainless steel mesh electrodes were placed in the mold prior to the mixing process. The mold used was a plastic container with a volume of 125 mL (Brand: Burkle, from ESSKA.de). To insert the electrode material, a Polyethylene (PE) insulation material with an inner diameter of 35 mm and a wall thickness of 9 mm was cut into four segments of 19 mm, 10 mm, 10 mm, and 10 mm, and 19 mm using a hot wire. A square stainless steel mesh with a side length of 30 mm was placed between each segment as the electrode material. Figure 36 shows the formwork for manufacturing samples to measure resistivity. The mold used to prepare cement anodes and for microstructural analysis is a transparent polypropylene container with an inner diameter of 34 mm and an overall height of 55 mm, purchased from Glas-Shop.com. To evaluate the strength of the concrete, flexural and compressive strength tests are performed in accordance with DIN EN 1015-11. The test pieces used are mortar prisms measuring 40 x 40 x 160 mm.

Figure 36: The formwork for manufacturing samples to measure resistivity.

4.2.7 Characterization methods for hardend PCG and GPG.

Compressive strength tests were conducted on prismatic samples with dimensions of 80 mm x 40 mm x 40 mm at a loading rate of 2.4 kN/s in accordance with DIN EN 196-1. The four-probe method was utilized to measure the DC resistance of all samples. The DC conductivity of PCG and GPG composites were evaluated in both fully saturated water (samples were immersed in deionized water for one day until mass stabilization) and dry conditions (samples were placed in a 105 °C oven for 7 days until mass stabilization), respectively. Laboratory power supplies were utilized to provide a 12 V

potential difference across the samples, while current and voltage measurements were performed using a desktop multimeter, respectively. The DC measurement's setup is shown in Figure 37. The conductivity of the material is measured and calculated using the method described in Chapter 3.1.3.

$$R = \frac{V}{I} = \frac{\rho L}{A} \qquad \rho = \frac{AV}{IL} = \frac{1}{\sigma}$$
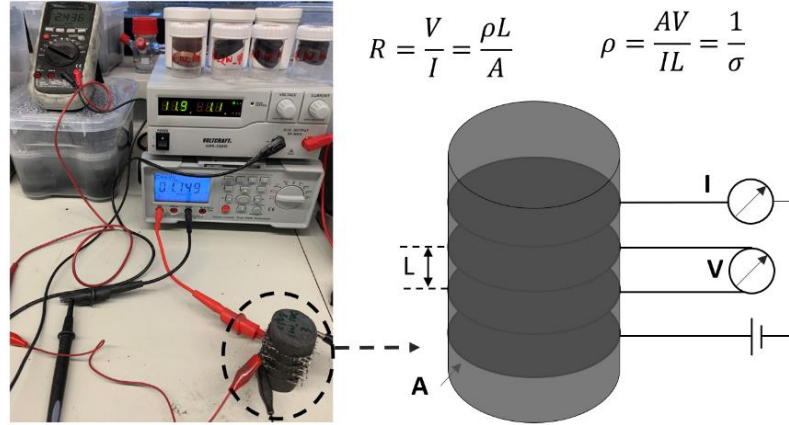
Figure 37: Set up for the DC measurement.

Additionally, mercury intrusion porosimetry (MIP) was conducted on 28-day cured specimens using a Pascal 140 and 440 Mercury Intrusion Porosimeter. SEM-EDS and back scattered electron (BSE) were used to analyze the graphite particles and distribution within the geopolymers. Cross-sections of the samples were impregnated with low-viscosity liquid epoxy resin, and polished using a semi-automatic polishing machine with diamond-based discs and polycrystalline diamond spray.

4.3 Results

4.3.1 DC electrical conductivity of PCG

The electrical resistance of the PCG (PC06 2C, PC06 3C and PC06 4C) was measured during the hydration process. The results of these measurements are illustrated in Figure 38. The resistivity of the PCG samples increases as the hydration reaction progresses, from an initial value of 180 − 220 Ohm·cm to a final value of 280 − 400 Ohm·cm. This increase in resistivity is attributed to the decrease in porosity caused by the hydration of the cement particles. The electrical resistance of the adhesive mixtures increases during the hydration process due to a decrease in porosity as the cement particles hydrate. As the hydration reaction proceeds, the cement particles grow and fill the pores in the mixture. Since only the pore spaces saturated with water or pore solution are electrically conductive, the electrical resistance increases as the pores become filled with solid cement particles, resulting in less conductive pathways for the electrical current to flow through. Additionally, the pore structure and the microstructure of the hydrated cement can also affect the conductivity. The specimens containing more graphite exhibit a similar trend, but with a less significant increase in resistance.
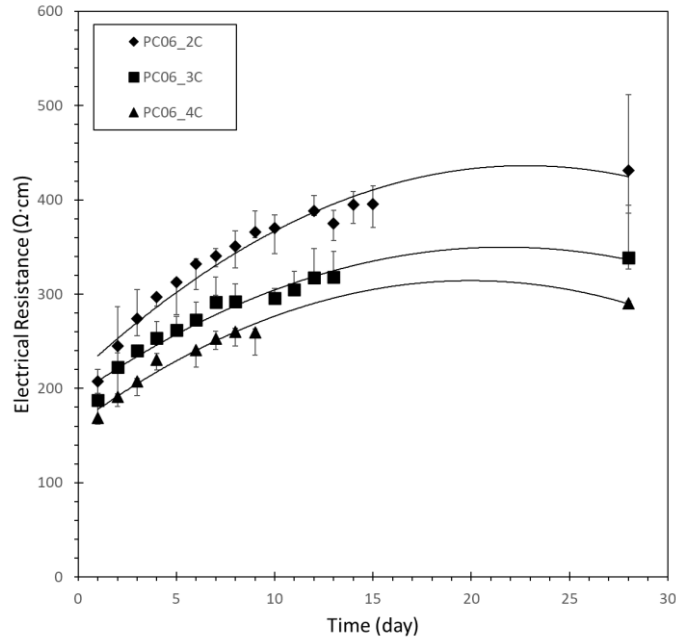
Figure 38: Measurement results of the electrical conductivity of PCG samples during the hydration phase.

The electrical conductivity of the PCGs was evaluated after the cement hydration was completed by measuring the resistance under varying applied voltages. As illustrated in Figure 39, as the applied voltage was increased from 1V to 23V, the measured voltage and current at both ends of the graphite-cement sample showed an approximately linear relationship. This indicates that the resistance of the graphite-cement composite exhibits ohmic behavior under steady-state conditions.
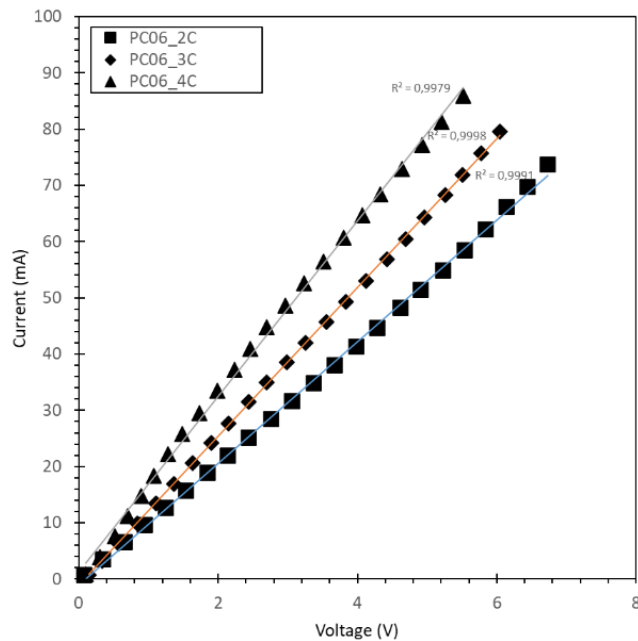
Figure 39: Variation of voltage and current at both ends of the graphite cement for different applied voltages.

63

At 28 days, the effect of pore saturation on electrical conductivity was further investigated. The electrical conductivity was measured on samples that were freshly taken from a water bath and were fully saturated, as well as on samples that were dried in an oven at 105°C until a constant weight was reached. The results of these measurements are shown in Figure 40. The fully saturated PCG samples showed some conductivity when the graphite volume fraction was less than 2 %, and its conductivity only slightly increased with increasing graphite content. In contrast, the conductivity of the dried PCG samples showed a significant percolation variation with increasing graphite content. The function curves indicate that at a graphite content of 8 vol-%, moisture no longer has a significant impact on the electrical conductivity. The maximum conductivity of the PCG samples are in the range of 10^{-5} to 10^{-4} S/m.
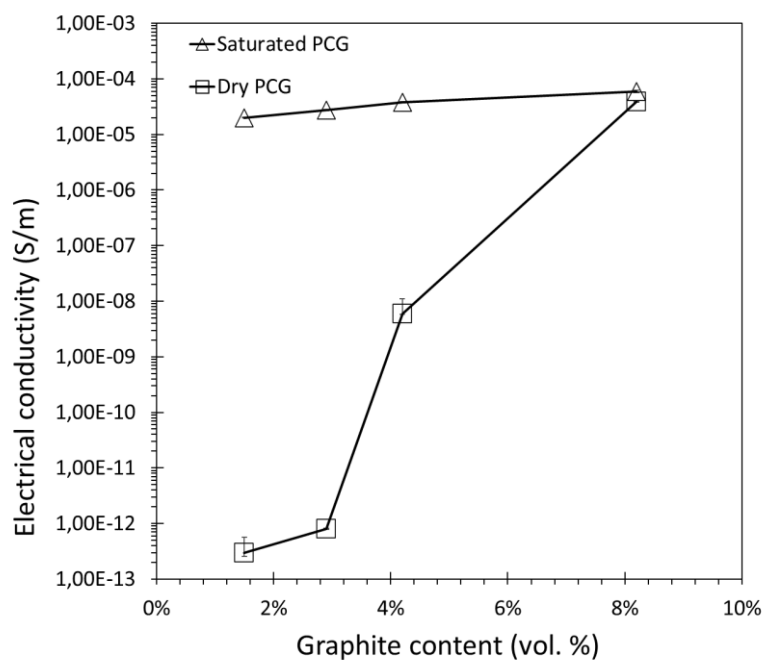
Figure 40: Electric conductivity of PCG (w/c=0.6) composites with different graphite content.

The electrical conductivity-graphite content curve of dried samples looks more like a percolation curve because the drying process affects the pore structure of the samples, which in turn affects the electrical conductivity.

In a percolation theory, electrical conductivity is dependent on the connectivity of conductive particles. The more conductive particles are connected, the more likely that an electrical current will flow through the material. In the case of dried samples, the drying process may cause shrinkage, which may lead to a more compact and less porous sample, resulting in less connected conductive particles. Therefore, as the graphite content increases, the electrical conductivity increases until a threshold is reached where a large enough network of conductive particles is formed, allowing for electrical current to flow through the material, known as percolation threshold.

On the other hand, for saturated samples, the pore structure is not affected by the drying process, and therefore the electrical conductivity increases only slightly with the increase of graphite content. The conductivity is not dependent on the connectivity of conductive particles, but on the amount of water present in the pores, which provides the ions necessary for electrical conductivity.

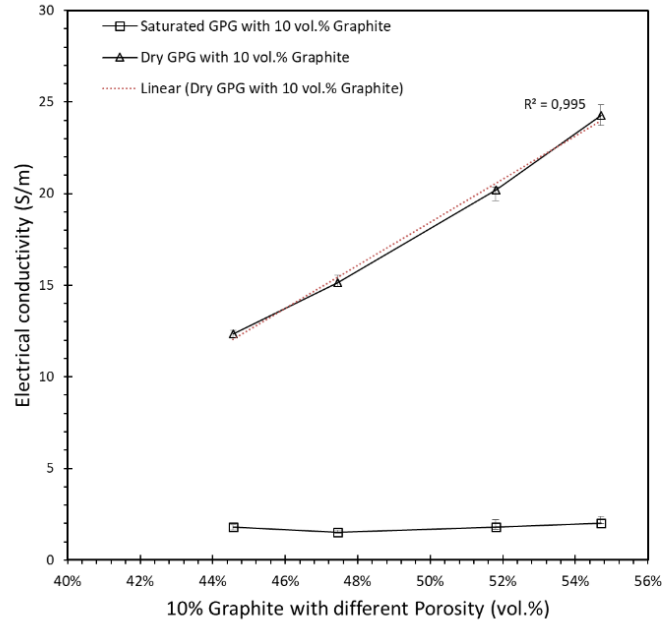### 4.3.2 DC electrical conductivity of GPG

After 14 days of hydration, the electrical conductivity was determined using the four-probe method under saturated and oven-dried conditions. The results are presented in Figure 41. The conductivity of the GPG samples that were saturated with water remained relatively constant and stable in the range of 1-2 S/m with increasing graphite content from 0 vol.% to 7 vol.%. This suggests that electron transfer in these samples is primarily dependent on ionic conductivity. However, the conductivity of the oven-dried GPG samples gradually increased after 7 vol.% graphite content and was significantly higher than that of the saturated samples. This can be attributed to two factors. First, when the sample is wet, the conductive pathway can be approximated as a combination of ion-conducting and electron-conducting paths, and during drying, the graphite particles that form the conductive network are freed from the ion-conducting bonds, resulting in a significant reduction in resistance during electron transfer. Second, the drying process causes the conductive network formed by the graphite particles to become denser, leading to an overall increase in electrical conductivity.
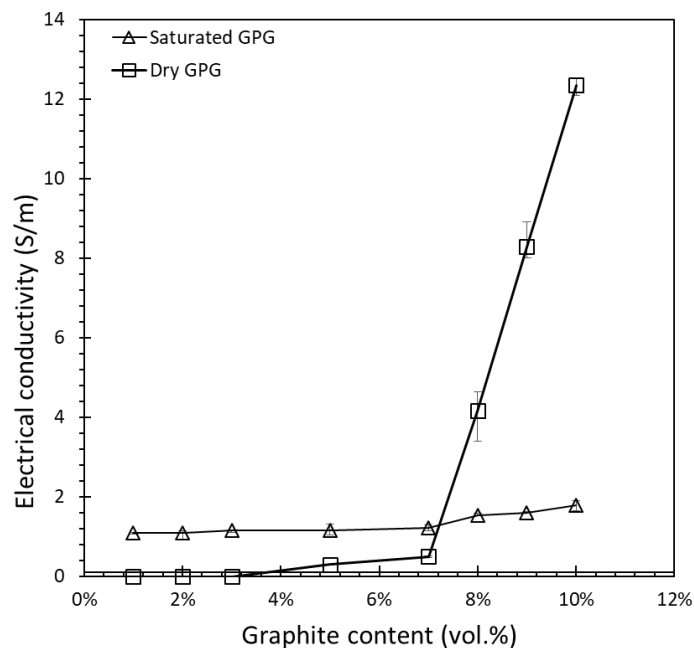
Figure 41: Electric conductivity of GPG (waterglass/metakaolin=0.8, water/graphite=1) composites with different graphite content.

As the content of graphite in GPG samples increases, the microstructure of the samples also changes. To evaluate the impact of microstructure on the electrical conductivity of the samples, samples with identical graphite content (10 vol.%) but varying porosity (ranging from 44% to 55%) were prepared

and the electrical conductivity was measured in both saturated and dried states. The results of these measurements are presented in Figure 42. In the dry state, the electrical conductivity of the samples increases with increasing porosity, indicating that for porous conductive composites, the electrical conductivity is closely linked to both the porosity of the matrix and the volume fraction of graphite.

Figure 42: Variation of the electrical conductivity of GPGs with porosity.

Before drying, the GPG samples have a higher ionic conductivity due to the presence of water in the pores and the ion-conducting bond between the graphite particles and the matrix. The water in the pores allows for the transfer of ions, which contributes to the overall conductivity of the sample. However, during the drying process, the water is removed and the graphite particles are freed from the ion-conducting bond, making the conductive network formed by the graphite particles denser. This leads to an increase in the overall electrical conductivity, which is now primarily dependent on the electron-conducting properties of the graphite particles (see Figure 43).
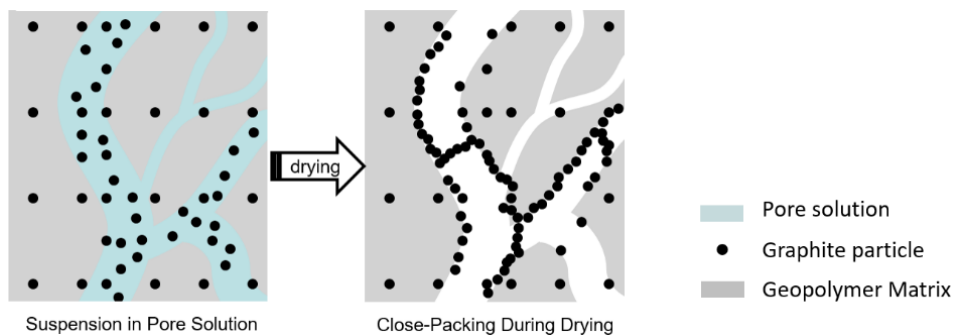

Figure 43: Close-packing of the graphite particles during drying [182].

The electrical conductivity of the GPG samples in the dry state is primarily dependent on the network of interconnected graphite particles. To account for this, an effective volume fraction V_{eff} is introduced:

$$V_{eff} = \frac{V_{graphite}}{V_{solid}}$$

(4-1)

where $V_{graphite}$ is the volume of graphite particle, V_{solid} is the sum of the volumes of graphite and other solid phases, is introduced to represent the volume fraction of graphite present in a solid matrix without the presence of air. The results are depicted in Figure 44. This calculation excludes the influence of pores on the conductivity of the mixture. The volume fraction of the conductive filler in the mixture is the proportion of its volume to the solid fraction. By introducing the effective volume fraction, the percolation threshold of the conductive mixture shifts from 8 vol.% to 12 vol.%.
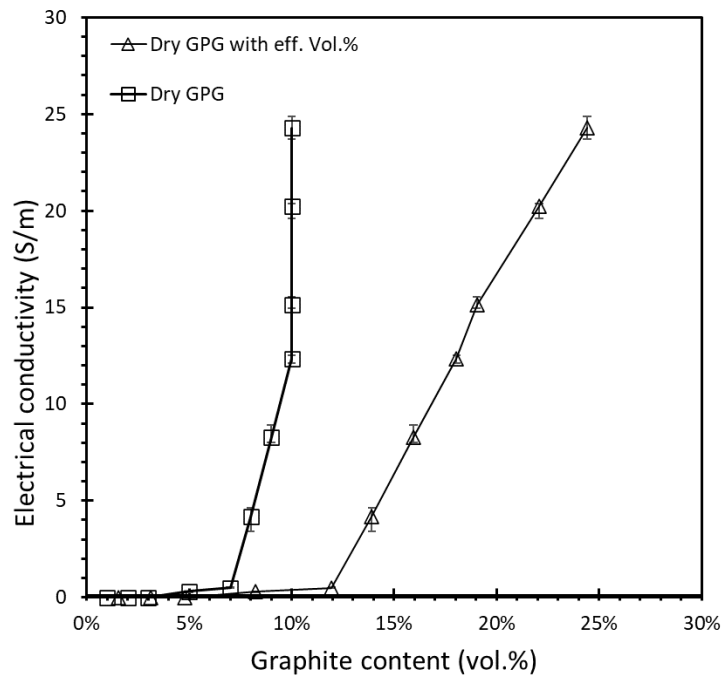
Figure 44: Variation of the GPG conductivity with the effective volume fraction.

4.3.3 Mechanical properties

In order to be able to assess the practical suitability of the anode material, the compressive strength of the hardened samples was determined by means of a compression test according to DIN EN 196-1. PC06_3F_8C, PC06_3F_9C, PC06_3F_10C, PC075_0F_8C, PC075_0F_9C and PC075_0F_10C were selected and tested. In order to ensure the workability of fresh mortar, a high water-to-cement ratio

of 0.6 was used. The compressive strength was negatively correlated with the graphite content. However, at graphite contents close to 10 vol.-%, the compressive strength of OPCG and GPG was still about 16 N/mm². The test results are shown in Figure 45.
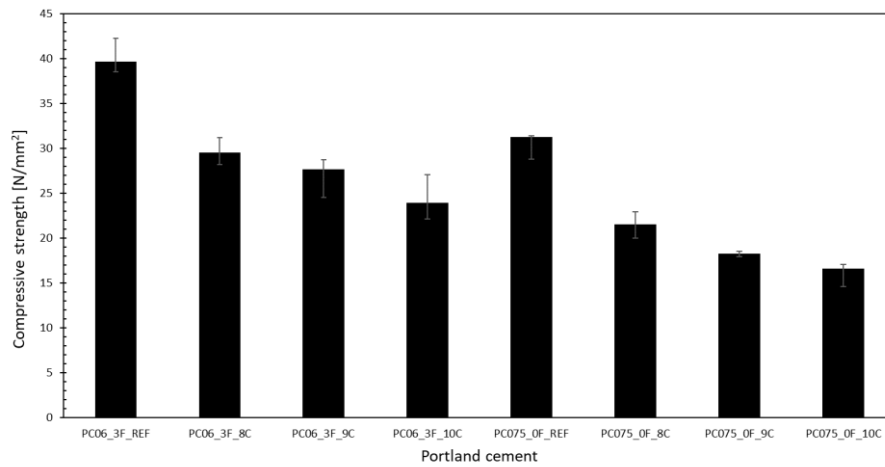
Figure 45: Compressive strengths of hardened cement paste PCG samples (PC06_3F_REF, PC06_3F_8C, PC06_3F_9C, PC06_3F_10C, PC075_0F_REF, PC075_0F_8C, PC075_0F_9C and PC075_0F_10C).

Figure 46 shows the compressive strength of GPG composites (GP08_REF, GP07_1W_1C, GP07_1W_2C, GP07_1W_3C, GP07_1W_5C, GP07_1W_6C, GP07_1W_8C, GP07_1W_9C, GP07_1W_10C) as a function of the volume percentage of graphite. The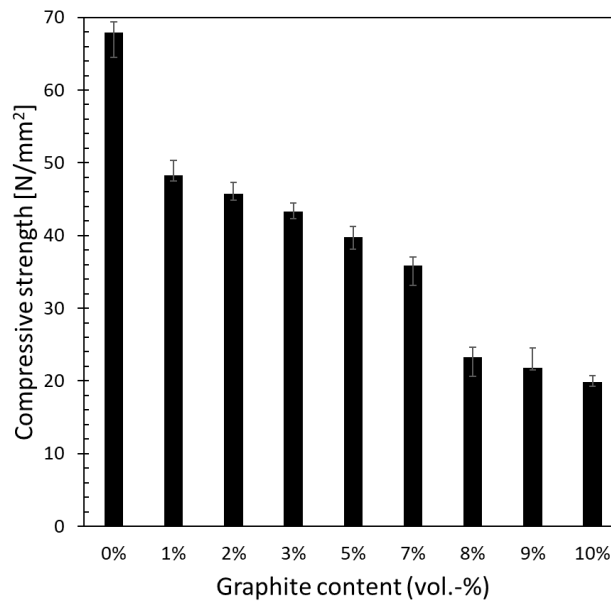 compressive strength is reported as the average value with standard deviation on three different specimens. The compressive strength of the reference samples is 68 N/mm2. As graphite content increases to 10 vol.%, the resistance decreases to 20 N/mm².

Figure 46: Compressive strengths of hardened cement paste PCG samples ((GP08_REF, GP07_1W_1C, GP07_1W_2C, GP07_1W_3C, GP07_1W_5C, GP07_1W_6C, GP07_1W_8C, GP07_1W_9C, GP07_1W_10C)).

68

### 4.3.4 Morphology and microstructure analysis

The pore size distributions of GPG and PCG samples were obtained using MIP, as shown in Figure 47. A significant difference was observed between GPG and PCG specimens. The pore system of GPG can be characterized by microcapillaries (pore diameter < 50 nm) resulting from the evaporation of water in the gel pores. The porosity of microcapillaries increased from 32% to 50% with an increasing water content. In contrast, the pore system of PCG belongs to macrocapillaries (50nm < pore diameter < 50 µm). The addition of fly ash and graphite particles refined the pore size distribution, resulting in more pore sizes less than 100nm. However, the majority of pore sizes was still above 50 nm. The pore size distribution in GPG was mainly concentrated in the range of 3 – 10 nm, with an increasing porosity with water content, but a majority of the pore sizes were still concentrated in the 10nm range. As Bhattacharya has mentioned in his book [159], a distance of 10 nm is still an effective distance for electron tunneling. Therefore, the pores in the geopolymer graphite mixture do not negatively impact the overall conductivity of the mixture. In fact, the pores act as a good separation for the material, allowing the graphite particles in GPG to be more tightly connected to each other, further contributing to the electrical conductivity. On the other hand, the pore size distribution in PCG samples is more extensive compared to GPG, with most of them being distributed around 50nm. This prevents electron tunneling from forming in PCG and the flow of electrons is negatively affected by the pore structure in PCG. As a result, the effective electrical conductivity of PCG is much lower than that of GPG.
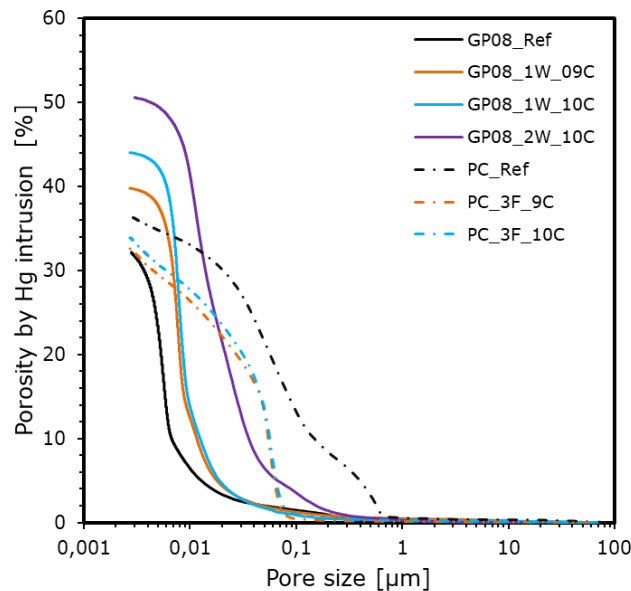
Figure 47: Pore size distribution of the GPG and PCG samples.

Scanning electron microscopy micrographs of GPG samples were analyzed as shown in Figure 48. As the graphite content increases, the graphite particles within the samples gradually form a continuous conductive network, as indicated by the red shading in Figure 48. The percolation threshold of 7 vol.% graphite content is reached when the graphite particles form a cohesive conductive network, as seen

in Figure 48 d. With a stabilized overall graphite content of 10 vol.%, increasing the porosity of the mixture leads to a more tightly bound network of graphite particles, resulting in an increased volume fraction of interconnected particles and an improvement in the electrical conductivity of GPG composites, as seen in Figure 48 f-h.
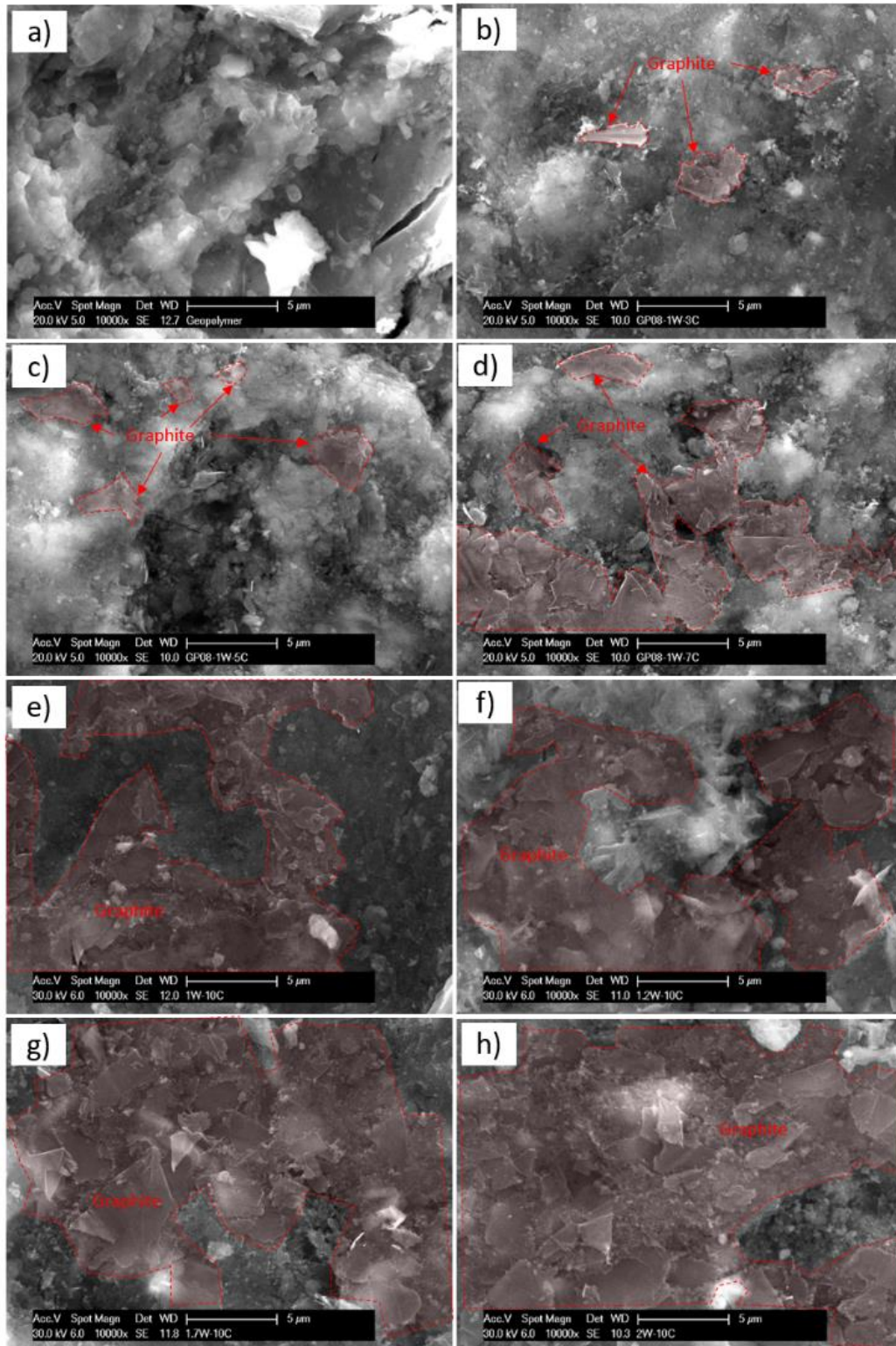
Figure 48: SEM micrographs of samples: a) GP08_Ref; b) GP08_1W_3C; c) GP08_1W_5C; d) GP08_1W_7C; e) GP08_1W_10C; f) GP08_1.2W_10C; g) GP08_1.7W_10C; h) GP08_2W_10C.

The elemental distribution of GPG was exemplarily analyzed for GP08_1W_10C using energy-dispersive spectroscopy (EDS) and backscattered electron (BSE) imaging, as shown in Figure 49. The BSE gray scale (inversely proportional to atomic number) and individual element maps for C (carbon), O (oxygen), Al (aluminum), Si (silicon), and K (potassium) are also provided. In the EDS results, it was found that the graphite particles were not evenly distributed, but were separated by solid volume properties. This could be due to the presence of oxide compounds in the geopolymer that act as an separating volume for the graphite particles. Possible sequestered volumes in geopolymers could be unreacted metakaolin (high Si and Al) as well as quartz (high Si) or feldspars (if all the metakaolin is reacted).
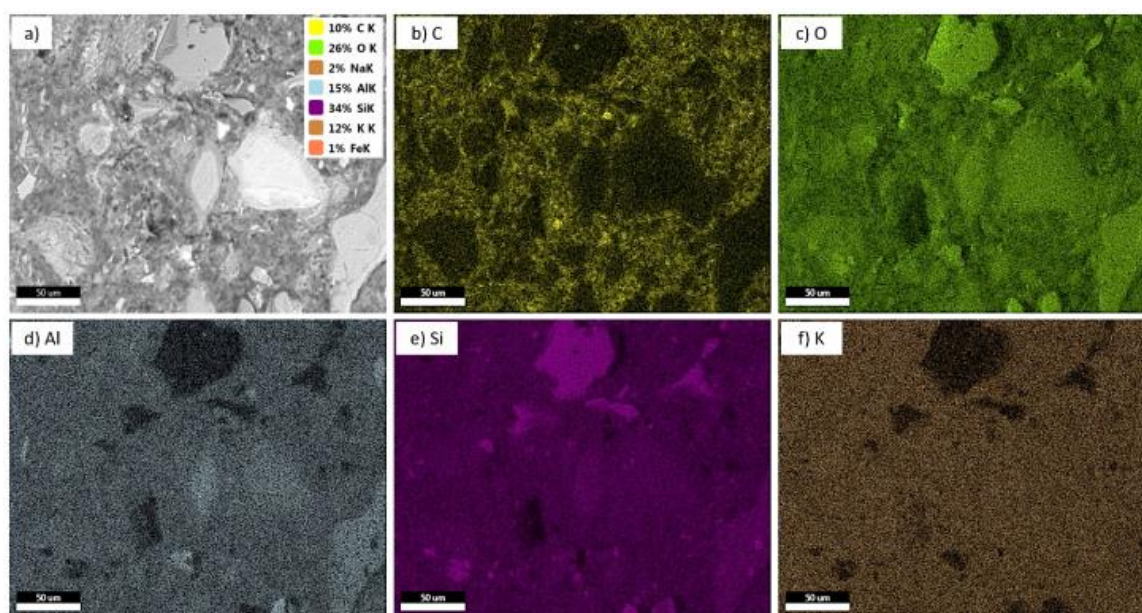
Figure 49: Elemental distribution (color) of GP08_1W_10C. a) BSE detector. EDS detector: b) elements C: Carbon; c) elements O: oxygen; d) elements Al: aluminum; e) elements Si: silicon; f) elements K: potassium.

4.4 Summary and Discussion

In summary, the electrical conductivity of graphite-cement and graphite-geopolymer mixtures were investigated. It was found that the conductivity of the mixtures increased with the addition of conductive filler in a dry condition. The percolation threshold for both PCG and GPG was determined to be around 8 vol.%. However, a significant difference in conductivity was observed between PCG and GPG in the percolation region, with conductivity values of 1×10^{-5} S/m and 12 S/m, respectively.

Hardened cement paste and geopolymers have porous structures that allow for the absorption of water into their pores in their natural state. Even without the addition of conductive fillers, they exhibit some conductivity in wet conditions, as shown in Figure 50. However, there is a fundamental difference between ionic conductivity and electronic conductivity. In terms of conductive efficiency, electronic conductivity is superior to ionic conductivity, as the movement of ions is significantly slower compared

to that of electrons. The formation of an electron-conducting network in the mixture results in higher conductivity. The theory of percolation and the electron tunneling effect are crucial for the formation of these networks. Achieving optimal electrical conductivity with cost-effective and high-quality materials is essential for the production of high-quality electrode materials.

The concept of effective volume fraction was also introduced in order to better understand the conductivity mechanism of GPG and exclude the effect of pores. Additionally, electron microscopy was used to confirm the percolation phenomenon occurring in GPG, and it was observed that when the volume fraction of conductive filler was greater than the percolation threshold, the graphite in the mixture formed a continuous network, resulting in a significant increase in conductivity.

The pore structure of PCG and GPG was also analyzed and it was observed that both materials had porosities of 30 – 40 %. The main difference in pore structure was that the pore size distribution in PCG was mainly concentrated in the range of 100 nm or greater, whereas the pore size distribution in GPG was mainly concentrated in the range of 3 – 10 nm. This smaller pore structure in GPG was found to greatly facilitate the formation of conductive networks in the form of electron hopping, resulting in a higher conductivity.
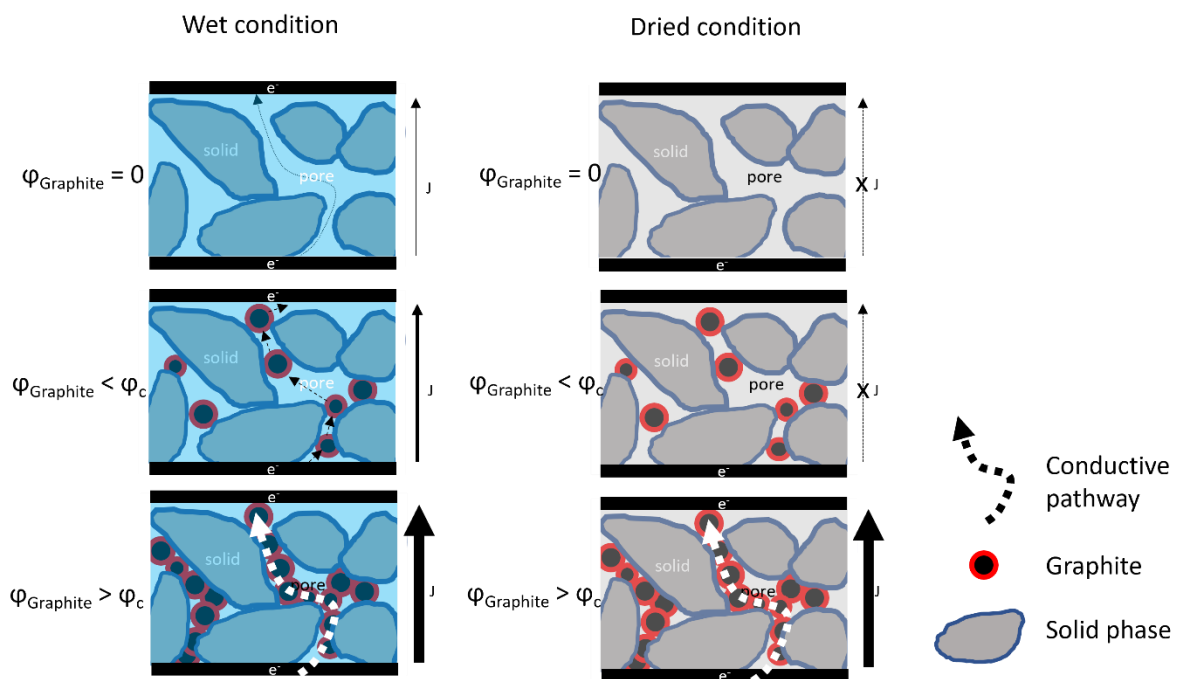
Figure 50: Formation of conductive pathways in the case of dried and wet conductive mixtures.

Carbon-based materials and stainless steel-based materials are the two main materials used in fuel cells. This study did not consider metal materials due to the potential corrosion problems that can arise when using them as electrode materials in microbial fuel cells. The cost of carbon-based materials varies depending on the particle size, with smaller particle sizes resulting in higher prices. While carbon nanomaterials have the advantage of small particle size, they can form a conductive network at lower volume fractions and do not negatively impact the strength of the geopolymer. However, their high

cost makes them unsuitable for large-scale applications. In terms of cost, natural graphite is an attractive option. Its unique sheet-like structure also allows for a low percolation threshold. As a single conductive material, graphite is an ideal choice for producing inexpensive, high-quality electrodes. Using graphite as the base material and a small amount of mixed carbon fibers to form a three-phase conductive mixture may provide even better results.

5 Modeling the Electrical Conductivity of Geopolymer Systems

The electrical conductivity of a dry conductive composite material is greatly influenced by the connectivity of the conductive filler. As the conductive filler forms a network, the volume fraction reaches the percolation threshold, resulting in a substantial increase in conductivity of the composite material. In order to enhance the electrical conductivity of composite mineral materials, a thorough understanding of electron transport phenomena in multi-phase and porous microstructures is essential. The connectivity of the conductive filler can largely be determined after homogeneous mixing of the paste, which is related to the particle size distribution of each phase material of the matrix mixture and the porosity in the composite structure. Traditional empirical methods often do not yield satisfactory results as they do not approximate the true physical process.

This chapter combines the Monte Carlo method and effective medium theory to simulate the conductivity of compounds. This chapter is structured as follows (Figure 51):
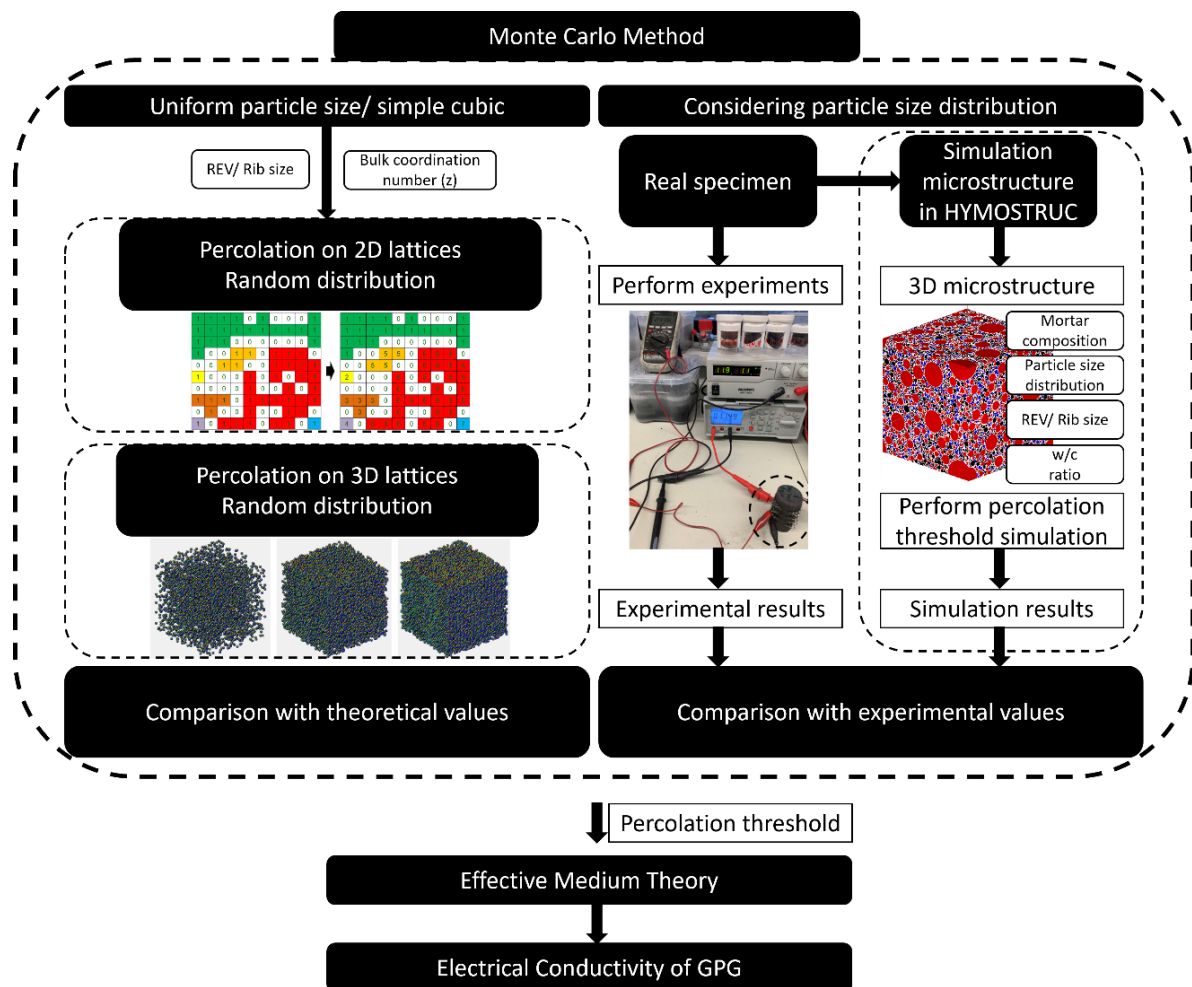
Figure 51: Schematic presentation of percolation threshold simulated by Monte Carlo Method and the electrical conductivity simulated with Effective Medium Theory.

First, without considering the particle size distribution, the distribution of the conductive filler in 2D and 3D cases is simulated using pseudo-random numbers in MATLAB, and its connectivity is analyzed, compared with the theoretical percolation threshold. Subsequently, the HYMOSTRUC program is used to generate 3D microstructures based on the random distribution of metakaolin particles in predetermined representative elementary volumes (REVs), the particle size distribution, the random distribution of graphite particles, and the water to binder ratio. In this stage, interparticle interactions are neglected and the effect of particle size distribution and porosity on the percolation threshold is considered. The percolation thresholds obtained from the simulations are consistent with experimental values. Finally, the effective electrical conductivity of GPG is simulated using EMT and the simulated percolation threshold. The percolation threshold can provide information about the connectivity of the conductive filler, which is an important factor in determining the conductivity of the composite material. The EMT can be used to estimate the effective conductivity of a composite material based on the conductivities and volume fractions of its constituent phases. By combining the information from the percolation threshold and the EMT, it may be possible to develop a more accurate simulation of the overall electrical conductivity of GPG.

5.1   Monte Carlo Method

The Monte Carlo method can be used to simulate the conductive percolation threshold of a compound [148] [116]. The percolation threshold is a critical point in the behavior of a composite material, and it is determined by the connectivity of the conductive filler. When the conductive filler forms a connected network, the volume fraction reaches the percolation threshold, resulting in a substantial increase in the conductivity of the composite material. In order to use the Monte Carlo method to simulate the conductive percolation threshold of a compound, a probabilistic model of the system needs to be constructed.

The basic procedure for solving a practical problem by the Monte Carlo method is as follows [183]:
1. Construct a simple and achievable probabilistic statistical model based on the practical problem. The proposed solution is precisely the probability distribution or mathematical expectation of the problem being solved.
2. Identify the sampling methods for the various random variables with different distributions in the model.
3. Perform statistical processing of the simulation results to obtain an estimate of the solution.

In the case of simulating the conductive percolation threshold of a compound, the probabilistic model would involve randomly occupying sites in a network with conductors or insulators. The simulated electrical conductivity is then used to determine the probability of percolation, which is the threshold point where the cluster of connected conductors spans the entire network. The Monte Carlo method is well suited for simulating filled composite systems, as it allows for the continuous generation of stochastic numbers.

To determine the percolation threshold of a compound containing conductive filler, a stochastic process is first established where the volume fraction of the conductive filler in the compound is set to the solution of the problem. The connectivity of the conductive filler is then observed by incrementally increasing the volume fraction of the conductive filler, leading to an approximate value of the solution.

5.1.1 Percolation on 2D uniform lattices

Percolation is a phenomenon in which a connected cluster of conductive particles spans the entire system. In the context of composite materials, percolation is used to describe the threshold at which the electrical conductivity of the material increases significantly as a result of the formation of a connected network of conductive particles. One method for studying percolation is the Monte Carlo method on 2D uniform lattices. This involves randomly occupying sites in a lattice with conductors or insulators and determining the probability of percolation as the volume fraction of the conductive particles is incrementally increased. To perform this simulation, a 2D matrix can be created in MATLAB, where each element represents a conductor or insulator (as shown in the Figure 52 and Figure 53). The connectivity of the conductive particles can then be determined by implementing algorithms such as the Hoshen-Kopelman or Union-Find algorithm. It is important to consider the number of iterations in the simulation and the choice of random number generator as they both affect the accuracy and computation time of the results.

After identifying the connected regions of conductive particles within the matrix, numerical values are assigned to these regions based on their connectivity. Specifically, the bwlabeln function (Union-Find algorithm) is utilized to systematically traverse the matrix and assign unique numerical values to each region of connected particles. The assigned numerical values can be used to determine the relative size of each cluster and its connectivity. The cluster with the greatest number of connected particles is typically designated as the largest cluster. Observations of the conductive percolation threshold can be made by analyzing the cluster sizes of the conductive particles as the volume fraction of conductive filler in the composite material is incrementally increased. At volume fractions below the percolation threshold (P=20 vol.%), the clusters of conductive particles tend to be relatively small and not connected to one another (see Figure 52).
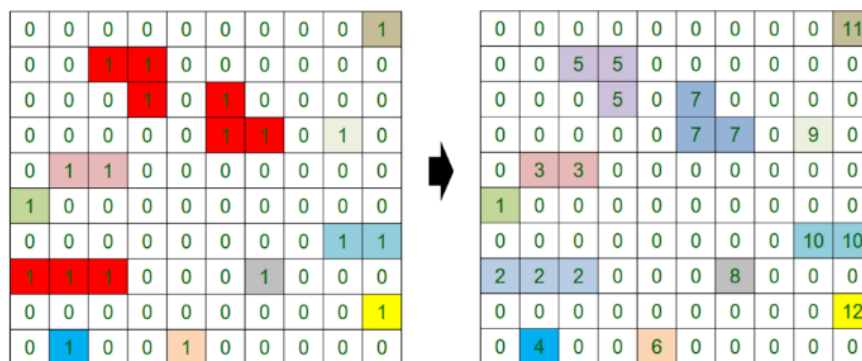
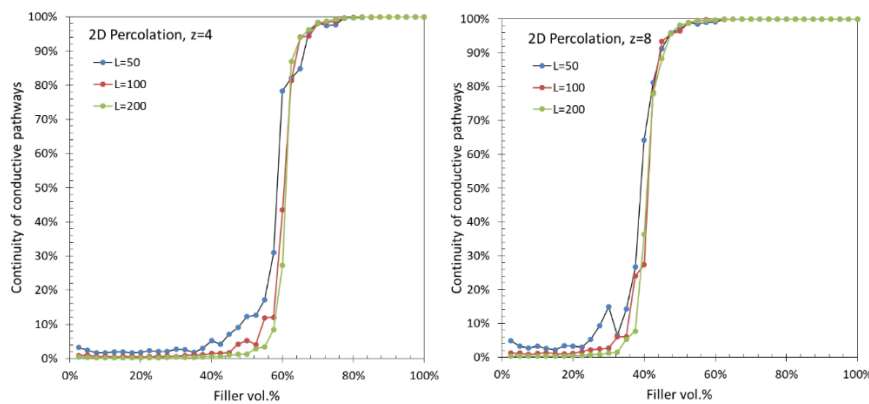**Figure 52:** Percolation on 2D uniform lattices, filler volume fraction P = 20 vol.-%, Coordination number z=4.

As the volume fraction of conductive filler increases and approaches the percolation threshold (P = 60 vol.%), the clusters of conductive particles tend to become larger and more varied in size (Figure 53). Once the volume fraction surpasses the percolation threshold, the clusters begin to merge and form a large, connected network of conductive particles that spans the entire matrix.
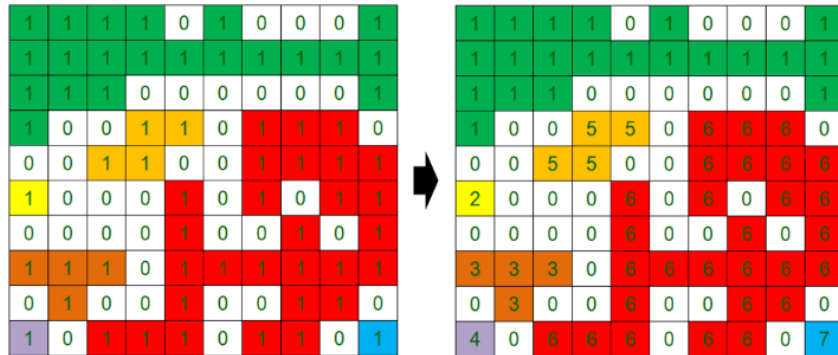
Figure 53: Percolation on 2D uniform lattices, filler volume fraction P = 60 vol.-% , coordination number z=4.

The connectivity of the two-dimensional system is evaluated according to two criteria: the coordination number z = 4, which assumes that the object under study is connected to only four neighboring pixels in the upward direction, and the coordination number z = 8, which assumes that the object under study is potentially connected to all eight surrounding pixels.

The simulation results, as shown in Figure 54, are plotted with the volume fraction of the conductive filler on the horizontal axis and the maximum connectivity (expressed as a percentage of the total substrate area) on the vertical axis. The results of the simulation fluctuate significantly for small matrix sizes (L=50) near the percolation threshold. However, as the size of the matrix increases from L=50 to L=200, the simulated percolation threshold tends to converge to the actual value. The results of the simulation show that the percolation threshold of the system is 40 vol.% and 60 vol.% for the coordination numbers z = 4 and z = 8 respectively. It is important to note that the size of the substrate (matrix L) is an important parameter that affects the accuracy of the simulation. As the size of the substrate increases, the percolation threshold asymptotically approaches.

Figure 54: Site percolation on 2D uniform lattices Size L = 50, 100 and 200. Left: Coordination number z=4, Right : Coordination number z=8.

This method approximates the percolation threshold of a composite material by randomly replacing values within a two-dimensional matrix according to a predetermined volume fraction of conductive filler, and analyzing the connectivity of the resulting clusters using the bwlabeln function in MATLAB. The results can be visualized by assigning values to the connected areas of the matrix according to their numbers, where when the volume fraction P of the conductive filler is less than the percolation threshold, clusters tend to be small and not connected. At the percolation threshold, there are larger clusters and a variety of different cluster sizes, and when the volume fraction P of the conductive filler is close to and larger than the percolation threshold, clusters tend to merge and stabilize the region. The percolation threshold obtained using this method, which fits well with the results in the literature, is shown in the following table (Table 11).

Table 11: Comparison of theoretical percolation thresholds on 2D lattices with simulation results.

| Lattice	z	Site percolation threshold	Ref.	Simulation
Square	4	0.5927	[184]	0.6
Square	8	0.407	[184]	0.4

5.1.2   Percolation on 3D uniform lattices

Simulating percolation on a 3D uniform lattice using the Monte Carlo method involves the following steps:

- Generate a 3D lattice of a specified size (e.g. NxNxN) and initialize all sites as unoccupied.
- Randomly occupy a specified fraction of the sites with an "occupied" state (e.g. conductive particles) and the remaining sites with an "unoccupied" state (e.g. dielectrics).
- Identify clusters of occupied sites by starting with an occupied site, then recursively checking its neighboring sites and adding them to the cluster if they are also occupied, continuing until all occupied sites have been assigned to a cluster.
- Check if any of the clusters percolate across the entire lattice, indicating that it spans the entire lattice, by checking if there are clusters that connect opposite faces of the lattice.
- Repeat steps 2 – 4 many times to obtain a statistically meaningful sample of the percolation probability.

In MATLAB, the bwlabeln algorithm can also be used to analyze the connectivity of the filler to solve 3D percolation problems. The algorithm uses the following general procedure: it scans all image pixels, assigns preliminary labels to nonzero pixels, and records label equivalences in a union-find table. It then resolves the equivalence classes using the union-find algorithm, and finally, the pixels are relabeled according to the resolved equivalence classes.[185].

For the three-dimensional uniform lattices, there are three cases to determine whether a point is connected to the surrounding points (as shown in the Figure 55 below). The probability of its connectivity with the surrounding points is 6, 18 and 26, respectively,.
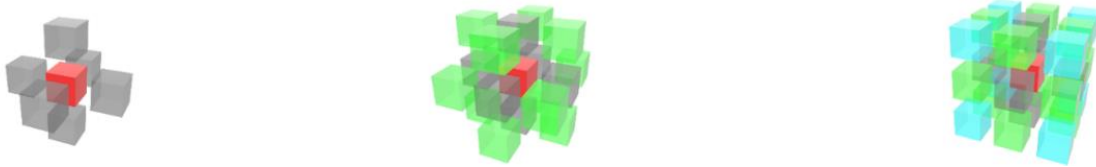
Figure 55: Probability of the connectivity in 3D System. Left: Coordination number z = 6, middle: Coordination number z = 18, right: Coordination number z = 26.

The simulation results for the percolation threshold of a three-dimensional uniform lattice are presented in Figure 56. The simulation was performed for three different lattice sizes, L = 10, 20, and 50, respectively. It is observed that the simulation results become more consistent as the lattice size increases. The results are shown for three different coordination numbers, z = 6, 18, and 24, from left to right. The connectivity of the conductive filler in the system was analyzed using the bwlabeln algorithm in MATLAB. The percolation thresholds for the system were determined to be 30 vol.%, 15 vol.%, and 10 vol.%, respectively, for coordination numbers z = 6, 18, and 24. These results are in agreement with the percolation thresholds reported in the literature, as listed in Table 12.
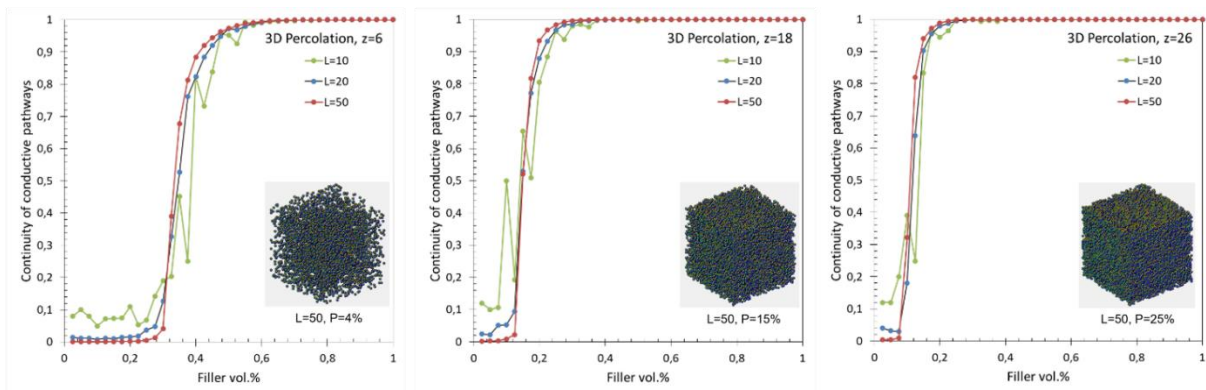
Figure 56: 3D Site Percolation with different probability of connectivity.

Table 12: Comparison of theoretical percolation thresholds on 2D lattices with simulation results.

Lattice	z	Site percolation threshold	Ref.	Simulation
Simple cubic	6	0.307	[186]	0.3
Simple cubic	18	0.1595	[187]	0.15
Simple cubic	18	0.137	[188]	
Simple cubic	26	0.1133	[186]	0.1
Simple cubic	26	0.097	[189]	

The percolation threshold simulations for a single particle size filler in two and three dimensions using the Monte Carlo method provide a strong validation of the method's reliability. These results are found to be in concordance with the values obtained through mathematical modelling in the literature. The agreement between the simulation results and those obtained through mathematical models further supports the validity of the Monte Carlo method as a robust approach for predicting percolation thresholds in composite materials [184], [186]–[189].

5.2 Modelling the electrical percolation threshold of GPG systems

In order to model the three-dimensional microstructure of composite materials, the HYMOSTRUC3D model [106], [190], developed by Delft University of Technology, is utilized. This model is well-established in the field for simulating the three-dimensional hydration process of cementitious materials [191], [192]. The model employs digital spheres to represent all relevant particles, which are randomly distributed within a three-dimensional domain based on parameters such as particle size distribution, effectively simulating the distribution of particles with varying size distributions after mixing. As previously established, the particle size and geometry of the material have a direct impact on the percolation threshold of the mixture system. In particular, smaller particle sizes and larger aspect ratios result in a lower percolation threshold. For this study, it is assumed that all fillers are spherical and the effect of filler material morphology on the percolation threshold is not considered, a contact number of 26 is utilized to mitigate any potential impact of this assumption on the results.

5.2.1 HYMOSTRUC3D Model

HYMOSTRUC3D is a computer program that uses a combination of analytical and numerical methods to simulate the microstructure and properties of porous materials [193]. It can be used to generate random, representative microstructures of porous materials, taking into account the particle size distribution, porosity, and other factors that can affect the properties of the material. HYMOSTRUC3D is based on the original HYMOSTRUC model developed by Van Breugel [194] [193] and later extended by Koenders [190] [195], who incorporated an algorithm in HYMOSTRUC to simulate the random spatial distribution of cement particles in the representative elementary volume of cement paste, and Ye [196] ,who incorporated a pixel-based algorithm in HYMOSTRUC to analyze the pores of the simulated microstructure, to simulate the reaction process and formation of microstructure in hydrating pure PC.

The Rosin-Rammler function [197] is a probability density function used to model size distributions of particulate materials. It is often used in the field of particle technology to describe the distribution of particle sizes in powders, granules, and other particulate materials. The function is defined as:

$$Y = 1 - exp(-\frac{x}{D_n})^n \qquad (5\text{-}1)$$

where Y is the fraction of particles smaller than size x, D_n is the particle size for which Y = 1/e (about 0.37) and n is the shape parameter that characterizes the slope of the distribution function. n <1 describes a wide distribution, n >1 describes a narrow distribution and n = 1 describes a symmetric distribution. The Rosin-Rammler function is a useful tool for characterizing the size distribution of a particulate material, and it is often used in the design and optimization of particle processing operations, such as grinding, classification, and separation.

The Rosin-Rammler function in HYMOSTRUC3D [190], [195] is:

$$G(x) = 1 - \exp{(-b \cdot x^n)} \tag{5-2}$$

with:
$$b = \left(\frac{1}{D_n}\right)^n$$

where $G(x)$ is a cumulative distribution function that is commonly used to describe the particle size distribution of a material, x represents the particle size, b is a fitting parameter, and n is the distribution parameter.

The function describes the probability that a particle size is less than or equal to x. It is typically used to represent the particle size distribution of powders and granular materials, and is often used in combination with the Rosin-Rammler equation. The cumulative distribution function $G(x)$ is used to calculate the volume fraction of particles in a certain size range, and can be used to evaluate the particle size distribution of the materials and estimate the percolation threshold in composites.

In the process of simulating three-dimensional microstructures using the HYMOSTRUC model, it is necessary to consider the digitization of the particles. Specifically, while the pixel points in the 3D matrix are represented as unit cubes, the particles simulated using HYMOSTRUC are represented as spheres (see Figure 57). This simplification results in a reduction of the effective volume fraction of the conductive particles, as compared to the true volume fraction of the filler. This discrepancy can be addressed by introducing a correction factor k (k = 1.24) to account for the difference in volume representation between the spheres and cubes.
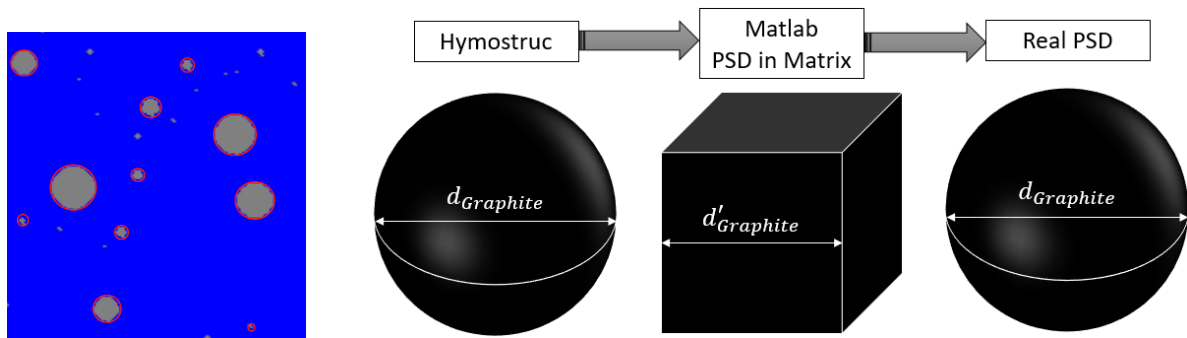

Figure 57: Digitization of the particles in HYMOSTRUC3D and MATLAB.

In the simulation process, a trade-off exists between the resolution and computing power. Theoretically, the closer the resolution of the simulation is to the true particle size, the more accurate the simulated PSD will be. However, due to limitations in computing power, it may not be feasible to achieve a maximum resolution. Therefore, to account for the PSD variation caused by this simplification, an equivalent PSD correction factor k is introduced when the resolution is 1μm/pixel. By the relationship that the graphite volume is equal before and after, the following calculation can be obtained, that is, the total volume of the sphere is equal to the total volume of the cube after exporting to MATLAB in the case of equal number of particles.

$$Graphite\ vol.\% = Graphite'\ vol.-\%$$

$$V_{Graphite} = V'_{Graphite}$$

$$\frac{1}{6}\pi d^3 = d'^3$$

$$d = \sqrt[3]{\frac{6}{\pi}}d' = kd' = 1.24d'$$

The results of the PSD analysis were then fitted to a Rosin-Rammler function. The fitting parameters for the PSDs of graphite and metakaolin are shown in Table 13. These parameters were further corrected using a correction factor k, to ensure consistency between the volume fraction of the conductive filler in the 3D matrix generated using MATLAB and the model in HYMOSTRUC3D, thus ensuring the accuracy of the simulation results.

Table 13: Parameters of Rosin-Rammler function used in HYMOSTRUC3D.

Material	Dn	b	n
Graphite	6	0.04755	1.7
With correction factor K	7.44	0.032986	1.7
Geopolymer	42	0,0346	0,9
With correction factor K	52,08	0,02851	0,9

5.2.2 Representative Elementary Volumes

Representative Elementary Volume [195] is a concept used in materials science and engineering, which refers to the smallest volume of a material that contains all the microstructural features of the bulk material. It is critical for the simulation results because, in order to obtain accurate results, the simulated volume must be large enough to contain a sufficient number of microstructural features [195]. The size of the REV depends on the material being studied and the length scale at which the properties of interest are being measured.

To determine the appropriate REV size for a given material, the chi-square equation is often used. The chi-square equation is a statistical tool that compares the observed frequencies of an event with the expected frequencies of that event. The goal is to minimize the chi-square value, which is a measure of the deviation between the observed and expected frequencies. By minimizing the chi-square value, the REV size that best represents the bulk material can be determined.

In order to find the most suitable REV size, a statistical analysis method based on the chi-square criterion was used. The idea of this method is to calculate the connectivity of graphite in the system versus graphite content in five separate times for different sizes of mixtures to obtain five different percolation models. The distribution of graphite particles in the system is generated randomly each time. The graphite volume fraction at the time of percolation occurring on five occasions was recorded to find the REV by the following chi-square equation (5-3):

$$\chi^2 = \frac{\sum_{i=1}^{m}(\varphi_i - \varphi_a)^2}{\varphi_a} \qquad (5\text{-}3)$$

where φ_i is the current conductive percolation threshold of the graphite-containing compound. φ_a is the average value of all φ_i and m is the number of realizations of the current rib size. Here m equal to five.

The results of the REV size determination are presented in Figure 58. The chi-squared values were found according to the prescribed accuracy of 95 % (p = 0.05). If a chi-square for 95 % probability accuracy was accepted, which meant there was a 95 % chance that the rib size was representative for the real sample. When the size of the system is larger than 200 µm, the percolation thresholds of the five calculations remain basically the same and no longer have large fluctuations. In order to obtain more accurate percolation thresholds, the following simulations were performed with a size of 300 µm.
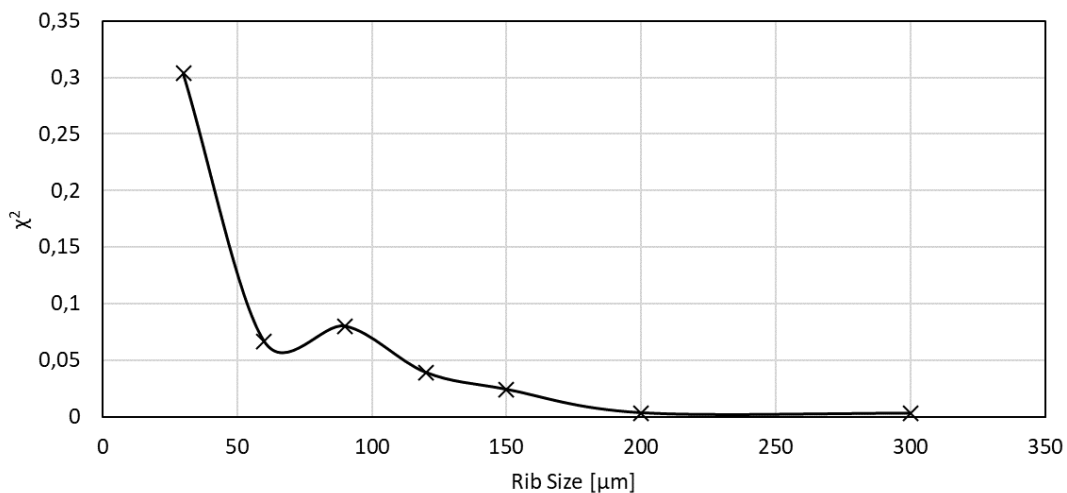
Figure 58: Representative elementary volumes for GPGs.

Figure 59 illustrates the relationship between various filler volume fractions and the maximum interconnected cluster. Percolation threshold simulations were performed on models with rib sizes of 30, 50, 90, 120, 150, and 200 µm, and the results were subsequently input into equation 5 – 3 for calculation. When the rib size is equal to 30 µm (Figure 59-a), it is difficult to obtain consistent results from the five simulations of the percolation threshold. However, when the rib size is equal to 200 µm (Figure 59-f), the results of the five simulations are nearly identical.
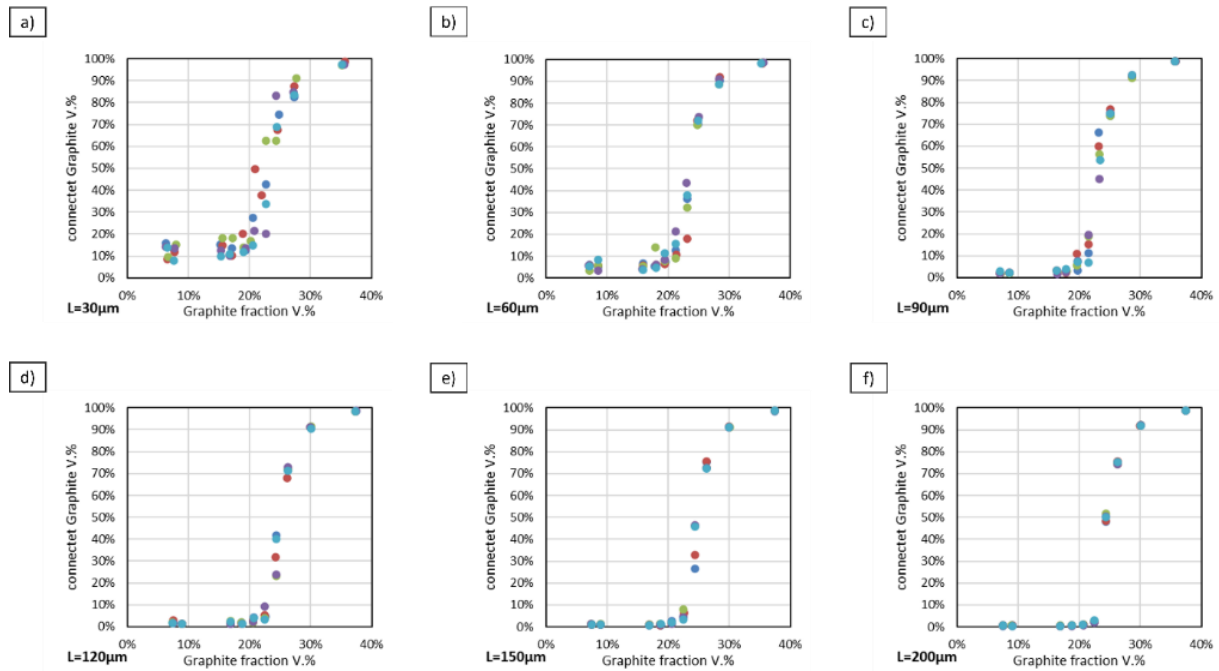
Figure 59: Variability of the electrical conductive percolation threshold vs. rib size. a)=30 µm, b)=60 µm, c)=90 µm, d)=120 µm, e)=150 µm, f)=200 µm.

5.2.3   Percolation threshold analyzed with MATLAB

In order to investigate the relationship between the percolation threshold of conductive filler and the particle size distribution of graphite, the porosity of the mixture, and the particle size distribution of metakaolin, four different scenarios were considered. These scenarios are:

1)   consideration of only the particle size distribution of graphite,
2)   consideration of both the particle size distribution of graphite and the porosity of the mixture,
3)   consideration of both the particle size distribution of graphite and metakaolin,
4)   consideration of the particle size distribution of graphite, the particle size distribution of metakaolin, and the porosity of the mixture.

The simulation procedure consisted of the following steps: first, the three-dimensional microstructure of the mixture was generated using the HYMOSTRUC3D model, which is widely recognized for simulating the three-dimensional hydration process of cementitious materials. The time point chosen for the simulation was the early stage of hydration, as the effect of the hydration process

was not considered and the distribution of graphite particles in the multiphase mixture at this point was assumed to remain constant. The 3D model generated by HYMOSTRUC3D was then exported into several 2D images. These images were analyzed by assigning different numbers to the pixel points of different phases and forming a three-dimensional matrix of these pixel points.

The following code is an implementation of a for loop that iterates over a specified range of frame numbers, defined by the variable "frameNumber." For each iteration, it creates a file name using a predefined format, consisting of a string "Bitmap" followed by a five-digit number, with leading zeroes, corresponding to the current value of "frameNumber." The full file path is then constructed by concatenating this file name with a pre-defined path stored in the variable "pathName_uic." The imread function is then used to read the image file located at the constructed file path and store it as a 2D matrix, "pix3D_single." This 2D matrix is then assigned to a specific slice of a 3D matrix "pix3D" with the same index as the current value of "frameNumber." This process is repeated for each iteration of the loop, effectively creating a 3D matrix composed of 2D slices, each representing a single frame from the image sequence. This loop allows to read a set of image files, usually in bitmap format, and then store them as a 3D matrix where each slice represents an image, the size of the matrix depends on the number of images, and the size of each image. This allows analyzing a series of 2D images of the 3D spatial structure derived by HYMOSTRUC3D and extracting information about the distribution of graphite particles therein.

```
for frameNumber = 1: Rib_size
    baseFileName = sprintf('Bitmap %05d.bmp', frameNumber-1);
    fullFileName = fullfile(pathName_uic, baseFileName);
    pix3D_single = imread(fullFileName);
    pix3D(:,:,frameNumber) = pix3D_single;
end
```

After converting the 3D information into a 3D matrix by the above code, each number represents a type of material. To facilitate the analysis of the connectivity of graphite in 3D, all the numbers representing other materials in the space are converted to 0 and the numbers representing graphite particles are converted to 1 by the following code. Subsequently, a 3D 0,1 matrix is obtained.

```
for frameNumber = 1:Rib_size
 for  j=1:Rib_size
    for i=1:Rib_size
        if  pix3D_Graphite(i,j,frameNumber)==9  %9 % Graphite
             pix3D_Graphite(i,j,frameNumber)=1;
        elseif pix3D_Graphite(i,j,frameNumber)==8 % Metakaolin
             pix3D_Graphite(i,j,frameNumber)=0;
        elseif pix3D_Graphite(i,j,frameNumber)==7 % Pore/Water
             pix3D_Graphite(i,j,frameNumber)=0;
        elseif  pix3D_Graphite(i,j,frameNumber)==6 % Binder Matrix
            pix3D_Graphite(i,j,frameNumber)=0;
        end
    end
 end
end
```

The next step in the analysis process is to identify and quantify the clusters of graphite particles within the 3D matrix. The following code block represents the process of identifying and isolating clusters of graphite particles within the 3D matrix (pix3D_Graphite) using the bwlabeln function in MATLAB. This function employs a 26-connectivity criterion, which defines a particle as connected to its 26 neighboring pixels in 3D space. The output of this function is a matrix (Graphite) in which each connected cluster of graphite particles is assigned a unique label. The maximum label value is stored in the variable LargeGraphite. Then, a loop is used to count the number of pixels belonging to each cluster and store the result in the VolumeGraphite array. The total number of graphite pixels is calculated by summing the elements of VolumeGraphite array using the 'all' option and stored in the variable Filler. Finally, the filler fraction is computed by dividing Filler by the total number of pixels in the 3D matrix (Rib_size^3) and stored in the variable Fillerfractal.

```
Graphite = bwlabeln(pix3D_Graphite,26);
LargeGraphite = max(Graphite,[],'all');
for i = 1:LargeGraphite
    VolumeGraphite(i)=length(find(Graphite(:,:)==i));
end
V=max(VolumeGraphite);
Filler=sum(GMMM,'all');
Fillerfractal=Filler/Rib_size^3;
```

5.2.4   Results

The three-dimensional structure of the simulated mixture was generated using the HYMOSTRUC3D program. The simulated structure is illustrated in Figure 60, where the red color represents the matrix and metakaolin, the black color represents the graphite particles, and the blue color represents the pores in the system, which are created by the excess water after drying. The particle size distribution of the phases of the mixture is represented by the coefficients of the modified Rosin-Rammler function. The size of the Rib, a fixed parameter in the simulation, is set to 300 µm.

In Figure 60, Case 1, the simulation considers only the distribution of graphite particles in the matrix and their particle size distribution. The volume fraction of graphite particles is incrementally increased from left to right, with values of 1.5 vol.%, 3.7 vol.%, 5.1 vol.%, 10.9 vol.%, and 14.7 vol.% respectively. It can be observed that at lower graphite contents, the graphite particles are uniformly distributed in the matrix. However, as the graphite content increases, the volume of the connected graphite particles becomes larger. Case 2 of Figure 60 takes into account the effect of the particle size distribution of graphite particles on the percolation threshold, in addition to the porosity in the system. This is significant because the conductivity of all test blocks was measured under completely dry conditions in the experimental section of Chapter 3, thus the porosity can be considered as the volume fraction of unreacted water in the system. Case 3 considers the particle size distributions of both graphite and metakaolin solids. Finally, in Case 4, the simulation takes into account the effect of the excess water in the system, in addition to the particle size distribution of the individual solid phases.
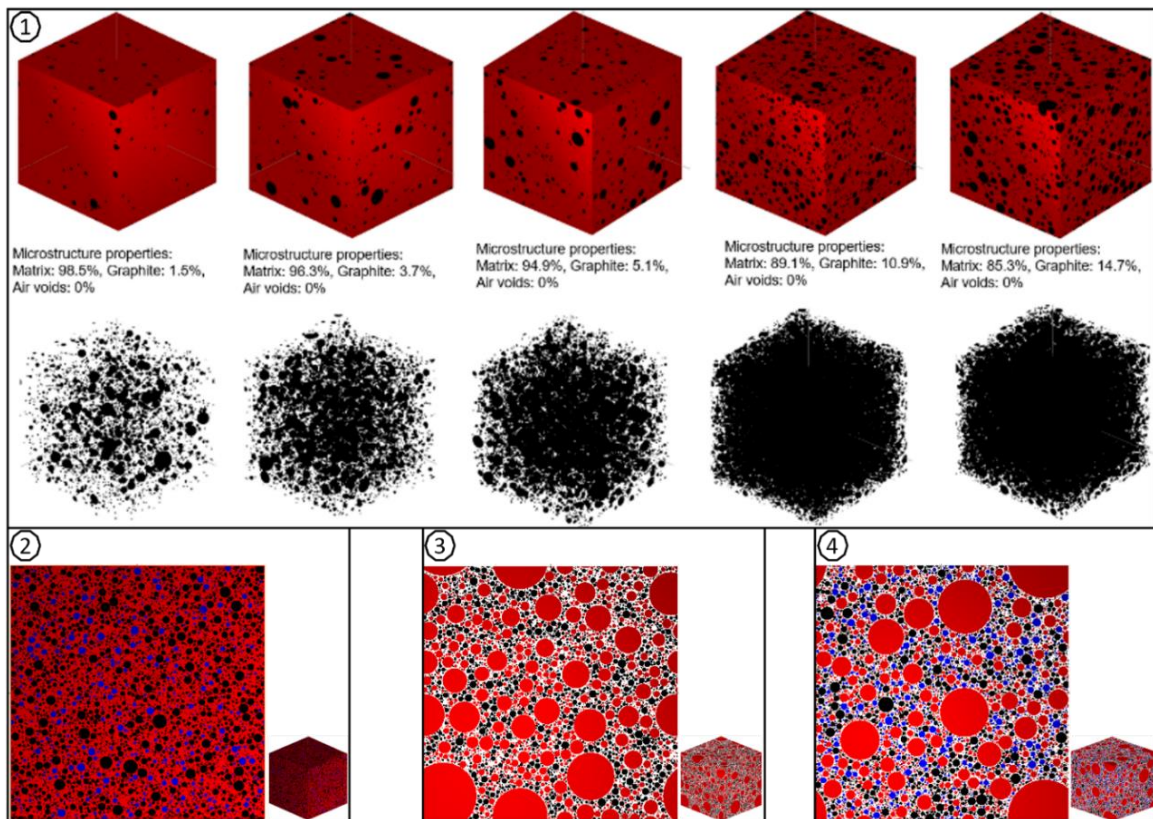
Figure 60: Four different scenarios considered when simulating percolation thresholds using hymostruc (rib size = 300um) and Matlab. 1) consideration of only the particle size distribution of graphite, 2) consideration of both the particle size distribution of graphite and the porosity of the mixture, 3) consideration of both the particle size distribution of graphite and metakaolin, 4) consideration of the PSD of graphite, the particle size distribution of metakaolin, and the porosity of the mixture. Where the red part represents the Matrix of the mixture, black circles represent graphite particles, red circles represent metakaolin, and blue prototypes represent water or pores.

Case 1: consideration of only the particle size distribution of graphite

By incrementally increasing the volume fraction of graphite particles, various three-dimensional structures are generated using HYMOSTRUC3D. The results, analyzed using MATLAB, are displayed in Figure 61. The x-axis represents the volume fraction of graphite particles, while the y-axis represents the ratio of the maximum volume of the connected graphite particles to the total volume of the matrix. It can be observed that when the volume fraction of graphite particles is less than 20 vol.%, the graphite particles in the system form clusters, but their volumes are small and not interconnected. As the number of graphite particles increases, their connectivity undergoes a sudden change at a volume fraction of 24.4 vol.%. Since graphite has superior electronic conductivity compared to the dry matrix, the overall conductivity of the system undergoes a sudden change when the graphite particles form a continuous unit, which is at this volume fraction the percolation threshold of the system. In comparison to percolation on uniform lattices, when coordination numbers are also equal to 26, the percolation threshold occurs at a volume fraction of 10 vol.%. When the material has a particle size distribution characteristic, it has a negative impact on its percolation threshold in the system.
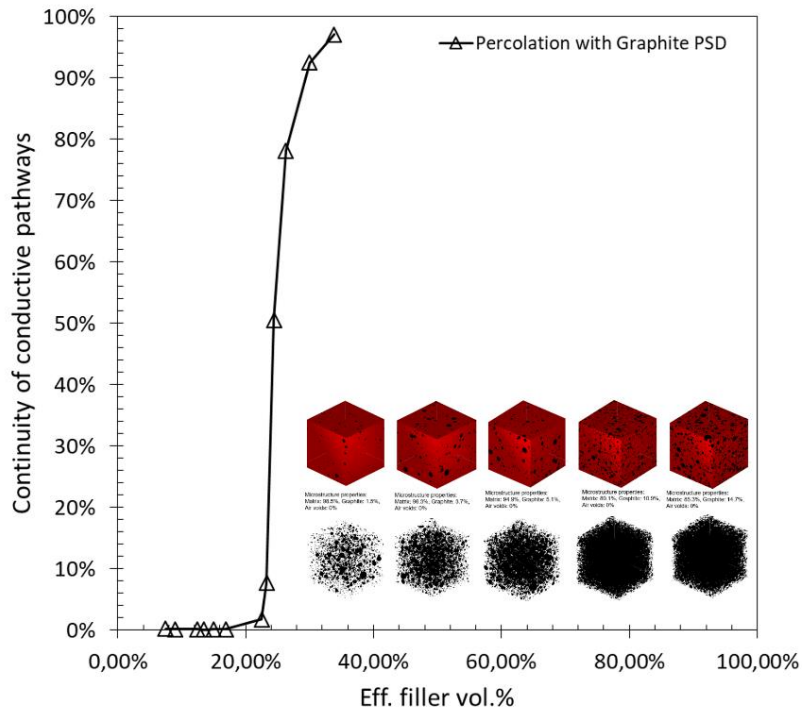
Figure 61: Graphite connectivity as a function of graphite volume fraction. The rib size of REV is 300 µm. The numerical resolution of the PSD structure is 1 µm/pixel. The Graphite PSD followed the Rosin-Rammler distribution curve and used a correction factor k. The parameters are distributed as b = 0.032986, n = 1.7. Porosity and the metakaolin PSD are not considered. The fraction width (step) was 1 µm.

Case 2: consideration of both the particle size distribution of graphite and the porosity of the mixture

In order to investigate the impact of porosity on the percolation threshold of graphite, it is assumed that since all test blocks were evaluated for conductivity in a dry state, the drying process causes graphite particles dissolved in the pore solution to aggregate and form a structure akin to that impeded by air bubbles. Thus, the presence of air bubbles is employed as a simulation for the occupied volume within the mixture to represent the effect of the drying process on the distribution of graphite particles (see Figure 62). In this representation, black dots represent graphite particles. The white regions represent the matrix, and the blue regions represent pore solution. Prior to drying, graphite particles are evenly distributed within the matrix and the pore solution. Under the effect of drying, the position of graphite particles that are fixed within the matrix remains unchanged. However, graphite particles that are present in the pore solution tend to aggregate due to the drying effect. This process causes the dispersed graphite particles in the pore solution to transition into a connected state, thereby increasing the potential for connectivity among graphite particles.

The percolation threshold of graphite with particle size distribution between 0 – 100 microns and porosity of 6 vol.%, 18 vol.%, and 30 vol.% was simulated. The results are shown in Figure 63 (red representing the matrix and metakaolin mixture, black representing the graphite particles, and blue representing the pores). As the porosity increases, the percolation threshold of the mixture also

decreases (see Figure 63 left). Since the graphite particles are only distributed within the solid matrix, the concept of effective volume fraction was introduced to better observe the effect of porosity on the percolation threshold (Figure 63 right). The effective volume fraction of graphite is the ratio of the volume of graphite to the volume fraction of solids in the mixture. The results showed that the percolation threshold of the mixture's effective volume fraction is constant at different porosities, therefore, the effect of porosity on the mixture's percolation threshold can be eliminated by considering the effective volume fraction.
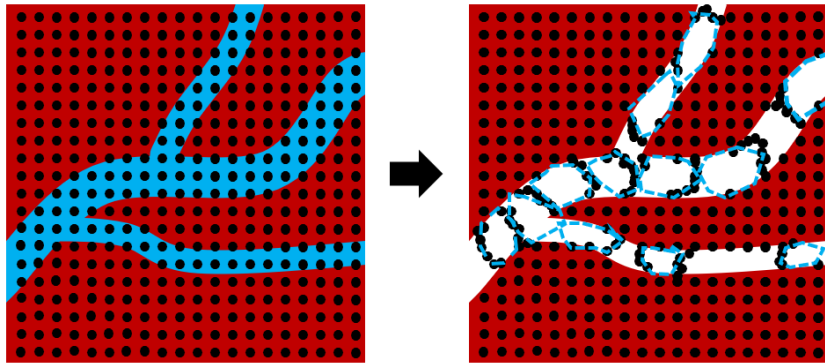

Figure 62: Drying effect on the Graphite distribution. The red color represents the hardened mineral polymer. Black represents graphite particles. Blue represents the pore solution within the mixture. Before drying (left), the graphite particles fixed within the matrix remain unchanged, and the graphite dissolved in the pore solution is more dispersed and not connected to each other. Under the drying action, the pore water evaporates (right). At this point, it is assumed that the graphite particles in the pore solution are connected into multiple conductive pathways due to the evaporation effect.

This can be understood as a mixture of graphite, geopolymer, and pores, with a total volume of V. When represented as a three-dimensional cube with side length rib_size, the presence of pores changes the dimensionality of this solid phase compared to a three-dimensional cube containing only graphite and geopolymer. This results in a reduction of the percolation threshold of graphite within V. When considering only the volume fraction of graphite in the solid composed of graphite and geopolymer, the percolation threshold of this system remains constant and independent of the amount of pore space present in V.

According to Sahalianov's research [133], the difference between the size of segregated particles and filler particles significantly influences the resulting percolation threshold and conductivity of composites. The ratio of the particle size of the segregated volume to the particle size that causes percolation, instead of just the segregated volume, has a greater impact on the percolation threshold. When the ratio of segregated volume to percolating particle size is between 3-10, it has the greatest positive impact on the percolation threshold. As this ratio continues to increase to 20 and 30, the positive impact on the percolation threshold gradually decreases. This also supports the observation of the decrease in the percolation threshold of the systems as the porosity increases. The percolation threshold of the system was stabilized at 23.8 vol. % after the introduction of the effective volume. In

contrast to the system containing only graphite particles, the percolation threshold of the mixture was reduced by 2.45%. This is due to the presence of pores that change the dimensionality of the matrix.
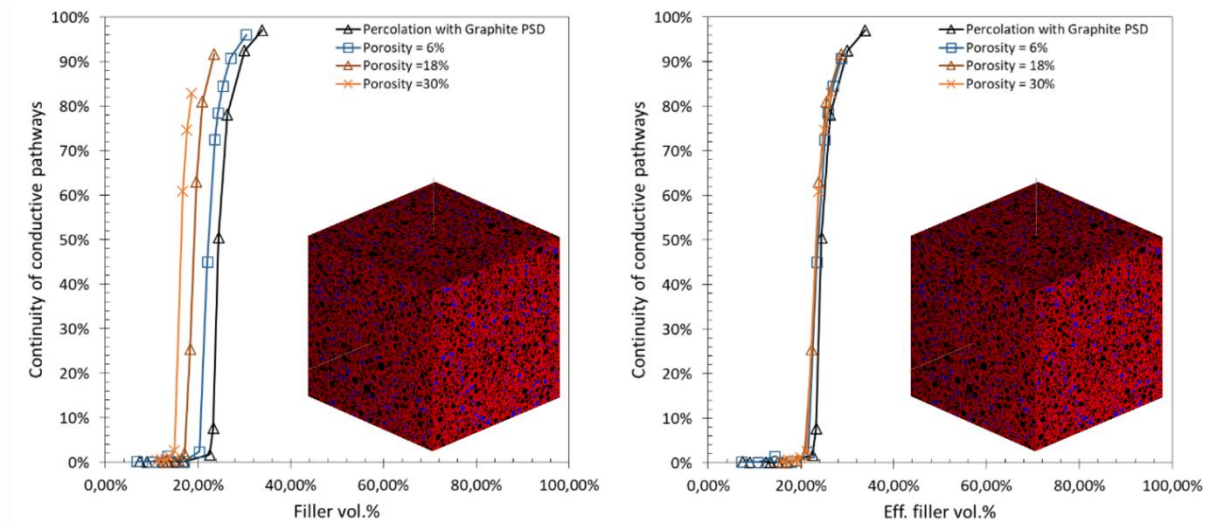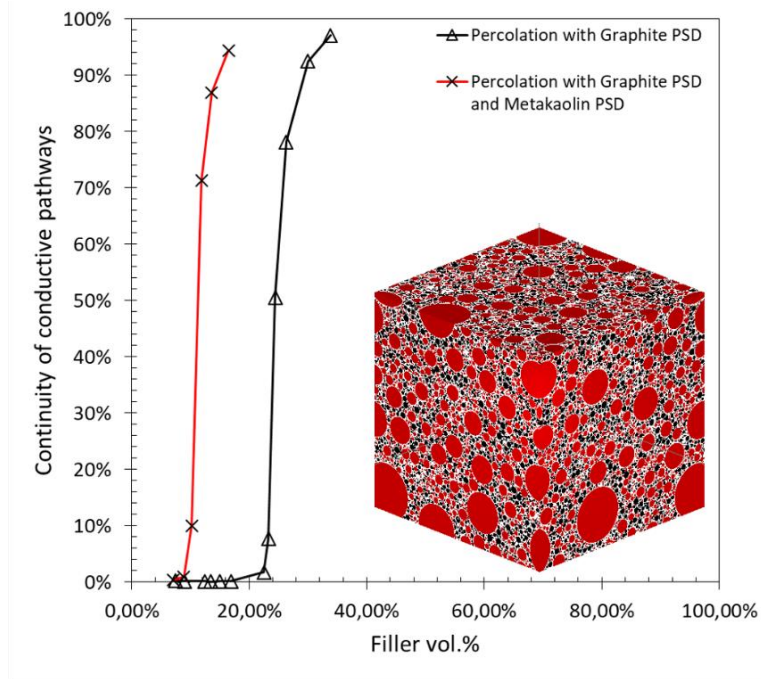

Figure 63: Graphite connectivity as a function of graphite volume fraction left) and effective graphite volume fraction (right). Effective graphite volume fraction = graphite volume/solid volume. The rib size of REV is 300 µm. The numerical resolution of the PSD structure is 1 µm/pixel. The Graphite PSD followed the Rosin-Rammler distribution curve and used a correction factor k. The parameters are distributed as b = 0.032986, n = 1.7. The black lines indicate graphite. Porosity (colored lines) is 6%, 18% and 30% respectively. The fraction width (step) was 1µm.

Case 3: consideration of both the particle size distribution of graphite and metakaolin

The simulation results presented in Figure 64 (red line) demonstrate the relationship between the degree of graphite connectivity and the volume fraction of graphite for microstructures generated using PSDs of both graphite and metakaolin. The rib size of REV is 300 µm. The numerical resolution of the PSD structure is 1 µm/pixel. Both PSDs followed the Rosin-Rammler distribution curve and used a correction factor k. Their parameters were distributed as graphite: b = 0.032986, n = 1.7. metakaolin: b = 0.02851, n = 0.9. The maximum particle sizes of the two PSDs were graphite:10 µm, and metakaolin: 100 µm, respectively. Here the porosity is not considered. The fraction width (step) was 1µm.

The effective particle size of metakaolin is 42 µm, and the effective particle size of graphite particles is 6 µm, with a ratio of 7 < 10. As per Sahalianov and Lazarenko theory [133], the addition of graphite particles to metakaolin particles results in a significant effect on the percolation threshold of the mixed system. The simulation results indicate that the percolation threshold of the system decreases from 24.4 vol.-% to 11.9 vol.-% as a result of the mixing of these two phases.
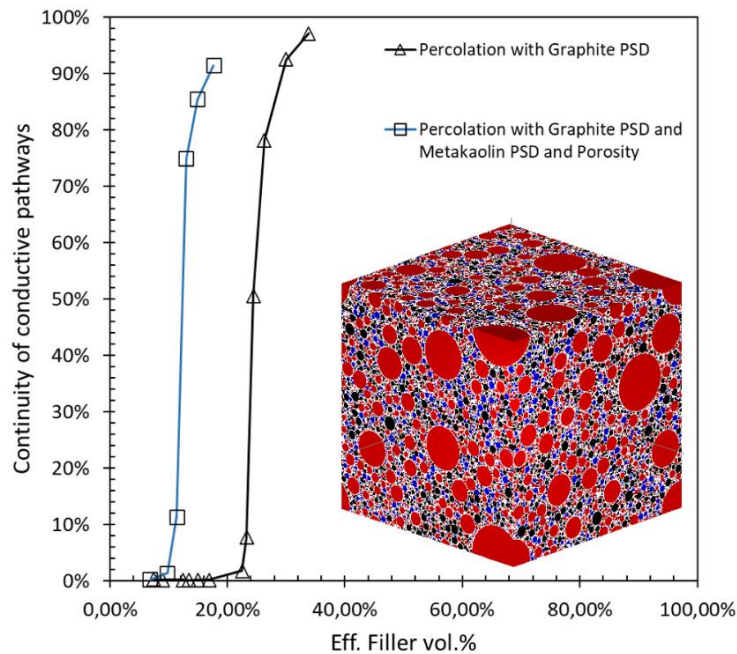
Figure 64: Graphite connectivity as a function of graphite volume fraction. The rib size of REV is 300 µm. The numerical resolution of the PSD structure is 1 µm/pixel. Both PSDs followed the Rosin-Rammler distribution curve and used a correction factor k. Their parameters were distributed as graphite:b = 0.032986, n = 1.7. metakaolin:b = 0.02851, n = 0.9. The maximum particle sizes of the two PSDs were graphite:10 µm, and metakaolin: 100 µm, respectively. Porosity is not considered. The fraction width (step) was 1µm.

Case 4: consideration of the particle size distribution of graphite, the particle size distribution of metakaolin, and the porosity of the mixture.

The results of Case 3 demonstrate that the percolation threshold of the system remains stable when considering the effective volume fraction, regardless of the porosity present in the system. In the simulation conducted using HYMOSTRUC3D, the porosity was set to 6 %. By taking into account the effective volume fraction, this simulation can accurately reflect the impact of increasing dimensionality of the solid mixture due to porosity on the graphite percolation threshold. As the porosity increases, the percolation threshold based on the effective volume fraction remains constant.

As shown in Figure 65, the connectivity of graphite is plotted as a function of effective graphite volume fraction. The rib size of the REV is 300 micrometers, and the numerical resolution of the PSD structure is 1 micrometer per pixel. The PSDs for both graphite and metakaolin particles were modeled using the Rosin-Rammler distribution curve, with correction factors applied. The distribution parameters for graphite were b = 0.032986 and n = 1.7, while the parameters for metakaolin were b = 0.02851 and n = 0.9. The maximum particle sizes for the two PSDs were 10 micrometers for graphite and 100 micrometers for metakaolin. The system has a porosity of 1 %. The fraction width (step) for the data points is 1 micrometer.

The results of the simulation showed that the percolation threshold of the system increased by 2.35 % from 11.9 vol.-% to 12.18 vol.-% after the introduction of porosity and effective volume fraction. In the three-phase mixture system of graphite, metakaolin and pores, it was found that the effect of metakaolin on the percolation threshold was greater than the effect of porosity on the threshold, once the effective volume fraction was taken into account.

Figure 65: Graphite connectivity as a function of effective graphite volume fraction. The rib size of REV is 300 µm. The numerical resolution of the PSD structure is 1 µm/pixel. Both PSDs followed the Rosin-Rammler distribution curve and used a correction factor k. Their parameters were distributed as graphite:b = 0.032986, n = 1.7. metakaolin:b = 0.02851, n = 0.9. The maximum particle sizes of the two PSDs were graphite:10 µm, and metakaolin: 100 µm, respectively. Porosity is 1%. The fraction width (step) was 1µm.

5.3 Simulation of Electrical conductivity with effective medium theory

In Chapter 3.4, various theoretical models for simulating the conductivity of mixtures have been described and compared. Percolation models are based on the idea that the electrical conductivity of a composite material depends on the connectivity of the conductive particles within the material. Since the percolation threshold is closely related to the particle shape, size, and interaction of each phase of the mixture, the percolation threshold obtained from simulations in HYMOSTRUC3D was used as the percolation threshold of graphite particles in geopolymer mixtures used in this study. The percolation threshold of the graphite geopolymer mixture was simulated by Monte Carlo method and the volume fraction of graphite particles where percolation occurs was 12.18 vol.-%. The Bruggeman EMT is a widely used method for predicting the effective electrical conductivity of composite materials, and it considers the volume fractions of the different phases and their conductivities. By inputting the percolation thresholds simulated from the HYMOSTRUC program, which considers the particle size

distribution and porosity, into the Bruggeman EMT, the overall electrical conductivity of the GPG material can be estimated.

In the dry condition, the electrical conductivity of the geopolymer itself is 0. At this point, σ_1=0 S/m, the above equation (3-12) can be written as:

$$\frac{\varphi_2(\sigma_2 - \sigma_{eff})}{\sigma_2 + A\sigma_{eff}} - \frac{\sigma_{eff}(1 - \varphi_2)}{A\sigma_{eff}} = 0 \qquad (5\text{-}4)$$

where σ_{eff} is the effective conductivity of the composite, σ_1 is the conductivity of the low-conductivity phase (geopolymer) and equals 0 S/m here, σ_2 is the conductivity of the high-conductivity phase (graphite), φ_c is the percolation threshold and φ_2 is the volume fraction of the high-conductivity phase (graphite).

The theoretical conductivity of pure graphite was determined to be 183.265 S/m (Chapter 4.2.4). Using the Bruggeman EMT, the relationship between the effective volume fraction of graphite particles and the conductivity of the mixture was analyzed, as depicted in Figure 66. The x-axis represents the effective volume fraction of graphite, which is calculated as the ratio of the volume of graphite particles to the total volume of graphite and metakaolin. The y-axis represents the conductivity of the mixture.
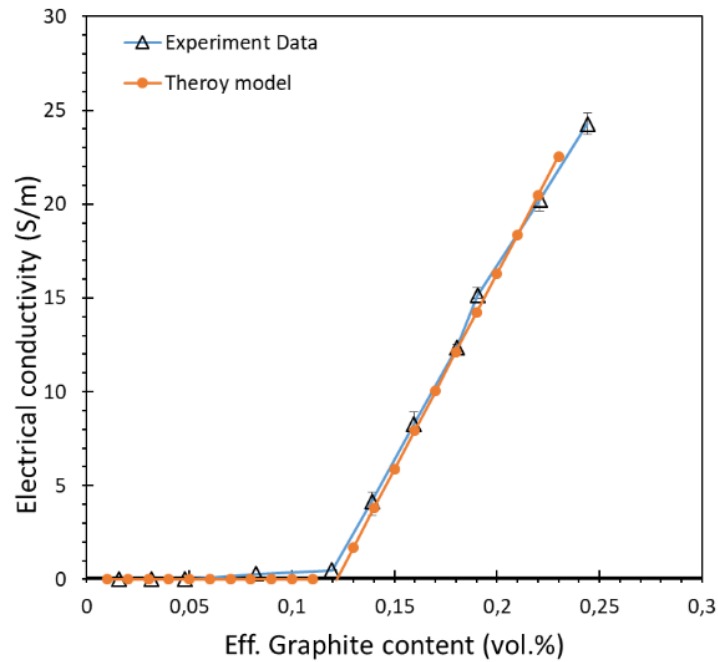
Figure 66: Variation of the conductivity of the compound with the effective volume fraction of graphite. Blue line: the relationship between the effective graphite volume fraction and the measured conductivity of the mixture. Orange line: the variation of the effective conductivity of the mixture with graphite content fitted using the Bruggeman effective medium theory equation after incorporating the graphite particle percolation threshold simulated using HYMOSTRUC3D (ϕ_c=0.1218).

As presented by the experimental data in Chapter 4.3.2, the conductivities of the mixtures with various graphite contents were measured using a 4-point measurement technique. After excluding the pore volume, the relationship between the effective graphite volume fraction and the conductivity of the mixture is represented by the blue line. The orange line illustrates the variation of the effective conductivity of the mixture with graphite content, which was fitted using the Bruggeman EMT equation after incorporating the graphite particle percolation threshold simulated using the HYMOSTRUC program ($\phi\_c=0.1218$). The simulation results showed good agreement with the experimental results (see Figure 66).

5.4 Summery and Discussion

In this section, the percolation threshold of a mixture is simulated using the Monte Carlo method. Initially, the percolation problem was examined separately for two-dimensional and three-dimensional mixtures with a constant particle size. The resulting percolation thresholds agreed with those reported in the literature.

The particle size distribution of the mixed phase was introduced using the software program HYMOSTRUC3D. The three-dimensional structure model of the mixture generated by HYMOSTRUC3D was analyzed using MATLAB and the effect of the particle size distribution of the mixed phase on the percolation threshold of the overall mixture was investigated. Upon consideration of the particle size distribution of graphite particles, the percolation threshold was found to be 24.4 vol.-%. In contrast, the percolation threshold for a single particle size was approximately 10 vol.-%, indicating a significant change in the percolation threshold after the introduction of the particle size distribution.

Subsequently, the effect of introducing a segregated volume in the system on the overall percolation threshold of the two-phase mixture was analyzed. After drying, graphite particles dissolved in the pore solution of the graphite geopolymer mixture aggregate together along with the drying action. Therefore, the air bubbles are used to simulate the mixture after drying. In this case, the air pores affect the percolation threshold of graphite particles in the form of separated volume. According to the results of the simulation, the percolation threshold of the two-phase system decreases with increasing porosity. To observe more intuitively the effect of porosity on the percolation threshold of the system, the concept of effective volume fraction was introduced. At this point, the effective volume fraction of the conductive filler is the ratio of the volume fraction of graphite to the total solid volume after excluding the segregated volume. It was found that a change in porosity does not affect the effective volume fraction of graphite when percolation occurs, i.e., the effective percolation threshold of the system remains unchanged. The effective percolation threshold of the system changed by 2.45 % after the introduction of pores compared to the percolation threshold of single-phase graphite. This is due to the fact that the pores change the dimensionality of the solid mixture. After this, the change in the percolation threshold of the system was studied when metakaolin was used as the segregation

volume. At this point, the percolation threshold of the mixture changed from 24.4 vol.-% to 11.9 vol.-%. This significant change is mainly due to the fact that the ratio of the effective particle size of metakaolin to that of graphite particles is 7, which is less than the 10 proposed by Sahalianov and Lazarenko [133].

Finally, the percolation threshold problem for the three-phase mixture of metakaolin, graphite, and pore was simulated. After the introduction of the effective percolation threshold, the percolation threshold of the system is 12.18 vol.-%. Compared to the effect of metakaolin on the percolation threshold of graphite, the effect of porosity on the effective percolation threshold is minimal. On the one hand, according to the results of MIP in Chapter 3, the pore size distribution in the geopolymer is mostly concentrated around 0.1 µm, and the ratio of its effective particle size to that of graphite is close to zero, so it can be neglected. In addition, the ratio of pore size to graphite particles in the segregated volume caused by capillary water drying is again much larger than 10. Therefore, the addition of the pore phase makes the overall effective percolation threshold of the system change to 12.18 vol. -%, which is an increase of 2.35 %.

The effective medium model proposed by Bruggeman [167]was used to simulate the variation pattern of conductivity of the mixture with increasing graphite content in combination with the percolation threshold of the system simulated by Monte Carlo method (Chapter 5.1). The simulation results were in strong agreement with the experimental results.

6 Electrochemical analysis of microbial fuel cells using *Geobacter sulfurreducens*

6.1 Introduction

Mineral electrodes were tested as anode materials for microbial fuel cells (Chapter 4). Additionally, graphite was investigated as a reference material. The work was conducted at Dechema Research Institute [182].

Geobacter sulfurreducens was selected as the electroactive model organism for the study. It is an obligate anaerobic Gram-negative proteobacterium that can use acetate as a carbon and energy source and solid electrodes as a terminal electron acceptor, among others [26], [48]. In pure culture, *Geobacter sulfurreducens* transfers electrons through direct electron transfer and has been described as a good biofilm former [198]. *Geabacter sulfurreducens* has also been successfully used as a microbiological catalyst for electricity production in microbial fuel cells by Stöckl et al. [199]. The work of Stöckl et al. [199] forms the methodological basis for the commissioned investigations. Laboratory-scale fuel cells were used for the tests. The geometric anode area investigated was 4.9 cm^2 in each case. The anodes were polarized against silver chloride with a holding potential of 400 mV during the test period and the respective anodic current was plotted against time, the test period was a maximum of 7 days. The tests of the materials were carried out in 3- or 5-fold determination. Before the respective measurements, electrochemical impedance measurements were performed to determine the ohmic resistances of the electrode materials. After completion of the respective tests, the electrode materials were frozen for further investigations.

6.2 Materials and Methods

6.2.1 Electrode materials and the used chemical compounds

In the experiments, various electrode materials (Chapter 4.2, Table 14) were utilized as anodes in microbial fuel cells with *Geobacter sulfurreducens* as the biocatalyst.

The concrete electrodes were first cured and shaped in a 35 mm diameter mold and removed after the hydration reaction was complete. The electrode material was then cut into sheets of 8mm thickness using a cutting machine and the electrode material was sanded to 5mm thickness using a 3D printing tool with 80 grit sandpaper. Finally, the surface was sanded with 180 grit sandpaper for 10 cycles in each direction. The graphite electrode's thickness was also 5mm and the surface was sanded with 180 grit sandpaper and the same method for spare.

Table 14: Name and composition of the electrode materials based on PC and GP (w-water, c-cement, f-fly ash, PCE-superplasticiser, G-Graphite, wg-waterglass, mtk-metakaolin).

PCG	*w/c* in wt%	*f/c* in wt%	G in vol.-%	PCE/G in wt%
PC Ref.	0.6	0	0	0
PC06 1C	0.6	0	1	0
PC06 3C	0.6	0	3	0
PC06 4C	0.6	0	4	0
PC06 9C	0.6	0	9	0.1
PC06 3F 8C	0.6	0.3	8	0.1
PC06 3F 9C	0.6	0.3	9	0.1
PC06 3F 10C	0.6	0.3	10	0.1
PC75 8C	0.75	0	8	0.1
PC75 9C	0.75	0	9	0.1
PC75 10C	0.75	0	10	0.1
GPG	***wg/mtk* in wt%**	***w/G* in wt%**	**G in vol.-%**	**PCE/G in wt%**
GP Ref.	0.8	-	0	0.1
GP08 1W 1C	0.8	1	1	0.1
GP08 1W 2C	0.8	1	2	0.1
GP08 1W 3C	0.8	1	3	0.1
GP08 1W 5C	0.8	1	5	0.1
GP08 1W 7C	0.8	1	7	0.1
GP08 1W 8C	0.8	1	8	0.1
GP08 1W 9C	0.8	1	9	0.1
GP08 1W 10C	0.8	1	10	0.1
GP08 1.2W 10C	0.8	1.2	10	0.1
GP08 1.7W 10C	0.8	1.7	10	0.1
GP08 2W 10C	0.8	2	10	0.1

Reagents of analytical grade, including NH_4Cl (from Merck), Na_2HPO_4 (anhydrous, from Merck) KCl ($\geq$ 99.5 %, from Carl Roth GmbH & Co KG)), sodium acetate ($\geq$ 99 %, anhydrous, from Carl Roth GmbH & Co KG), $NaHCO_3$ (from Merck), disodium fumarate (98 %, anhydrous, from Sigma Aldrich Chemie GmbH), and a gas mixture of 80% N_2 and 20% CO_2 (air liquid) were used. Graphite counter electrodes (PPG86 from Eisenhut GmbH & Co. KG) were also obtained.

6.2.2   Electrochemical Impedance Spectroscopy

Electrochemical Impedance Spectroscopy was employed to determine the ohmic resistances (RΩ) of the examined electrode materials prior to the polarization experiments in microbial fuel cells (MFCs). The MFCs were connected in a three-electrode configuration, and the EIS measurements thus represent the RΩ of the electrode material and the electrolyte solution between the electrode surface and the tip of the Haber Lugging capillary, which holds the reference electrode, at a distance of 15 mm from the anode. The measurements were conducted at open circuit potential by applying an alternating current (AC) voltage excitation with an amplitude of 10 mV in the frequency range from 100 kHz to 100 mHz. The evaluation of RΩ was performed manually in the high frequency range (10

kHz to 100 kHz) of the obtained data using a Reference 600+ potentiostat (Gamry Instruments, Warminster, USA).

6.2.3 Preparation of the *Geobacter sulfurreducens* culture medium

In order to prepare the *Geobacter*-nutrient medium (Composition of 1 L *Geobacter* culture medium for growing the precultures is shown in Table 15), the following steps were taken (as shown in Figure 67): First, ammonium chloride, disodium hydrogen phosphate, potassium chloride, and sodium acetate were dissolved in 980 mL of ultrapure water in a 2 L laboratory threaded bottle. The solution was heated to boiling while stirring, and then cooled to room temperature in an ice bath. The solution was then gassed with a mixture of 80% N_2 and 20% CO_2. Once the temperature had fallen below 50°C, sodium hydrogen carbonate, a trace element solution, a vitamin solution, and a selenite tungstate solution were added to the solution. The resulting solution was then filled into septa bottles (250 mL) and sealed gas-tight with butyl septa.

The following steps are shown in Figure 68. The septa bottles were then vented 5 times in a vacuum line to approximately 200 mbar and gassed with 80% N_2 + 20% CO_2 to create anoxic conditions. After these purging steps, a positive pressure of 800 mbar was applied to the gas mixture. The septa bottles were then sterilized in an autoclave. Finally, 2.5 mL of an anoxic disodium fumarate solution (16% w/v) was added to each of the solutions using a syringe and cannula via a sterile filter. The disodium fumarate solution was also de-aerated 5 times in the vacuum line to approximately 200 mbar and gassed with 80% N_2 + 20% CO_2 before use.
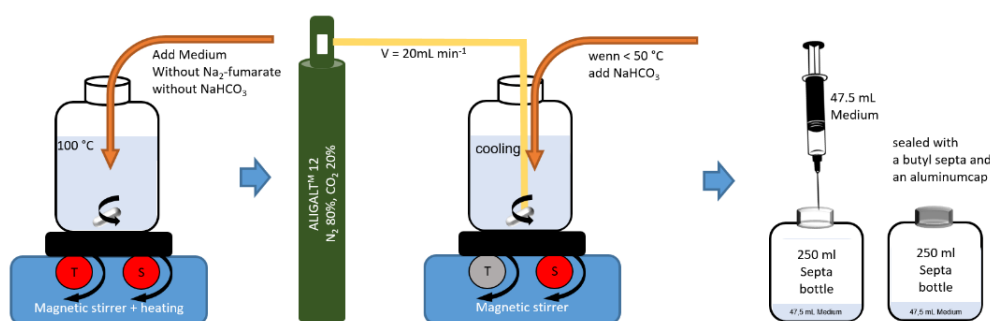

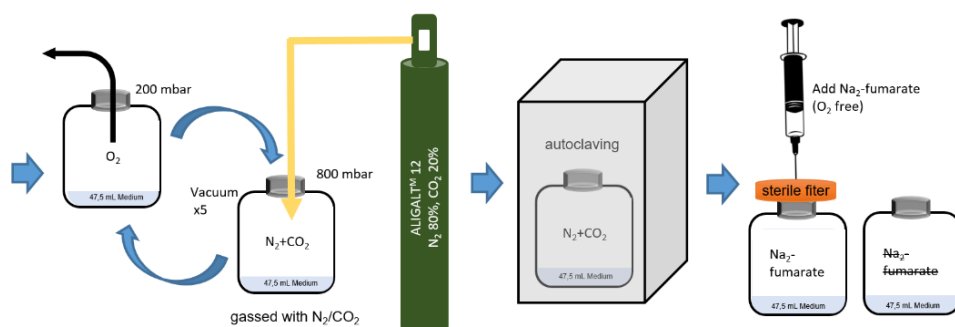**Figure 67:** Preparation of the *Geobacter*-nutrient medium. Step 1.

Figure 68: Preparation of the *Geobacter*-nutrient medium. Step 2.

The resulting medium and sterilized septa bottles were used for cultivation and storage of the model

organism *Geobacter sulfurreducens*. The composition of the trace element solution (used for prepare medium 141, see Appendix-A22), the vitamin solution (used for prepare medium 141, see Appendix-A23), and the selenite tungstate solution (used for prepare medium 385, see Appendix-A25) can be found in the DSMZ media preparation instructions (826. GEOBACTER MEDIUM). To prepare the *Geobacter* medium without fumarate (refer to Table 16), all chemicals and solutions were dissolved in 980 mL of ultrapure water in a 1 liter laboratory bottle with a threaded cap and then sterilized in an autoclave.

Table 15: Composition of 1 liter *Geobacter* culture medium for growing the precultures.

Chemicals	Weights/volumes
NH_4Cl	1,50 g
Na_2HPO_4	0,60 g
KCL	0,10 g
Natriumacetat	0,82 g
$NaHCO_3$	2,50 g
Spurenelementlösung (Medium 141)	10,00 ml
Vitamin Lösung (Medium 141)	10,00 ml
Selenit-Wolframatlösung (Medium (385)	1,00 ml
Dinatriumfumarat	8,00 g

Table 16: Composition of 1 liter fuel cell medium.

Chemicals	Weights/volumes
NH_4Cl	1,50 g
Na_2HPO_4	0,60 g
KCL	0,10 g
Natriumacetat	0,82 g
$NaHCO_3$	2,50 g
Spurenelementlösung (Medium 141)	10,00 ml
Vitamin Lösung (Medium 141)	10,00 ml
Selenit-Wolframatlösung (Medium 385)	1,00 ml

6.2.4 Cultivation of *Geobacter sulfurreducens*

The *Geobacter sulfurreducens* cultures were consistently cultivated using a standardized protocol for all experiments. A 7-day culture was established every 8 days, after a growth phase of 3 days, using a series of subcultures to propagate the pre-cultures. These pre-cultures were then prepared after an additional 2 days and used in fuel cell tests. The experiments were conducted in a consistent and cyclical manner, and were completed within a maximum of 7 days.

Figure 70 shows the schematic procedure of *Geobacter* sulfurreducens precultivation and deployment in MFCs. On day 1, a 7-day culture of *Geobacter sulfurreducens* was prepared by inoculating 1 mL of culture medium from a pre-existing culture into a new septa bottle containing *Geobacter* culture medium in a sterile environment. On day 4, preliminary cultures for use in fuel cells were prepared by taking 1 mL of culture medium from the 7-day culture created on day 1 and inoculating it into 4 septa bottles containing *Geobacter* culture medium in a sterile environment. On day 5, fuel cells were assembled and sterilized using the electrode materials to be investigated, as shown in Figure 69. The fuel cells were filled with ultrapure water and sealed, and then sterilized in an autoclave for 20 minutes at 120°C before being temporarily stored under sterile conditions.

**Figure 69:** Prepared *Geobacter* culture that read for use.

On the 6th day, the four fuel cells were prepared in a sterile workbench. The working electrode (WE) chamber was filled with 120 mL of *Geobacter* medium without fumarate, and the counter electrode (CE) chamber was filled with 105 mL of the same medium. The Haber-Luggin capillaries, which were previously sterilized in 70 % ethanol, were inserted into the screw caps with fixing rings of the WE chambers and sealed gas-tight with sealing film. Subsequently, the reference electrodes were inserted into the Haber-Luggin capillaries filled with KCl_{sat}. To enable gassing of the WE chamber, sterile filters were placed on the cannulas. Electrochemical impedance measurements (EIS) were performed to determine the ohmic resistances of the electrode materials. The impedance measurements were conducted at rest potential, using a potentiostatic method, with an excitation amplitude of 10 mV, and in the frequency range from 100 kHz to 100 mHz. The fuel cells were then placed in an incubator at 30°C, on magnetic stirring plates that were switched on. The gas supply tubes were placed on the cannulas with the sterile filters, and the gas supply was activated. Finally, the electrodes were electrically contacted. Prior to adding *Geobacter sulfurreducens*, the WE chambers were gassed with approximately 40-60 mL/min of 80% N_2 + 20% CO_2 for 90 minutes, to establish anoxic conditions in the WE chamber. 30 minutes before addition, the WE were polarized with a holding potential of 400 mV relative to the reference potential (Ag/AgCl/KCl*sat*). During this process, the recording of the polarization currents against time was initiated.

In order to collect and add the *Geobacter sulfurreducens*, 1 mL samples were taken from each of the 4 septa inoculated with *Geobacter sulfurreducens* on day 4, and the optical density (OD_{600}) was

measured photometrically at a wavelength of 600 nm (Biochrom WPA CO8000). An average value (OD_{MW}) was determined from the measured OD_{600} and the volume to be sampled (Vol_{MW}) was calculated using equation 6-1 to obtain a final OD (OD_{target}) of 0.1 in each 120 mL (V) of the working electrode chamber.
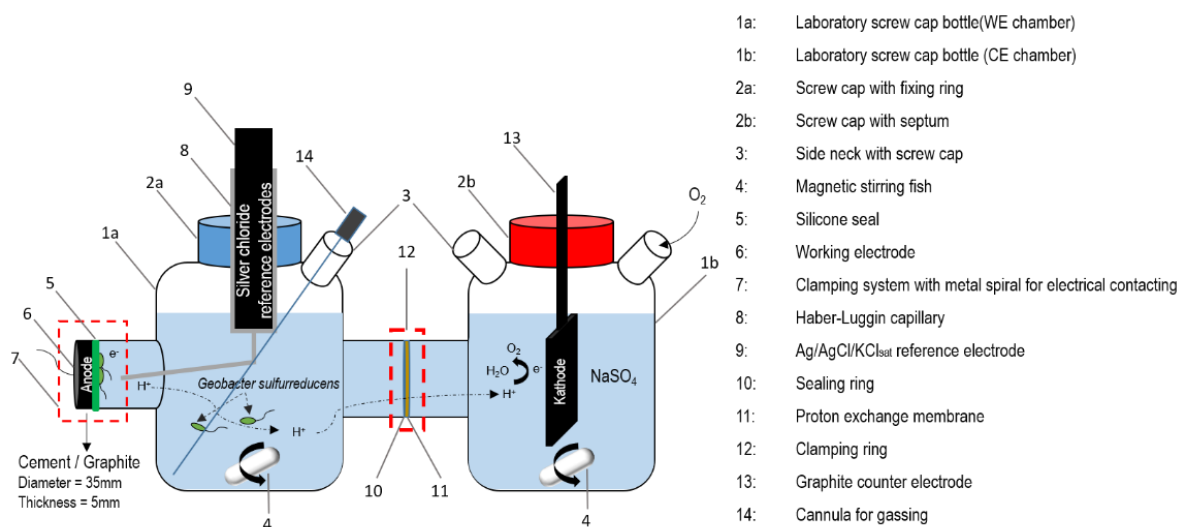
$$Vol_{MW} = \frac{V \cdot OD_{Ziel}}{OD_{MW}} \qquad (6\text{-}1)$$

In a controlled environment (glovebox, STERIL-VBH), the septa bottles were opened and their contents were combined to form a composite sample. From this mixture, the calculated Vol_{MW} with an additional 12% markup was pipetted into 4 centrifuge tubes, which were then sealed and centrifuged for 20 minutes at 4000 rpm and 30°C. The supernatant was discarded in the glovebox and the resulting cultures were resuspended in 5 mL of anoxic *Geobacter* medium without fumarate, which was taken shortly before using 4 syringes from the respective WE chambers of the fuel cells. The resuspended cultures were then injected into the respective WE chambers of the fuel cells.
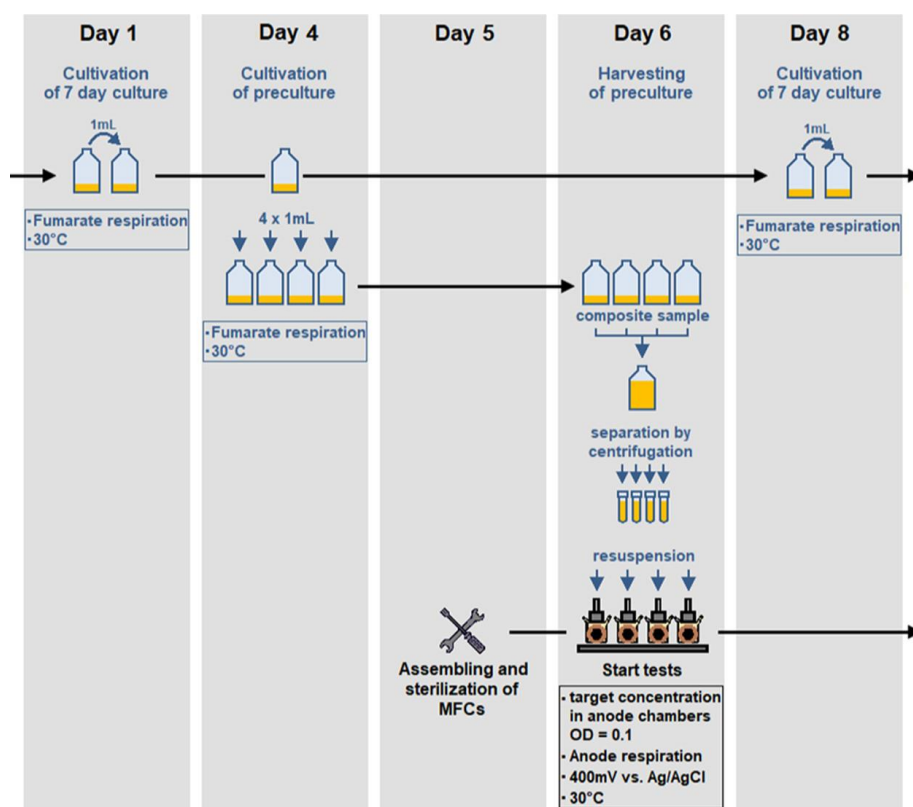
Figure 70: Schematic procedure of *G. sulfurreducens* precultivation and deployment in MFCs. Every 8 days, a fresh 7 day culture was set up. After 3 days of growth to the stationary phase, four fresh cultures were inoculated as precultures for the MFC experiments. In the last step, after another 2 days, the cultivated precultures were combined and cells were harvested by centrifugation and used in the tests with MFCs as the biocatalyst. The cells were cultivated in 250 mL septum flasks containing 50 mL of growth medium. Four MFC experiments were started in parallel. The tests were always started in the same rhythm and ended after max. 7 days **[182]**.

6.2.5 Laboratory electrochemical H-Cell and experimental setup

For the investigation of electrode materials as anodes, using *Geobacter sulfurreducensas* an electroactive biofilm former, a modified H-cell setup was used as a fuel cell (see Figure 71). The H-shaped reactor consists of two modified laboratory threaded bottles (100 mL Schott), each connected to the other by a flange. Between the flanges, which are fixed with the aid of a clamping ring, there is a circular proton exchange membrane resting on a sealing ring. A second flange is attached to the working electrode chamber (WE chamber), over which the working electrode (WE) to be examined is attached from the outside with the aid of a clamping system. 1 mm thick, circular silicone seal is located between the working electrode and the flange for sealing. The inner diameter of the flange is 2.5 cm and the geometrically accessible area is 4.9 cm^2. In the counter-electrode chamber (CE chamber) there is a graphite electrode (immersed geometric area approx. 20cm^2), which is inserted via the bottle neck, through a screw cap with septum. Silver chloride reference electrodes (Ag/AgCl/KCl$_{sat}$) in Haber-Luggin capillaries filled with KCl were used for potential control of the WE. The Haber-Luggin capillaries are inserted into the WE chamber with fixing rings in the screw caps, the fixed distance to the working electrodes is made possible and they are sealed gastight with sealing foil. Each WE chamber is gassed with a gas mixture of 80% N_2+ 20% CO_2 through a sterile filter (pore size = 0.22 µm) via a cannula inserted through a side neck with screw cap and septum.

1a:	Laboratory screw cap bottle(WE chamber)
1b:	Laboratory screw cap bottle (CE chamber)
2a:	Screw cap with fixing ring
2b:	Screw cap with septum
3:	Side neck with screw cap
4:	Magnetic stirring fish
5:	Silicone seal
6:	Working electrode
7:	Clamping system with metal spiral for electrical contacting
8:	Haber-Luggin capillary
9:	Ag/AgCl/KCl$_{sat}$ reference electrode
10:	Sealing ring
11:	Proton exchange membrane
12:	Clamping ring
13:	Graphite counter electrode
14:	Cannula for gassing

Figure 71: Schematic of a fuel cell (H-Shaped reactor) **[199]**.

The microbial fuel cells (MFCs) were assembled and placed on a multi-position magnetic stirrer within an incubator (TH 30, Edmund Bühler GmbH, Hechingen, Germany) maintained at a temperature of 30 degrees Celsius. The MFCs were operated using a multipotentiostat system from IPS Elektronik GmbH & Co KG (PGUMOD, Münster, Germany). The electrochemical impedance measurements were performed with a potentiostat from Gamry (Reference 600+). As reference electrodes Ag/AgCl/KCl$_{sat}$ reference electrodes from Sensortechnik Meinsberg were used and as membranes Nafion 117 from Sigma Aldriche was used. The graphite electrodes used were manufactured by Eisenhuth GmbH & Co.

KG(PPG86). The H-cells were positioned on magnetic stirring plates inside the incubator and connected to gas supply tubes that were connected to cannulas equipped with sterile filters, as illustrated in Figure 72.

Figure 72: Operation of 4 fuel cells on magnetic stirring plates in one incubator [182].

Experiments were carried out for 160 hours. In order to evaluate the current production, the surface charge density σ160 was determined from the recorded current density curves referring to following the equation:

$$\sigma_{160} = \frac{Q_{160}}{A} \tag{6-2}$$

where σ_{160} is the surface charge density, Q_{160} is the charge passed from the time of the start of polarization to the time of 160 hours, A is the geometric, electrochemically active electrode area of 4.9 cm^2.

6.2.6 Measurement series

The tests were carried out in several test series, with 4 fuel cells per test series being used with the respective electrodes to be tested. The tested electrodes were of different porosity and partly brittle, which caused some electrodes to break during sterilization. The broken electrodes were replaced in a sterile workbench with new electrodes that were sterilized with a 70 % ethanol solution prior to the tests. Due to the porosity of some of the electrodes, some of the medium diffused through the electrodes during the tests, resulting in different levels decreasing in the anode chambers and the formation of salt deposits on the outside of the samples. The measurement series are listed in Appendix, Table 18.

6.2.7   Electrode and biofilm imaging

A variable-pressure scanning electron microscope (SEM) (FlexSEM 1000, Hitachi, Japan) was utilized to image the electrodes after the microbial fuel cell (MFC) experiments. The SEM was equipped with a backscattered electrons (BSE) and secondary electrons (SE) detector and an energy-dispersive X-ray spectroscopy (EDX) system (Quantax75, Bruker). The air-dried electrodes were further dried in a vacuum chamber at 20 mbar for 20 minutes and then affixed to a sample stub using graphite tape. The sample stubs were placed directly in the SEM vacuum compartment and examined at an accelerating voltage of 20 kV.

For fluorescence imaging of the biofilms formed on the electrodes, a confocal laser scanning microscope (Leica TCS SP8, Leica Microsystems, Germany) was employed. The microscope was outfitted with a HC PL Fluotar 5x dry immersion objective (N.A. 0.15; free-working distance 13.7 mm), a 488 nm laser (1.5% intensity) and a PMT detector (501 nm-546 nm, gain 781 V, scanning speed 400 Hz) and DD 488/552 excitation beam splitter. The image evaluation was done by using Leica software LAS X version 3.5.5 (Leica Microsystems CMS GmbH, Wetzlar, Germany).

Finally, At the end of the polarization experiment the working electrode (WE) was disassembled from the outer H-cell flange and frozen at -20 °C until imaging. The electrodes were thawed and biofilms were stained with 3 µM Syto 9 Green Fluorescent Nucleic Acid Stain (Thermo Fisher Scientific Inc., USA) for 15 minutes in the dark. Stained biofilms were washed once with 0.125 M phosphate buffer (pH = 6.8) to remove remaining staining solution and imaged as described above.

6.3   Results

6.3.1   Electrochemical Cultivation and Electrode Performance

The electrodes made of PC produce either no or very low currents. It is noticeable that all PC electrodes have a relatively high ohmic resistance (approx. 2-50 kΩ). To the tested PC electrodes that produced current, relatively little *G. sulfurreducens* medium without fumarate had to be added to the working electrode chamber. Utilizing PC electrode material, it was observed that *G. sulfurreducens* did not generate any current, except for PC06 3F 10C, on which a relatively low maximum current of 2.3 µA·cm^{-2} was observed with an average charge density $\bar{\sigma}_{160}$ of 1.2 As·cm^{-2}. The electrodes marked GP (geopolymer) produce all current except the reference electrodes without graphite (GP_Ref). The measured ohmic resistances of the GP electrodes are relatively low, the resistances of the current-producing GP electrodes are between 0.08 kΩ and 1 kΩ (Table 17).

For all GP electrodes tested, *G. sulfurreducens* medium without fumarate had to be added to the working electrode chambers during operation to maintain the levels. High water/graphite ratios have a negative effect on the mechanical stability of the electrodes, all GP electrodes with a water ratio between 1.2 and 2 are very brittle.

GP electrodes of a water/graphite ratio of 1.7 or 2 and with a high graphite content of 10 vol.-% (GP08_1.7W_10C and GP08_2W_10C) showed the smallest ohmic resistances of about 0.08 to 0.2 kΩ and the highest maximum increases in current densities i_{max} as well as the highest areal charge densities σ_{160} of the electrodes tested, with up to 201.1 A·s/cm^2 (Table 17). The determined areal charge densities σ_{160} of GP electrodes with the same composition (e.g., GP08_1.7W_10C and GP08_2W_10C) differ significantly, and the amounts of *G. sulfurreducens* medium without fumarate that had to be added during the tests also differ. This behavior shows that the consistency of the electrodes or their surfaces are not uniform, making reproducible growth of the *G. sulfurreducens* cultures on the electrodes difficult. The average current density curves of *G. sulfurreducens* on GPG electrodes with different graphite and water contents (black), including standard deviations (gray), and results for graphite electrodes (positive control) are presented in Figure 73.

Table 17: Tested Electrode Materials (the Number of Experiments Carried Out Are Given in Brackets), Mean Values M of Ohmic Resistances RΩ, and Their Standard Deviations SD (The mean values M of maximum increase in recorded current densities i_{max}, as well as their standard deviations SD, and the mean values M of the surface charge densities $\overline{\sigma}_{160}$ during 160 h of operation, and the standard deviation SD of the surface charge densities) [182].

Electrode Material	R_Ω (kΩ) M ± SD	i_{max} (μA cm^{-2}) M ± SD	$\overline{\sigma}_{160}$ (As cm^{-2}) M ± SD
PCG			
PC Reference (3)	30 ± 17.3	-	-
PC75 0F 8C	2.5 ± 0.5	-	-
PC75 0F 9C	3 ± 1.0	-	-
PC75 0F 10C	3.2 ± 1.6	-	-
PC06 3F 8C (3)	5.1 ± 4.3	-	-
PC06 3F 9C (3)	2 ± 0.01	-	-
PC06 3F 10C (3)	3.9 ± 2.0	2.3 ± 2.3	1.2 ± 1.0
GPG			
GP Reference (3)	2.7 ± 1.2	-	-
GP08 1W 8C (3)	0.8 ± 0.3	148.0 ± 107.1	67.4 ± 49.5
GP08 1W 10C (3)	1 ± 0.01	157.0 ± 42.3	72.0 ± 11.6
GP08 1.2W 10C (3)	0.4 ± 0.2	166.3 ± 52.3	78.2 ± 24.3
GP08 1.7W 10C (5)	0.1 ± 0.04	380.4 ± 129.5	155.9 ± 45.2
GP08 2W 10C (5)	0.1 ± 0.05	356.2 ± 178.2	140.7 ± 58.5
Graphite (5)	0.1 ± 0.05	401.3 ± 51.3	144.5 ± 19.9

The examined graphite electrodes (reference material) show relatively low ohmic resistances in the range between 0.1 kΩ and 0.2 kΩ and the mean value of the surface charge density is 144.5 A·s/cm^2 (see in Appendix, Table 18). Overall, the obtained surface charge densities are the most reproducible

of all the electrodes tested, with a standard deviation of about 14%. The small fluctuations are explained by the uniform consistency of the electrode surface, the electrodes are manufactured in industrial production. For all examined graphite electrodes, the current production reaches a maximum after approx. 72 hours of operation, after which the current flow decreases. The reason for this behavior is that no *G. sulfurreducens* medium was added during the tests and the acetate concentration in the medium decreases over time. In addition, a decrease of the pH-value at the electrode surface due to the accumulation of protons in the biofilm has been described, which also leads to a decrease of the biological activity.
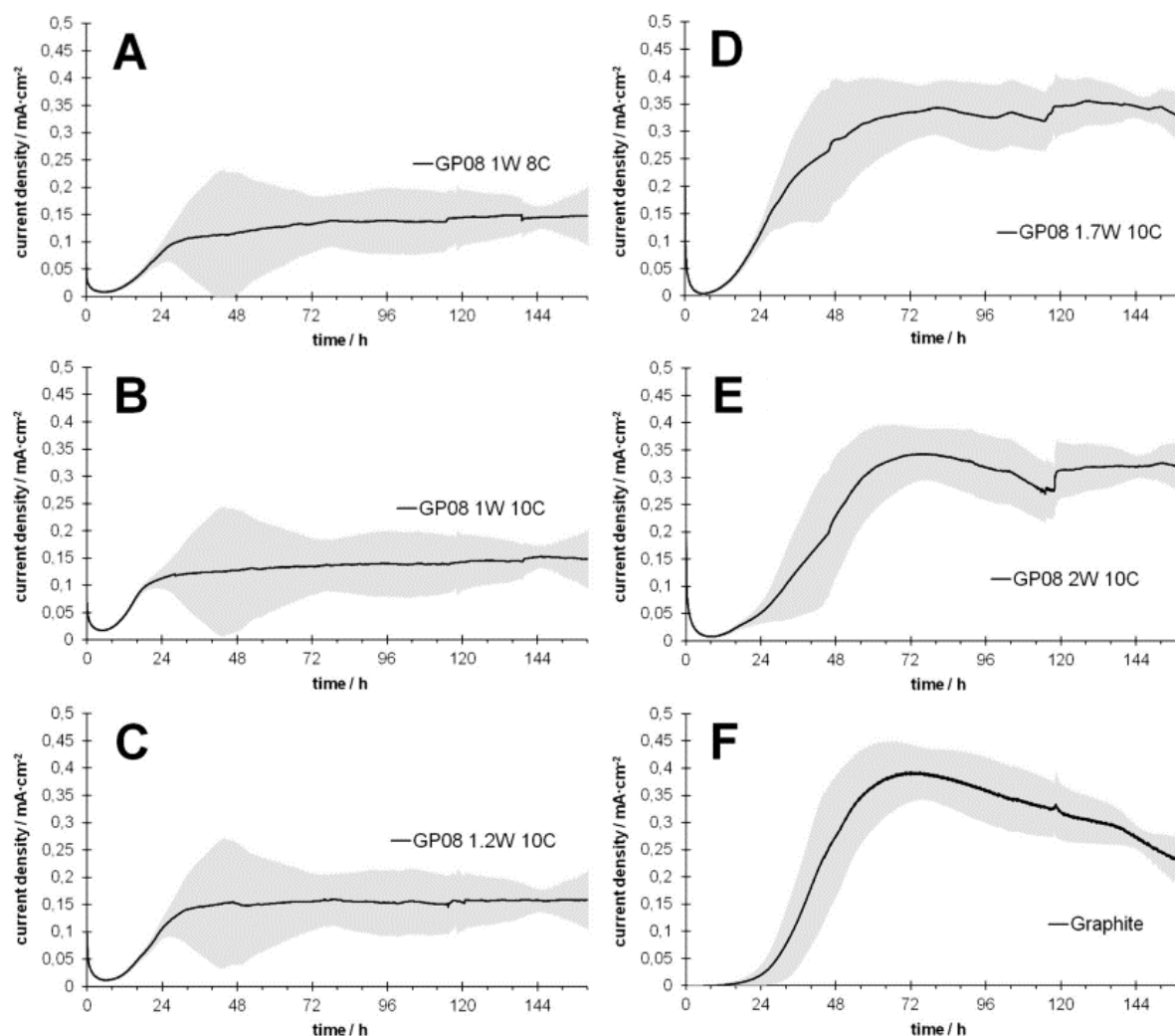
Figure 73: Mean current density curves for cultivations of G. sulfurre-ducens in H-cell MFCs on different GP electrodes with variable graphite and water content, as well as MFC on graphite elec-trodes (anoxic Geobacter medium with acetate, without fumarate; electron acceptor: anode; 30 °C; anaerobic). Current density is referred to the geometrical WE surface (4.9 cm^2). Standard deviations (of 3 to 5 individual runs) are shown in gray. Electrode types: A) GP08 1W 8C, B) GP08 1W 10C, C) GP08 1.2W 10C, D) GP08 1.7W 10C, E) GP08 2W 10C, F) Reference graphite electrode [182].

6.3.2 Analysis of biofilms: CLSM and SEM Imaging

In order to examine the surface morphology and biofilm formation of *Geobacter sulfurreducens* on the electrode materials during microbial fuel cell (MFC) experiments, scanning electron microscopy (SEM) and confocal laser scanning microscopy (CLSM) were employed. Four representative electrodes were selected for imaging and the results are presented in Figure 74. Prior to the MFC experiments, SEM images were taken of fresh electrodes to visualize surface morphology on the microscale. After the MFC experiments, photographs of the electrodes and images from the fluorescence microscope

were taken to illustrate bacterial biofilm formation. The biofilms were stained with the fluorescent DNA stain Syto™ 9.
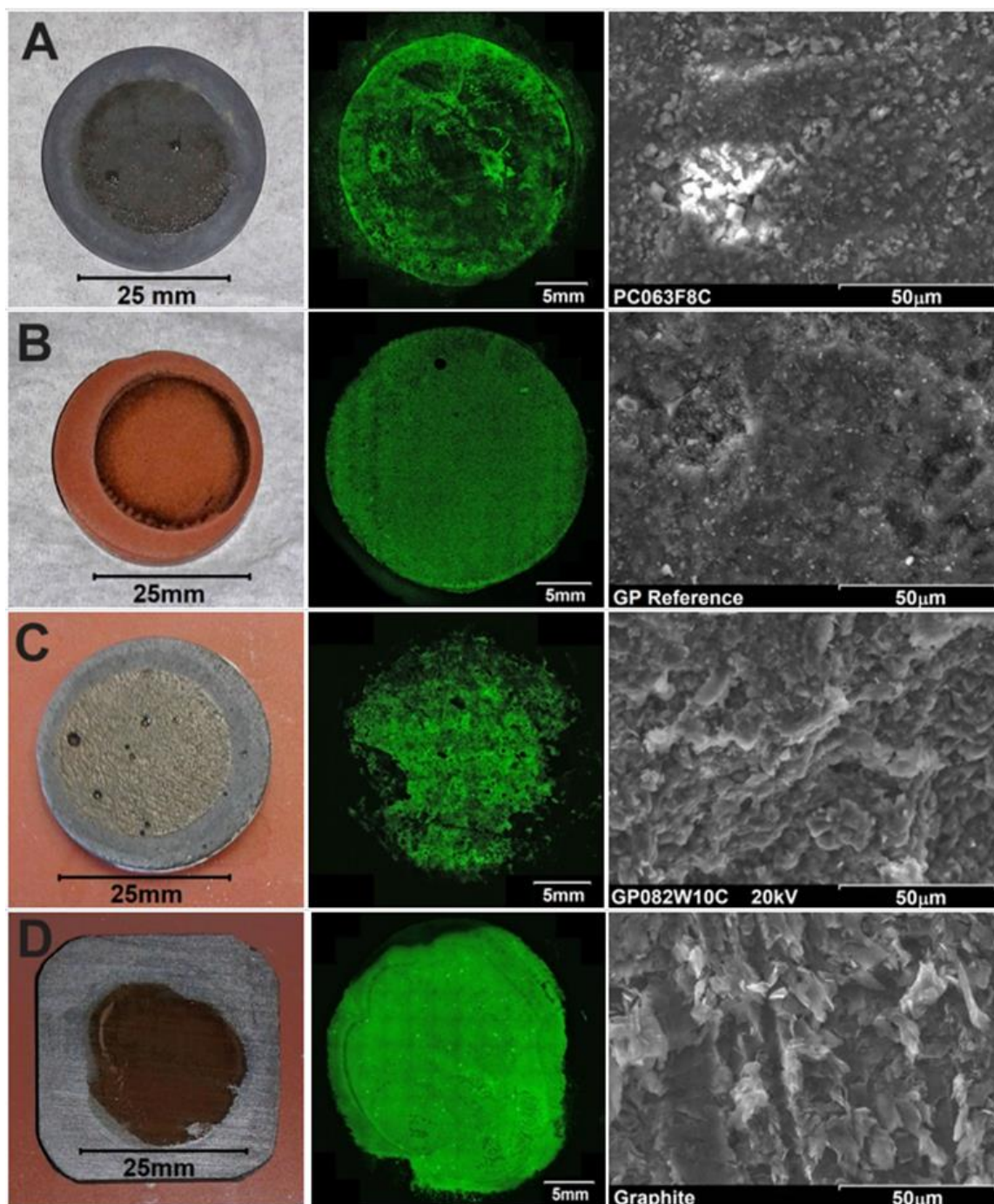
Figure 74: Four different electrode materials after application as anodes in polarized MFC experiments are shown. From left to right depicted: Photograph of the electrode, Confocal laser scanning microscope (CLSM) image of the Syto™ 9 stained biofilm and SEM image of the fresh electrode surface without biofilm. A: PC06 3F 8C which produced no current. B: GP Reference which as well produced no current. C: GP08 2W 10C electrode. D: Reference graphite electrode [182].

The SEM images of GP08 2W 10C and graphite exhibit similar surface roughness, which is primarily due to the structure of the graphite. However, the morphology of the deposited biofilms is distinct,

with a smooth surface for the graphite and a non-uniform surface on the GP08 2W 10C electrode. Despite these differences, both biofilms performed similarly in the MFC, indicating that the MFC performance of an electrode material cannot be inferred from biofilm morphology. PC06 3F 8C and GP Reference show less granulation in the SEM images and evidence of biomass deposition, even though no current was produced. The presence of biomass without current generation on the anode may indicate the presence of an alternative electron acceptor. Since fumarate was omitted, residual oxygen present in the medium or diffusing through the porous anodes could have served as an electron acceptor for *Geobacter sulfurreducens*. While previously classified as an obligate anaerobic bacterium, recent studies have shown that it can tolerate small amounts of oxygen and even utilize it as an electron acceptor. After the MFC experiments, the electrode samples were freeze-preserved. Photographs and images of the electrodes were taken with a fluorescent microscope to illustrate the formation of bacterial biofilms. The biofilms were stained with the fluorescent DNA stain Syto™9. First, biofilm formation was found on the surface of all the materials tested, and the surface they were all biocompatible. One of the biofilms grown on graphite and the biofilm grown on GP08 2W 10C electrode showed one uniform and one rough from the appearance. However, both biofilms behaved similarly in MFC, which means that no conclusions about the MFC performance of the electrode materials can be drawn from the morphology of the biofilms (Figure 74).

6.4 Summery and Discussion

In this chapter, MFCs were prepared using different mineral electrodes, electrochemically cultured with *Geobacter sulfurreducens* and tested for the performance of the electrodes. The electrodes prepared with PC are not suitable for direct use as electrodes for MFC because of their large resistance. On the contrary, the electrodes prepared from GP, with their superior electrical conductivity, proved the feasibility of utilizing mineral electrodes for the fabrication of MFC.

The graphite content of any GPG anode above the percolation threshold can be utilized as an MFC anode. As the graphite content increases, the electrode conductivity and the current density of the MFC also increase. The biocompatibility of the GPG electrode has been demonstrated in the presented experiments. Increasing the porosity of GPG compounds provides more space for microorganisms in the sample and increases the electrochemically active surface in addition to improving the electrical conductivity of the mixture. Therefore, the high water content of the GPG anode significantly leads to a similar current output compared to the graphite electrode.

Compared with the traditional graphite anode material, the microbial anode prepared by GP has considerable performance and great price advantage, and is an electrode material worthy to be studied in depth. GP08_1,7W_10C has a positive effect on the current production of *Geobacter sulfurreducens* cultures, indicating favorable conditions for the growth of *Geobacter sulfurreducens* cultures. For electrode GP08_1.7W_10C, the mean value of the areal charge density σ_{160} was 155.9 A·s/cm^2 with a standard deviation of about 29 %. The tests with the reference material graphite were

the most reproducible. The mean value of the obtained areal charge density σ_{160} was 144.5 A·s/cm^2, the second highest of the tested electrodes, and the standard deviation was about 14 %.

At this point, the study of the theoretical part of the MFC made of mineral anode material will come to an end. Due to the power limitation of a single MFC, most of its application situations are characterized by the joint collaboration of multiple MFCs. The next section will discuss the working performance and application cases of MFC systems made with mineral anodes by analyzing the connection methods of MFCs and combining them with practical prototype applications.

7 Scaling up MFC: Transfer to a practical application

Although microbial fuel cells possess various advantages and have a wide range of potential applications, their low power output remains a significant bottleneck in the realization of their practical use. This low power is primarily due to the small cathode-anode potential difference and low efficiency of electron transfer [200]. In order to address this issue, a significant amount of research has been conducted to enhance MFCs' electrical energy output, such as through the optimization of electrode materials and surface catalysts, alteration of cathode and anode reaction substrates, improvement of the MFC structure, and the selection of more efficient electricity-producing microorganisms. However, these efforts are still faced with challenges, such as high costs and low practicality [201]. Utilizing mineral anodes effectively reduces the production costs of MFCs and provides a foundation for their practical application. Among the different configurations, the air cathode microbial fuel cell is considered an ideal choice for large-scale application, both from a structural perspective and from a cost standpoint. The power production performance of MFCs is closely linked to the electrode area, and increasing the electrode area can lead to an increase in the attachment of microorganisms and the contact area with air, thereby enhancing the power output of MFCs. The output power does not increase in proportion to the volume of an individual reactor or the area of the electrode [202].

Connecting multiple MFC reactor electrodes in series or in parallel to form an MFC stack is an effective means of boosting MFCs' power production, and this connection method and number are flexible. In theory, connecting MFCs in series can double the output voltage, connecting MFCs in parallel can double the current, and a combination of series and parallel connection can increase both the voltage and current simultaneously. MFCs cannot be considered as ideal power sources due to their high internal resistance.

In this chapter, the impact of series and parallel connection on the overall performance of microbial fuel cells will be studied, along with the prospects of micro-energy harvesting and application, with a focus on soil microbial fuel cells.
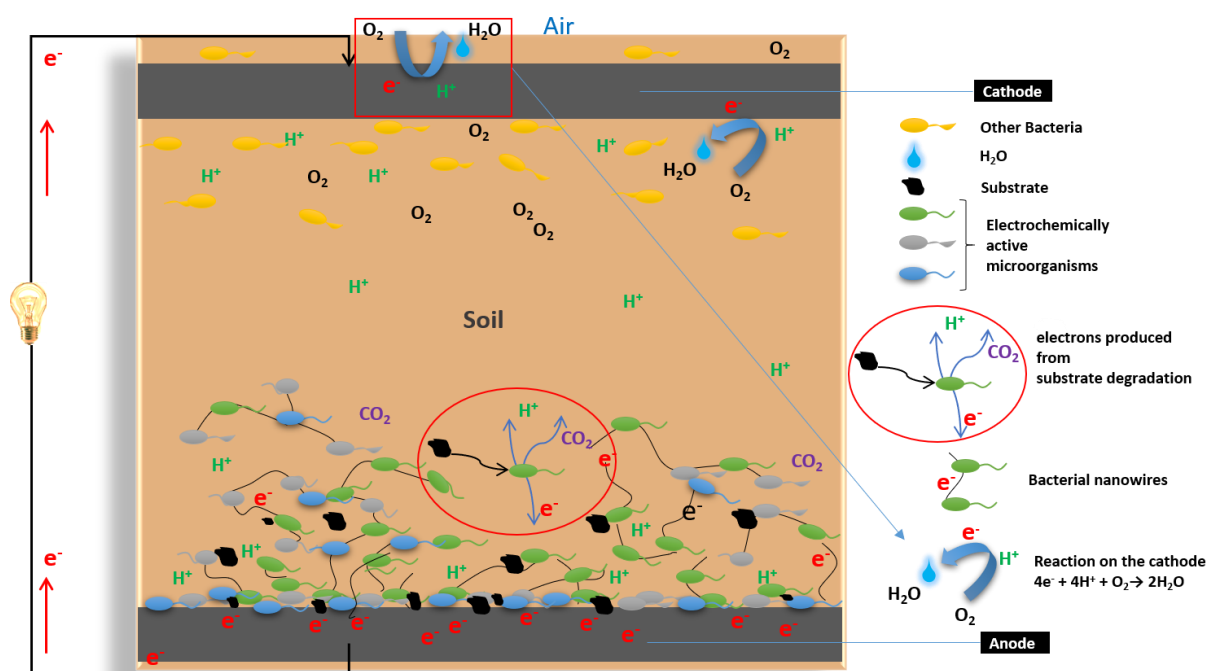
7.1 Soil-based microbial fuel cell

A soil-based microbial fuel cell (SB-MFC) is a bioelectrochemical system that utilizes naturally occurring microorganisms present in soil to convert organic matter into electrical energy (Figure 75). The device consists of a single chamber that serves as both the anodic and cathodic compartment. The anodic compartment is filled with soil, which serves as the substrate for the microorganisms. The microorganisms present in the soil convert the organic matter within the soil into electrons and protons through the process of metabolism. These electrons are conducted through an external circuit to the cathode, where they are harnessed to generate electricity or power a load. The protons, on the

other hand, migrate across a proton exchange membrane, if present, to the cathode where they combine with oxygen to form water.

SB-MFCs have the potential to generate electricity from the organic matter present in soil such as plant roots and dead plant matter, and can be utilized for a variety of applications such as powering sensors or other low-power electronic devices in remote locations. Additionally, SB-MFCs can be used to monitor soil quality, detect pollutants or study the microbial activity in soil.

Most of the currently discovered electrochemically active microorganisms (EAM) used in SB-MFCs are anaerobic [203]. They congregate in deeper soil areas and gradually form a biofilm on the surface of the anode. The anode collects the free electrons released by the metabolism of the EAMs, which enter the cathode via an external conductor. The hydrogen ions produced by the metabolism of the microorganisms move through the soil to the cathode. At the cathode, the free electrons, hydrogen ions, and oxygen molecules combine to form water.

Figure 75: Scheme of a single chamber soil-based microbial fuel cell.

7.1.1   Soil

To verify the differences in power output performance of different soils, and to select better microorganisms and fuel sources, four different types of soils were tested: forest, garden, flowering and chemical fertilizer soils. The open circuit voltage (OCV) was measured to determine the performance of the soils, and the results were depicted in Figure 76. The OCV of the system was measured every 25 minutes. As shown in the left of Figure 76, the OCV test of forest soil performed

the best, with a stable increase from 250mV to about 300mV. The OCV of the garden soil, although greater than 200mV at the beginning of the test, gradually decreased to 100mV over time. The performance of the flowering earth and chemozem was relatively poor, with their OCV remaining below 50mW. Subsequently, with forest soil as a reference, the OCV was tested when increasing the water content in the soil, as shown in the right of Figure 76. With the increase of water content, the OCV of the soil increased from 250 mV to 325 mV. A more water content can ensure the stability and even growth of OCV output. The results of the OCV test of the four soils, which used the same electrode material and electrode spacing, were significantly different, which demonstrates the significance of selecting appropriate microorganisms and soil types for optimal performance of SB-MFCs.
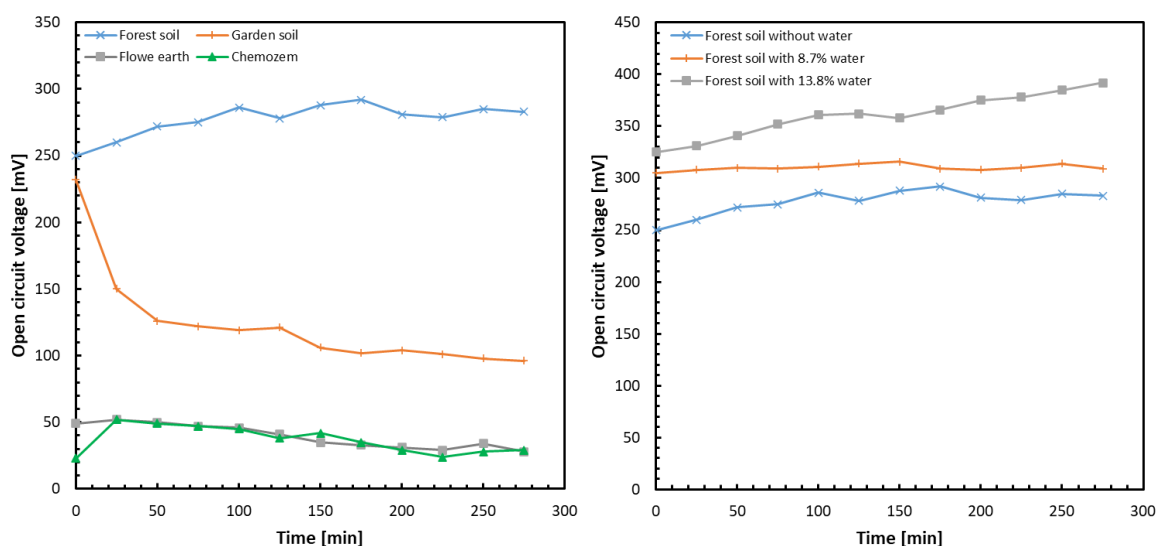
Figure 76: Variation in voltage output when different soil types were used (left), Variation in voltage output when the water content of the soil was altered (right).

In addition to variations in microbial colonies, variations in the carbon sources present in the soil can also affect the performance of soil-based microbial fuel cells. Hao et al. [204] tested four different carbon sources (acetate, glucose, citric acid, and starch) and found that the maximum power densities were 589.1 mW/m^2, 445.6 mW/m^2, 555.0 mW/m^2, and 555.0 mW/m^2, respectively, with 390.6 mW/m^2, respectively. This research shows that an increase in the complexity of the carbon source structure in the soil reduces the degradation rate by microorganisms, resulting in a decrease in power density. The presence of a sufficient and stable carbon source is crucial for ensuring the stable operation of SB-MFCs.

The utilization of soil as the anodic substrate in a soil-based microbial fuel cell presents a unique challenge due to the limited electrical conductivity of soil. This limited conductive capacity results in a large internal resistance, hindering the transfer of free electrons near the anode and impeding the performance of the SB-MFC. To overcome this limitation, researchers have investigated various strategies to increase the electrical conductivity of the soil near the anode. Since the effective distance

for microbial-dominated direct electron transfer is within 100 µm, free electrons that are farther away need to be transferred to the anode by electron shuttles from the soil species [205], [206]. One such strategy is the use of conductive carbon fibers, which have been shown to effectively assist the anode in collecting electrons and significantly improve the electrical performance of the SB-MFC. Li et al.[207] reported that the maximum current density, maximum power density, and cumulative charge output of SB-MFCs mixed with carbon fibers were increased by 10, 22, and 16 times, respectively. This highlights the potential of anthropogenic interventions to increase the electrical conductivity of the soil as a means to improve the performance of SB-MFCs.

Proton migration rate to the cathode plays a significant role in determining the electrical performance of soil-based microbial fuel cells. Microelectrode testing, as performed by Li et al. [208], revealed that incorporating silica into the soil can improve internal mass transfer within the SB-MFC and enhance degradation of petroleum hydrocarbons. Proton migration is facilitated through the transfer of water molecules. Increasing the water content of the soil can therefore promote proton migration to the cathode and increase the activity of microorganisms. As depicted in Figure 76, increasing the water content from 0 – 13.8 % significantly increases the open-circuit voltage. A moderate water content ensures that microorganisms are metabolically active, resulting in the release of more free electrons. Conversely, a high water content can lead to anaerobic environment destruction at the anode and lower voltage.

The performance of microbial fuel cells is also highly dependent on the temperature as it plays a crucial role in the growth and proliferation of microorganisms. Optimal temperatures can enhance the power production performance of MFCs by promoting the enrichment and multiplication of microorganisms. Conversely, low temperatures can inhibit the activity of microorganisms and result in MFC failure.

7.1.2   SB-MFC set up

In single-chambered microbial fuel cells, the distance between the cathode and anode is important because it prevents direct electron transfer from the microorganisms to the cathode. Direct electron transfer can lead to a decreased power output and efficiency of the device. The proton exchange membrane in dual-chambered microbial fuel cells serves a similar purpose by separating the anode and cathode compartments and preventing direct electron transfer. The use of a proton exchange membrane also allows for efficient proton transfer, which is necessary for the generation of electrical energy. Additionally, maintaining a certain distance between the cathode and anode also increases the mass transfer resistance and allows the system to have more controlled conditions that can result in better performance.

The figure (Figure 77) illustrates the open-circuit voltage (OCV) at various electrode spacings. In this experiment, forest soil was used as the material and no additional water was added. Stainless steel mesh was used as the electrode material with a constant area of 100 cm^2 for both the anode and

cathode. The distance between the anode and cathode was adjusted from 0.5 cm to 5.5 cm in increments of 0.5 cm. The OCV was recorded and the experiment was repeated three times for each distance. The results show that, when using forest soil, the SB-MFC had the highest OCV of 324 mV when the distance between the anode and cathode was 2 cm. Increasing or decreasing the distance between the anode and cathode in a single-chambered microbial fuel cell will result in a decrease in open-circuit voltage (OCV) as it affects the mass transfer resistance and subsequently the electrical performance of the cell.
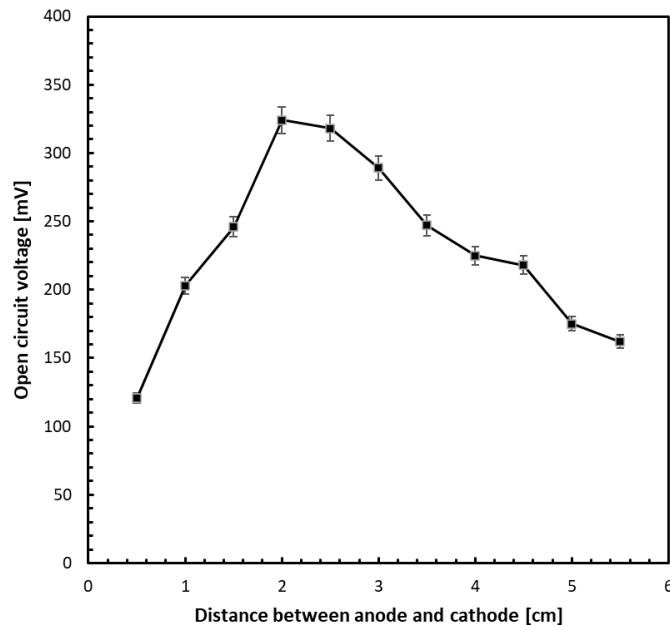
Figure 77: Voltage variation by change the distance between the electrodes.

The anode and cathode of a microbial fuel cell exhibit differential reaction kinetics. Oxygen molecules in the air have greater contact area at the cathode, facilitating the conversion of hydrogen ions and free electrons to water. The anodic reaction is slower than the cathodic reaction, making it the rate-limiting step for the overall performance of the microbial fuel cell [209]. Hong et al. [210] found that when the anode-to-cathode area ratio is 5:1, the voltage remains stable and current output is consistent. Furthermore, when the anode area is doubled, the output power of the soil microbial fuel cell nearly triples

The output of soil-based microbial fuel cells is affected by several factors, both in the soil and in the design of the electrodes. Factors in the soil include the composition and diversity of the microbial colonies, the availability of carbon sources, the water content, and the temperature. The use of different types of soils, such as forest, garden, flowering and chemical fertilizer soils, can lead to significant differences in output performance. Additionally, the carbon source used in the soil can also affect the performance of SB-MFCs, with complex carbon sources leading to a decrease in power density. The water content of the soil is also an important factor, as it can promote the migration of

protons to the cathode and increase the activity of microorganisms. However, when the water content is too high, it can destroy the anaerobic environment of the anode and reduce the voltage.

On the other hand, the design of the electrodes, such as the distance between the cathode and anode and the electrode material, also plays a crucial role in the output performance of SB-MFCs. A smaller distance between the cathode and anode can reduce mass transfer resistance. However, for single-chambered microorganisms, a certain distance between the cathode and anode is necessary to prevent direct electron transfer from the microorganism to the cathode. The use of conductive carbon fibers can also improve the electrical performance of SB-MFCs by increasing the maximum current density, maximum power density and cumulative charge output.

7.2 Maximizing Output Power in Microbial Fuel Cells

7.2.1 Single Microbial Fuel Cell Power Generation

A single microbial fuel cell (MFC) has a limited output power and is not a suitable source of energy on its own. To increase output voltage and current, multiple MFCs must be connected in series or parallel. Each MFC can be viewed as an element with a specific internal resistance and voltage output. However, MFCs are complex dynamic systems when in operation. Direct series-parallel connection is not an efficient method of harnessing electrical energy. A more effective approach is to store the electrical energy for optimal maximum power point tracking (MPPT) and for planned utilization of its production. As discussed in Chapter 2 (equation 2-10), the electric potential of an MFC is equal to the theoretical electric potential minus the internal resistance losses:

$$E_{cell} = E_{emf} - \eta_{act} - \eta_{ohmic} - \eta_{conc} = E_{emf} - IR_{int} \qquad (7\text{-}1)$$

where E_{emf} is the maximum cell potential, η_{act} is the activation loss, η_{ohmic} is the ohmic loss and η_{conc} is the concentration loss and IR_{int} is the sum of all internal losses of the MFC.

The above equation describes the electric potential (E_{cell}) of a microbial fuel cell (MFC). The electric potential is equal to the theoretical electric potential (E_{emf}) minus the energy losses due to internal resistance (R_{int}) activation overpotential (η_{act}), ohmic overpotential (η_{ohmic}) and concentration overpotential (η_{conc}). E_{emf} refers to the theoretical electric potential that can be generated by the MFC when the reactants and products are at standard conditions [66]. R_{int} is the internal resistance of the MFC, which is determined by the resistance of the electrolyte and the contact resistance between the electrodes and the electrolyte. η_{act} , η_{ohmic} , and η_{conc} are the overpotentials, representing energy losses caused by the activation of the electrode reactions, the resistance of the electrolyte, and the difference in the concentration of reactants and products, respectively. The difference between the theoretical electric potential and the actual electric potential is caused by energy losses in the form of overpotentials, and the internal resistance of the MFC. Therefore, the

actual electric potential is always lower than the theoretical electric potential. In order to increase the electric potential, efforts should be made to reduce the internal resistance of the MFC and the overpotentials. Figure 78 shows the equivalent circuit of an MFC under open-circuit conditions and with an external resistance, R_{ext}. The dotted box represents a single MFC, which has an electric potential of E_{cell}. This E_{cell} is the difference between the theoretical electric potential, E_{emf}, and the internal losses, as shown in equation 7-1. When an external resistance with a value of R_{ext} is added.
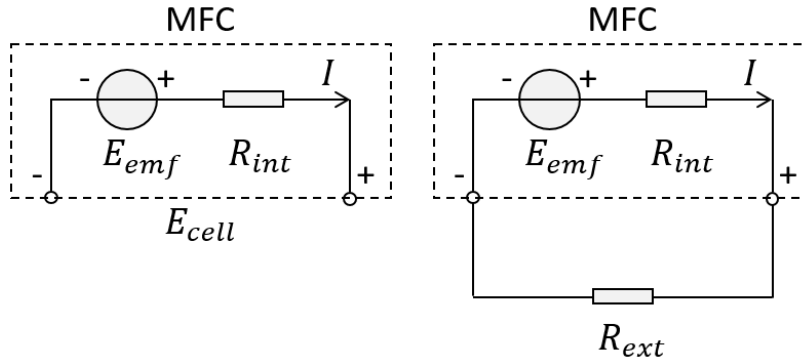
Figure 78: Equivalent circuit of an MFC under open-circuit conditions (left) and with an external resistance (right).

When the current is constant, the power is inversely proportional to the resistance. Therefore, the actual output power ($P_{max,emf}$) of the MFC is directly proportional to the internal resistance and the external resistance. This relationship is represented in equation 7-2, where the theoretical output power of the MFC is represented by the open-circuit voltage, E_{emf}, and the internal and external resistances, R_{int} and R_{ext}, respectively. [66]

$$P_{max,emf} = \frac{E_{emf}^2 R_{ext}}{(R_{int} + R_{ext})^2} \tag{7-2}$$

7.2.2   The Impact of Series Connection on Microbial Fuel Cell Power Output

The earliest MFC scaling up studies appeared in the 1940s and were also of interest in the 1960s and 1970s [200]. In the past decade or so, with the rapid development of bioelectrochemical technology, MFC series and parallel studies have received renewed attention, and made great progress in both theory and application. Most of the current practical environmental applications of MFCs use multi-electrode or multiple MFCs in series and parallel structures [51], [211]. However, there are still some problems that need to be solved for the further performance optimization and popularization of the MFC series-parallel system.

When two microbial fuel cells (MFCs), MFC1 and MFC2, are connected in series, the negative electrode of MFC1 and the positive electrode of MFC2 are at the same potential. Under the assumption that the external load resistance is much greater than the internal resistance of each MFC, the total

output voltage is the sum of the voltage outputs of MFC1 and MFC2, regardless of whether the sizes of MFC1 and MFC2 are the same. In this case, the total internal resistance of the power source is equal to the sum of the internal resistances of MFC1 and MFC2 (Figure 79).

$$E_{cell} = E_{cell1} + E_{cell2}$$

$$R_{int} = R_{int1} + R_{int2}$$
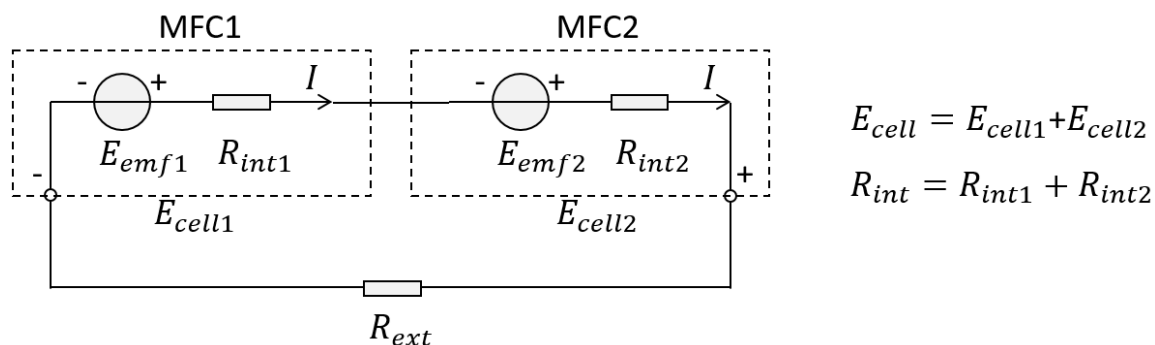
Figure 79: Equivalent circuit MFCs in series connection.

7.2.3   The Impact of Parallel Connection on Microbial Fuel Cell Power Output

The main reason for connecting MFCs in parallel is to increase the overall current output of the system. When MFCs are connected in parallel, the current from each individual MFC flows into a common load, resulting in a higher total current output.

When connecting two microbial fuel cells (MFCs) in parallel, the potential difference between their positive electrodes is the same. This allows for an increase in current intensity in the system. However, this ideal scenario is not always practical for microbial fuel cells. When the potential difference between the two MFCs is not equal, connecting them in parallel can result in a short circuit and a loop current. To prevent this, a diode can be added to the circuit to allow for current flow in one direction only, from the negative electrode to the positive electrode (Figure 80). However, this can result in one MFC being disconnected from the circuit, and it will not contribute to the overall power output of the system.
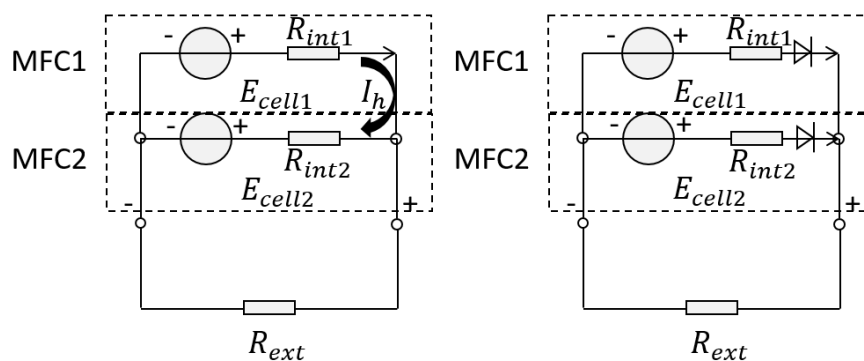
Figure 80: Equivalent circuit for MFCs in parallel connection.

7.3 Design and Fabrication of Soil-based Microbial Fuel Cell Systems

The optimal connection method for an MFC system charging a battery would involve a combination of both series and parallel connections. This is because connecting MFCs in series can increase the overall voltage output, while connecting them in parallel can increase the overall current output. In order to charge a battery with an input voltage range of 2.5 – 4.2 V, it is important to ensure that the combined voltage output of the MFC system falls within this range. The specific configuration will depend on the individual voltage and current output of the MFCs being used, as well as the desired output voltage for charging the battery. It is important to note that careful monitoring of the system is necessary to ensure that the MFCs are operating within safe limits and that the battery is being charged efficiently.

7.3.1 Connection of soil based microbial fuel cells systems

The anode and cathode of the SB-MFC were constructed separately using mineral materials (GP08_1.7W_10C) and assembled as illustrated in Figure 81. Each cell consists of a mineral anode, an electron collector (stainless steel mesh), soil, graphite, another electron collector (stainless steel mesh), additional soil, and a plant. The open-circuit voltage (OCV) of the SB-MFC obtained ranges between 0.25-0.4V.
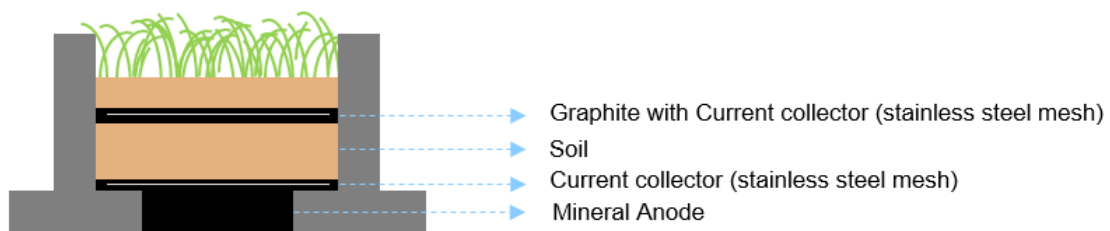
Figure 81: Configuration of the Soil based Microbial fuel cells.

To meet the requirements for connecting multiple microbial fuel cells (MFCs) in series or parallel, it is necessary to maximize the number of MFCs that can be placed in a compact space. The TTR-MultiDrain-Plus 2000 by Hübner-Lee was used as the base plate for the soil-based MFC system in this study. As seen in Figure 82, the module is made of 100 % recycled plastic, measuring 800 mm x 400 mm x 60 mm and featuring 32 containers, each measuring 80 mm x 80 mm. Up to 3.125 of these modules can be placed per square meter.
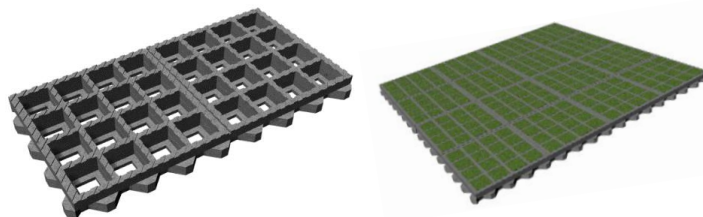
Figure 82: TTR-MultiDrain-Plus 2000 from Hübner-Lee.

In order to increase the output voltage, 32 MFCs were connected in series. Each group of 8 consecutive MFCs were connected in series, resulting in a total of 4 groups. These groups were then connected in parallel with the addition of diodes in series, resulting in a system that was able to successfully power light-emitting diode (LED).

These 32 MFCs are connected in the way shown in the Figure 83. The figure illustrates the connection scheme of the microbial fuel cells (MFCs) in the system. The diagram shows that the 32 MFCs are connected in a specific configuration to increase the output voltage. The MFCs are grouped together in series, with each group consisting of 8 consecutive MFCs. The design utilized mineral-based electrodes for the anode and cathode of the microbial fuel cell, as shown in Figure 82. The MFCs were connected in series to increase the output voltage and then connected in parallel with the use of diodes. This configuration successfully powered a green LED for a period of three days. However, due to lack of water control, the LED eventually shut off. Upon the introduction of water, the LED was successfully re-illuminated. This experiment highlights the importance of proper water management in maintaining the function of a microbial fuel cell system utilizing mineral-based electrodes and the specific configuration of series and parallel connections as a means of increasing output voltage and current. It also shows the potential of using this type of MFCs for low power applications such as lighting. However, it is important to note that for longer-term or higher power applications, further optimization and control of various parameters such as water management, electrode materials, and microbial populations is necessary.
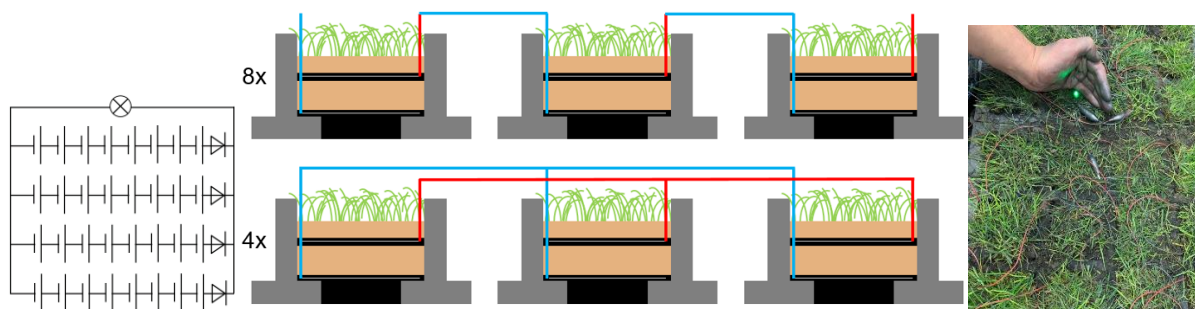
Figure 83: Connection scheme of the soil based microbial fuel cells in the system.

As MFCs generate electricity on a continuous basis, unlike other renewable energy sources that are dependent on environmental factors such as sunlight or wind. Thus, the most efficient utilization of the energy generated by MFCs is to store it in a battery. This allows for not only maximum utilization of the generated electricity but also ensures stable output during power usage. Of course, to overcome the instability of MFC output, special devices are required to collect it.

7.3.2   Application prototype: Lighting system for bicycle carport

In this study, a bike shed was designed and manufactured with the aim of demonstrating the feasibility of microbial fuel cell (MFC) systems in real-world applications. The shed was built with a steel structure and a sandwich element roof (Figure 84). Due to the early onset of darkness during the winter months, lighting was needed for the convenience of the bicycle users. To achieve this, a soil-based MFC system was designed and placed on the top of the shed. The system was composed of 224 individual MFCs, which were connected in series in groups of 16 to form a total of 14 groups (see Figure 85). These groups were then connected in parallel with diodes added. The energy harvesting technology was applied in this system, and a custom-designed control and storage module was used to collect the electrical energy produced by the MFCs in a lithium-ion battery.

Figure 84: Bicycle carport at the camps of Technische Universität Darmstadt. Left: front view, Right: Top view.
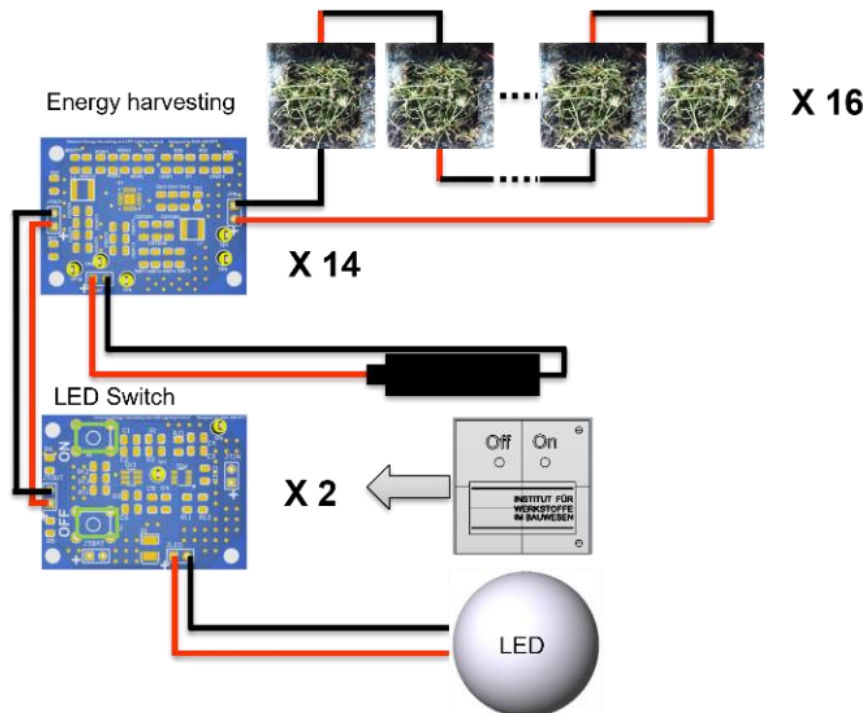
Figure 85: Soil-based MFC LED system: 224 individual MFCs, which were connected in series in groups of 16 to form a total of 14 groups.

The output power of a microbial fuel cell varies with the external environment, and in order to always operate at maximum output power, the help of circuit design is needed. In addition, storing the electrical energy produced by the MFC is also the key to avoid waste. In this chapter, the main objective of the led lighting is to illustrate the feasible solutions for energy harvesting, energy storage and energy usage of microbial fuel cells.

One of the most critical concern in the power stage design is the characteristic of ultra-low power generated by each MFC. Each cell provides power from 10^{-6} to 10^{-3} W according to the experimental results. The conversion loss for each component should be evaluated very carefully. Besides, it is reasonable to use the maxim power point tracking(MPPT) technique to maximize the output power and improve the efficiency.

The main scheme of the power conversions consists of three parts: the battery charging and discharging that stores the power generated by the cells; the voltage regulating that provides a constant DC voltage for the lighting and onboard chips; and the manual switch controller that provides a timed driving for the LED. The final selection of the IC is the BQ25570 solutions by Texas Instrument. The chip is suitable for the ap-plications of energy harvesting down to a power of 10^{-6} W and 100mV to 5V input. The MPPT is also configurable according to the user's requirements. The power system is designed with a two stages structure: the energy harvesting and the LED driver.

The main schematic circuit of the energy harvesting stage is shown in Figure 86. The MFC cells are series connected to generate a high module voltage 2.5 to 4.5 V. The IC BQ25570 has a built-in boost converter that converts from the input 2.5V~4.2 V for the Li-on battery and the charging and discharging. Another buck converter on-chip regulates the voltage from the CSTOR capacitors to stabilize the output at 3.3 V. The next stage, the LED driver board is connected at the terminal that provides the energy for the lighting. All these on-chip converters are switching power converters that have an efficiency as high as 98 %. These switching power supplies would make the energy harvesting more efficient and reliable.
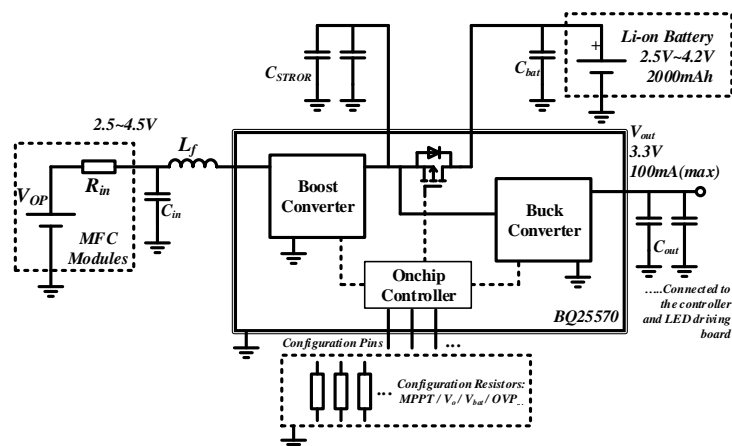
Figure 86: The schematic circuit of the energy harvesting module.

The BQ25570 has a configurable MPPT function de-fined by the settable resistors. The MFC modules can be treated as a weak voltage source with a very high inner resistance. According the equivalent circuits of the modules, the maximum power point happens when the module output voltage is equal to half of the modules' open circuit voltage (OCV). Despite of the linear feature of the OCV and inner resistance, the MPPT is still a worthy step.

In order to evaluate the charging performance of the energy harvesting module, 96 mini soil microbial fuel cells were fabricated and charged using graphite electrodes SB-MFC. The open circuit voltage of the coin battery was monitored using a voltmeter, as depicted in the Figure 87, during the charging process at a rate of 7.5 mV/min.
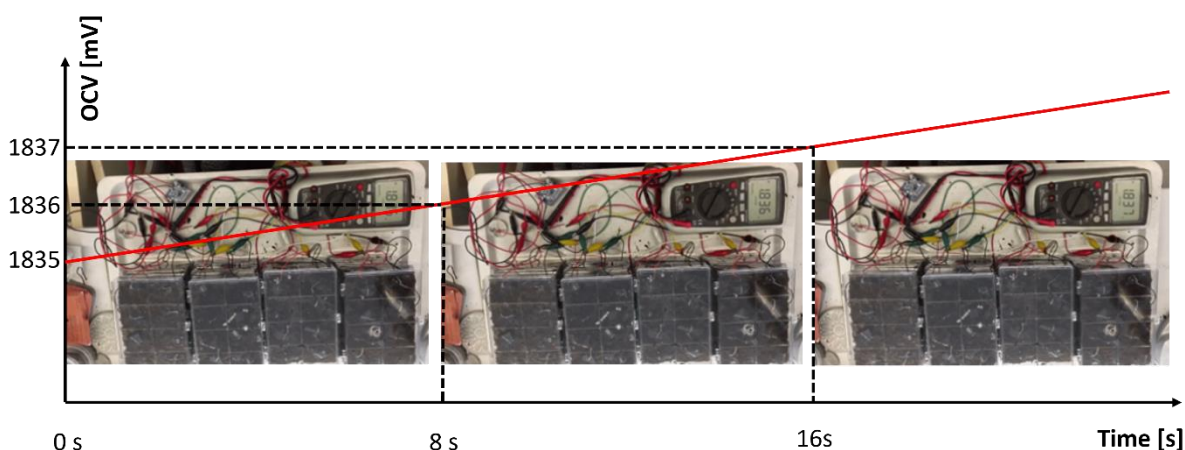
Figure 87: Charging performance test of the energy harvesting module.

7.4 Summary and Discussion

The MFC lighting system in the bike shed successfully operated for one year. Unfortunately, the system failed due to water infiltration in the circuit boards caused by a lack of proper sealing in the enclosure housing the circuit boards. Despite this setback, the project demonstrated the feasibility of MFC systems in real-world applications.

The idea of using microbial fuel cells (MFCs) for power generation is a promising concept in the field of renewable energy. MFCs have the potential to generate electricity continuously and sustainably by harnessing the metabolic activity of microorganisms. They can be applied in various environments and settings, such as wastewater treatment plants and remote locations where traditional power sources are unavailable. Furthermore, MFCs can be used in combination with other energy harvesting technologies to increase overall energy efficiency. However, the technology still faces challenges in terms of scalability and cost-effectiveness. Additional research and development is need to optimize the performance and efficiency of MFCs, as well as to reduce the costs of materials and fabrication.

8 Conclusion and outlook

8.1 Conclusion

Microbial fuel cells have attracted significant attention as a sustainable energy source due to their ability to convert organic matter into electrical energy. However, one of the main challenges in MFC development is low power production. To address this issue, mineral anodes have been investigated as a cost-effective alternative to traditional graphite anodes. Additionally, the use of mineral anodes in the form of three-dimensional electrodes provides a larger living space for the power-generating microorganisms, providing a prerequisite for further improving their power generation performance.

In this study, the potential of mineral materials as anode materials for MFCs was investigated. Two mineral cementitious materials, Portland cement and geopolymer, were used to prepare conductive mixtures with the addition of graphite as a conductive filler. The percolation thresholds for the two mineral cementitious mixes were reached at 8 and 7 vol.% graphite content, respectively. As the graphite content increased, the overall electrical conductivity of the system changed from ionic to electronic conductivity, with the graphite particles forming a coherent conductive network. The total electrical conductivity of the mixes prepared from geopolymers (12 S/m) was found to be much higher than that of the mixes prepared from Portland cement (10^{-4} S/m) due to the different pore structure of the systems.

In order to gain a deeper understanding of the conductive mechanism of the conductive mixture, the percolation threshold of conductive mixtures containing graphite was simulated using the Monte Carlo method and the software HYMOSTRUC and MATLAB. The electrical conductivity of the mixture as a function of graphite content was then modeled using Bruggman's effective medium theory. By introducing the concept of effective volume, the simulated electrical conductivity variation is in agreement with the results obtained from experiments.

A dual-chamber microbial fuel cell with a mineral material anode was fabricated using Geobacter and the performance of this anode material was investigated. Most electrodes fabricated using Portland cement as the cementitious material did not produce electricity due to their high resistive losses. However, the electrode materials made with geopolymer as the matrix functioned properly and produced current, with a maximum operating current of 155.9 A·s/cm². This is higher than the maximum operating current of 144.5 A·s/cm² for graphite electrodes, indicating the potential of mineral materials as electrode materials for MFCs.

In order to investigate the feasibility of applying microbial fuel cells (MFCs) in practical settings, a series-parallel connection of multiple MFCs using graphite-mineral geopolymer as the electrodes was constructed and successfully lit a green LED. To optimize the collection and utilization of these micro-energies and address the instability issues in MFC operation, a maximum power point tracking (MPPT) circuit module was employed to control the total power generation output, effectively circumventing

the instability in the operation of the MFCs and maintaining their output power at the maximum possible value. This sets a direction for future large-scale applications. Overall, the use of mineral anodes shows great potential for MFCs and requires further research for optimization of performance.

8.2 Outlook

8.2.1 Modules functional plate

The utilization of mineral materials as electrodes for the production of multiple microbial fuel cells has potential for future development due to its modular design, which allows for the consideration of creating different functional modules using multiple MFCs. This can lead to the realization of combinations of power generation, energy storage, and various functional modules as shown in Figure 88. Various MFC system modules were produced using TTR-MultiDrain-Plus 2000 and mineral electrodes, and each module was connected through the same interface. The advantage of this design is that it enables the creation of enough power generation modules according to demand and the combination of necessary functional modules. Such combinations can provide suitable solutions for application scenarios with sufficient space. Because it combines green plants and MFCs, and can withstand certain pressure.

Basic Modular

Steckdose Modular

Speicher Modular

Wifi Modular
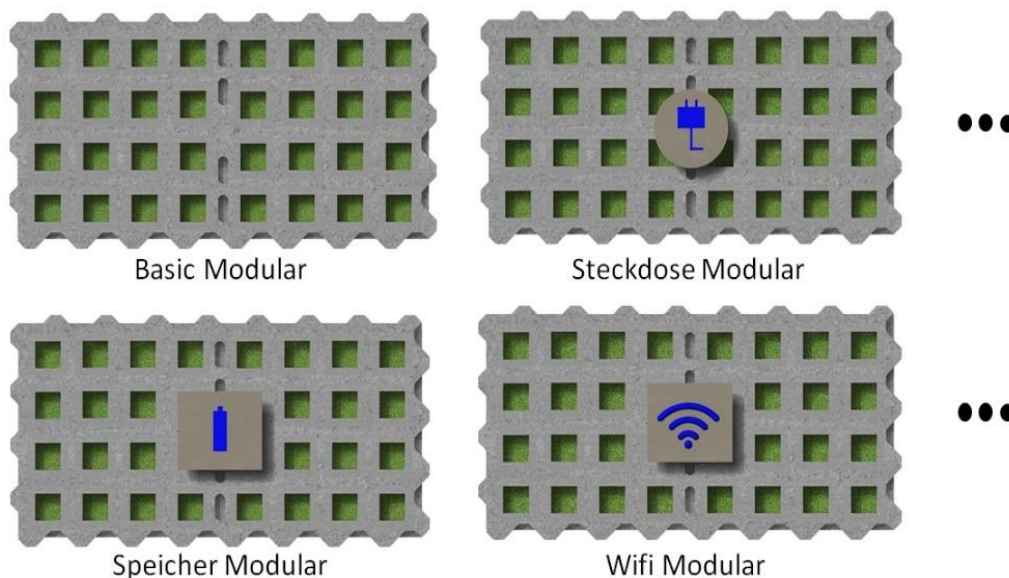
Figure 88: Different functional modules of soil microbial fuel cells (MFCs) fabricated using TTR-MultiDrain-Plus 2000 and mineral electrodes.

8.2.2 Smart and green city

Due to its versatility, the microbial fuel cell (MFC) has a significant market potential as a product (Figure 89). The robust horizontal or vertical design of the MFC, which continuously generates

electricity even at relatively low power levels, has a wide range of applications. In public spaces, for example, vertical street furniture elements with multiple interactive functions can be implemented. In addition to providing positive environmental and acoustic benefits, illuminated quiet zones can also serve as interactive advertising spaces. Wireless access points or Bluetooth beacons can also be integrated without the need for additional electrical infrastructure. Such installations can serve as a foundation for modern smart cities.
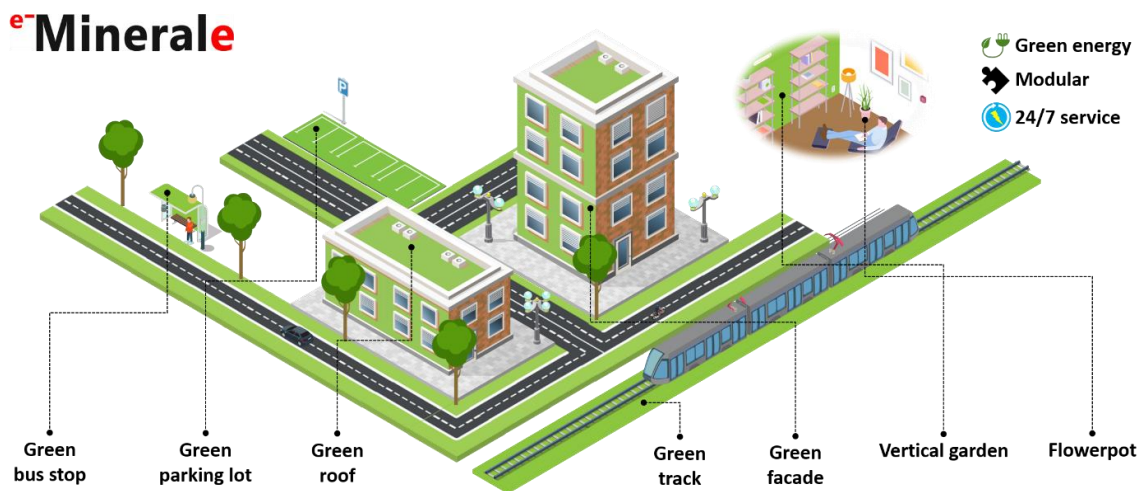
Figure 89: Further applications of soil based microbial fuel cells made of mineral electrodes: smart and green city.

In the transportation sector, the application of modular biofuel cells in green track beds has been proposed as a retrofit solution. Integrated linear LED lighting system eliminates the need for additional electrical infrastructure to announce the passage of trains. A recent study by the Institute for Agricultural and Urban Ecological Projects at Humboldt University in Berlin estimates that at least 450 km of grass paths in Germany alone could be equipped with such a system.

8.2.3   Rechargeable battery and supercapacitor made of GPG

Due to its good conductivity, GPG can be used as an electrode in batteries. Compared to traditional battery electrode materials, GPG has good mechanical properties and can be manufactured into various electrode shapes with the help of molds. Its manufacturing cost is also lower, making it more widely applicable. Using GPG to make batteries can result in lower internal resistance and improved battery performance compared to batteries made with Portland cement as the material.

This makes it possible to use building structures as a new form of energy storage. In the future, as the proportion of new energy sources continues to increase, places that are not convenient for electricity transportation can also use building foundations to store new energy.

In addition, GPG can also be used to make solid-state electrolytes with its excellent ion conductivity, and applied in supercapacitors. Compared to traditional batteries, supercapacitors can charge and

discharge very quickly and have a high power density. They also have a longer lifespan and can withstand a large number of charge-discharge cycles. GPG has a high surface area, which can store a large amount of charge, making it a potential candidate material for supercapacitor electrode materials.

Literatur

[1] K. Keramidas et al., Global energy and climate outlook 2019: electrification for the low-carbon transition : the role of electrification in low-carbon pathways, with a global and regional focus on EU and China. 2020. Accessed: Jan. 05, 2021. [Online]. Available: https://op.europa.eu/publication/manifestation_identifier/PUB_KJNA30053ENN

[2] K. Rabaey, "Bioelectrochemical Systems: From Extracellular Electron Transfer to Biotechnological Application," Water Intell. Online, vol. 8, Dec. 2009, doi: 10.2166/9781780401621.

[3] F. Zhao, R. C. T. Slade, and J. R. Varcoe, "Techniques for the study and development of microbial fuel cells: an electrochemical perspective," Chem. Soc. Rev., vol. 38, no. 7, p. 1926, 2009, doi: 10.1039/b819866g.

[4] H. Ren, H. Tian, C. L. Gardner, T.-L. Ren, and J. Chae, "A miniaturized microbial fuel cell with three-dimensional graphene macroporous scaffold anode demonstrating a record power density of over 10 000 W m $^{-3}$," Nanoscale, vol. 8, no. 6, Art. no. 6, 2016, doi: 10.1039/C5NR07267K.

[5] A. Gurung and S.-E. Oh, "The Improvement of Power Output from Stacked Microbial Fuel Cells (MFCs)," Energy Sources Part Recovery Util. Environ. Eff., vol. 34, no. 17, pp. 1569–1576, Jun. 2012, doi: 10.1080/15567036.2012.660561.

[6] P. Tanikkul and N. Pisutpaisal, "Performance of A Membrane-Less Air-Cathode Single Chamber Microbial Fuel Cell in Electricity Generation from Distillery Wastewater," Energy Procedia, vol. 79, pp. 646–650, Nov. 2015, doi: 10.1016/j.egypro.2015.11.548.

[7] M. Stöckl, Attachment under current − biofilm formation by electroactive bacteria. in Schriftenreihe des DECHEMA-Forschungsinstituts, no. Band 14. Aachen: Shaker Verlag, 2018.

[8] B. E. Logan and K. Rabaey, "Conversion of Wastes into Bioelectricity and Chemicals by Using Microbial Electrochemical Technologies," Science, vol. 337, no. 6095, pp. 686–690, Aug. 2012, doi: 10.1126/science.1217412.

[9] K. Rabaey et al., "Microbial ecology meets electrochemistry: electricity-driven and driving communities," ISME J., vol. 1, no. 1, pp. 9–18, May 2007, doi: 10.1038/ismej.2007.4.

[10] Y. Xiao, F. Zhao, and H. Cheng, Eds., Electrochemically Active Microorganisms. in Frontiers Research Topics. Frontiers Media SA, 2018. doi: 10.3389/978-2-88945-651-2.

[11] C. Dumas, R. Basseguy, and A. Bergel, "Electrochemical activity of Geobacter sulfurreducens biofilms on stainless steel anodes," Electrochimica Acta, vol. 53, no. 16, Art. no. 16, Jun. 2008, doi: 10.1016/j.electacta.2008.02.056.

[12] Y. A. Gorby et al., "Electrically conductive bacterial nanowires produced by Shewanella oneidensis strain MR-1 and other microorganisms," Proc. Natl. Acad. Sci., vol. 103, no. 30, Art. no. 30, Jul. 2006, doi: 10.1073/pnas.0604517103.

[13] Y.-C. Zhang, Z.-H. Jiang, and Y. Liu, "Application of Electrochemically Active Bacteria as Anodic Biocatalyst in Microbial Fuel Cells," Chin. J. Anal. Chem., vol. 43, no. 1, pp. 155–163, Jan. 2015, doi: 10.1016/S1872-2040(15)60800-3.

[14] T. J. DiChristina, C. M. Moore, and C. A. Haller, "Dissimilatory Fe(III) and Mn(IV) Reduction by Shewanella putrefaciens Requires ferE, a Homolog of the pulE (gspE) Type II Protein Secretion Gene," J BACTERIOL, vol. 184, p. 10, 2002.

[15] N. S. Malvankar et al., "Tunable metallic-like conductivity in microbial nanowire networks," Nat. Nanotechnol., vol. 6, no. 9, pp. 573–579, Sep. 2011, doi: 10.1038/nnano.2011.119.

[16] Y. A. Gorby et al., "Electrically conductive bacterial nanowires produced by Shewanella oneidensis strain MR-1 and other microorganisms," Proc. Natl. Acad. Sci., vol. 103, no. 30, Art. no. 30, Jul. 2006, doi: 10.1073/pnas.0604517103.

[17] D. F. Call and B. E. Logan, "A method for high throughput bioelectrochemical research based on small scale microbial electrolysis cells," Biosens. Bioelectron., vol. 26, no. 11, pp. 4526–4531, Jul. 2011, doi: 10.1016/j.bios.2011.05.014.

[18] G. Reguera, K. D. McCarthy, T. Mehta, J. S. Nicoll, M. T. Tuominen, and D. R. Lovley, "Extracellular electron transfer via microbial nanowires," Nature, vol. 435, no. 7045, Art. no. 7045, Jun. 2005, doi: 10.1038/nature03661.

[19] H. Zhang, X. Chen, D. Braithwaite, and Z. He, "Phylogenetic and Metagenomic Analyses of Substrate-Dependent Bacterial Temporal Dynamics in Microbial Fuel Cells," PLoS ONE, vol. 9, no. 9, Art. no. 9, Sep. 2014, doi: 10.1371/journal.pone.0107460.

[20] C. Leang, N. S. Malvankar, A. E. Franks, K. P. Nevin, and D. R. Lovley, "Engineering Geobacter sulfurreducens to produce a highly cohesive conductive matrix with enhanced capacity for current production," Energy Environ. Sci., vol. 6, no. 6, Art. no. 6, 2013, doi: 10.1039/c3ee40441b.

[21] Y. Cao et al., "Electricigens in the anode of microbial fuel cells: pure cultures versus mixed communities," Microb. Cell Factories, vol. 18, no. 1, Art. no. 1, Dec. 2019, doi: 10.1186/s12934-019-1087-z.

[22] S. A. Patil, C. Hägerhäll, and L. Gorton, "Electron transfer mechanisms between microorganisms and electrodes in bioelectrochemical systems," in Advances in Chemical Bioanalysis, F.-M. Matysik, Ed., Cham: Springer International Publishing, 2012, pp. 71–129. doi: 10.1007/11663_2013_2.

[23] D. R. Lovley, "Electromicrobiology," Annu. Rev. Microbiol., vol. 66, no. 1, Art. no. 1, Oct. 2012, doi: 10.1146/annurev-micro-092611-150104.

[24] A. Sydow, T. Krieg, F. Mayer, J. Schrader, and D. Holtmann, "Electroactive bacteria—molecular mechanisms and genetic tools," Appl. Microbiol. Biotechnol., vol. 98, no. 20, pp. 8481–8495, Oct. 2014, doi: 10.1007/s00253-014-6005-z.

[25] H. J. Kim, H. S. Park, M. S. Hyun, I. S. Chang, M. Kim, and B. H. Kim, "A mediator-less microbial fuel cell using a metal reducing bacterium, Shewanella putrefaciens," Enzyme Microb. Technol., vol. 30, no. 2, Art. no. 2, Feb. 2002, doi: 10.1016/S0141-0229(01)00478-1.

[26] D. R. Bond and D. R. Lovley, "Electricity Production by Geobacter sulfurreducens Attached to Electrodes," Appl. Environ. Microbiol., vol. 69, no. 3, Art. no. 3, Mar. 2003, doi: 10.1128/AEM.69.3.1548-1555.2003.

[27] N. S. Malvankar, S. E. Yalcin, M. T. Tuominen, and D. R. Lovley, "Visualization of charge propagation along individual pili proteins using ambient electrostatic force microscopy," Nat. Nanotechnol., vol. 9, no. 12, Art. no. 12, Dec. 2014, doi: 10.1038/nnano.2014.236.

[28] M. L. Fultz and R. A. Durst, "Mediator compounds for the electrochemical study of biological redox systems: a compilation," Anal. Chim. Acta, vol. 140, no. 1, Art. no. 1, Aug. 1982, doi: 10.1016/S0003-2670(01)95447-9.

[29] L. E. P. Dietrich, A. Price-Whelan, A. Petersen, M. Whiteley, and D. K. Newman, "The phenazine pyocyanin is a terminal signalling factor in the quorum sensing network of Pseudomonas aeruginosa," Mol. Microbiol., vol. 61, no. 5, Art. no. 5, Sep. 2006, doi: 10.1111/j.1365-2958.2006.05306.x.

[30] K. Rabaey, N. Boon, S. D. Siciliano, M. Verhaege, and W. Verstraete, "Biofuel Cells Select for Microbial Consortia That Self-Mediate Electron Transfer," Appl. Environ. Microbiol., vol. 70, no. 9, Art. no. 9, Sep. 2004, doi: 10.1128/AEM.70.9.5373-5382.2004.

[31] C. I. Torres, A. K. Marcus, H.-S. Lee, P. Parameswaran, R. Krajmalnik-Brown, and B. E. Rittmann, "A kinetic perspective on extracellular electron transfer by anode-respiring bacteria," FEMS Microbiol. Rev., vol. 34, no. 1, Art. no. 1, Jan. 2010, doi: 10.1111/j.1574-6976.2009.00191.x.

[32] R. M. Donlan, "Biofilms: Microbial Life on Surfaces," Emerg. Infect. Dis., vol. 8, no. 9, Art. no. 9, Sep. 2002, doi: 10.3201/eid0809.020063.

[33] M. E. Davey and G. A. O'toole, "Microbial Biofilms: from Ecology to Molecular Genetics," Microbiol. Mol. Biol. Rev., vol. 64, no. 4, Art. no. 4, Dec. 2000, doi: 10.1128/MMBR.64.4.847-867.2000.

[34] P. Stoodley, K. Sauer, D. G. Davies, and J. W. Costerton, "Biofilms as Complex Differentiated Communities," Annu. Rev. Microbiol., vol. 56, no. 1, Art. no. 1, Oct. 2002, doi: 10.1146/annurev.micro.56.012302.160705.

[35] D. Monroe, "Looking for Chinks in the Armor of Bacterial Biofilms," PLoS Biol., vol. 5, no. 11, Art. no. 11, Nov. 2007, doi: 10.1371/journal.pbio.0050307.

[36] K. Guo, A. Prévoteau, S. A. Patil, and K. Rabaey, "Engineering electrodes for microbial electrocatalysis," Curr. Opin. Biotechnol., vol. 33, pp. 149–156, Jun. 2015, doi: 10.1016/j.copbio.2015.02.014.

[37] K. A. Soni, A. K. Balasubramanian, A. Beskok, and S. D. Pillai, "Zeta Potential of Selected Bacteria in Drinking Water When Dead, Starved, or Exposed to Minimal and Rich Culture Media," Curr. Microbiol., vol. 56, no. 1, Art. no. 1, Jan. 2008, doi: 10.1007/s00284-007-9046-z.

[38] A. Terada, K. Okuyama, M. Nishikawa, S. Tsuneda, and M. Hosomi, "The effect of surface charge property on Escherichia coli initial adhesion and subsequent biofilm formation," Biotechnol. Bioeng., vol. 109, no. 7, Art. no. 7, Jul. 2012, doi: 10.1002/bit.24429.

[39] T. R. Scheuerman, A. K. Camper, and M. A. Hamilton, "Effects of Substratum Topography on Bacterial Adhesion," J. Colloid Interface Sci., vol. 208, no. 1, Art. no. 1, Dec. 1998, doi: 10.1006/jcis.1998.5717.

[40] K. Bazaka, R. J. Crawford, and E. P. Ivanova, "Do bacteria differentiate between degrees of nanoscale surface roughness?," Biotechnol. J., vol. 6, no. 9, Art. no. 9, Sep. 2011, doi: 10.1002/biot.201100027.

[41] V. K. Truong et al., "Effect of ultrafine-grained titanium surfaces on adhesion of bacteria," Appl. Microbiol. Biotechnol., vol. 83, no. 5, Art. no. 5, Jul. 2009, doi: 10.1007/s00253-009-1944-5.

[42] L. D. Renner and D. B. Weibel, "Physicochemical regulation of biofilm formation," MRS Bull., vol. 36, no. 5, Art. no. 5, May 2011, doi: 10.1557/mrs.2011.65.

[43] B. Bian et al., "3D printed porous carbon anode for enhanced power generation in microbial fuel cell," Nano Energy, vol. 44, pp. 174–180, Feb. 2018, doi: 10.1016/j.nanoen.2017.11.070.

[44] M. C. Potter, "Electrical effects accompanying the decomposition of organic compounds," Proc. R. Soc. Lond. Ser. B Contain. Pap. Biol. Character, vol. 84, no. 571, Art. no. 571, Sep. 1911, doi: 10.1098/rspb.1911.0073.

[45] B. Cohen, "The bacterial culture as an electrical half-cell," J Bacteriol, vol. 21, no. 1, pp. 18–19, 1931.

[46] G. H. Rohrback, W. R. Scott, and J. H. Canfield, "Biochemical fuel cells.," presented at the In Proceedings of the 16th Annual Power Sources Conference, Atlantic City, NJ, USA, 1962.

[47] G. M. Delaney, H. P. Bennetto, J. R. Mason, S. D. Roller, J. L. Stirling, and C. F. Thurston, "Electron-transfer coupling in microbial fuel cells. 2. performance of fuel cells containing selected microorganism-mediator-substrate combinations," J. Chem. Technol. Biotechnol. Biotechnol., vol. 34, no. 1, Art. no. 1, Apr. 2008, doi: 10.1002/jctb.280340104.

[48] D. R. Bond, D. E. Holmes, L. M. Tender, and D. R. Lovley, "Electrode-Reducing Microorganisms That Harvest Energy from Marine Sediments," Sci. New Ser., vol. 295, no. 5554, Art. no. 5554, 2002.

[49] H. Liu and B. E. Logan, "Electricity Generation Using an Air-Cathode Single Chamber Microbial Fuel Cell in the Presence and Absence of a Proton Exchange Membrane," Environ. Sci. Technol., vol. 38, no. 14, Art. no. 14, Jul. 2004, doi: 10.1021/es0499344.

[50] B. Logan, S. Cheng, V. Watson, and G. Estadt, "Graphite Fiber Brush Anodes for Increased Power Production in Air-Cathode Microbial Fuel Cells," Environ. Sci. Technol., vol. 41, no. 9, Art. no. 9, May 2007, doi: 10.1021/es062644y.

[51] L. M. Tender et al., "The first demonstration of a microbial fuel cell as a viable power supply: Powering a meteorological buoy," J. Power Sources, vol. 179, no. 2, Art. no. 2, May 2008, doi: 10.1016/j.jpowsour.2007.12.123.

[52] Q. Liao, J. Chang, C. Herrmann, and A. Xia, Eds., Bioreactors for Microbial Biomass and Energy Conversion. in Green Energy and Technology. Singapore: Springer Singapore, 2018. doi: 10.1007/978-981-10-7677-0.

[53] A. Nawaz et al., "Microbial fuel cells: Insight into simultaneous wastewater treatment and bioelectricity generation," Process Saf. Environ. Prot., vol. 161, pp. 357–373, May 2022, doi: 10.1016/j.psep.2022.03.039.

[54] G. J. Tsekouras et al., "Microbial Fuel Cell for Wastewater Treatment as Power Plant in Smart Grids: Utopia or Reality?," Front. Energy Res., vol. 10, p. 843768, Apr. 2022, doi: 10.3389/fenrg.2022.843768.

[55] M. T. Amen, A. S. Yasin, M. I. Hegazy, M. A. H. M. Jamal, S.-T. Hong, and N. A. M. Barakat, "Rainwater-driven microbial fuel cells for power generation in remote areas," R. Soc. Open Sci., vol. 8, no. 11, p. 210996, Nov. 2021, doi: 10.1098/rsos.210996.

[56] S. Qiu, L. Wang, Y. Zhang, and Y. Yu, "Microbial Fuel Cell-Based Biosensor for Simultaneous Test of Sodium Acetate and Glucose in a Mixed Solution," Int. J. Environ. Res. Public. Health, vol. 19, no. 19, p. 12297, Sep. 2022, doi: 10.3390/ijerph191912297.

[57] G.-H. Xu, Y.-K. Wang, G.-P. Sheng, Y. Mu, and H.-Q. Yu, "An MFC-Based Online Monitoring and Alert System for Activated Sludge Process," Sci. Rep., vol. 4, no. 1, p. 6779, Oct. 2014, doi: 10.1038/srep06779.

[58] S. B. Pasupuleti, S. Srikanth, S. Venkata Mohan, and D. Pant, "Continuous mode operation of microbial fuel cell (MFC) stack with dual gas diffusion cathode design for the treatment of dark fermentation effluent," Int. J. Hydrog. Energy, vol. 40, no. 36, pp. 12424–12435, Sep. 2015, doi: 10.1016/j.ijhydene.2015.07.049.

[59] A. P. Borole, J. R. Mielenz, T. A. Vishnivetskaya, and C. Y. Hamilton, "Controlling accumulation of fermentation inhibitors in biorefinery recycle water using microbial fuel cells," Biotechnol. Biofuels, vol. 2, no. 1, p. 7, 2009, doi: 10.1186/1754-6834-2-7.

[60] G. Papaharalabos, A. Stinchcombe, I. Horsfield, C. Melhuish, J. Greenman, and I. Ieropoulos, "Autonomous Energy Harvesting and Prevention of Cell Reversal in MFC Stacks," J. Electrochem. Soc., vol. 164, no. 3, pp. H3047–H3051, 2017, doi: 10.1149/2.0081703jes.

[61] S. G. A. Flimban, T. Kim, I. M. I. Ismail, and S.-E. Oh, "Overview of Microbial Fuel Cell (MFC) Recent Advancement from Fundamentals to Applications: MFC Designs, Major Elements, and Scalability," ENGINEERING, preprint, Nov. 2018. doi: 10.20944/preprints201810.0763.v1.

[62] B. Min, S. Cheng, and B. E. Logan, "Electricity generation using membrane and salt bridge microbial fuel cells," Water Res., vol. 39, no. 9, Art. no. 9, May 2005, doi: 10.1016/j.watres.2005.02.002.

[63] G. Buitrón and C. Cervantes-Astorga, "Performance Evaluation of a Low-Cost Microbial Fuel Cell Using Municipal Wastewater," Water. Air. Soil Pollut., vol. 224, no. 3, Art. no. 3, Mar. 2013, doi: 10.1007/s11270-013-1470-z.

[64] L. Khotseng, "Fuel Cell Thermodynamics," in Thermodynamics and Energy Engineering, P. Vizureanu, Ed., IntechOpen, 2020. doi: 10.5772/intechopen.90141.

[65] B. E. Logan et al., "Microbial Fuel Cells: Methodology and Technology $^+$," Environ. Sci. Technol., vol. 40, no. 17, Art. no. 17, Sep. 2006, doi: 10.1021/es0605016.

[66] B. E. Logan, Microbial fuel cells. Hoboken, N.J.: Wiley-Interscience, 2008. Accessed: Apr. 01, 2021. [Online]. Available: http://www.dawsonera.com/depp/reader/protected/external/AbstractView/S9780470258583

[67] D. Ucar, Y. Zhang, and I. Angelidaki, "An Overview of Electron Acceptors in Microbial Fuel Cells," Front. Microbiol., vol. 8, Apr. 2017, doi: 10.3389/fmicb.2017.00643.

[68] R. K. Thauer, K. Jungermann, and K. Decker, "Energy Conservation in Chemotrophic Anaerobic Bacteria," vol. 41, p. 81, 1977.

[69] J. Larminie and A. Dicks, Fuel cell systems explained, 2nd ed. Chichester, West Sussex: J. Wiley, 2003.

[70] Md. T. Noori, M. M. Ghangrekar, C. K. Mukherjee, and B. Min, "Biofouling effects on the performance of microbial fuel cells and recent advances in biotechnological and chemical strategies for mitigation," Biotechnol. Adv., vol. 37, no. 8, p. 107420, Dec. 2019, doi: 10.1016/j.biotechadv.2019.107420.

[71] M. Sievers and Clausthaler Umwelttechnik-Institut, Machbarkeitsstudie für die Anwendung einer mikrobiellen Brennstoffzelle im Abwasser- und Abfallbereich: Abschlussbericht ; Berichtszeitraum: 16.12.2008 bis 31.08.2010. 2010. [Online]. Available: https://books.google.de/books?id=Ne2DmwEACAAJ

[72] X. Wang, S. Cheng, Y. Feng, M. D. Merrill, T. Saito, and B. E. Logan, "Use of Carbon Mesh Anodes and the Effect of Different Pretreatment Methods on Power Production in Microbial Fuel Cells," Environ. Sci. Technol., vol. 43, no. 17, pp. 6870–6874, Sep. 2009, doi: 10.1021/es900997w.

[73] D. Massazza, R. Parra, J. P. Busalmen, and H. E. Romeo, "New ceramic electrodes allow reaching the target current density in bioelectrochemical systems," Energy Environ. Sci., vol. 8, no. 9, Art. no. 9, 2015, doi: 10.1039/C5EE01498K.

[74] X. Xie et al., "Three-Dimensional Carbon Nanotube–Textile Anode for High-Performance Microbial Fuel Cells," Nano Lett., vol. 11, no. 1, Art. no. 1, Jan. 2011, doi: 10.1021/nl103905t.

[75] A. Baudler, M. Langner, C. Rohr, A. Greiner, and U. Schröder, "Metal-Polymer Hybrid Architectures as Novel Anode Platform for Microbial Electrochemical Technologies," ChemSusChem, vol. 10, no. 1, pp. 253–257, Jan. 2017, doi: 10.1002/cssc.201600814.

[76] H. I. Park et al., "Effective and Low-Cost Platinum Electrodes for Microbial Fuel Cells Deposited by Electron Beam Evaporation," Energy Fuels, vol. 21, no. 5, pp. 2984–2990, Sep. 2007, doi: 10.1021/ef070160x.

[77] X. Peng et al., "Enhanced performance and capacitance behavior of anode by rolling Fe3O4 into activated carbon in microbial fuel cells," Bioresour. Technol., vol. 121, pp. 450–453, Oct. 2012, doi: 10.1016/j.biortech.2012.06.021.

[78] Y. Fan, S. Xu, R. Schaller, J. Jiao, F. Chaplen, and H. Liu, "Nanoparticle decorated anodes for enhanced current generation in microbial electrochemical cells," Biosens. Bioelectron., vol. 26, no. 5, pp. 1908–1912, Jan. 2011, doi: 10.1016/j.bios.2010.05.006.

[79] A. Baudler, I. Schmidt, M. Langner, A. Greiner, and U. Schröder, "Does it have to be carbon? Metal anodes in microbial fuel cells and related bioelectrochemical systems," Energy Environ. Sci., vol. 8, no. 7, pp. 2048–2055, 2015, doi: 10.1039/C5EE00866B.

[80] S. F. Ketep, A. Bergel, A. Calmet, and B. Erable, "Stainless steel foam increases the current produced by microbial bioanodes in bioelectrochemical systems," Energy Env. Sci, vol. 7, no. 5, pp. 1633–1637, 2014, doi: 10.1039/C3EE44114H.

[81] R. D. Cusick et al., "Performance of a pilot-scale continuous flow microbial electrolysis cell fed winery wastewater," Appl. Microbiol. Biotechnol., vol. 89, no. 6, pp. 2053–2063, Mar. 2011, doi: 10.1007/s00253-011-3130-9.

[82] E. Kipf, R. Zengerle, J. Gescher, and S. Kerzenmacher, "How Does the Choice of Anode Material Influence Electrical Performance? A Comparison of Two Microbial Fuel Cell Model Organisms," ChemElectroChem, vol. 1, no. 11, pp. 1849–1853, Nov. 2014, doi: 10.1002/celc.201402036.

[83] T. Shimoyama, S. Komukai, A. Yamazawa, Y. Ueno, B. E. Logan, and K. Watanabe, "Electricity generation from model organic wastewater in a cassette-electrode microbial fuel cell," Appl. Microbiol. Biotechnol., vol. 80, no. 2, p. 325, Aug. 2008, doi: 10.1007/s00253-008-1516-0.

[84] S. You et al., "A graphite-granule membrane-less tubular air-cathode microbial fuel cell for power generation under continuously operational conditions," J. Power Sources, vol. 173, no. 1, pp. 172–177, Nov. 2007, doi: 10.1016/j.jpowsour.2007.07.063.

[85] B. Zhang, H. Zhao, S. Zhou, C. Shi, C. Wang, and J. Ni, "A novel UASB–MFC–BAF integrated system for high strength molasses wastewater treatment and bioelectricity generation," Bioresour. Technol., vol. 100, no. 23, pp. 5687–5693, Dec. 2009, doi: 10.1016/j.biortech.2009.06.045.

[86] R. K. Brown et al., "Evaluating the effects of scaling up on the performance of bioelectrochemical systems using a technical scale microbial electrolysis cell," Bioresour. Technol., vol. 163, pp. 206–213, Jul. 2014, doi: 10.1016/j.biortech.2014.04.044.

[87] S. Chen et al., "Layered corrugated electrode macrostructures boost microbial bioelectrocatalysis," Energy Environ. Sci., vol. 5, no. 12, p. 9769, 2012, doi: 10.1039/c2ee23344d.

[88] V. Lanas and B. E. Logan, "Evaluation of multi-brush anode systems in microbial fuel cells," Bioresour. Technol., vol. 148, pp. 379–385, Nov. 2013, doi: 10.1016/j.biortech.2013.08.154.

[89] B. Min, J. Kim, S. Oh, J. M. Regan, and B. E. Logan, "Electricity generation from swine wastewater using microbial fuel cells," Water Res., vol. 39, no. 20, pp. 4961–4968, Dec. 2005, doi: 10.1016/j.watres.2005.09.039.

[90] E. Blanchet, E. Desmond, B. Erable, A. Bridier, T. Bouchez, and A. Bergel, "Comparison of synthetic medium and wastewater used as dilution medium to design scalable microbial anodes: Application to food waste treatment," Bioresour. Technol., vol. 185, pp. 106–115, Jun. 2015, doi: 10.1016/j.biortech.2015.02.097.

[91] D. Pocaznoi, A. Calmet, L. Etcheverry, B. Erable, and A. Bergel, "Stainless steel is a promising electrode material for anodes of microbial fuel cells," Energy Environ. Sci., vol. 5, no. 11, p. 9645, 2012, doi: 10.1039/c2ee22429a.

[92] S. Chen et al., "Electrospun and solution blown three-dimensional carbon fiber nonwovens for application as electrodes in microbial fuel cells," Energy Environ. Sci., vol. 4, no. 4, p. 1417, 2011, doi: 10.1039/c0ee00446d.

[93] H. Liu, S. Cheng, and B. E. Logan, "Power Generation in Fed-Batch Microbial Fuel Cells as a Function of Ionic Strength, Temperature, and Reactor Configuration," Environ. Sci. Technol., vol. 39, no. 14, pp. 5488–5493, Jul. 2005, doi: 10.1021/es050316c.

[94] J. Kim, S. Jung, J. Regan, and B. Logan, "Electricity generation and microbial community analysis of alcohol powered microbial fuel cells," Bioresour. Technol., vol. 98, no. 13, pp. 2568–2577, Sep. 2007, doi: 10.1016/j.biortech.2006.09.036.

[95] M. Zhou, M. Chi, J. Luo, H. He, and T. Jin, "An overview of electrode materials in microbial fuel cells," J. Power Sources, vol. 196, no. 10, pp. 4427–4435, May 2011, doi: 10.1016/j.jpowsour.2011.01.012.

[96] M. Lu, Y. Qian, L. Huang, X. Xie, and W. Huang, "Improving the Performance of Microbial Fuel Cells through Anode Manipulation," ChemPlusChem, vol. 80, no. 8, Art. no. 8, Aug. 2015, doi: 10.1002/cplu.201500200.

[97] Lu Z.-K., Fu Y.-B., Xu Q., Liu Y.-Y., and Zhang Y.-L., "Application of Modified Foam Graphite Anode with Low Potential in Marine Benthic Microbial Fuel Cell: Application of Modified Foam Graphite Anode with Low Potential in Marine Benthic Microbial Fuel Cell," J. Inorg. Mater., vol. 28, no. 3, Art. no. 3, Jun. 2013, doi: 10.3724/SP.J.1077.2013.12245.

[98] J. Liu, J. Liu, W. He, Y. Qu, N. Ren, and Y. Feng, "Enhanced electricity generation for microbial fuel cell by using electrochemical oxidation to modify carbon cloth anode," J. Power Sources, vol. 265, pp. 391–396, Nov. 2014, doi: 10.1016/j.jpowsour.2014.04.005.

[99] S. Cheng and B. E. Logan, "Ammonia treatment of carbon cloth anodes to enhance power generation of microbial fuel cells," Electrochem. Commun., vol. 9, no. 3, Art. no. 3, Mar. 2007, doi: 10.1016/j.elecom.2006.10.023.

[100] Y. Zhang et al., "A graphene modified anode to improve the performance of microbial fuel cells," J. Power Sources, vol. 196, no. 13, Art. no. 13, Jul. 2011, doi: 10.1016/j.jpowsour.2011.02.067.

[101] J. Liu, Y. Qiao, C. X. Guo, S. Lim, H. Song, and C. M. Li, "Graphene/carbon cloth anode for high-performance mediatorless microbial fuel cells," Bioresour. Technol., vol. 114, pp. 275–280, Jun. 2012, doi: 10.1016/j.biortech.2012.02.116.

[102] Y. Qiao, X.-S. Wu, C.-X. Ma, H. He, and C. M. Li, "A hierarchical porous graphene/nickel anode that simultaneously boosts the bio- and electro-catalysis for high-performance microbial fuel cells," RSC Adv, vol. 4, no. 42, pp. 21788–21793, 2014, doi: 10.1039/C4RA03082F.

[103] H. Zhu et al., "Lightweight, conductive hollow fibers from nature as sustainable electrode materials for microbial energy harvesting," Nano Energy, vol. 10, pp. 268–276, Nov. 2014, doi: 10.1016/j.nanoen.2014.08.014.

[104] A. Revil and P. W. J. Glover, "Theory of ionic-surface electrical conduction in porous media," Phys. Rev. B, vol. 55, no. 3, pp. 1757–1773, Jan. 1997, doi: 10.1103/PhysRevB.55.1757.

[105] W. Chen and H. J. H. Brouwers, "A method for predicting the alkali concentrations in pore solution of hydrated slag cement paste," J. Mater. Sci., vol. 46, no. 10, pp. 3622–3631, May 2011, doi: 10.1007/s10853-011-5278-1.

[106] P. Gao, "Simulation of hydration and microstructure development of blended cements," Delft University of Technology, 2018. doi: 10.4233/UUID:5BB2F97B-55F7-4AFA-B6F4-F18F16543273.

[107] R. S. Waremra and P. Betaubun, "Analysis of Electrical Properties Using the four point Probe Method," E3S Web Conf., vol. 73, p. 13019, 2018, doi: 10.1051/e3sconf/20187313019.

[108] Prachurya Bharadwaj, "Van der Pauw Resisitivity Measurement," 2017, doi: 10.13140/RG.2.2.23468.67208.

[109] S. Huber, M. Wicinski, and A. W. Hassel, "Suitability of Various Materials for Probes in Scanning Kelvin Probe Measurements," Phys. Status Solidi A, vol. 215, no. 15, p. 1700952, Aug. 2018, doi: 10.1002/pssa.201700952.

[110] Z. Bekzhanova, S. A. Memon, and J. R. Kim, "Self-Sensing Cementitious Composites: Review and Perspective," Nanomaterials, vol. 11, no. 9, p. 2355, Sep. 2021, doi: 10.3390/nano11092355.

[111] S. R. Broadbent and J. M. Hammersley, "Percolation processes: I. Crystals and mazes," Math. Proc. Camb. Philos. Soc., vol. 53, no. 3, pp. 629–641, Jul. 1957, doi: 10.1017/S0305004100032680.

[112] K. Malarz and S. Galam, "Square-lattice site percolation at increasing ranges of neighbor bonds," Phys. Rev. E, vol. 71, no. 1, Art. no. 1, Jan. 2005, doi: 10.1103/PhysRevE.71.016125.

[113] D. Stauffer and A. Aharony, Introduction To Percolation Theory: Second Edition. CRC Press, 2018. [Online]. Available: https://books.google.de/books?id=E0ZZDwAAQBAJ

[114] P. J. Brigandi, J. M. Cogen, and R. A. Pearson, "Electrically conductive multiphase polymer blend carbon-based composites," Polym. Eng. Sci., vol. 54, no. 1, pp. 1–16, Jan. 2014, doi: 10.1002/pen.23530.

[115] J. L. Jacobsen, "High-precision percolation thresholds and Potts-model critical manifolds from graph polynomials," ArXiv14017847 Cond-Mat Physicsmath-Ph, Jul. 2015, Accessed: Apr. 02, 2021. [Online]. Available: http://arxiv.org/abs/1401.7847

[116] Y. Deng and H. W. J. Blöte, "Monte Carlo study of the site-percolation model in two and three dimensions," Phys. Rev. E, vol. 72, no. 1, p. 016126, Jul. 2005, doi: 10.1103/PhysRevE.72.016126.

[117] H. Kesten, Percolation theory for mathematicians. in Progress in probability and statistics, no. v. 2. Boston: Birkhäuser, 1982.

[118] C. D. Lorenz and R. M. Ziff, "Precise determination of the bond percolation thresholds and finite-size scaling corrections for the s.c., f.c.c., and b.c.c. lattices," Phys. Rev. E, vol. 57, no. 1, pp. 230–236, Jan. 1998, doi: 10.1103/PhysRevE.57.230.

[119] P. Grassberger, "Critical percolation in high dimensions," Phys. Rev. E, vol. 67, no. 3, p. 036101, Mar. 2003, doi: 10.1103/PhysRevE.67.036101.

[120] Y. Sun, H.-D. Bao, Z.-X. Guo, and J. Yu, "Modeling of the Electrical Percolation of Mixed Carbon Fillers in Polymer-Based Composites," Macromolecules, vol. 42, no. 1, pp. 459–463, Jan. 2009, doi: 10.1021/ma8023188.

[121] W. Xu and Y. Jiao, "Theoretical framework for percolation threshold, tortuosity and transport properties of porous materials containing 3D non-spherical pores," Int. J. Eng. Sci., vol. 134, pp. 31–46, Jan. 2019, doi: 10.1016/j.ijengsci.2018.10.004.

[122] X. Jing, W. Zhao, and L. Lan, "The effect of particle size on electric conducting percolation threshold in polymer/conducting particle composites," p. 3.

[123] M. H. Polley and B. B. S. T. Boonstra, "Carbon Blacks for Highly Conductive Rubber," Rubber Chem. Technol., vol. 30, no. 1, Art. no. 1, Mar. 1957, doi: 10.5254/1.3542660.

[124] W. Heisenberg, "Über den anschaulichen Inhalt der quantentheoretischen Kinematik und Mechanik," Z. Für Phys., vol. 43, no. 3, pp. 172–198, Mar. 1927, doi: 10.1007/BF01397280.

[125] L. Mandelstam and Ig. Tamm, "The Uncertainty Relation Between Energy and Time in Non-relativistic Quantum Mechanics," in Selected Papers, B. M. Bolotovskii, V. Ya. Frenkel, and R. Peierls, Eds., Berlin, Heidelberg: Springer Berlin Heidelberg, 1991, pp. 115–123. doi: 10.1007/978-3-642-74626-0_8.

[126] A. I. Medalia, "Electrical Conduction in Carbon Black Composites," Rubber Chem. Technol., vol. 59, no. 3, pp. 432–454, Jul. 1986, doi: 10.5254/1.3538209.

[127] L. K. H. Van Beek and B. I. C. F. Van Pul, "Non-ohmic behavior of carbon black-loaded rubbers," Carbon, vol. 2, no. 2, pp. 121–126, Oct. 1964, doi: 10.1016/0008-6223(64)90051-X.

[128] E. K. Sichel, J. I. Gittleman, and P. Sheng, "Transport properties of the composite material carbon-poly(vinyl chloride)," Phys. Rev. B, vol. 18, no. 10, pp. 5712–5716, Nov. 1978, doi: 10.1103/PhysRevB.18.5712.

[129] R. D. Sherman, L. M. Middleman, and S. M. Jacobs, "Electron transport processes in conductor-filled polymers," Polym. Eng. Sci., vol. 23, no. 1, pp. 36–46, Jan. 1983, doi: 10.1002/pen.760230109.

[130] I. Balberg, "Tunneling and nonuniversal conductivity in composite materials," Phys. Rev. Lett., vol. 59, no. 12, pp. 1305–1308, Sep. 1987, doi: 10.1103/PhysRevLett.59.1305.

[131] D. S. McLachlan, M. Blaszkiewicz, and R. E. Newnham, "Electrical Resistivity of Composites," J. Am. Ceram. Soc., vol. 73, no. 8, pp. 2187–2203, Aug. 1990, doi: 10.1111/j.1151-2916.1990.tb07576.x.

[132] N. F. Mott, "Electrons in disordered structures," Adv. Phys., vol. 16, no. 61, pp. 49–144, Jan. 1967, doi: 10.1080/00018736700101265.

[133] I. Sahalianov and O. Lazarenko, "Enhancement of electroconductivity and percolation threshold by the morphology of dielectric network in segregated polymer/nanocarbon composites," Mater. Res. Express, vol. 6, no. 9, p. 095019, Jul. 2019, doi: 10.1088/2053-1591/ab2d5a.

[134] L. Wang and F. Aslani, "A review on material design, performance, and practical application of electrically conductive cementitious composites," Constr. Build. Mater., vol. 229, p. 116892, Dec. 2019, doi: 10.1016/j.conbuildmat.2019.116892.

[135] Y.-X. Pan, Z.-Z. Yu, Y.-C. Ou, and G.-H. Hu, "A new process of fabricating electrically conducting nylon 6/graphite nanocomposites via intercalation polymerization," p. 8.

[136] I. Krupa, I. Novák, and I. Chodák, "Electrically and thermally conductive polyethylene/graphite composites and their mechanical properties," Synth. Met., vol. 145, no. 2–3, pp. 245–252, Sep. 2004, doi: 10.1016/j.synthmet.2004.05.007.

[137] M. Sun, Z. Li, Q. Mao, and D. Shen, "Study on the Hole Conduction Phenomenon in Carbon Fiber-Reinforced Concrete," Cem. Concr. Res., vol. 28, no. 4, pp. 549–554, Apr. 1998, doi: 10.1016/S0008-8846(98)00011-8.

[138] D. Frattini, G. Accardo, C. Ferone, and R. Cioffi, "Fabrication and characterization of graphite-cement composites for microbial fuel cells applications," Mater. Res. Bull., vol. 88, pp. 188–199, Apr. 2017, doi: 10.1016/j.materresbull.2016.12.037.

[139] M. Frąc and W. Pichór, "Piezoresistive properties of cement composites with expanded graphite," Compos. Commun., vol. 19, pp. 99–102, Jun. 2020, doi: 10.1016/j.coco.2020.03.005.

[140] J. Davidovits, "PROPERTIES OF GEOPOLYMER CEMENTS," p. 19, 1994.

[141] S. Hanjitsuwan, S. Hunpratub, P. Thongbai, S. Maensiri, V. Sata, and P. Chindaprasirt, "Effects of NaOH concentrations on physical and electrical properties of high calcium fly ash geopolymer paste," Cem. Concr. Compos., vol. 45, pp. 9–14, Jan. 2014, doi: 10.1016/j.cemconcomp.2013.09.012.

[142] S. Hanjitsuwan, P. Chindaprasirt, and K. Pimraksa, "Electrical conductivity and dielectric property of fly ash geopolymer pastes," Int. J. Miner. Metall. Mater., vol. 18, no. 1, pp. 94–99, Feb. 2011, doi: 10.1007/s12613-011-0406-0.

[143] C. Mizerová, I. Kusák, and P. Rovnaník, "ELECTRICAL PROPERTIES OF FLY ASH GEOPOLYMER COMPOSITES WITH GRAPHITE CONDUCTIVE ADMIXTURES," Acta Polytech. CTU Proc., vol. 22, pp. 72–76, Jul. 2019, doi: 10.14311/APP.2019.22.0072.

[144] P. Rovnaník, I. Kusák, P. Bayer, P. Schmid, and L. Fiala, "Electrical and Self-Sensing Properties of Alkali-Activated Slag Composite with Graphite Filler," Materials, vol. 12, no. 10, p. 1616, May 2019, doi: 10.3390/ma12101616.

[145] J. C. Maxwell, "A Treatise on Electricity and Magnetism," Nature, vol. 7, no. 182, pp. 478–480, Apr. 1873, doi: 10.1038/007478a0.

[146] Lord Rayleigh, "LVI. On the influence of obstacles arranged in rectangular order upon the properties of a medium," Lond. Edinb. Dublin Philos. Mag. J. Sci., vol. 34, no. 211, pp. 481–502, Dec. 1892, doi: 10.1080/14786449208620364.

[147] A. Einstein, "Eine neue Bestimmung der Moleküldimensionen," Ann. Phys., vol. 324, no. 2, pp. 289–306, 1906, doi: 10.1002/andp.19063240204.

[148] T. Zhang and Y. B. Yi, "Monte Carlo simulations of effective electrical conductivity in short-fiber composites," J. Appl. Phys., vol. 103, no. 1, p. 014910, Jan. 2008, doi: 10.1063/1.2828180.

[149] M. Weber and M. R. Kamal, "Estimation of the volume resistivity of electrically conductive composites," Polym. Compos., vol. 18, no. 6, pp. 711–725, Dec. 1997, doi: 10.1002/pc.10324.

[150] Y. Dai, M. Sun, C. Liu, and Z. Li, "Electromagnetic wave absorbing characteristics of carbon black cement-based composites," Cem. Concr. Compos., vol. 32, no. 7, pp. 508–513, Aug. 2010, doi: 10.1016/j.cemconcomp.2010.03.009.

[151] J. Wu, J. Liu, and F. Yang, "Three-phase composite conductive concrete for pavement deicing," Constr. Build. Mater., vol. 75, pp. 129–135, Jan. 2015, doi: 10.1016/j.conbuildmat.2014.11.004.

[152] G. E. Archie, "The Electrical Resistivity Log as an Aid in Determining Some Reservoir Characteristics," Trans. AIME, vol. 146, no. 01, pp. 54–62, Dec. 1942, doi: 10.2118/942054-G.

[153] P. W. J. Glover, M. J. Hole, and J. Pous, "A modified Archie's law for two conducting phases," Earth Planet. Sci. Lett., p. 15.

[154] S. Kirkpatrick, "Percolation and Conduction," Rev. Mod. Phys., vol. 45, no. 4, pp. 574–588, Oct. 1973, doi: 10.1103/RevModPhys.45.574.

[155] M. Sumita, S. Asai, N. Miyadera, E. Jojima, and K. Miyasaka, "Electrical conductivity of carbon black filled ethylene-vinyl acetate copolymer as a function of vinyl acetate content," Colloid Polym. Sci., vol. 264, no. 3, pp. 212–217, Mar. 1986, doi: 10.1007/BF01414955.

[156] S. K. Bhattacharya, Metal Filled Polymers. in Plastics Engineering. Taylor & Francis, 1986. [Online]. Available: https://books.google.de/books?id=AJs5qRjJv0cC

[157] T. Słupkowski, "Electrical conductivity of mixtures of conducting and insulating particles," Phys. Status Solidi A, vol. 83, no. 1, pp. 329–333, May 1984, doi: 10.1002/pssa.2210830137.

[158] C. Rajagopal and M. Satyam, "Studies on electrical conductivity of insulator-conductor composites," J. Appl. Phys., vol. 49, no. 11, pp. 5536–5542, Nov. 1978, doi: 10.1063/1.324474.

[159] A. Malliaris and D. T. Turner, "Influence of Particle Size on the Electrical Resistivity of Compacted Mixtures of Polymeric and Metallic Powders," J. Appl. Phys., vol. 42, no. 2, pp. 614–618, Feb. 1971, doi: 10.1063/1.1660071.

[160] S. K. Bhattacharya and A. C. D. Chaklader, "Review on Metal-Filled Plastics. Part1. Electrical Conductivity," Polym.-Plast. Technol. Eng., vol. 19, no. 1, pp. 21–51, Jan. 1982, doi: 10.1080/03602558208067726.

[161] R. L. McCullough, "Generalized Combining Rules for Predicting Transport Properties of Composite Materials," p. 19.

[162] L. E. Nielsen, "The Thermal and Electrical Conductivity of Two-Phase Systems," Ind. Eng. Chem. Fundam., vol. 13, no. 1, pp. 17–20, Feb. 1974, doi: 10.1021/i160049a004.

[163] Z. Hashin and S. Shtrikman, "A variational approach to the theory of the elastic behaviour of multiphase materials," J. Mech. Phys. Solids, vol. 11, no. 2, pp. 127–140, Mar. 1963, doi: 10.1016/0022-5096(63)90060-7.

[164] H. S. Waff, "Theoretical considerations of electrical conductivity in a partially molten mantle and implications for geothermometry," J. Geophys. Res., vol. 79, no. 26, pp. 4003–4010, Sep. 1974, doi: 10.1029/JB079i026p04003.

[165] F. R. Schilling et al., "Partial Melting in the Central Andean Crust: a Review of Geophysical, Petrophysical, and Petrologic Evidence," in The Andes, O. Oncken, G. Chong, G. Franz, P. Giese, H.-J. Götze, V. A. Ramos, M. R. Strecker, and P. Wigger, Eds., in Frontiers in Earth Sciences. Springer Berlin Heidelberg, 2006, pp. 459–474. doi: 10.1007/978-3-540-48684-8_22.

[166] J. C. Maxwell, A Treatise on Electricity and Magnetism, no. Bd. 1. in A Treatise on Electricity and Magnetism. Clarendon Press, 1873. [Online]. Available: https://books.google.de/books?id=92QSAAAAIAAJ

[167] D. A. G. Bruggeman, "Berechnung verschiedener physikalischer Konstanten von heterogenen Substanzen. I. Dielektrizitätskonstanten und Leitfähigkeiten der Mischkörper aus isotropen Substanzen," Ann. Phys., vol. 416, no. 7, pp. 636–664, 1935, doi: 10.1002/andp.19354160705.

[168] D. A. G. Bruggeman, "Berechnung verschiedener physikalischer Konstanten von heterogenen Substanzen. II. Dielektrizitätskonstanten und Leitfähigkeiten von Vielkristallen der nichtregulären Systeme," Ann. Phys., vol. 417, no. 7, pp. 645–672, 1936, doi: 10.1002/andp.19364170706.

[169] D. A. G. Bruggeman, "Berechnung verschiedener physikalischer Konstanten von heterogenen Substanzen. III. Die elastischen Konstanten der quasiisotropen Mischkörper aus isotropen Substanzen," Ann. Phys., vol. 421, no. 2, pp. 160–178, 1937, doi: 10.1002/andp.19374210205.

[170] D. S. McLachlan, "An equation for the conductivity of binary mixtures with anisotropic grain structures," J. Phys. C Solid State Phys., vol. 20, no. 7, pp. 865–877, Mar. 1987, doi: 10.1088/0022-3719/20/7/004.

[171] B. Derrida, D. Stauffer, H. J. Herrmann, and J. Vannimenus, "Transfer matrix calculation of conductivity in three-dimensional random resistor networks at percolation threshold," J. Phys. Lett., vol. 44, no. 17, pp. 701–706, 1983, doi: 10.1051/jphyslet:019830044017070100.

[172] A. Boudenne, L. Ibos, Y. Candau, and S. Thomas, Handbook of Multiphase Polymer Systems. Wiley, 2011. [Online]. Available: https://books.google.de/books?id=z4c_VsH8YskC

[173] D. M. Bigg, "Thermal conductivity of heterophase polymer compositions," in Thermal and Electrical Conductivity of Polymer Materials, in Advances in Polymer Science, vol. 119. Berlin/Heidelberg: Springer-Verlag, 1995, pp. 1–30. doi: 10.1007/BFb0021279.

[174] R. Landauer, "The Electrical Resistance of Binary Metallic Mixtures," J. Appl. Phys., vol. 23, no. 7, pp. 779–784, Jul. 1952, doi: 10.1063/1.1702301.

[175] W. Cai and V. Shalaev, Optical Metamaterials. New York, NY: Springer New York, 2010. doi: 10.1007/978-1-4419-1151-3.

[176] M. Wang and N. Pan, "Predictions of effective physical properties of complex multiphase materials," Mater. Sci. Eng. R Rep., vol. 63, no. 1, pp. 1–30, Dec. 2008, doi: 10.1016/j.mser.2008.07.001.

[177] D. E. Aspnes, "Local-field effects and effective-medium theory: A microscopic perspective," Am. J. Phys., vol. 50, no. 8, pp. 704–709, Aug. 1982, doi: 10.1119/1.12734.

[178] R. Landauer, "Electrical conductivity in inhomogeneous media," in AIP Conference Proceedings, AIP, 1978, pp. 2–45. doi: 10.1063/1.31150.

[179] P. A. Maksym and T. Chakraborty, "Effect of electron-electron interactions on the magnetization of quantum dots," Phys. Rev. B, vol. 45, no. 4, pp. 1947–1950, Jan. 1992, doi: 10.1103/PhysRevB.45.1947.

[180] D. S. McLachlan, "Measurement and analysis of a model dual-conductivity medium using a generalised effective-medium theory," J. Phys. C Solid State Phys., vol. 21, no. 8, pp. 1521–1532, Mar. 1988, doi: 10.1088/0022-3719/21/8/025.

[181] F. Brouers, "Percolation threshold and conductivity in metal-insulator composite mean-field theories," J. Phys. C Solid State Phys., vol. 19, no. 36, pp. 7183–7193, Dec. 1986, doi: 10.1088/0022-3719/19/36/010.

[182] S. Zhang et al., "Conductive Geopolymers as Low-Cost Electrode Materials for Microbial Fuel Cells," ACS Omega, vol. 6, no. 43, pp. 28859–28870, Nov. 2021, doi: 10.1021/acsomega.1c03805.

[183] R. Eckhardt, "STAN ULAM, JOHN VON NEUMANN, and the MONTE CARLO METHOD," Los Alamos Sci. Spec. Issue 1987, no. 15, Art. no. 15, 1987.

[184] K. Malarz and S. Galam, "Square-lattice site percolation at increasing ranges of neighbor bonds," Phys. Rev. E, vol. 71, no. 1, p. 016125, Jan. 2005, doi: 10.1103/PhysRevE.71.016125.

[185] S. Robert, Algorithms in C.: Fundamentals, data structures, sorting, searching. Addison-Wesley, 1998.

[186] M. F. Sykes and J. W. Essam, "Critical Percolation Probabilities by Series Methods," Phys. Rev., vol. 133, no. 1A, pp. A310–A315, Jan. 1964, doi: 10.1103/PhysRev.133.A310.

[187] K. Malarz, "Simple cubic random-site percolation thresholds for neighborhoods containing fourth-nearest neighbors," Phys. Rev. E, vol. 91, no. 4, p. 043301, Apr. 2015, doi: 10.1103/PhysRevE.91.043301.

[188] W. Dalton, "Crystal statistics with long-range forces? I, The equivalent neighbour model," p. 14.

[189] N. W. Dalton, C. Domb, and M. F. Sykes, "Dependence of critical concentration of a dilute ferromagnet on the range of interaction," Proc. Phys. Soc., vol. 83, no. 3, pp. 496–498, Mar. 1964, doi: 10.1088/0370-1328/83/3/118.

[190] E. A. B. Koenders, Simulation of volume changes in hardening cement-based materials. Delft: Delft University Press, 1997.

[191] K. van Breugel, "Numerical simulation of hydration and microstructural development in hardening cement-based materials (I) theory," Cem. Concr. Res., vol. 25, no. 2, pp. 319–331, Feb. 1995, doi: 10.1016/0008-8846(95)00017-8.

[192] K. van Breugel, "NUMERICAL SIMULATION OF HYDRATION AND MICROSTRUCTURAL DEVELOPMENT IN HARDENING CEMENT-BASED MATERIALS (II) Applications," p. 9.

[193] K. van Breugel, Simulation of hydration and formation of structure in hardening cement-based materials, 2nd ed. Delft, The Netherlands: Delft University Press, 1997.

[194] K. van Breugel, "Numerical simulation of hydration and microstructural development in hardening cement-based materials (I) theory," Cem. Concr. Res., vol. 25, no. 2, Art. no. 2, Feb. 1995, doi: 10.1016/0008-8846(95)00017-8.

[195] N. Ukrainczyk and E. A. B. Koenders, "Representative elementary volumes for 3D modeling of mass transport in cementitious materials," Model. Simul. Mater. Sci. Eng., vol. 22, no. 3, p. 035001, Apr. 2014, doi: 10.1088/0965-0393/22/3/035001.

[196] G. Ye, Experimental study and numerical simulation of the development of the microstructure and permeability of cementious materials. Delft: Delft University Press, 2003.

[197] P. A. Vesilind, "The Rosin-Rammler particle size distribution," Resour. Recovery Conserv., vol. 5, no. 3, pp. 275–277, Sep. 1980, doi: 10.1016/0304-3967(80)90007-4.

[198] K. P. Nevin et al., "Anode Biofilm Transcriptomics Reveals Outer Surface Components Essential for High Density Current Production in Geobacter sulfurreducens Fuel Cells," PLoS ONE, vol. 4, no. 5, Art. no. 5, May 2009, doi: 10.1371/journal.pone.0005628.

[199] M. Stöckl, N. C. Teubner, D. Holtmann, K.-M. Mangold, and W. Sand, "Extracellular Polymeric Substances from Geobacter sulfurreducens Biofilms in Microbial Fuel Cells," ACS Appl. Mater. Interfaces, vol. 11, no. 9, Art. no. 9, Mar. 2019, doi: 10.1021/acsami.8b14340.

[200] C. Santoro, C. Arbizzani, B. Erable, and I. Ieropoulos, "Microbial fuel cells: From fundamentals to applications. A review," J. Power Sources, vol. 356, pp. 225–244, Jul. 2017, doi: 10.1016/j.jpowsour.2017.03.109.

[201] B. E. Logan, M. J. Wallack, K.-Y. Kim, W. He, Y. Feng, and P. E. Saikaly, "Assessment of Microbial Fuel Cell Configurations and Power Densities," Environ. Sci. Technol. Lett., vol. 2, no. 8, Art. no. 8, Aug. 2015, doi: 10.1021/acs.estlett.5b00180.

[202] T. Ewing, P. T. Ha, J. T. Babauta, N. T. Tang, D. Heo, and H. Beyenal, "Scale-up of sediment microbial fuel cells," J. Power Sources, vol. 272, pp. 311–319, Dec. 2014, doi: 10.1016/j.jpowsour.2014.08.070.

[203] D. B. Ringelberg, K. L. Foley, and C. M. Reynolds, "Electrogenic capacity and community composition of anodic biofilms in soil-based bioelectrochemical systems," Appl. Microbiol. Biotechnol., vol. 90, no. 5, Art. no. 5, Jun. 2011, doi: 10.1007/s00253-011-3264-9.

[204] L. Hao, B. Zhang, M. Cheng, and C. Feng, "Effects of various organic carbon sources on simultaneous V(V) reduction and bioelectricity generation in single chamber microbial fuel cells," Bioresour. Technol., vol. 201, pp. 105–110, Feb. 2016, doi: 10.1016/j.biortech.2015.11.060.

[205] A. E. Franks, K. P. Nevin, R. H. Glaven, and D. R. Lovley, "Microtoming coupled to microarray analysis to evaluate the spatial metabolic status of Geobacter sulfurreducens biofilms," ISME J., vol. 4, no. 4, Art. no. 4, Apr. 2010, doi: 10.1038/ismej.2009.137.

[206] A. E. Franks, N. Malvankar, and K. P. Nevin, "Bacterial biofilms: the powerhouse of a microbial fuel cell," Biofuels, vol. 1, no. 4, Art. no. 4, Jul. 2010, doi: 10.4155/bfs.10.25.

[207] X. Li, X. Wang, Q. Zhao, L. Wan, Y. Li, and Q. Zhou, "Carbon fiber enhanced bioelectricity generation in soil microbial fuel cells," Biosens. Bioelectron., vol. 85, pp. 135–141, Nov. 2016, doi: 10.1016/j.bios.2016.05.001.

[208] X. Li, X. Wang, Z. J. Ren, Y. Zhang, N. Li, and Q. Zhou, "Sand amendment enhances bioelectrochemical remediation of petroleum hydrocarbon contaminated soil," Chemosphere, vol. 141, pp. 62–70, Dec. 2015, doi: 10.1016/j.chemosphere.2015.06.025.

[209] S. K. Dentel, B. Strogen, and P. Chiu, "Direct generation of electricity from sludges and other liquid wastes," Water Sci. Technol., vol. 50, no. 9, pp. 161–168, Nov. 2004, doi: 10.2166/wst.2004.0561.

[210] S. W. Hong, I. S. Chang, Y. S. Choi, and T. H. Chung, "Experimental evaluation of influential factors for electricity harvesting from sediment using microbial fuel cell," Bioresour. Technol., vol. 100, no. 12, Art. no. 12, Jun. 2009, doi: 10.1016/j.biortech.2009.01.030.

[211] C. Zhou et al., "Structure design and performance comparison of large-scale marine sediment microbial fuel cells in lab and real sea as power source to drive monitoring instruments for long-term work," Ionics, vol. 24, no. 3, Art. no. 3, Mar. 2018, doi: 10.1007/s11581-017-2251-2.

Appendix

Table 18: Series of measurements performed with comments on the series of measurements, indication of the electrodes tested, indication of whether current production started, indication of the amount of *Geobacter* medium without fumarate added to the anode electrode chamber during the tests, and comments on the electrodes.

Series	Tested electrode	Electricity-production	Medium addition (mL)	Note
1	GP08_1W_10C_1	Y	50	Failure of measurement data acquisition for GP_Ref_3
	GP_Ref_3	N	-	
	PC06_3F_10C_3	N	-	
	PC_Ref_1	N	-	
2	GP_Ref_2	N	50	-
	GP08_1W_10C_2	Y	70	-
	PC06_3F_10C_2	Y	10	-
	PC_Ref_3	N	10	-
3	GP_Ref_1	N	10	-
	PC06_3F_10C_1	N	17	-
	PC06_3F_8C_1	N	10	-
	GP08_1W_8C_1	Y	25	-
4	PC06_3F_9C_1	N	-	-
	GP08_1W_8C_2	Y	47	-
	PC06_3F_8C_3	N	-	The electrode is broken during sterilization
	Graphit_1	Y	10	-
5	GP08_2W_10C_1	Y	90	-
	PC_Ref_2	N	-	-
	PC06_3F_8C_4	N	-	-
	Graphit_2	Y	-	-
6	PC06_3F_9C_2	N	-	-
	GP08_2W_10C_3	Y	80	The electrode broke during sterilization. During the weekend, the level in the anode electrode chamber dropped sharply, 60mL of medium was added on Monday. The cathode electrode chamber was leaking here 50mL medium was missing, which was added again on Monday.
	Graphit_3	Y	-	-
	PC06_3F_9C_4	N	-	The electrode is broken during sterilization
7	GP08_1W_10C_3	Y	60	-
	GP08_1W_8C_3	Y	65	-
	GP08_1W_9C_1	Y	55	-
	GP08_1W_9C_2	Y	70	-
8	GP08_2W_10C_4	Y	95	The electrode is broken during sterilization
	GP08_1W_9C_3	Y	30	
	GP08_1.2W_10C_1	Y	30	The electrode is broken during sterilization
	GP08_1.2W_10C_3	Y	35	
9	GP08_1.7W_10C_1	Y	40	The electrode is broken during sterilization
	GP08_1.2W_10C_2	Y	50	-
	GP08_1.7W_10C_2	Y	50	-
	GP08_1.7W_10C_3	Y	55	-

10	PC75_0F_8C_1	N	-	Failure of the incubation hood in the period between 47h-115h operation, the temperature drops from 30°C to about 20°C.
	PC75_0F_8C_2	N	-	
	PC75_0F_9C_1	N	-	
	PC_75_0F_9C_2	N	-	
11	PC75_0F_10C_1	N	-	-
	PC75_0F_8C_3	N	-	-
	PC75_0F_9C_3	N	-	-
	PC75_0F_10C_2	Y	-	-
	PC75_0F_10C_3	N	-	-
12	GP08_1.7W_10C_4	Y	80	During the weekend, the level in the anode electrode chamber decreased sharply, and 50 ml of medium was added on Monday.
	GP08_1.7W_10C_5	Y	85	During the weekend, the level in the anode electrode chamber decreased sharply, and 55 ml of medium was added on Monday.
	GP08_2W_10C_4	Y	50	Replacing the highly porous electrode after sterilization
13	GP08_2W_10C_5	Y	55	Failure of the incubation hood in the period between 47h-60h operation, the temperature drops from 30°C to about 25°C.
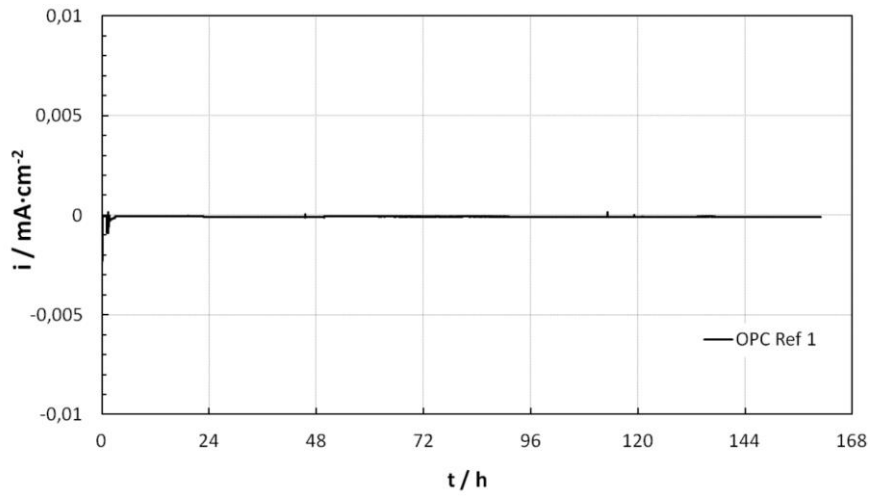
Figure 90: Current density-time curve of electrode PC Ref 1, from measurement series 1.
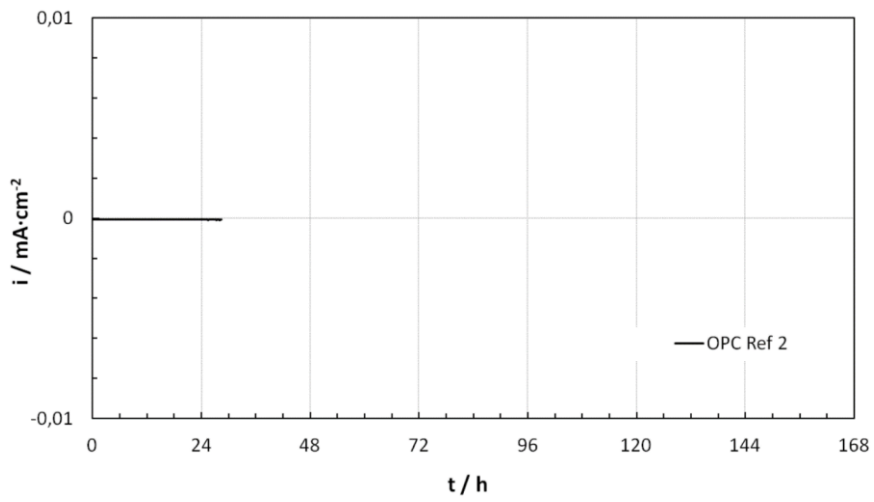
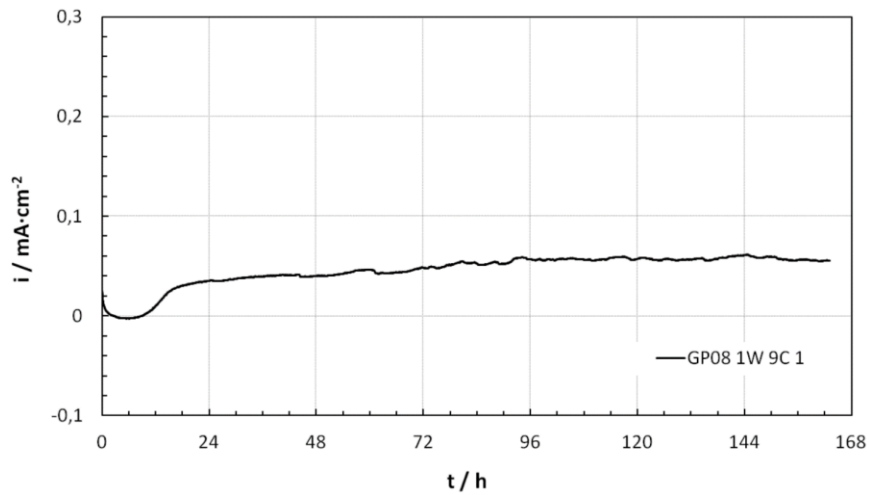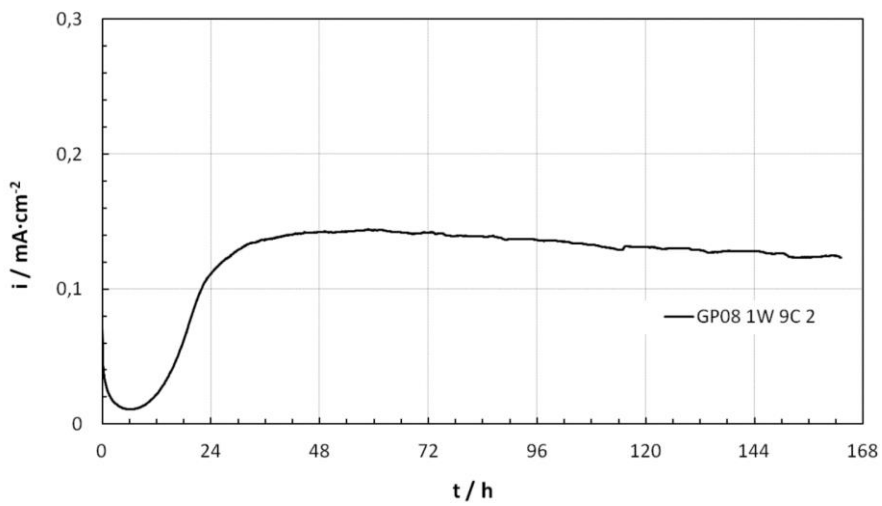**Figure 91:** Current density-time curve of electrode PC Ref 2, from measurement series 5.
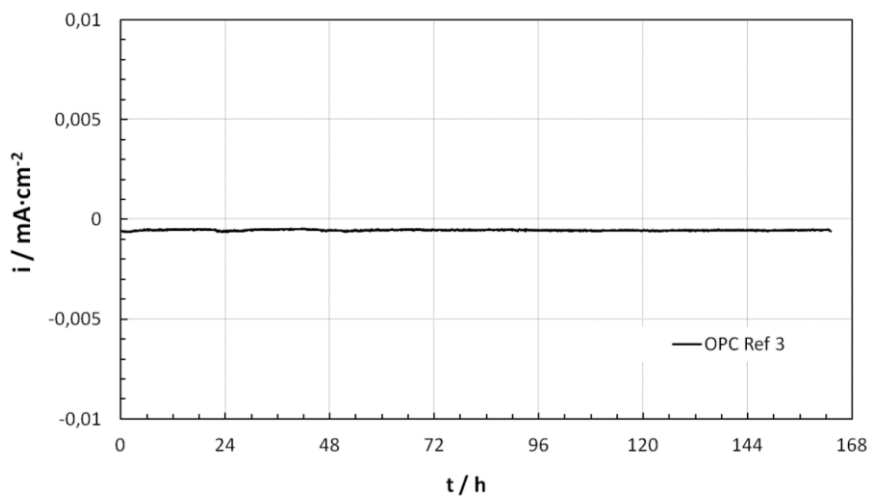
Figure 92: Current density-time curve of electrode PC Ref 3, from measurement series 2.
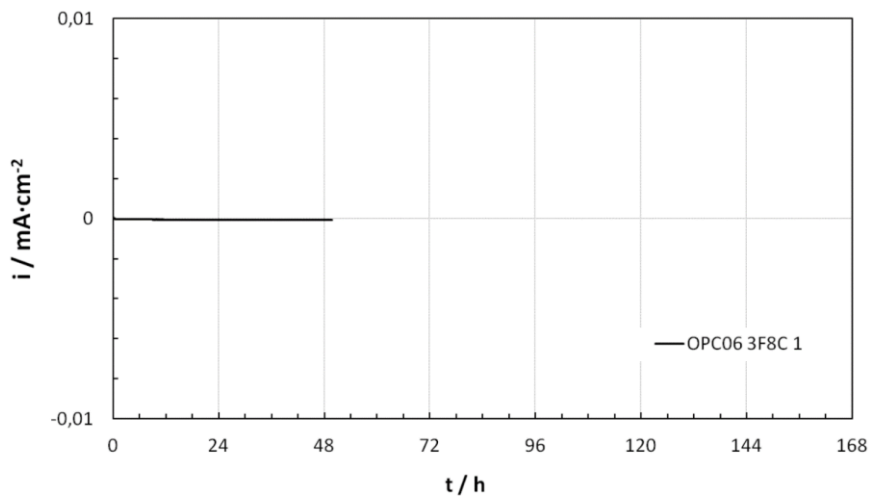
Figure 93: Current density-time curve of electrode PC06 3F 8C 1, from measurement series 3.
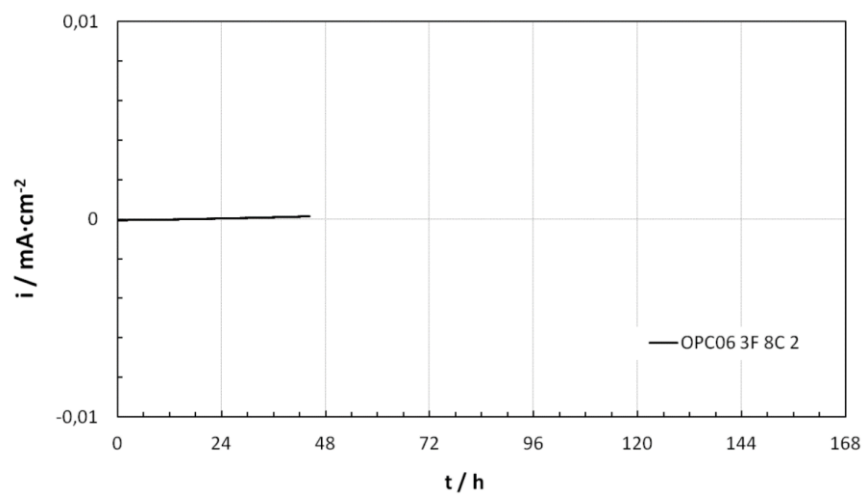
Figure 94: Current density-time curve of electrode PC06 3F 8C 2, from measurement series 4.
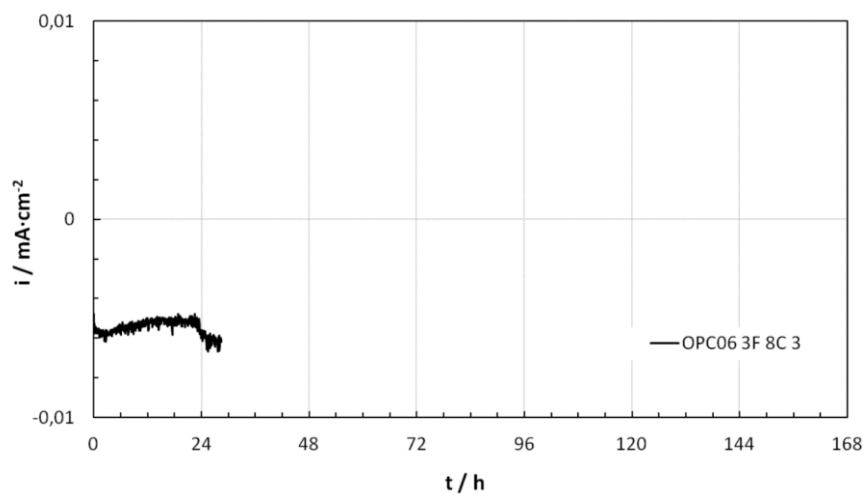
Figure 95: Current density-time curve of electrode PC06 3F 8C 3, from measurement series 5.
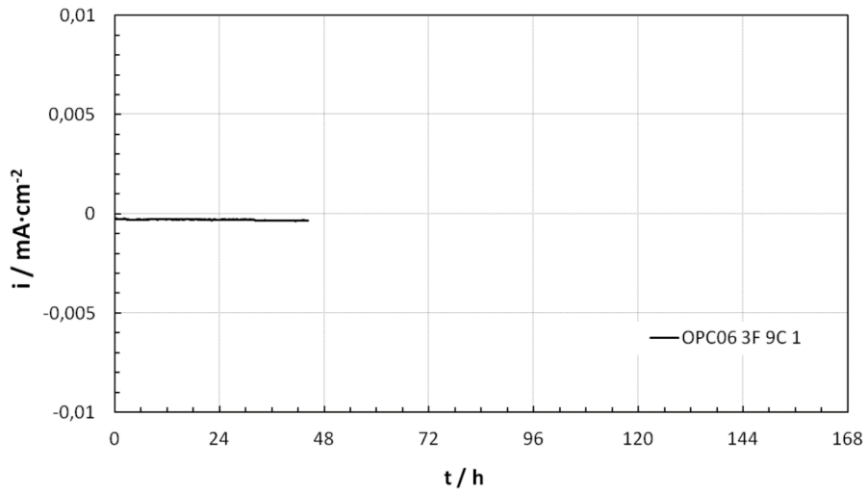
Figure 96: Current density-time curve of electrode PC06 3F 9C 1, from measurement series 4.
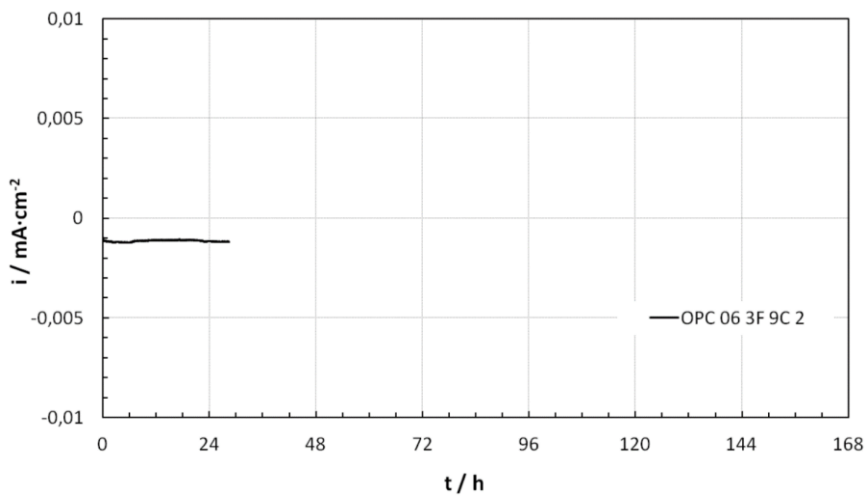
Figure 97: Current density-time curve of electrode PC06 3F 9C 2, from measurement series 6.
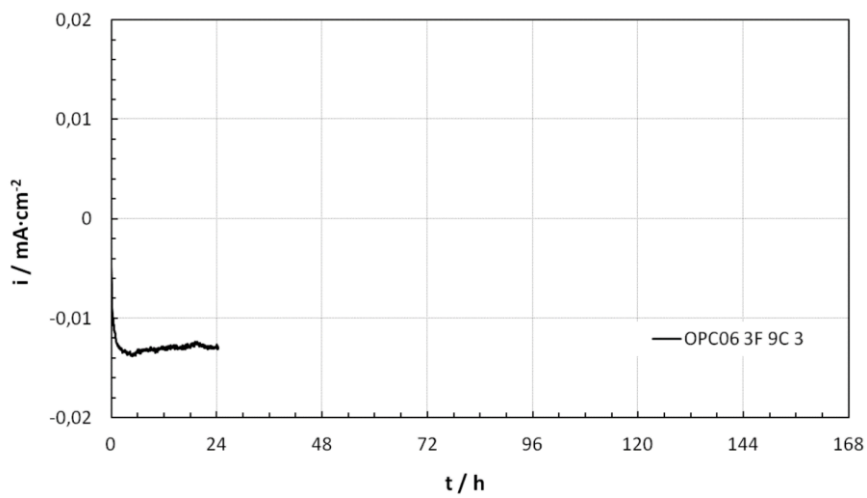
Figure 98: Current density-time curve of electrode PC06 3F 9C 3, from measurement series 7.
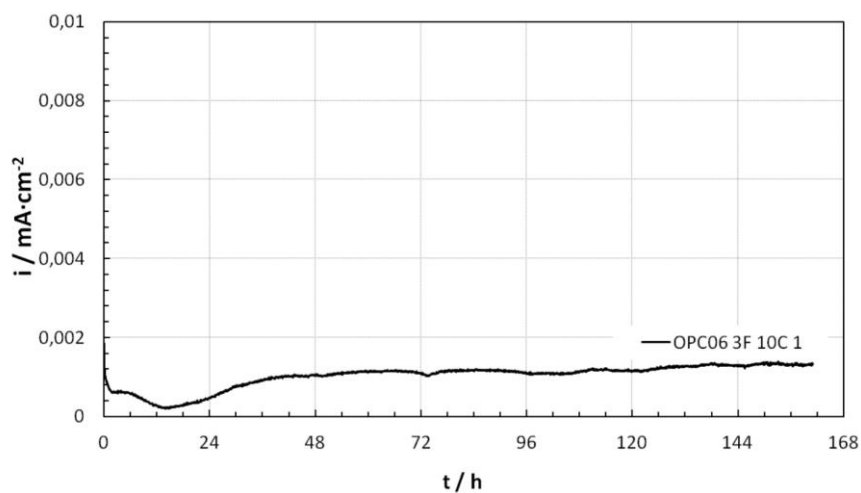
Figure 99: Current density-time curve of electrode PC06 3F 10C 1, from measurement series 3.
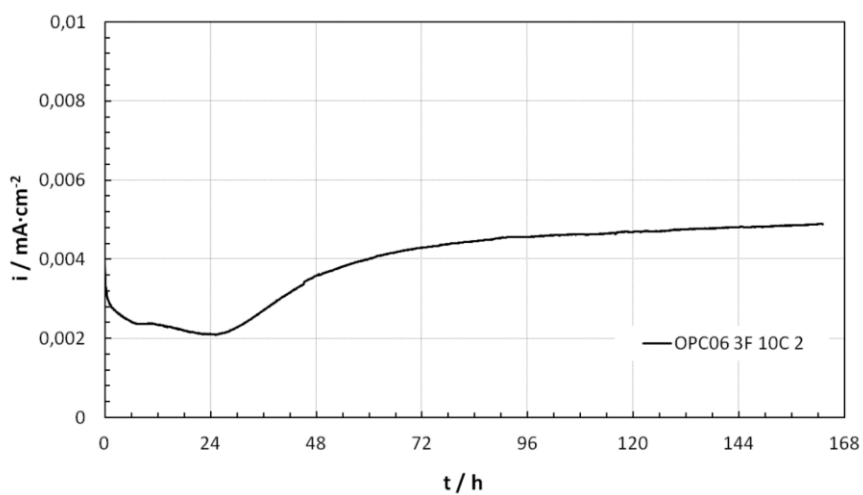
Figure 100: Current density-time curve of electrode PC06 3F 10C 2, from measurement series 2.
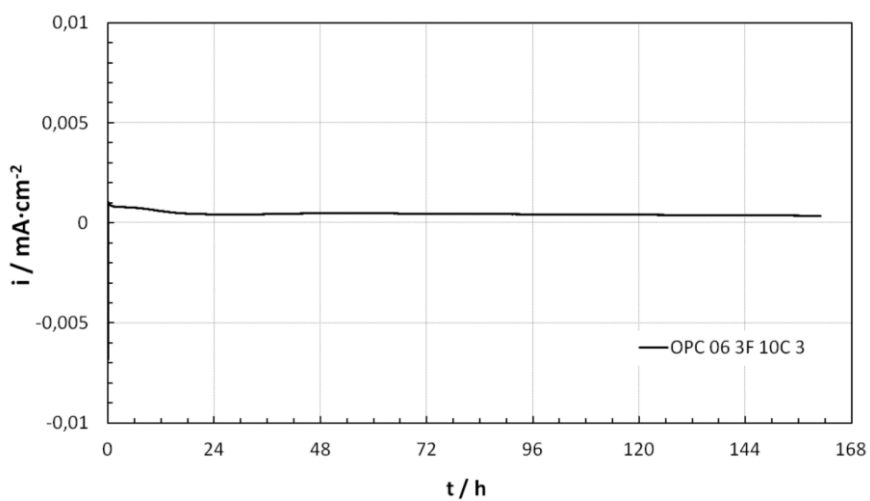
Figure 101: Current density-time curve of electrode PC06 3F 10C 3, from measurement series 1.
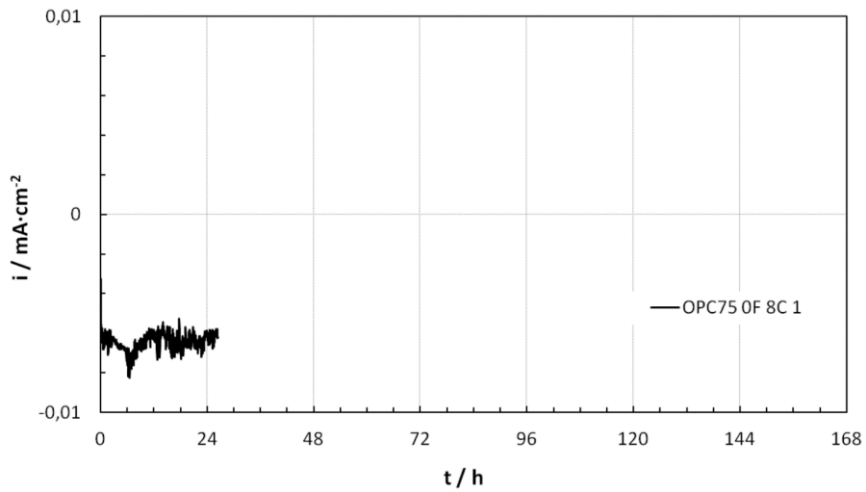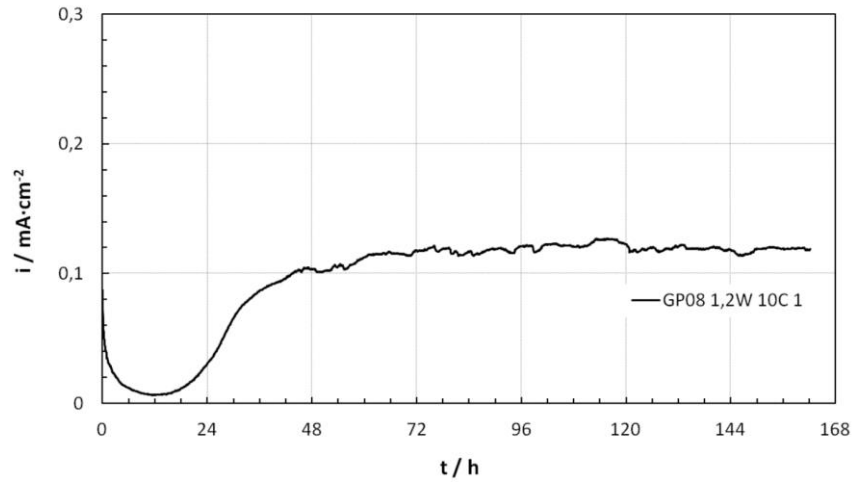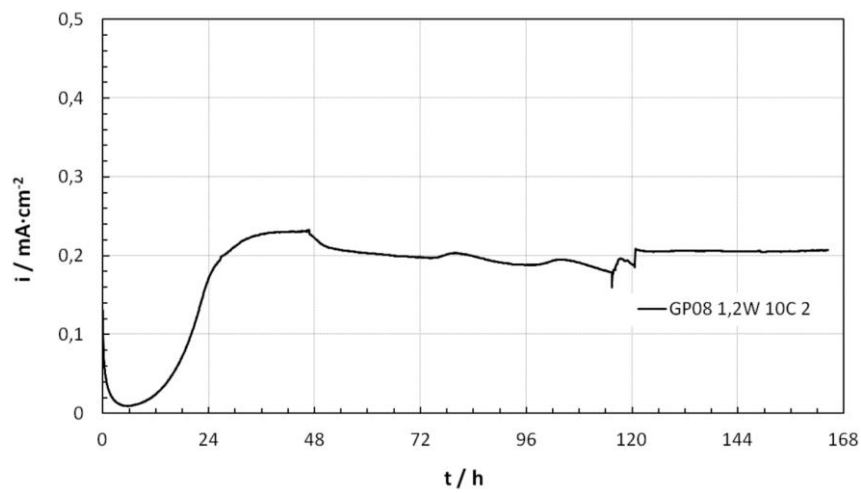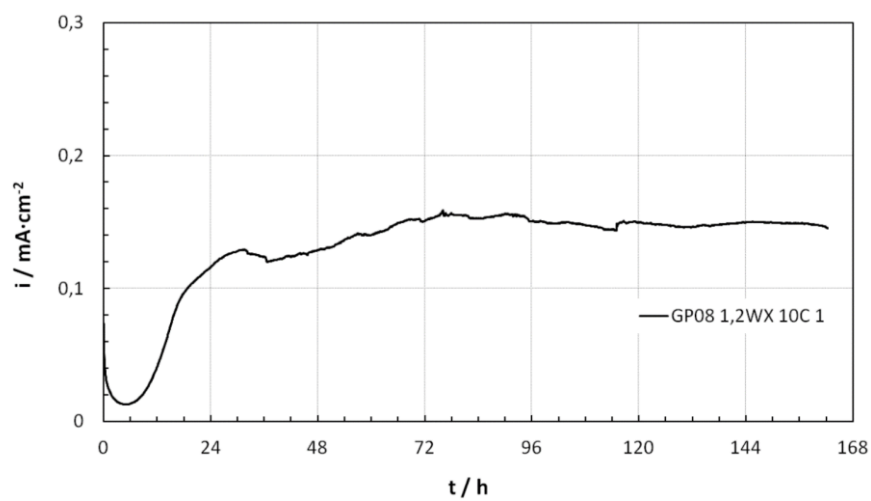
Figure 102: Current density-time curve of electrode PC75 0F 8C 1, from measurement series10.
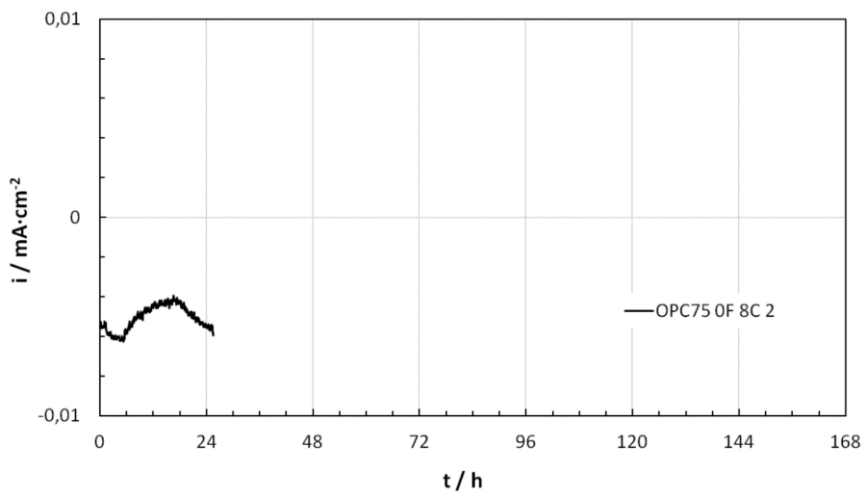
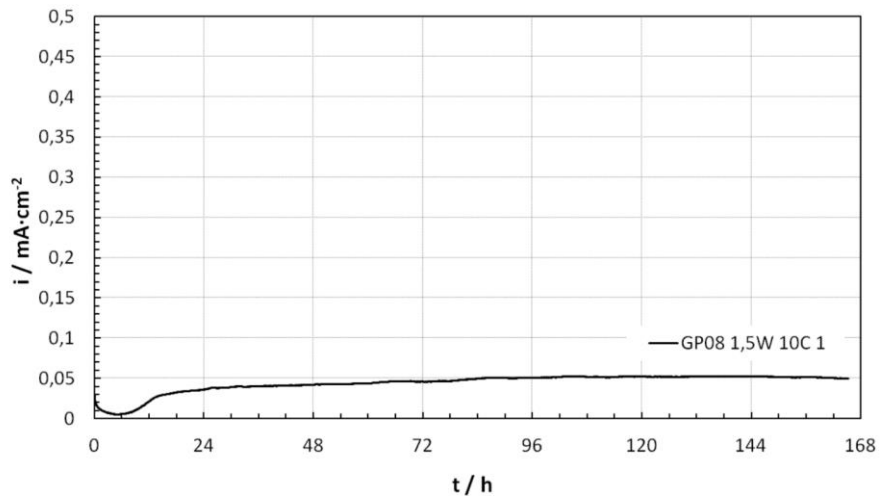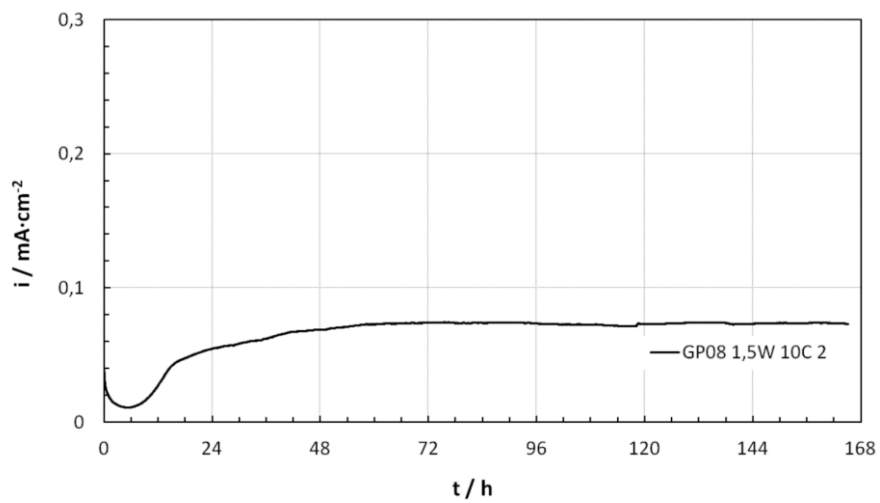**Figure 103:** Current density-time curve of electrode PC75 0F 8C 2, from measurement series 11.
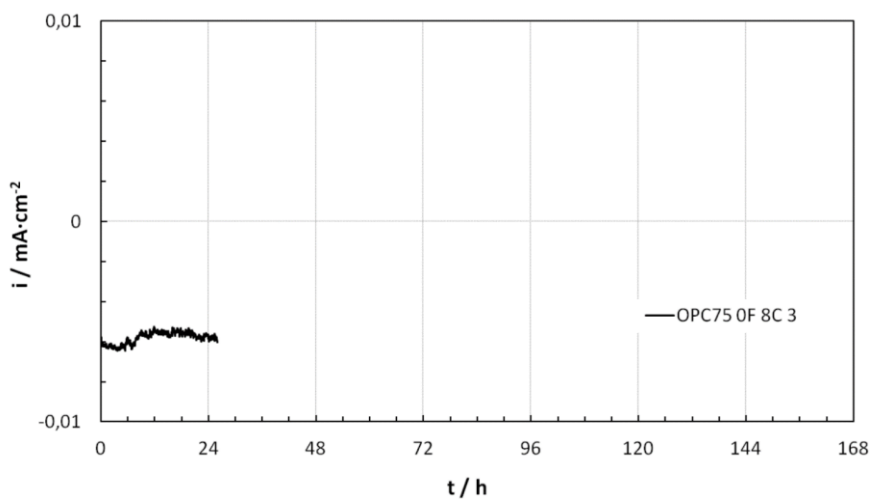
Figure 104: Current density-time curve of electrode PC75 0F 8C 3, from measurement series 12.
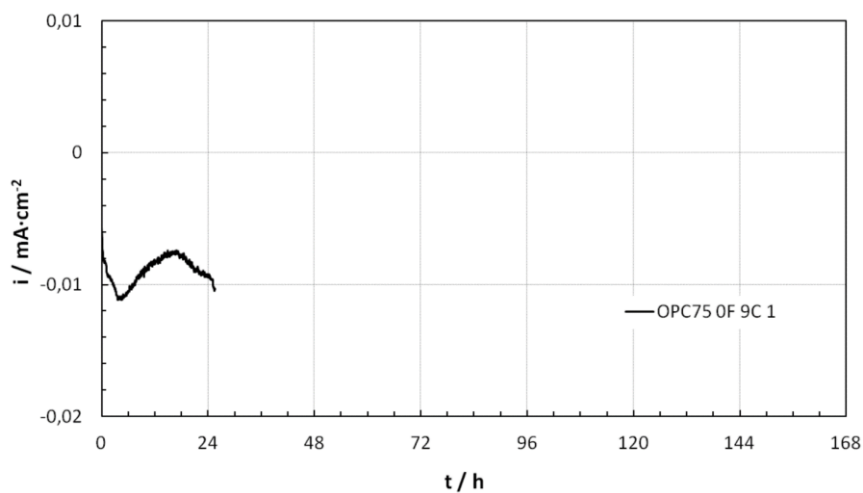
Figure 105: Current density-time curve of electrode PC75 0F 9C 1, from measurement series 11.
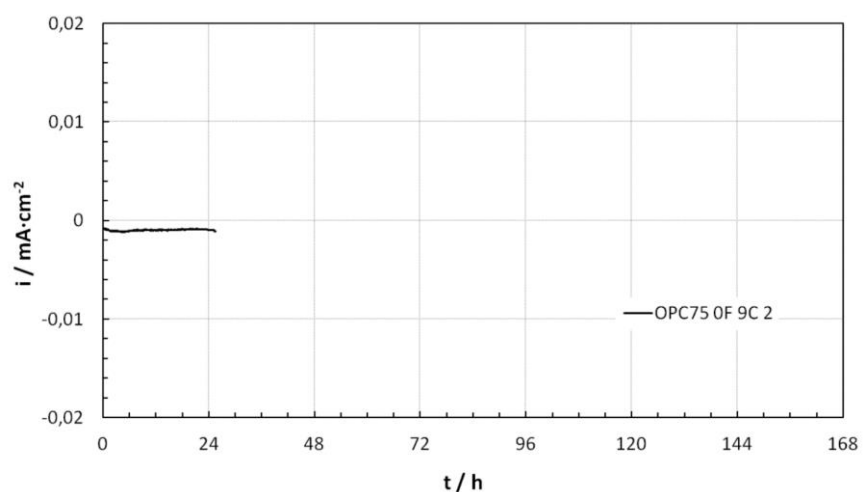
Figure 106: Current density-time curve of electrode PC75 0F 9C 2, from measurement series 11.
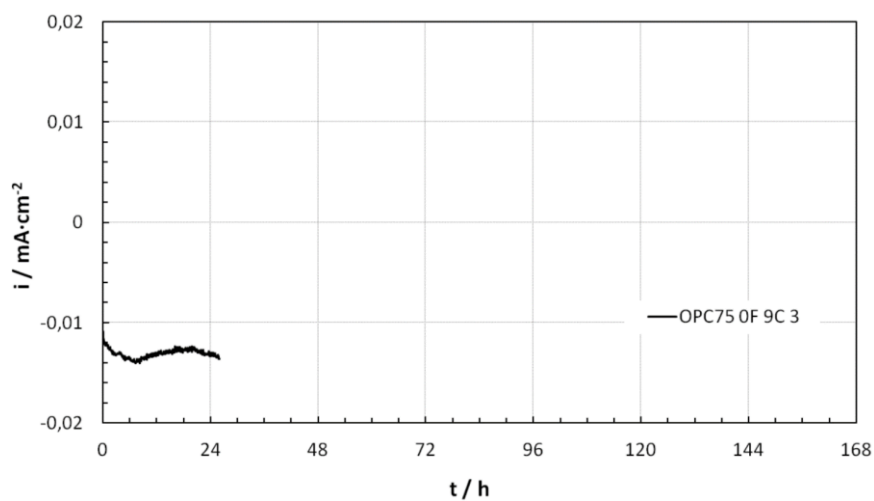
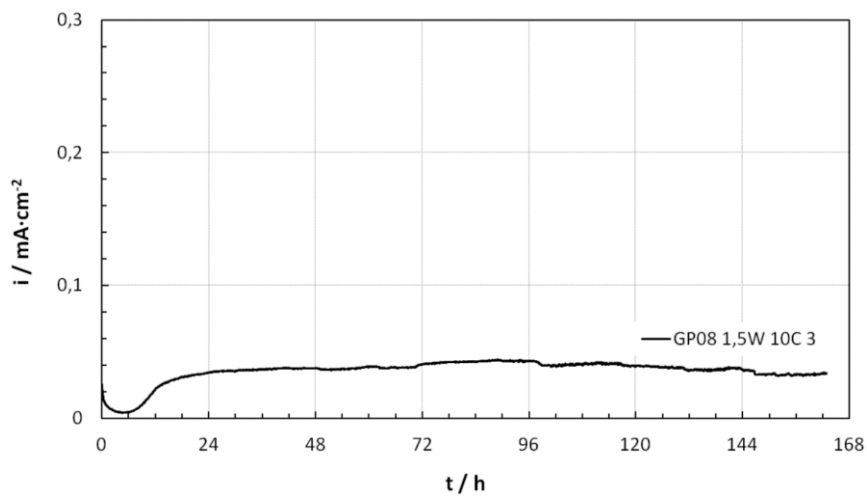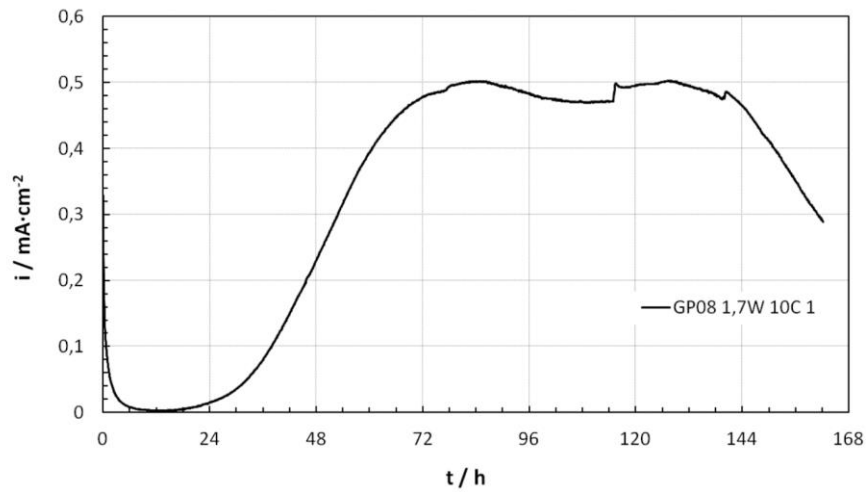**Figure 107:** Current density-time curve of electrode PC75 0F 9C 3, from measurement series 12.
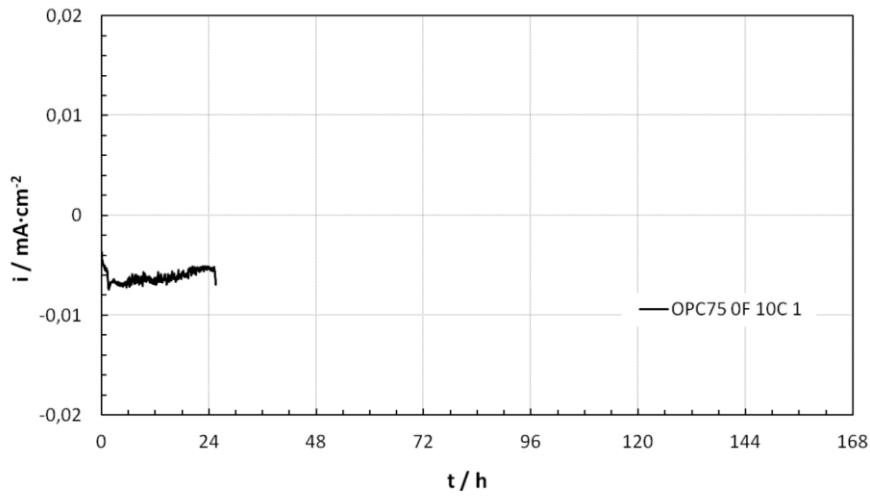
Figure 108: Current density-time curve of electrode PC75 0F 10C 1, from measurement series 11.
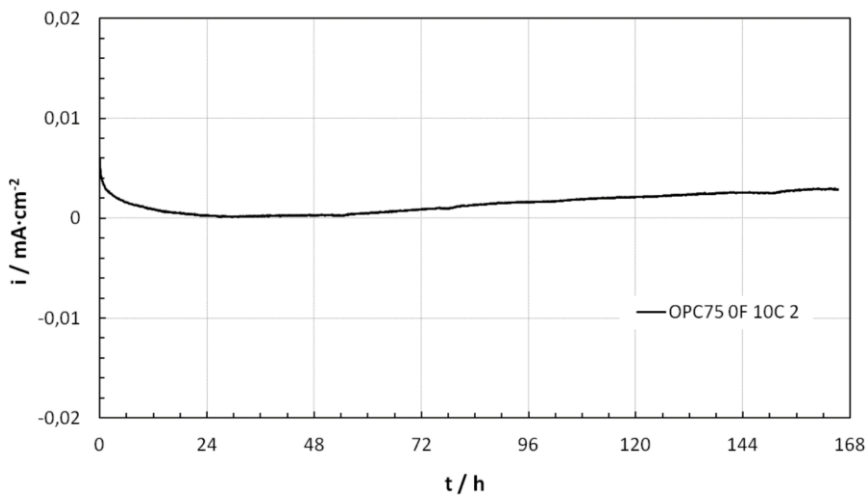
Figure 109: Current density-time curve of electrode PC75 0F 10C 2, from measurement series 12.
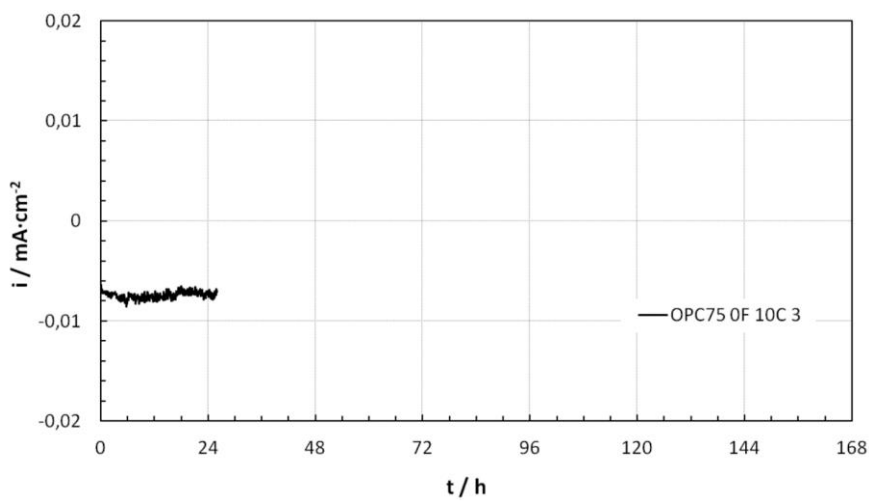
Figure 110: Current density-time curve of electrode PC75 0F 10C 3, from measurement series 12.
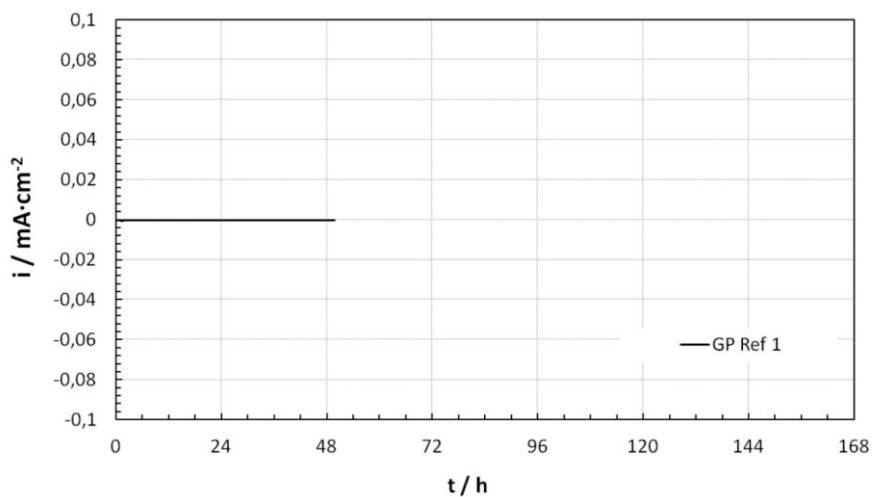
Figure 111: Current density-time curve of electrode GP Ref 1, from measurement series 3.
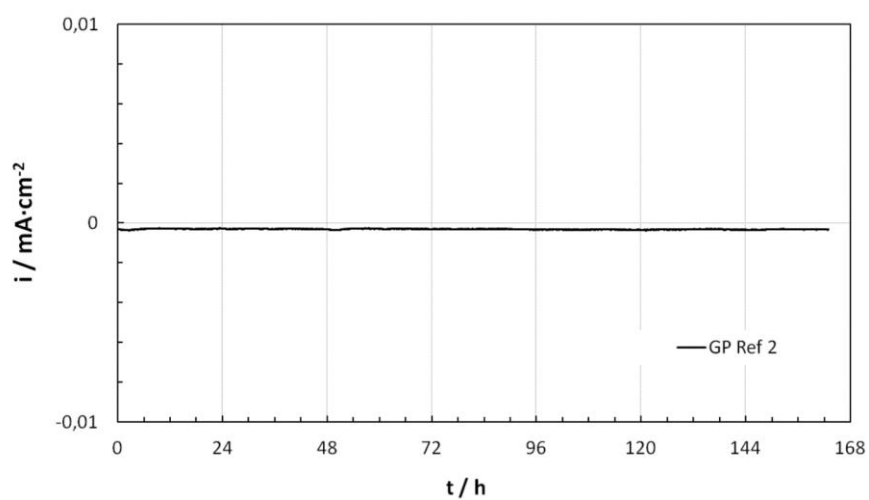
Figure 112: Current density-time curve of electrode GP Ref 2, from measurement series 2.
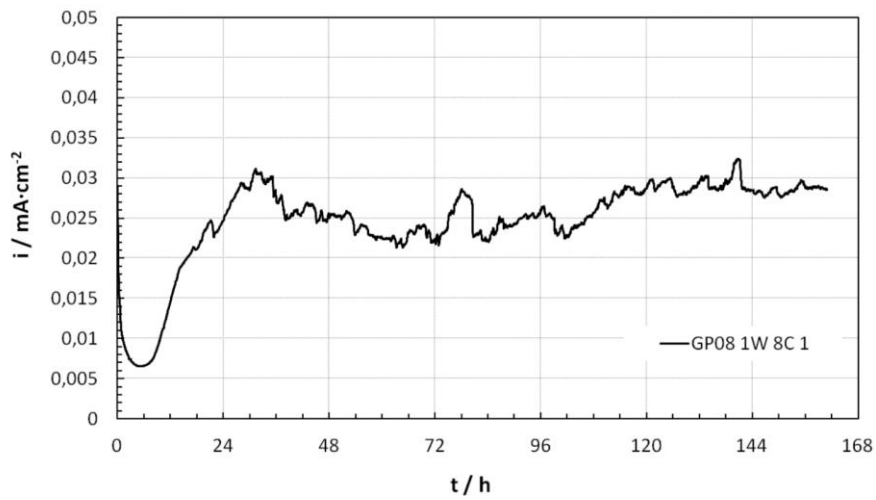
Figure 113: Current density-time curve of electrode GP08 1W 8C 1, from measurement series 3.

+
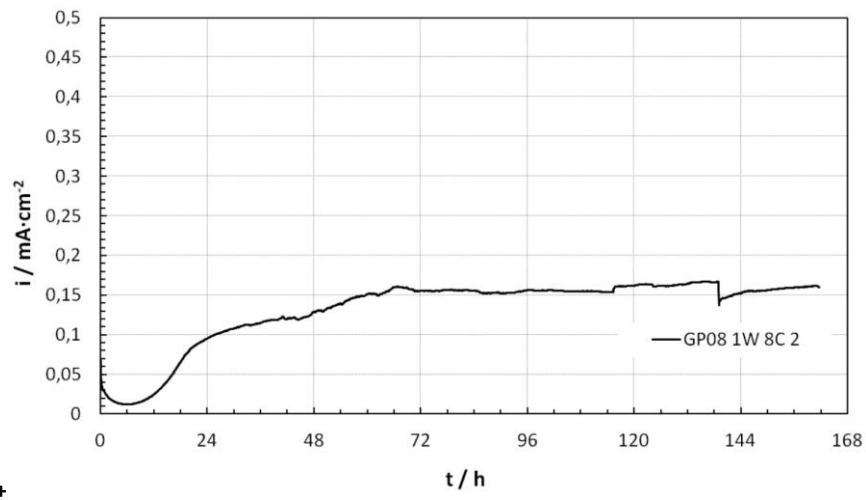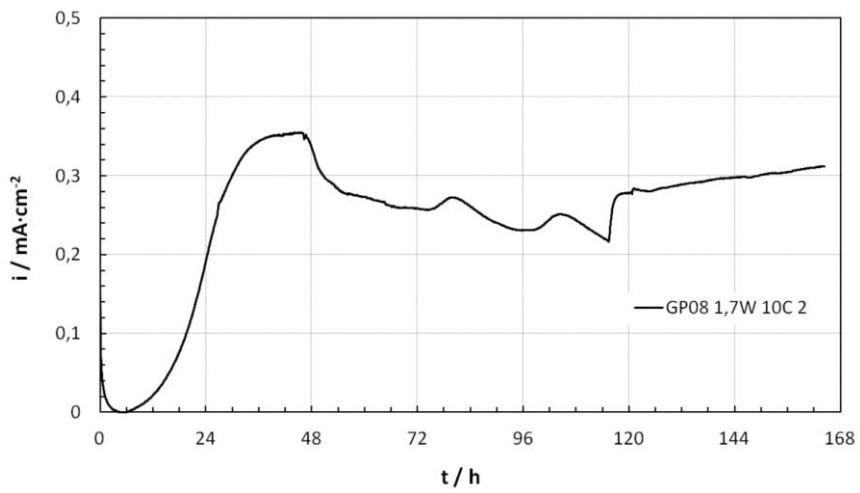
Figure 114: Current density-time curve of electrode GP08 1W 8C 2, from measurement series 4.
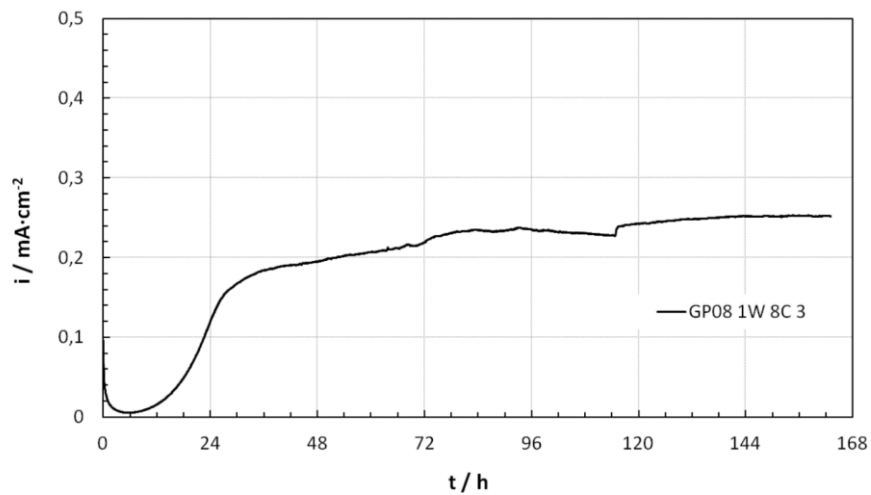
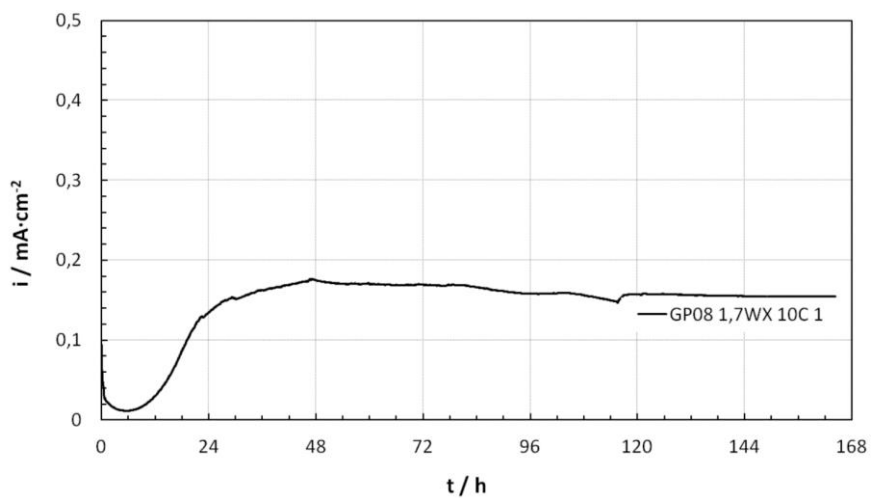

Figure 115: Current density-time curve of electrode GP08 1W 8C 3, from measurement series 8.

Figure 116: Current density-time curve of electrode GP08 1W 9C 1, from measurement series 8.

Figure 117: Stromdichte-Zeit-Kurve der Elektrode GP08 1W 9C 2, aus Messreihe 8.
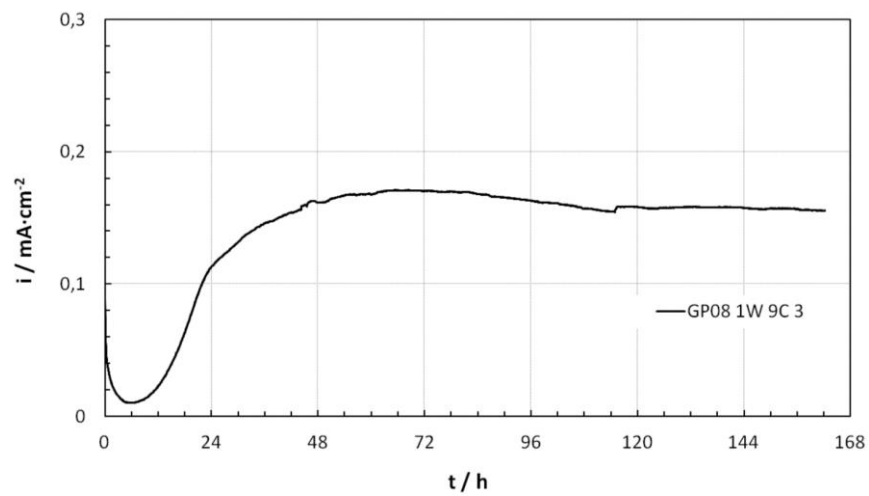
**Figure 118:** Stromdichte-Zeit-Kurve der Elektrode GP08 1W 9C 3, aus Messreihe 9.
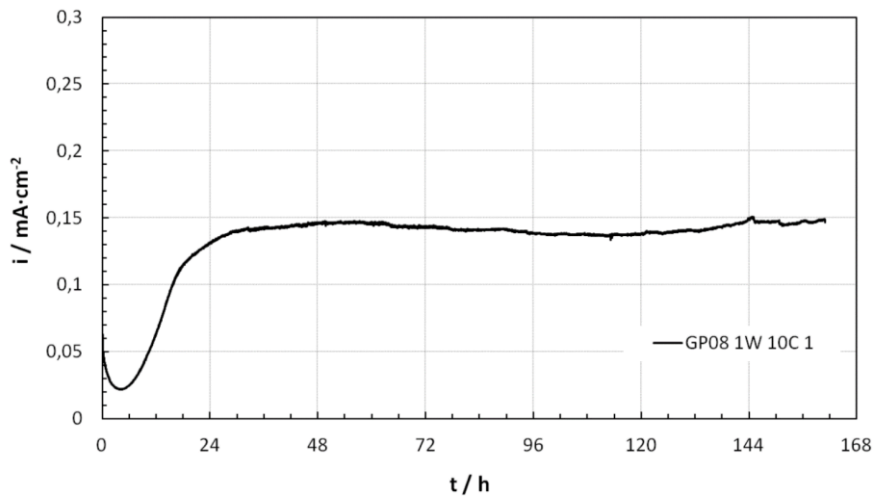
Figure 119: Current density-time curve of electrode GP08 1W 10C 1, from measurement series 1.
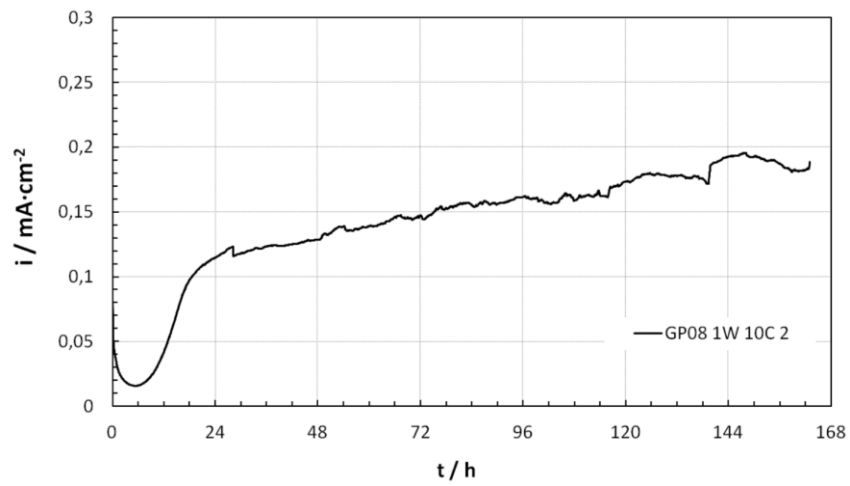
Figure 120: Current density-time curve of electrode GP08 1W 10C 2, from measurement series 2.
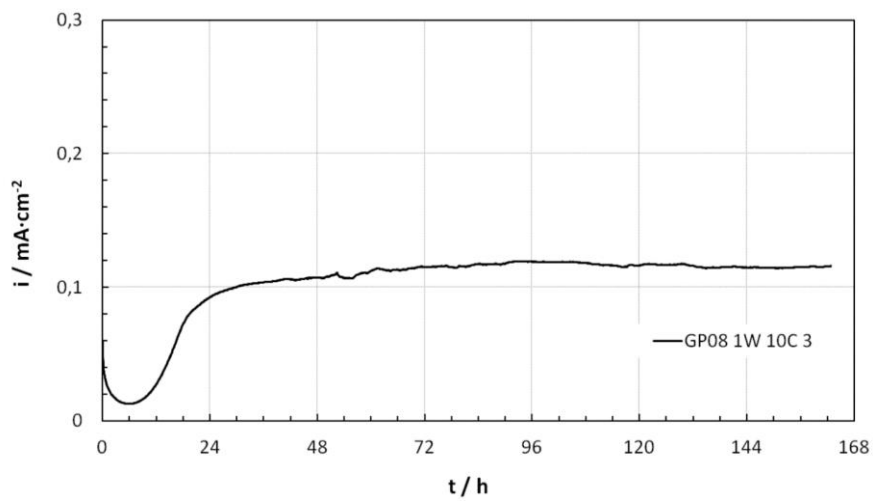
Figure 121: Current density-time curve of electrode GP08 1W 10C 3, from measurement series 7.

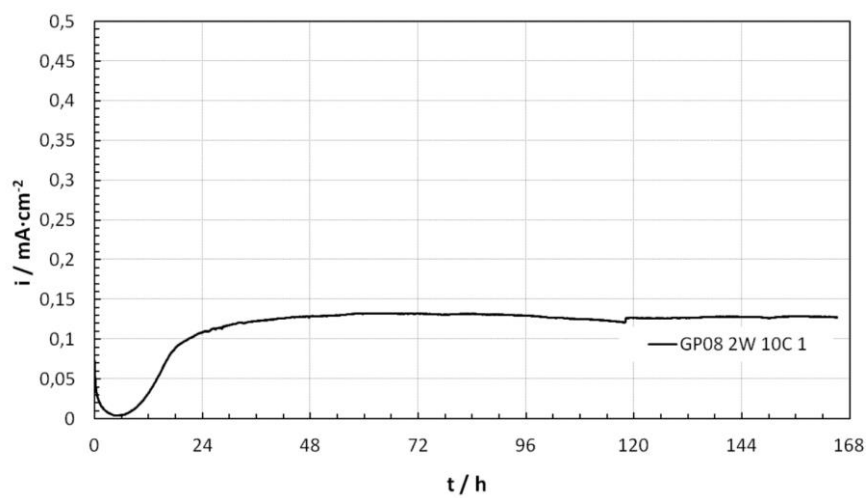**Figure 122:** Current density-time curve of electrode GP08 1.2W 10C 1, from measurement series 9.

**Figure 123:** Stromdichte-Zeit-Kurve der Elektrode GP08 1.2W 10C 2, aus Messreihe 9.

Figure 124: Current density-time curve of electrode GP08 1.2WX 10C 1, from measurement series 10.

Figure 125: Current density-time curve of electrode GP08 1.5W 10C 1, from measurement series 5.

Figure 126: Current density-time curve of electrode GP08 1.5W 10C 2, from measurement series 6.

Figure 127: Current density-time curve of electrode GP08 1.5W 10C 3, from measurement series 7.

Figure 128: Current density-time curve of electrode GP08 1.7W 10C 1, from measurement series 9.

Figure 129: Current density-time curve of electrode GP08 1.7W 10C 2, from measurement series 10.

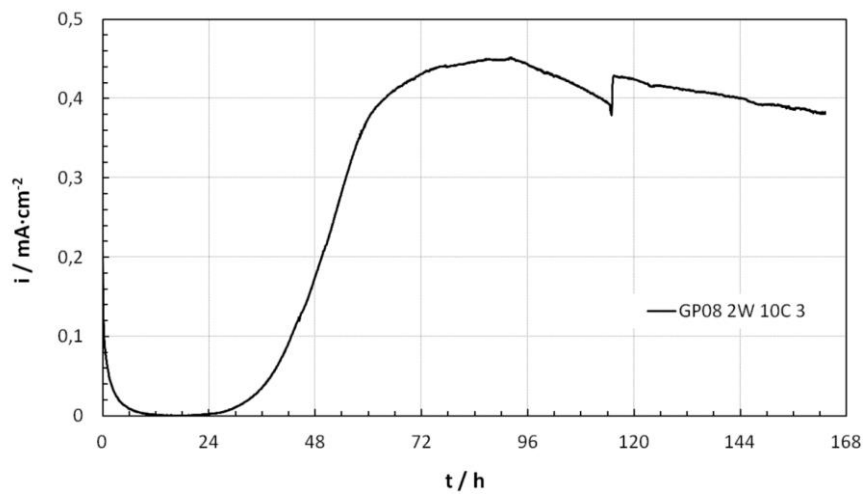**Figure 130:** Current density-time curve of electrode GP08 1.7WX 10C 1, from measurement series 10.

A-16
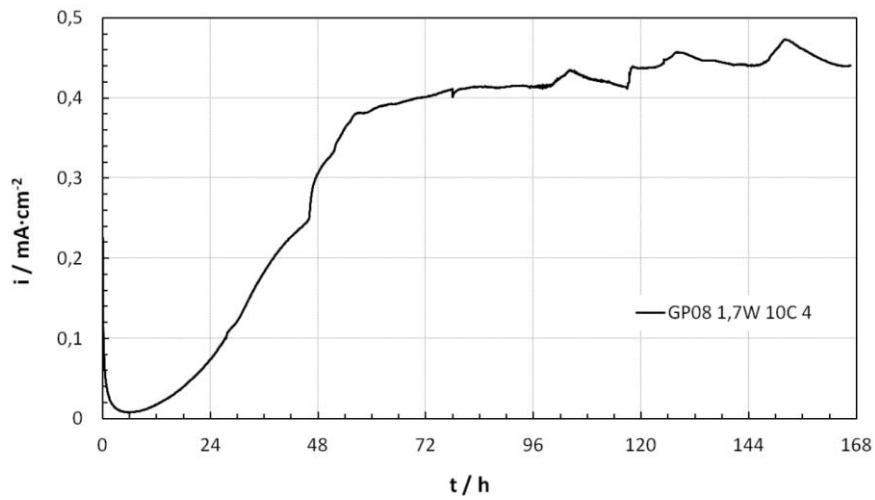
Figure 131: Current density-time curve of electrode GP08 1.7W 10C 4, from measurement series 13.
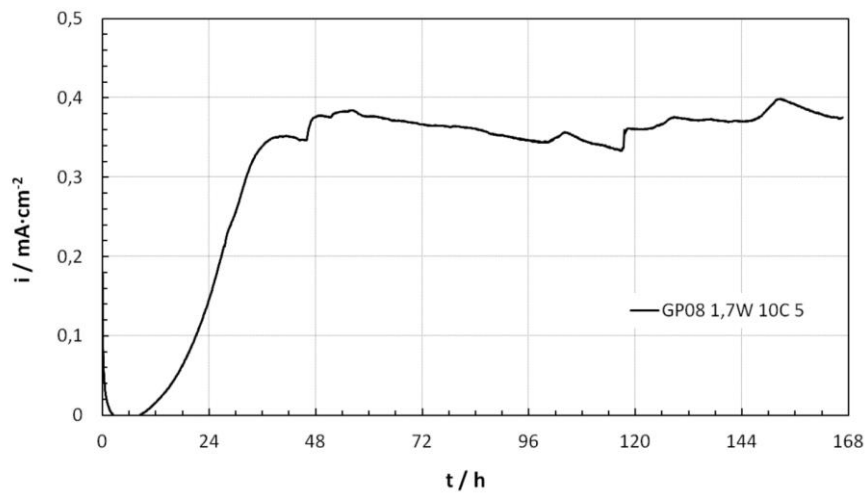
Figure 132: Current density-time curve of electrode GP08 1.7W 10C 5, from measurement series 13.
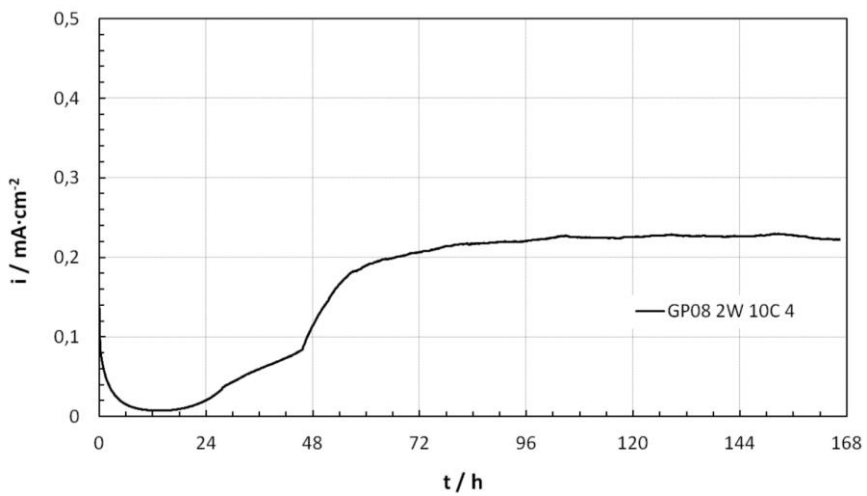

Figure 133: Current density-time curve of electrode GP08 2W 10C 1, from measurement series 5.
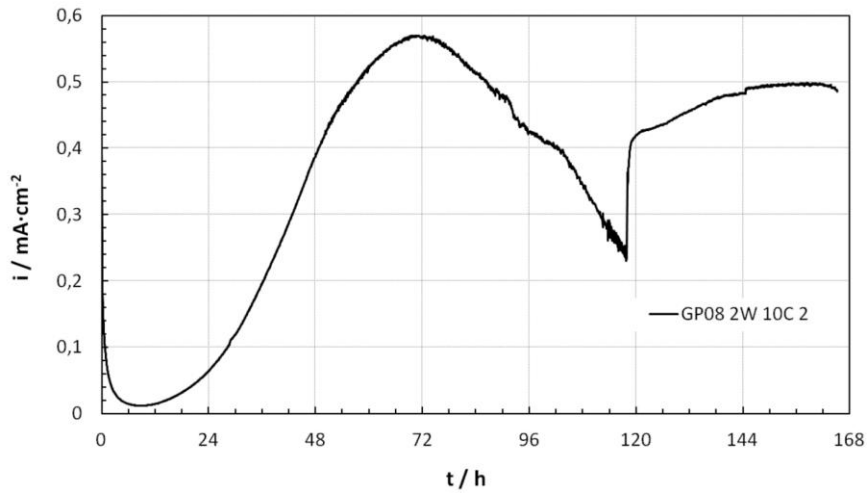
Figure 134: Current density-time curve of electrode GP08 2W 10C 2, from measurement series 6.
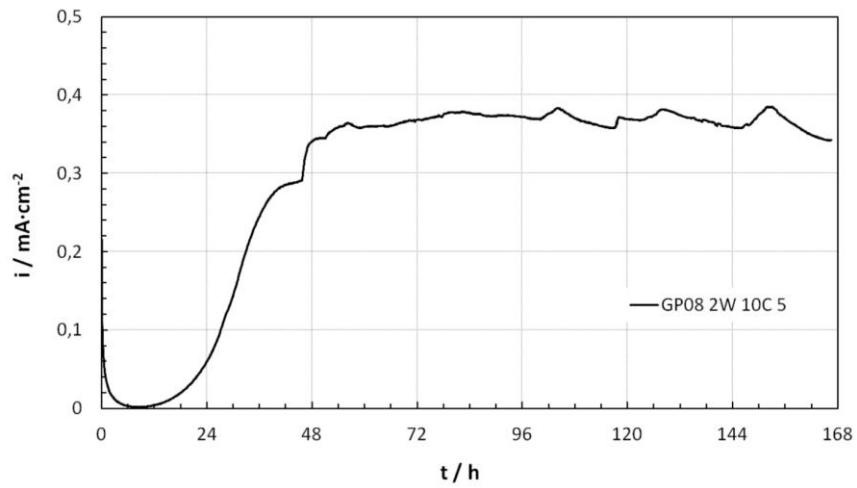

Figure 135: Current density-time curve of electrode GP08 2W 10C 3, from measurement series 8.
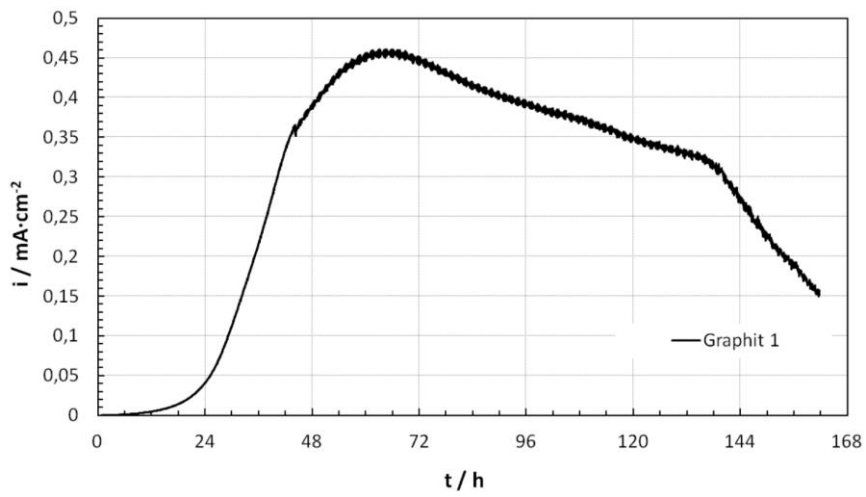

Figure 136: Current density-time curve of electrode GP08 2W 10C 4, from measurement series 13.
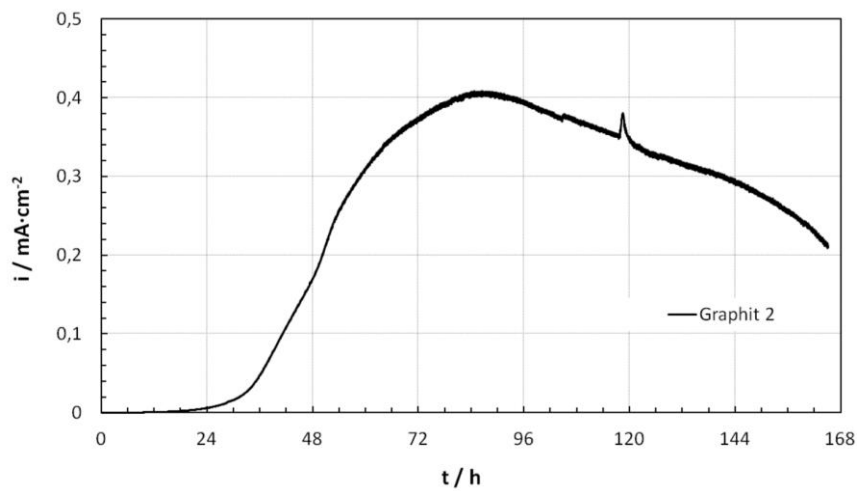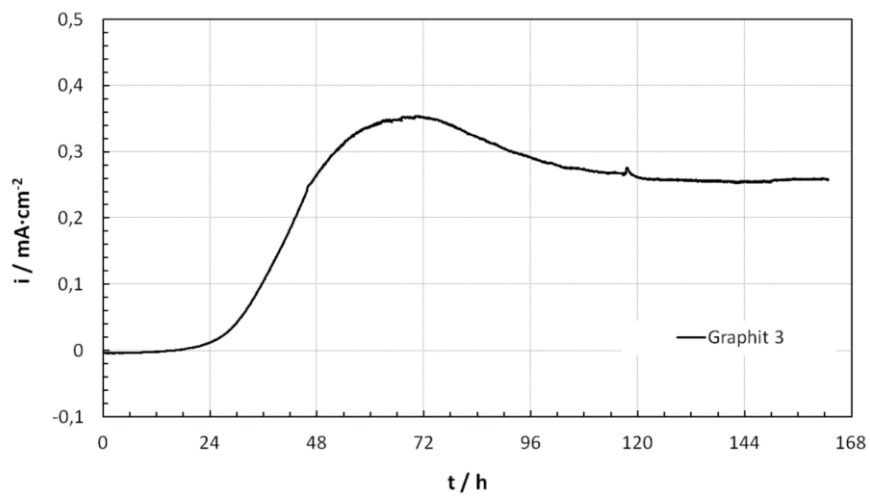
Figure 137: Current density-time curve of electrode GP08 2W 10C 5, from measurement series 13.

Figure 138: Current density-time curve of electrode graphite 1, from measurement series 4.

Figure 139: Current density-time curve of electrode graphite 2, from measurement series 6.

Figure 140: Current density-time curve of electrode graphite 3, from measurement series 7.

826. GEOBACTER MEDIUM

NH₄Cl	1.50	g
Na₂HPO₄	0.60	g
KCl	0.10	g
Na-acetate	0.82	g
Trace element solution (see medium 141)	10.00	ml
Vitamin solution (see medium 141)	10.00	ml
Selenite-tungstate solution (see medium 385)	1.00	ml
Na₂-fumarate	8.00	g
NaHCO₃	2.50	g
Distilled water	980.00	ml

Dissolve ingredients (except fumarate and $NaHCO_3$), bring to a boil, cool down to room temperature while gasing the medium with 80% N_2 + 20% CO_2, and add the bicarbonate. Equilibrate the medium with the gas to reach a pH of 6.8. Dispense the medium in anoxic vials under N_2 + CO_2 gas atmosphere. After autoclaving add fumarate from an anoxic filter sterilized stock solution (e.g. 16% w/v Na_2-fumarate; add 0.5 ml/10 ml medium). Check medium pH which should be around 6.8.

141. METHANOGENIUM MEDIUM (H$_2$/CO$_2$)

KCl	0.34	g
MgCl$_2$ x 6 H$_2$O	4.00	g
MgSO$_4$ x 7 H$_2$O	3.45	g
NH$_4$Cl	0.25	g
CaCl$_2$ x 2 H$_2$O	0.14	g
K$_2$HPO$_4$	0.14	g
NaCl	18.00	g
Trace elements (see below)	10.00	ml
Fe(NH$_4$)$_2$(SO$_4$)$_2$ x 6 H$_2$O	2.00	mg
Na-acetate	1.00	g
Yeast extract (Oxoid)	2.00	g
Trypticase peptone (BD BBL)	2.00	g
Resazurin	1.00	mg
NaHCO$_3$	5.00	g
Vitamin solution (see below)	10.00	ml
L-Cysteine-HCl x H$_2$O	0.50	g
Na$_2$S x 9 H$_2$O	0.50	g
Distilled water	1000.00	ml

Dissolve ingredients (except bicarbonate, vitamins, cysteine and sulfide), bring medium to the boil, then cool to room temperature under 80% H$_2$ and 20% CO$_2$ gas mixture. Add and dissolve bicarbonate and adjust pH to 7.0, then autoclave under 80% H$_2$ and 20% CO$_2$ gas mixture. After sterilization add cysteine and sulfide from sterile anoxic stock solutions autoclaved under 100% N$_2$ gas. Vitamins are prepared under N$_2$ gas atmosphere and sterilized by filtration. For incubation use 80% H$_2$ and 20% CO$_2$ gas mixture at two atmospheres of pressure. Adjust pH of final medium to 6.8 – 7.0. If the medium is being used without gas mixture overpressure then adjust pH with a small amount of sterile anoxic 1 N HCl, if necessary.

Trace element solution:

Nitrilotriacetic acid	1.50	g
MgSO$_4$ x 7 H$_2$O	3.00	g
MnSO$_4$ x H$_2$O	0.50	g
NaCl	1.00	g
FeSO$_4$ x 7 H$_2$O	0.10	g
CoSO$_4$ x 7 H$_2$O	0.18	g
CaCl$_2$ x 2 H$_2$O	0.10	g
ZnSO$_4$ x 7 H$_2$O	0.18	g
CuSO$_4$ x 5 H$_2$O	0.01	g
KAl(SO$_4$)$_2$ x 12 H$_2$O	0.02	g

H_3BO_3	0.01	g
$Na_2MoO_4 \times 2\ H_2O$	0.01	g
$NiCl_2 \times 6\ H_2O$	0.03	g
$Na_2SeO_3 \times 5\ H_2O$	0.30	mg
Distilled water	1000.00	ml

First dissolve nitrilotriacetic acid and adjust pH to 6.5 with KOH, then add minerals. Final pH 7.0 (with KOH).

Vitamin solution:

Biotin	2.00	mg
Folic acid	2.00	mg
Pyridoxine-HCl	10.00	mg
Thiamine-HCl $\times$ 2 H_2O	5.00	mg
Riboflavin	5.00	mg
Nicotinic acid	5.00	mg
D-Ca-pantothenate	5.00	mg
Vitamin B_{12}	0.10	mg
p-Aminobenzoic acid	5.00	mg
Lipoic acid	5.00	mg
Distilled water	1000.00	ml

For DSM 1498, DSM 15558, and DSM 22353 adjust pH to 6.5.

For DSM 2373 increase the amount of trypticase to 6.00 g/l.

For DSM 4254 add a filter-sterilized, anoxic solution of L-histidine to a final concentration of 0.08 g/l.

For DSM 7268, DSM 7466, and DSM 15558 use only one atmosphere overpressure of 80% H_2 and 20% CO_2.

For DSM 15219, DSM 16458, DSM 18860, and DSM 21220 adjust pH to 7.5.

For DSM 15558 and DSM 16458 supplement medium after autoclaving with 0.50 g/l coenzyme M (mercaptoethanesulfonic acid) added from a filter-sterilized anoxic stock solution prepared under N_2. Use only one atmosphere overpressure of 80% H_2 and 20% CO_2.

385. DESULFOBACTERIUM CATECHOLICUM MEDIUM

Solution A:

Na$_2$SO$_4$	3.00	g
KH$_2$PO$_4$	0.20	g
NH$_4$Cl	0.30	g
NaCl	7.00	g
MgCl$_2$ x 6 H$_2$O	1.30	g
KCl	0.50	g
CaCl$_2$ x 2 H$_2$O	0.15	g
Resazurin	1.00	mg
Distilled water	870.00	ml

Solution B:

Trace element solution SL-10 (see medium 320)	1.00	ml

Solution C:

NaHCO$_3$	2.50	g
Distilled water	100.00	ml

Solution D:

Selenite-tungstate solution (see below)	1.00	ml

Solution E:

Na-benzoate	0.40	g
Distilled water	10.00	ml

Solution F:

Pyrocatechol	0.06	g
1 N HCl	0.06	ml
Distilled water	10.00	ml

Solution G:

Vitamin solution (see medium 141)	10.00	ml

Solution H:

Na$_2$S x 9 H$_2$O	0.40	g
Distilled water	10.00	ml

Solution A is gassed with 80% N$_2$ and 20% CO$_2$ gas mixture to reach a pH below 6 (at least 30 min), then autoclaved anoxically under the same gas mixture. Solutions B, D and H are autoclaved separately under 100% N$_2$ gas. Solution C is autoclaved under 80% N$_2$ and 20% CO$_2$ gas atmosphere. Solutions E, F and G are prepared under N$_2$ gas and sterilized by filtration. The pyrocatechol stock solution has to be prepared always freshly prior to use. Solution B to H are added to the sterile, cooled solution A in the sequence as indicated. The complete medium is distributed anoxically under 80% N$_2$ and 20% CO$_2$ gas atmosphere into appropriate vessels.